THE UNIVERSITY OF CHICAGO

PHOTONIC ENHANCEMENT OF SPIN QUBITS IN SILICON CARBIDE

A DISSERTATION SUBMITTED TO

THE FACULTY OF THE DIVISION OF THE PHYSICAL SCIENCES

IN CANDIDACY FOR THE DEGREE OF

DOCTOR OF PHILOSOPHY

DEPARTMENT OF PHYSICS

BY

ALEXANDER L. CROOK

CHICAGO, ILLINOIS

AUGUST 2021

Table of contents

List of figures

List of tables

Acknowledgements

The work presented in this thesis would not have been possible without the support of both faculty and friends. I have had the wonderful opportunity of meeting incredibly bright and charismatic individuals that have made graduate school a rich experience.

First and foremost, David has been a fantastic and supportive advisor. His unwavering belief in a difficult project was invaluable as I navigated through the trials and tribulations of silicon carbide nanofabrication. Despite the unfamiliar material system and many hours spent troubleshooting in the clean room, David provided a resolute faith in my abilities. He also helped facilitate my interactions with collaborators through graduate school from whom I learned a great deal about nanophotonics and fabrication. I also want to thank my committee members, David Schuster, Aashish Clerk, and Sidney Nagel, for their support throughout my graduate experience and their useful feedback on my progress.

My colleagues have been an essential part of my graduate school experience both academically and socially. When I first joined David's lab, the group had recently completed a transfer from UC Santa Barbara and was starting a fresh chapter in Chicago. The new Chicago students included me, Chris Anderson, Berk Kovos, Peter Mintun, Kevin Miao, and Sam Whiteley. The camaraderie we formed in the student office of the Jones lab was irreplaceable. In addition to working together all day on research, we would frequently stay up all night working together on problem sets or putting off those problem sets with videogames. On weekends we would go downtown and explore the vibrant city life with concerts, festivals, restaurants, bars, and sporting events all year round. Some of the fondest memories of my life were spent hanging out with my close colleagues in lab, as well as the with the rest of the physics and PME classes.

Specifically, I want to thank Chris Anderson for being the bedrock of our lab and an amazing friend throughout graduate school. Peter Mintun has been a beacon of joy always a willing companion for ice skating, golf, or going to get iced coffee in the dead of winter. Kevin Miao has been a dear friend and a close partner for silicon carbide research, the Chicago nightlife, and helping direct our PME summer softball team. Sam Whiteley and I braved the gauntlet of first-year physics classes together and also spent time exploring the city, struggling in the clean room, and performing experiments at Argonne. Berk Kovos was a steadying force in our rambunctious group, always displaying kindness and incredible hospitality in inviting us over for his decadent homemade brunches.

Of course, I wouldn't be where I am today without the guidance and mentorship of senior students and postdocs in the lab. Abram Falk oversaw my initial work with photonic crystals and set me on the path to continue the nanophotonics endeavor undertaken by Greg Calusine. Paolo Andrich was the first student I closely worked with and was a fantastic mentor for both clean room work and color center experiments. He was also one of the most hilarious members of lab and a true lifeforce of the group. David Christle was also an amazing colleague and mentor as I delved into the divacancy in silicon carbide. Chris Yale, Joseph Heremans, and Brian Zhou were also an inspiration to me and always willing to answer my questions. The 2017 Gordon research conference at Hong Kong with Brian, Masaya and I remains one of my favorite highlights from graduate school! Andrew Yeats, Paul Klimov, and Charlie de las Casas all provided support and insight and were a joy to converse with.

As the group made the move into the new William Eckhardt Research Center labs, we took on more students to help propel our efforts. Alexandre Bourassa was truly invaluable for the development of the silicon carbide effort and also a close friend throughout graduate school. Paul

Jerger, Masaya Fukami, Erzsebet Vincent, Grant Smith, Jonathan Karsch, Pratiti Deb, Ben Soloway, and Jacob Feder have all done a fantastic job of maintaining our work in diamond and other systems outside of silicon carbide. The divacancy itself has a bright future with Elena Glen, Joseph Blanton, and Cyrus Zeledon and I'm excited to see the work that they will produce. Of course, no lab is complete without its postdocs. Yeghishe Tsaturyan, Leah Weiss, Sam Bayliss, Gary Wolfowicz have been irreplaceable additions to the group and have each had a tremendous impact in the group's research. As our group's involvement with Argonne national lab has strengthened, the contributions of Joseph Heremans, Nazar Delegan, Sean Sullivan, and Alan Dibos have been a major driving force towards more ambitious distant entanglement projects.

Additionally I want to thank the PNF staff for working closely with me to help troubleshoot various fabrication procedures. Peter Duda, despite being swamped as a director, was always willing to listen and help with incredibly specific process obstacles and tool issues. Anna Mukhortova and Mike Medina were also invaluable in helping debug processes across all facets of the clean room. Sally Wolcott was always a beam of positivity and I am deeply saddened by her passing.

I also want to specifically thank Mary Pat Mccullough for being an absolutely fantastic administrative assistant with her combination of thoughtfulness, kindness, and responsiveness. I also want to thank Quing, Akeem, Rhys, and Frankie at the Kitchen at Billings and the Lutheran school refectory for their exuberant service and always providing me with a bright spot in my day.

Outside of the university, I want to acknowledge our collaborators for their support. Takeshi Ohshima and Hiroshi Abe at the National Institutes for Quantum and Radiological Science and Technology at Takasaki, Japan have been truly irreplaceable. Their reliability, responsiveness, and dedication made our divacancy work possible, as relativistic electron irradiation is a vital step

towards creating high quality divacancies. Evelyn Hu's group at Harvard university provided thoughtful insight on silicon carbide photonics and photoelectrochemical etching. Specifically, David Bracher and Xingyu Zhang helped us spearhead the silicon carbide photonics platform and its successful integration with spin defects.

Lastly, I want to thank my family for encouraging me throughout my graduate school experience and my pursuit of science throughout my life. I truly would not be where I am today without their support!

Abstract

The emergence of controllable quantum systems has led to exciting applications for quantum computation, communication, and metrology. Among the many candidate systems, silicon carbide has attracted interest as a solid-state quantum platform in a technologically mature semiconductor material. When one creates atomic defects in silicon carbide lattice, individual electrons become trapped in isolated energy levels in the band gap. These electron spins can then be optically initialized and read out while being coherently controlled through microwave frequency fields. This interface between spin and photon quantum states provides exciting opportunities for creating remote entanglement on a macroscopic length scale.

This thesis discusses the foundations of the divacancy in silicon carbide as a spin qubit and then presents the photonic enhancement of this system. More specifically, nanoscale photonic crystal cavities in silicon carbide are fabricated in order to modify the divacancy's zero-phonon line optical emission. This is vital for facilitating spin-photon and spin-spin entanglement protocols which rely on the emission of indistinguishable photons without losing coherence to phonons emitted into the lattice. A combination of electron-beam lithography and photoelectrochemical etching is employed to create suspended nanocavities in the 4H polytype. The combination of this structure with a centralized divacancy forms the foundational atom-cavity system studied in cavity quantum electrodynamics. As predicted from interactions with the cavity mode, a substantial Purcell enhancement of the divacancy zero-phonon line and a reduced excited state lifetime are observed. Additionally, we demonstrate spin control and coherence in these devices for the first time. More broadly, the cavity-emitter interactions in this system allow us to study transduction between spin and photonic degrees of freedom and provide a first step towards next generation hybrid devices.

Chapter 1

Introduction To Quantum Two Level Systems

1.1 Introduction – Quantum states

In many fields of physics, it is a common goal to quantify a system's characteristics through physically measurable quantities such as mass, charge, or velocity. These quantities then influence the system's behavior over time and its interactions with other systems. This idea extends to the realm of quantum physics, where the same fundamental properties set the foundations of so-called quantum states. A key distinction, however, is that instead of a continuous set of values these states can only assume quantized measures. For example, the magnetic flux through a superconducting loop can only take on integer multiples of the flux quantum $\Phi_0 = h/2e$, where h is Planck's constant and e is the charge of an electron. Other examples of quantum states or "qubits" include the position of a particle, the spin of an electron, and the polarization of a photon. In each of these examples the quantity of interest takes discretized values. What can be continuous, however, is the linear combination of different quantum states, which we will see shortly.

Generally speaking, there has been a great interest in the exploration of quantum systems due to their insight into fundamental physics and their recent emergence into quantum technologies. The fields of quantum computing, quantum communication, and quantum sensing all leverage the

unique properties of quantum mechanical states to gain an advantage over their "classical" counterparts. In order to bring these applications to fruition, we must be able to both understand how a quantum state behaves and be able to influence the system directly.

To begin this discussion, we must establish a convention of how a quantum state is represented. This is broadly described by the "wavefunction" of a particle or a group of particles. The quantum state, whatever it happens to be, is usually represented using bra-ket notation with the Greek letter ψ:

$$\text{quantum state} = |\psi\rangle \tag{1.1}$$

For example, we could have the following quantum states:

$$\text{photon number,} \qquad \{|n=0\rangle, |n=1\rangle, |n=2\rangle \dots\} \tag{1.2}$$

$$\text{electron spin,} \qquad \{|\uparrow\rangle, |\downarrow\rangle\} \tag{1.3}$$

$$\text{magntic flux,} \qquad \left\{\left|\frac{h}{2e}\right\rangle, \left|\frac{2h}{2e}\right\rangle, \left|\frac{3h}{2e}\right\rangle \dots\right\} \tag{1.4}$$

To make further headway in a mathematical description, we will limit ourselves to the most basic dimensionality of a quantum state: the two-level system (sometimes abbreviated TLS). Although this is a simplification, almost all practical quantum applications can be described in the language of a two-level system, so it serves as an incredibly powerful tool.

The first decision to be made for the two-level system is what basis to choose to describe states. This is similar to how several equivalent coordinate systems can be used to describe position in three-dimensional space, with the axes such as x/y/z serving as the basis of the description. It is worth noting that this basis choice does not need to be a permanent, as the basis can be changed at any point to give a mathematically equivalent representation of the state. Although any basis that

spans the possibilities of quantum states (termed the Hilbert space) is allowed, often the physics of the system itself allows for a natural choice. For the following discussions we will pick the abstract basis of $\{|0\rangle, |1\rangle\}$, which could represent, for example, the two spin states of an electron.

With this basis in hand, a quantum state can be generally represented as a complex linear combination of the two states:

$$|\psi\rangle = (a + ib)|0\rangle + (c + id)|1\rangle \tag{1.5}$$

Or, written as a vector

$$|\psi\rangle = \begin{pmatrix} a + ib \\ c + id \end{pmatrix} \tag{1.6}$$

All states have to be "normalized", which means:

$$(a + ib)^2 + (c + id)^2 = 1 \tag{1.7}$$

Physically, this means that upon measurement the state *must* either be $|0\rangle$ or $|1\rangle$, with a total probability that adds to 1. Additionally, it is physically insignificant to add or remove a global phase from this state. This means we can write:

$$|\psi\rangle = \begin{pmatrix} a + ib \\ c + id \end{pmatrix}, \qquad \text{or} \qquad |\psi\rangle = e^{i\phi} \begin{pmatrix} a + ib \\ c + id \end{pmatrix} \tag{1.8}$$

These are the same state in the sense that any physical measurement will give the exact same result. This is in contrast to a relative phase, in which:

$$|\psi\rangle = \begin{pmatrix} a + ib \\ c + id \end{pmatrix} \neq \begin{pmatrix} a + ib \\ (c + id)e^{i\phi} \end{pmatrix} \tag{1.9}$$

A common convention is to make the first entry completely real. That is to say:

$$|\psi\rangle = \begin{pmatrix} a+ib \\ c+id \end{pmatrix} = \begin{pmatrix} \gamma \\ \alpha+i\beta \end{pmatrix} \tag{1.10}$$

Where:

$$\gamma = \sqrt{a^2+b^2}, \qquad \alpha = (ac+bd)\sqrt{\frac{1}{a^2+b^2}}, \qquad \beta = (ad-bc)\sqrt{\frac{1}{a^2+b^2}} \tag{1.11}$$

So more explicitly:

$$|\psi\rangle = \begin{pmatrix} a+ib \\ c+id \end{pmatrix} = \begin{pmatrix} \sqrt{a^2+b^2} \\ (ac+bd)\sqrt{\frac{1}{a^2+b^2}} + i(ad-bc)\sqrt{\frac{1}{a^2+b^2}} \end{pmatrix} \tag{1.12}$$

Already, the description of a state in a simple two-level system has become quite complicated. To help provide some intuition for these expressions, we can interpret a quantum state geometrically, as will be discussed in the next section.

1.2 Bloch sphere representation of a two-level state

Any state of a two-level system can be represented as a point on the surface of a three-dimensional unit sphere termed the "Bloch sphere". Mathematically, a two-dimensional vector with a complex component is mapped to a three-dimensional vector in Cartesian space with real components. In this formalism, the z-axis corresponds to the proportion of $|0\rangle$ or $|1\rangle$, the x-axis encodes a real phase between the states, and the y-axis encodes an imaginary phase between the states. This formalism proves useful for describing the evolution of two-level system states, as we will see later. A schematic of the Bloch sphere is shown in the figure below:

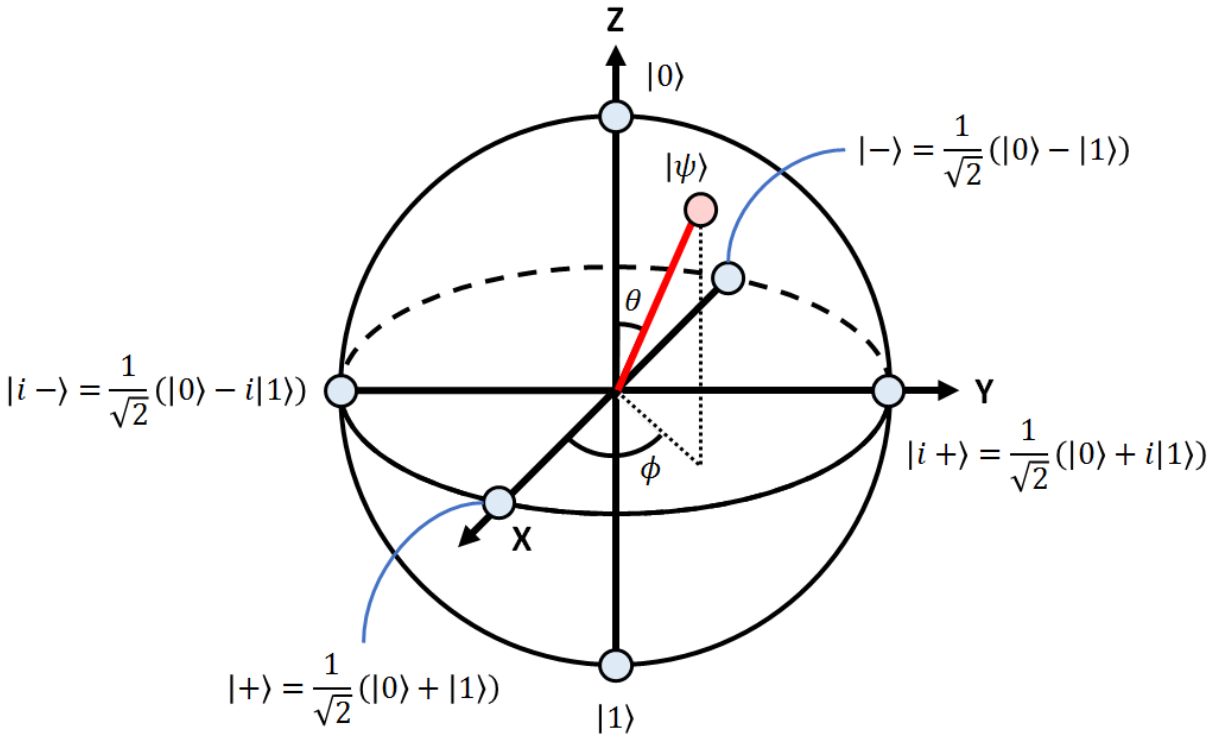

Figure 1.1 | The Bloch sphere. The red point represents an arbitrary state $|\psi\rangle$ with a polar angle θ and an azimuthal angle ϕ on the Bloch sphere. The six axis endpoints correspond to states as labeled in the figure.

The Bloch sphere uses the convention to make the first entry completely real:

$$\psi = \begin{pmatrix} \gamma \\ \alpha + i\beta \end{pmatrix}, \qquad \text{written as} \begin{pmatrix} |0\rangle \text{ component} \\ |1\rangle \text{ component} \end{pmatrix} \tag{1.13}$$

Where typically the first entry corresponds to the $|0\rangle$ state. In Bloch sphere coordinates, this state can be equivalently expressed as:

$$\psi = \begin{pmatrix} \cos\frac{\theta}{2} \\ e^{i\phi}\sin\frac{\theta}{2} \end{pmatrix} \tag{1.14}$$

Where θ is the polar angle with the z-axis and ϕ is the azimuthal angle with the x-axis. Using the above variables, the "Bloch sphere coordinates" of the quantum state ψ can be written as:

$$\text{Bloch sphere coordinates of } \psi, \qquad \vec{a} = \begin{pmatrix} x \\ y \\ z \end{pmatrix} = \begin{pmatrix} \sin\theta\cos\phi \\ \sin\theta\sin\phi \\ \cos\theta \end{pmatrix} = \begin{pmatrix} 2\alpha\gamma \\ 2\beta\gamma \\ 2\gamma^2 - 1 \end{pmatrix} \tag{1.15}$$

Or, if the original 2D state vector has two complex components:

$$\text{if } \psi = \begin{pmatrix} a + ib \\ c + id \end{pmatrix}, \qquad \text{then,} \qquad \vec{a} = \begin{pmatrix} 2(ac + bd) \\ 2(ad - bc) \\ 2(a^2 + b^2) - 1 \end{pmatrix} \tag{1.16}$$

Alternatively, if given an x, y, z coordinate of a Bloch sphere point, we can write the α, β, γ variables as:

$$x = 2\alpha\gamma, \qquad y = 2\beta\gamma, \qquad z = 2\gamma^2 - 1 \tag{1.17}$$

Which means

$$\alpha = \frac{x}{2}\sqrt{\frac{2}{z+1}}, \qquad \beta = \frac{y}{2}\sqrt{\frac{2}{z+1}}, \qquad \gamma = \sqrt{\frac{z+1}{2}} \tag{1.18}$$

With the Bloch sphere, time evolution and projective measurements now have a geometric interpretation. This interpretation is repeatedly used for two-level systems or any multi-level systems that can be reduced to two-level systems.

1.3 Measuring a quantum state

For practical applications we ultimately have to measure the quantum state, although there are several ways this can be done. Just as we had to pick a basis when representing a state, we also

must pick a basis for measurement. Once the basis is chosen, then each basis state can form its own "projection operator". For example for the $|0\rangle$ state,

$$|0\rangle = 0 \text{ state}, \qquad |0\rangle\langle 0| = 0 \text{ projection operator} \tag{1.19}$$

Measurements are then mathematically represented by sandwiching this projection operator with the wavefunction $|\psi\rangle$:

$$\langle\psi|0\rangle\langle 0|\psi\rangle = \text{returns value} \in [0,1] \text{ giving probability of measuring 0 state} \tag{1.20}$$

The returned quantity is the probability that measuring the wavefunction will return the projection operator state. This act of "sandwiching" an operator by the wavefunction ψ is more formally stated as the expectation value of the operator:

$$\langle\psi|A|\psi\rangle = \text{expectation value of operator } A \tag{1.21}$$

In this sense, the expectation value of the projection operator for a state $|x\rangle$ is the probability of finding the wavefunction in the $|x\rangle$ state. Probabilities must be normalized within a complete basis, so this means:

$$\langle\psi|0\rangle\langle 0|\psi\rangle + \langle\psi|1\rangle\langle 1|\psi\rangle = 1 \tag{1.22}$$

Sometimes, this is represented as the sum of squares of inner products:

$$|\langle\psi|0\rangle|^2 + |\langle\psi|1\rangle|^2 = 1 \tag{1.23}$$

After the measurement is made, the state will "collapse" to one of the eigenstates of the measurement basis, and that becomes the new state of the particle. Any previous superposition

information will disappear. In this sense the measurement of a quantum state entails some irreversible loss of information, as there are multiple starting states that can give the same measurement result.

Alternatively, for a two-level system we can geometrically project a state along a Cartesian axis on the Bloch sphere. Mathematically this can be represented as:

$$\langle \sigma_z \rangle = \langle \psi | \sigma_z | \psi \rangle = \text{returns value} \in [-1,1] \text{ giving projection along z axis} \tag{1.24}$$

Where the Pauli matrices are defined as:

$$\sigma_x = \begin{pmatrix} 0 & 1 \\ 1 & 0 \end{pmatrix}, \qquad \sigma_y = \begin{pmatrix} 0 & -i \\ i & 0 \end{pmatrix}, \qquad \sigma_z = \begin{pmatrix} 1 & 0 \\ 0 & -1 \end{pmatrix} \tag{1.25}$$

In this way the trio of expectation values of $\sigma_x, \sigma_y, \sigma_z$ uniquely defines a point on the Bloch sphere:

$$\langle \psi | \sigma_x | \psi \rangle = x, \qquad \langle \psi | \sigma_y | \psi \rangle = y, \qquad \langle \psi | \sigma_z | \psi \rangle = z \tag{1.26}$$

More generally, the expectation value of a spin operator gives the expected value of the spin when it is measured along the axis of the operator.

$$\langle \psi | S_i | \psi \rangle = \text{expected value of the spin when measured along axis } i \tag{1.27}$$

We will use this definition when dealing with the divacancy spin in chapter 2, which is a spin-1 system that occupies a three-dimensional Hilbert space.

1.4 Quantum dynamics of two-level systems

Now that we have outlined how to describe a stationary quantum state, it's now time to introduce the dynamics of quantum states. More specifically, this means the time evolution of a state either with or without an external field. This is where we first see the Hamiltonian and Schrodinger's equation put to use. It is no overstatement to say that the behavior predicted by these two components lay the foundation for nearly all of quantum mechanics. The ideas that are presented here for the two-level system will be extended to higher level systems in future chapters. By understanding how these systems naturally evolve, we can leverage their response to external fields to gain control over their behavior.

1.4.1 Hamiltonian of the two-level system

Up until now we have focused on characterizing of quantum states in a snapshot in time and measurement outcomes at an exact moment in time. We wish to broaden this discussion to time evolution of quantum states. To discuss this, we must introduce the Hamiltonian, which governs the time dynamics of a state. More specifically, we use the time-dependent Schrodinger equation to describe the dynamics of a closed quantum system:

$$i\hbar\frac{\partial}{\partial t}|\psi\rangle = \hat{H}|\psi\rangle \tag{1.28}$$

In the case of a two-level system, the Hamiltonian $\hat{H}$ is typically written as:

$$\widehat{H} = \frac{\hbar\omega_0}{2}(|e\rangle\langle e| - |g\rangle\langle g|) \tag{1.29}$$

where "e" denotes the excited state and "g" denotes the ground state, and $\hbar\omega_0$ is the energy splitting between the two states. If we choose the vector representation:

$$|e\rangle = \begin{pmatrix}1\\0\end{pmatrix}, \qquad |g\rangle = \begin{pmatrix}0\\1\end{pmatrix} \tag{1.30}$$

Then the Hamiltonian takes a 2x2 matrix form:

$$\widehat{H} = \frac{\hbar\omega_0}{2}\left(\begin{pmatrix}1\\0\end{pmatrix}(1 \quad 0) - \begin{pmatrix}0\\1\end{pmatrix}(0 \quad 1)\right) = \frac{\hbar\omega_0}{2}\begin{pmatrix}1 & 0\\0 & -1\end{pmatrix} \tag{1.31}$$

Note that this can also be written in terms of the more familiar Pauli z matrix:

$$\sigma_x = \begin{pmatrix}0 & 1\\1 & 0\end{pmatrix}, \qquad \sigma_y = \begin{pmatrix}0 & -i\\i & 0\end{pmatrix}, \qquad \sigma_z = \begin{pmatrix}1 & 0\\0 & -1\end{pmatrix} \tag{1.32}$$

So equivalently:

$$\widehat{H} = \frac{\hbar\omega_0}{2}\sigma_z \tag{1.33}$$

We are interested in the eigenvalues and corresponding eigenvectors of this Hamiltonian. Because the Hamiltonian matrix is already diagonal, they can be quickly determined as:

$$\lambda_1 = -\frac{\hbar\omega_0}{2}, \qquad \vec{v}_1 = \begin{pmatrix}0\\1\end{pmatrix} \tag{1.34}$$

$$\lambda_2 = +\frac{\hbar\omega_0}{2}, \qquad \vec{v}_2 = \begin{pmatrix}1\\0\end{pmatrix} \tag{1.35}$$

Here the eigenvalues represent the energies of the states. What the eigenvectors represent goes by many names. We could call these **stationary states, energy eigenstates, energy eigenkets, or energy eigenfunctions**. The point is that these states represent states with definite measurable energy. Furthermore (as given by the name "stationary") the energies of these states remain constant with time. I will use the term stationary states for this discussion. They are important for three main reasons:

1) The stationary states form an **orthonormal basis** that **spans the Hilbert space**. This means that any arbitrary state can be expressed as a complex linear combination of these stationary states.
2) They can be used to describe the **time-evolution of any state**. The general time-evolution of any state can be written as the sum of the separate time-evolution of each stationary state that composes the general state.
3) **The time evolution of stationary states is simple.** All that is needed is a multiplication by the time evolution operator $e^{-\frac{iEt}{\hbar}}$ (E is the energy of the state). Note that this only applies for stationary states!

It is worth expanding on point 3; where does this time-evolution operator come from? The fact that the stationary states are time-independent is important, as it allows us to use the **time-independent Schrodinger equation**:

$$\widehat{H}|\psi\rangle = E|\psi\rangle \tag{1.36}$$

This is a powerful step, as we can now make this substitution into the time-*dependent* Schrodinger equation:

$$i\hbar\frac{\partial}{\partial t}|\psi\rangle = \widehat{H}|\psi\rangle = E|\psi\rangle \tag{1.37}$$

Suddenly, with the Hamiltonian removed from the picture, this turns into a relatively simple first-order (only first derivatives) ordinary (only derivatives with respect to one variable) differential equation. This differential equation is also separable. We can rewrite this as:

$$\frac{\partial}{\partial t}|\psi\rangle = -\frac{iE}{\hbar}|\psi\rangle \tag{1.38}$$

This matches the form of the exponential differential equation:

$$\frac{dy}{dt} = ky, \qquad y(t) = Ce^{kt} \tag{1.39}$$

Applying this here, we have:

$$\psi(t) = Ce^{-\frac{iEt}{\hbar}} \tag{1.40}$$

Which gives the time-evolution operator. In this case the constant C is represents the initial state:

$$\psi(t) = \psi(0)e^{-\frac{iEt}{\hbar}} \tag{1.41}$$

What this means is that for a stationary state, we can obtain the state at any later time t by simply multiplying the state by the time-evolution operator $e^{-\frac{iEt}{\hbar}}$. This is the same statement as point 3 above.

We are now equipped to describe the time-evolution of any state in this two-level system. In the most general case, we have the state:

$$\Psi = \sum_{n=1}^{N} c_n \psi_n \tag{1.42}$$

In this case there are only two basis states, so N = 2. Here c_n is the (potentially complex) coefficient for the stationary state ψ_n. As per the above discussion, the time-evolution of this general state readily follows as:

$$\Psi(t) = \sum_{n=1}^{N} c_n \psi_n e^{-\frac{iE_n t}{\hbar}} \tag{1.43}$$

With the normalization condition:

$$\sum_{n=1}^{N} |c_n|^2 = 1 \tag{1.44}$$

Expanding $\Psi(t)$ for the two-level system, we have:

$$\Psi(t) = c_g \psi_g e^{-\frac{iE_g t}{\hbar}} + c_e \psi_e e^{-\frac{iE_e t}{\hbar}} \tag{1.45}$$

Here the labels "g" and "e" still denote "ground state" and "excited state". Making some substitutions of:

$$\psi_g = |g\rangle, \qquad \psi_e = |e\rangle, \qquad E_g = -\frac{\hbar\omega_0}{2}, \qquad E_e = \frac{\hbar\omega_0}{2} \tag{1.46}$$

Gives:

$$\Psi(t) = c_g |g\rangle e^{\frac{i\omega_0 t}{2}} + c_e |e\rangle e^{-\frac{i\omega_0 t}{2}} \tag{1.47}$$

This describes the time-evolution of any general state Ψ. In vector form, this is:

$$\Psi(t) = \begin{pmatrix} c_e e^{\frac{i\omega_0 t}{2}} \\ c_g e^{-\frac{i\omega_0 t}{2}} \end{pmatrix} \tag{1.48}$$

Note that we can factor out an exponential factor:

$$\Psi(t) = e^{\frac{i\omega_0 t}{2}}\left(c_g|g\rangle + c_e|e\rangle e^{-i\omega_0 t}\right) \tag{1.49}$$

Or, equivalently:

$$\Psi(t) = e^{-\frac{i\omega_0 t}{2}}\left(c_g|g\rangle e^{i\omega_0 t} + c_e|e\rangle\right) \tag{1.50}$$

The interpretation of this is phase is that each stationary state accumulates phase at a different rate, dependent on the energy difference between the states. In the Bloch sphere representation of a state, this is what is responsible for the natural "precession" of any state that is not at one of the poles. In this sense, the time-evolution operator itself is responsible for the natural rotation on the Bloch sphere. The time-evolution operator itself, in turn, comes from solving the exponential differential equation (i.e., the time-independent Schrodinger equation) for a stationary state ψ.

1.4.2 State evolutions on the Bloch sphere

The solution obtained in the previous section can be visualized as an evolution on the Bloch sphere. If we take the solution:

$$\Psi(t) = e^{\frac{i\omega_0 t}{2}}\left(c_g|g\rangle + c_e|e\rangle e^{-i\omega_0 t}\right) \tag{1.51}$$

And drop a global phase, we obtain:

$$\Psi(t) = c_g|g\rangle + c_e|e\rangle e^{-i\omega_0 t} \tag{1.52}$$

Or, following the Bloch sphere convention of $|g\rangle = |0\rangle$ and $|e\rangle = |1\rangle$:

$$\Psi(t) = c_0|0\rangle + c_1|1\rangle e^{-i\omega_0 t} \tag{1.53}$$

Keeping in mind the Bloch sphere coordinate of a state is:

$$|\psi\rangle = \begin{pmatrix} \cos\frac{\theta}{2} \\ e^{i\phi}\sin\frac{\theta}{2} \end{pmatrix} \tag{1.54}$$

This means that we have:

$$\Psi(t) = \begin{pmatrix} c_0 \\ c_1 e^{-i\omega_0 t} \end{pmatrix}, \qquad c_0 = \cos\frac{\theta}{2}, \qquad c_1 = \sin\frac{\theta}{2}, \qquad \phi = -\omega_0 t \tag{1.55}$$

The geometric interpretation of this is that the polar angle will be fixed depending on the values of c_0 and c_1 and the azimuthal angle will rotate in the clockwise direction (when viewed from +z) with an angular velocity of ω_0. This means that any pure state on the surface on the Bloch sphere will trace out a circle parallel to the xy plane as time elapses, regardless of what the fixed z-coordinate is. We refer to this as the Larmor precession of the state around the Bloch sphere. A sketch of this evolution is given in figure 1.2.

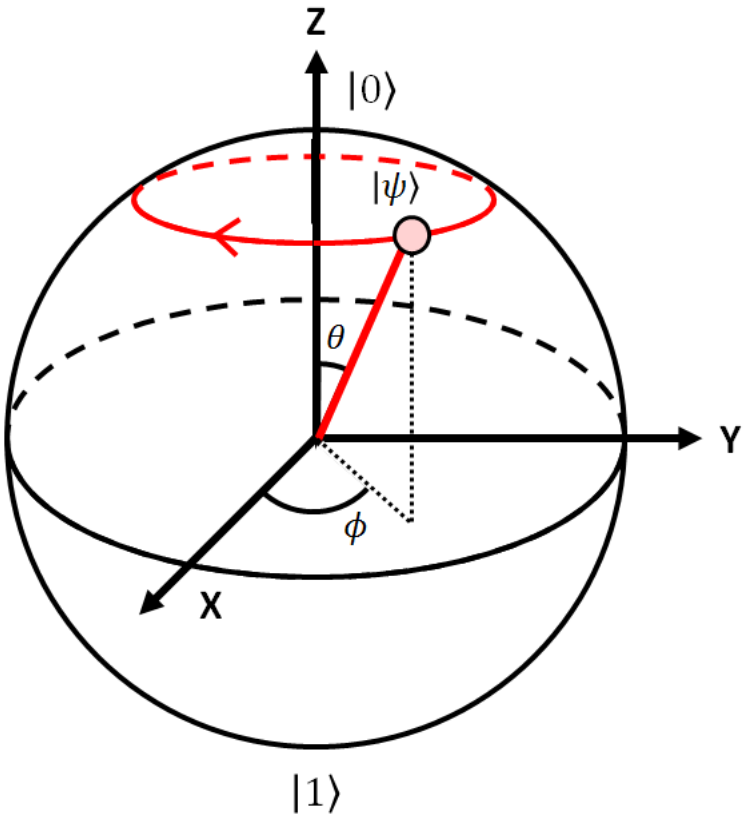

Figure 1.2 | Time evolution of a pure state on the Bloch sphere due to Larmor precession. Without external fields, a state $|\psi\rangle$ (red dot) will precess around the z-axis of the Bloch sphere (red circle). The speed of this precession is proportional to the energy different between the $|0\rangle$ and $|1\rangle$ states.

Given that the state is rotating uniformly around the z-axis, it is also possible to instead rotate the coordinate system itself such that the Bloch vector appears to be stationary. This is known as entering the "rotating frame" of the Bloch sphere, which is useful for visualizing rotations around the rotating x and y axes when microwave drives are added to the system.

1.5 Rabi oscillations of a two-level system

The interaction between a two-level system and a drive field, for our purposes, will be governed by the dipole interaction with either a magnetic or electric field. This is given by:

$$H_{field} = -\vec{d} \cdot \vec{E} \tag{1.56}$$

where $\vec{d}$ is the dipole moment operator and $\vec{E}$ is the applied electric field. We will focus on both of these elements individually before moving on.

We will be focusing on the example where the electric field is aligned along the axis of the dipole, so the dot product becomes a regular product. With this in mind, we turn to the form of the electric field. We will focus on a sinusoidally varying electric field. This is sometimes expressed as:

$$\vec{E}(t) = \vec{E}_0 e^{-i\omega_L t} + \vec{E}_0^* e^{i\omega_L t} \tag{1.57}$$

Where $\vec{E}_0^*$ is the complex conjugate of the amplitude $\vec{E}_0$. Assuming that these amplitudes are complex numbers of the same magnitude, they can be written in the form $Ae^{i\phi}$. In this form, we see that we are simply expressing an arbitrary phase ϕ on a cosine wave:

$$\vec{E}(t) = Ae^{i\phi} e^{-i\omega_L t} + Ae^{-i\phi} e^{i\omega_L t} \tag{1.58}$$

$$\vec{E}(t) = Ae^{-i(\omega_L t - \phi)} + Ae^{i(\omega_L t - \phi)} \tag{1.59}$$

$$\vec{E}(t) = A\left(e^{-i(\omega_L t - \phi)} + e^{i(\omega_L t - \phi)}\right) \tag{1.60}$$

$$\vec{E}(t) = A(2\cos(\omega_L t - \phi)) \tag{1.61}$$

$$\vec{E}(t) = 2A\cos(\omega_L t - \phi) \tag{1.62}$$

For simplicity, we will assume the phase of the electric field is zero, which gives:

$$\vec{E}(t) = \vec{E}_0 \cos \omega t\,, \qquad \vec{E}_0 = \vec{E}_0^* \left(\vec{E}_0 \in \mathbb{R}\right) \tag{1.63}$$

Assuming the electric field oscillations are along the axis of the dipole, we can drop the vectors:

$$E(t) = E_0 \cos \omega t \tag{1.64}$$

We will also need to introduce the dipole moment operator $\vec{d}$:

$$\vec{d} = -\left(\vec{d}_{eg}|e\rangle\langle g| + \vec{d}_{eg}^*|g\rangle\langle e|\right) \tag{1.65}$$

For the divacancy system, it is a safe assumption to say $\vec{d}_{eg} = \vec{d}_{eg}^*$. This will simplify the derivations in this section and later in chapter 2. In matrix form, $\vec{d}$ then becomes:

$$\vec{d} = -\begin{pmatrix} 0 & \vec{d}_{eg} \\ \vec{d}_{eg} & 0 \end{pmatrix} \tag{1.66}$$

So the Hamiltonian becomes:

$$H_{field} = -\begin{pmatrix} 0 & \vec{d}_{eg} \\ \vec{d}_{eg} & 0 \end{pmatrix} \cdot \vec{E}_0 \cos \omega t \tag{1.67}$$

Recalling that the dot product is a regular product here, the vector drops to give:

$$H_{field} = -\begin{pmatrix} 0 & d_{eg} E_0 \cos \omega t \\ d_{eg} E_0 \cos \omega t & 0 \end{pmatrix} \tag{1.68}$$

For further analysis, we will convert the cosine back to the complex exponential form:

$$H_{field} = -\begin{pmatrix} 0 & \frac{d_{eg} E_0}{2}\left(e^{i\omega t} + e^{-i\omega t}\right) \\ \frac{d_{eg} E_0}{2}\left(e^{i\omega t} + e^{-i\omega t}\right) & 0 \end{pmatrix} \tag{1.69}$$

We now define:

$$\hbar\Omega \equiv \frac{d_{eg}E_0}{2} \tag{1.70}$$

Which gives:

$$H_{field} = -\begin{pmatrix} 0 & \hbar\Omega\left(e^{i\omega t} + e^{-i\omega t}\right) \\ \hbar\Omega\left(e^{i\omega t} + e^{-i\omega t}\right) & 0 \end{pmatrix} \tag{1.71}$$

Dropping the negative sign:

$$H_{field} = \begin{pmatrix} 0 & \hbar\Omega\left(e^{i\omega t} + e^{-i\omega t}\right) \\ \hbar\Omega\left(e^{i\omega t} + e^{-i\omega t}\right) & 0 \end{pmatrix} \tag{1.72}$$

Keep in mind this can take the form $\hbar\Omega \approx \vec{\mu} \cdot \vec{B}$ for magnetic field driving. This H_{field} will be added to the bare two-level Hamiltonian:

$$\widehat{H}_{atom} = \frac{\hbar\omega_0}{2}\begin{pmatrix} 1 & 0 \\ 0 & -1 \end{pmatrix} \tag{1.73}$$

To give:

$$\widehat{H} = \hbar\begin{pmatrix} \frac{\omega_0}{2} & \Omega\left(e^{i\omega t} + e^{-i\omega t}\right) \\ \Omega\left(e^{i\omega t} + e^{-i\omega t}\right) & -\frac{\omega_0}{2} \end{pmatrix} \tag{1.74}$$

Solving for the time evolution of a state subject to this Hamiltonian is now difficult because we have time varying terms in the Hamiltonian itself. Ideally, we would be able to somehow remove this dependence and then use the same approach with time-evolution operators that we used for the bare two-level system. This is indeed possible for this particular situation, as we will outline in the next section.

1.5.1 Generalized interaction picture approach

At its heart, the "interaction picture" is simply the process inserting identities into Schrodinger's equation. Starting with the original time-dependent Schrodinger's equation:

$$i\hbar\frac{\partial}{\partial t}\Psi = H\Psi \tag{1.75}$$

We now insert the product PP^{-1} in various places in this equation, where the invertible matrix P is yet to be determined. Given that PP^{-1} is the identity matrix, this should have no effect on the equation:

$$i\hbar\frac{\partial}{\partial t}(PP^{-1}\Psi) = (PP^{-1})H(PP^{-1})\Psi \tag{1.76}$$

$$i\hbar\frac{\partial}{\partial t}(PP^{-1}\Psi) = P(P^{-1}HP)P^{-1}\Psi \tag{1.77}$$

If we now define a new wavefunction Φ given by:

$$\Phi \equiv P^{-1}\Psi \tag{1.78}$$

with the important matching initial condition:

$$\Phi(0) = \Psi(0) \tag{1.79}$$

Then the equation becomes:

$$i\hbar\frac{\partial}{\partial t}(P\Phi) = P(P^{-1}HP)\Phi \tag{1.80}$$

Using the chain rule for the time derivative:

$$i\hbar\left(\frac{\partial P}{\partial t}\Phi + P\frac{\partial \Phi}{\partial t}\right) = P(P^{-1}HP)\Phi \tag{1.81}$$

Rearranging:

$$i\hbar P\frac{\partial \Phi}{\partial t} = P(P^{-1}HP)\Phi - i\hbar\frac{\partial P}{\partial t}\Phi \tag{1.82}$$

$$i\hbar\frac{\partial \Phi}{\partial t} = (P^{-1}HP)\Phi - i\hbar P^{-1}\frac{\partial P}{\partial t}\Phi \tag{1.83}$$

$$i\hbar\frac{\partial \Phi}{\partial t} = \left(P^{-1}HP - i\hbar P^{-1}\frac{\partial P}{\partial t}\right)\Phi \tag{1.84}$$

This is the key result from the interaction picture.

For an appropriate choice of P, we can exchange our original Hamiltonian H for a new Hamiltonian of the form $\left(P^{-1}HP - i\hbar P^{-1}\frac{\partial P}{\partial t}\right)$. At the face of it this might just seem like an overcomplication, but the right choice of P can (eventually) remove the time dependence.

1.5.2 Application of interaction approach to two-level system

We start with the two-level system Hamiltonian with a field drive:

$$\widehat{H} = \hbar\begin{pmatrix} \frac{\omega_0}{2} & \Omega\left(e^{i\omega t} + e^{-i\omega t}\right) \\ \Omega\left(e^{i\omega t} + e^{-i\omega t}\right) & -\frac{\omega_0}{2} \end{pmatrix} \tag{1.85}$$

Our first choice for P will be given as follows, by convention:

$$P^{-1} = \exp\left(\frac{iH_{0,S}t}{\hbar}\right) \tag{1.86}$$

Here $H_{0,S}$ represents the time-independent part of the Hamiltonian, so:

$$H_{0,S} = \hbar\begin{pmatrix}\frac{\omega_0}{2} & 0\\ 0 & -\frac{\omega_0}{2}\end{pmatrix} \tag{1.87}$$

So:

$$P^{-1} = \exp\left(\frac{it}{\hbar}\hbar\begin{pmatrix}\frac{\omega_0}{2} & 0\\ 0 & -\frac{\omega_0}{2}\end{pmatrix}\right) = \exp\begin{pmatrix}\frac{i\omega_0 t}{2} & 0\\ 0 & -\frac{i\omega_0 t}{2}\end{pmatrix} \tag{1.88}$$

Diagonal matrices can be exponentiated element by element, so:

$$P^{-1} = \begin{pmatrix}\exp\left(\frac{i\omega_0 t}{2}\right) & 0\\ 0 & \exp\left(-\frac{i\omega_0 t}{2}\right)\end{pmatrix} \tag{1.89}$$

Which immediately gives P as:

$$P = \begin{pmatrix}\exp\left(-\frac{i\omega_0 t}{2}\right) & 0\\ 0 & \exp\left(\frac{i\omega_0 t}{2}\right)\end{pmatrix} \tag{1.90}$$

To get the full modified Hamiltonian, we can start with the product $P^{-1}HP$. Incidentally, this is sometimes called the "interaction part" of the Hamiltonian

$$P^{-1}HP = \begin{pmatrix} \exp\left(\frac{i\omega_0 t}{2}\right) & 0 \\ 0 & \exp\left(-\frac{i\omega_0 t}{2}\right) \end{pmatrix} \hbar \begin{pmatrix} \frac{\omega_0}{2} & \Omega\left(e^{i\omega t} + e^{-i\omega t}\right) \\ \Omega\left(e^{i\omega t} + e^{-i\omega t}\right) & -\frac{\omega_0}{2} \end{pmatrix} \cdot \begin{pmatrix} \exp\left(-\frac{i\omega_0 t}{2}\right) & 0 \\ 0 & \exp\left(\frac{i\omega_0 t}{2}\right) \end{pmatrix} \tag{1.91}$$

$$P^{-1}HP = \hbar \begin{pmatrix} \frac{\omega_0}{2} & \Omega\left(e^{i(\omega+\omega_0)t} + e^{-i(\omega-\omega_0)t}\right) \\ \Omega\left(e^{i(\omega-\omega_0)t} + e^{-i(\omega+\omega_0)t}\right) & -\frac{\omega_0}{2} \end{pmatrix} \tag{1.92}$$

Now moving on to the other component, $i\hbar P^{-1}\frac{\partial P}{\partial t}$:

$$i\hbar P^{-1}\frac{\partial P}{\partial t} = i\hbar \begin{pmatrix} \exp\left(\frac{i\omega_0 t}{2}\right) & 0 \\ 0 & \exp\left(-\frac{i\omega_0 t}{2}\right) \end{pmatrix} \frac{\partial}{\partial t} \begin{pmatrix} \exp\left(-\frac{i\omega_0 t}{2}\right) & 0 \\ 0 & \exp\left(\frac{i\omega_0 t}{2}\right) \end{pmatrix} \tag{1.93}$$

Derivatives are done element by element:

$$i\hbar P^{-1}\frac{\partial P}{\partial t} = i\hbar \begin{pmatrix} \exp\left(\frac{i\omega_0 t}{2}\right) & 0 \\ 0 & \exp\left(-\frac{i\omega_0 t}{2}\right) \end{pmatrix} \begin{pmatrix} -\frac{i\omega_0}{2}\exp\left(-\frac{i\omega_0 t}{2}\right) & 0 \\ 0 & \frac{i\omega_0}{2}\exp\left(\frac{i\omega_0 t}{2}\right) \end{pmatrix} \tag{1.94}$$

This simplifies to:

$$i\hbar P^{-1}\frac{\partial P}{\partial t} = \hbar \begin{pmatrix} \frac{\omega_0}{2} & 0 \\ 0 & -\frac{\omega_0}{2} \end{pmatrix} \tag{1.95}$$

Which here, is just the original Hamiltonian for the basic two-level system. So combined, the new Hamiltonian is:

$$H_{new} = P^{-1}HP - i\hbar P^{-1}\frac{\partial P}{\partial t} = \hbar\begin{pmatrix} 0 & \Omega\left(e^{i(\omega+\omega_0)t} + e^{-i(\omega-\omega_0)t}\right) \\ \Omega\left(e^{i(\omega-\omega_0)t} + e^{-i(\omega+\omega_0)t}\right) & 0 \end{pmatrix} \quad (1.96)$$

Applying the rotating wave approximation here gives:

$$H_{new} = \hbar\begin{pmatrix} 0 & \Omega\left(e^{-i(\omega-\omega_0)t}\right) \\ \Omega\left(e^{i(\omega-\omega_0)t}\right) & 0 \end{pmatrix} \quad (1.97)$$

Now is an appropriate time to define a detuning:

$$\Delta \equiv \omega - \omega_0 \quad (1.98)$$

So:

$$H_{new} = \hbar\begin{pmatrix} 0 & \Omega e^{-i\Delta t} \\ \Omega e^{i\Delta t} & 0 \end{pmatrix} \quad (1.99)$$

This satisfies the modified Schrodinger equation:

$$i\hbar\frac{\partial \Phi}{\partial t} = H_{new}\Phi \quad (1.100)$$

Where the modified wave function is:

$$\Phi = P^{-1}\Psi = \begin{pmatrix} \exp\left(\frac{i\omega_0 t}{2}\right) & 0 \\ 0 & \exp\left(-\frac{i\omega_0 t}{2}\right) \end{pmatrix}\Psi \quad (1.101)$$

We will now repeat this procedure, with

$$i\hbar\frac{\partial \Phi}{\partial t} = H_{new}\Phi \quad (1.102)$$

Being converted to:

$$i\hbar\frac{\partial\Theta}{\partial t}=\left(P^{-1}H_{new}P-i\hbar P^{-1}\frac{\partial P}{\partial t}\right)\Theta \tag{1.103}$$

Where:

$$\Theta\equiv P^{-1}\Phi \tag{1.104}$$

First let's diagonalize H_{new}:

$$H_{new}=\hbar\begin{pmatrix}0 & \Omega e^{-i\Delta t}\\ \Omega e^{i\Delta t} & 0\end{pmatrix}=\hbar\begin{pmatrix}e^{\frac{-i\Delta t}{2}} & 0\\ 0 & e^{\frac{i\Delta t}{2}}\end{pmatrix}\begin{pmatrix}0 & \Omega\\ \Omega & 0\end{pmatrix}\begin{pmatrix}e^{\frac{i\Delta t}{2}} & 0\\ 0 & e^{\frac{-i\Delta t}{2}}\end{pmatrix} \tag{1.105}$$

Or, rearranged:

$$\begin{pmatrix}e^{\frac{i\Delta t}{2}} & 0\\ 0 & e^{\frac{-i\Delta t}{2}}\end{pmatrix}H_{new}\begin{pmatrix}e^{\frac{-i\Delta t}{2}} & 0\\ 0 & e^{\frac{i\Delta t}{2}}\end{pmatrix}=\hbar\begin{pmatrix}0 & \Omega\\ \Omega & 0\end{pmatrix} \tag{1.106}$$

This immediately provides us with our P^{-1} and P for the second round:

$$P^{-1}=\begin{pmatrix}e^{\frac{i\Delta t}{2}} & 0\\ 0 & e^{\frac{-i\Delta t}{2}}\end{pmatrix},\qquad P=\begin{pmatrix}e^{\frac{-i\Delta t}{2}} & 0\\ 0 & e^{\frac{i\Delta t}{2}}\end{pmatrix} \tag{1.107}$$

Which gives:

$$P^{-1}HP=\hbar\begin{pmatrix}e^{\frac{i\Delta t}{2}} & 0\\ 0 & e^{\frac{-i\Delta t}{2}}\end{pmatrix}\begin{pmatrix}0 & \Omega e^{-i\Delta t}\\ \Omega e^{i\Delta t} & 0\end{pmatrix}\begin{pmatrix}e^{\frac{-i\Delta t}{2}} & 0\\ 0 & e^{\frac{i\Delta t}{2}}\end{pmatrix}=\hbar\begin{pmatrix}0 & \Omega\\ \Omega & 0\end{pmatrix} \tag{1.108}$$

And:

$$i\hbar P^{-1}\frac{\partial P}{\partial t}=i\hbar\begin{pmatrix}e^{\frac{i\Delta t}{2}} & 0\\ 0 & e^{\frac{-i\Delta t}{2}}\end{pmatrix}\begin{pmatrix}-\frac{i\Delta}{2}e^{\frac{-i\Delta t}{2}} & 0\\ 0 & \frac{i\Delta}{2}e^{\frac{i\Delta t}{2}}\end{pmatrix} \tag{1.109}$$

$$i\hbar P^{-1}\frac{\partial P}{\partial t}=\frac{\hbar\Delta}{2}\begin{pmatrix}1 & 0\\ 0 & -1\end{pmatrix} \tag{1.110}$$

So in total, we have:

$$P^{-1}HP - i\hbar P^{-1}\frac{\partial P}{\partial t} = \hbar\begin{pmatrix}0 & \Omega\\ \Omega & 0\end{pmatrix} - \frac{\hbar\Delta}{2}\begin{pmatrix}1 & 0\\ 0 & -1\end{pmatrix} \tag{1.111}$$

$$P^{-1}HP - i\hbar P^{-1}\frac{\partial P}{\partial t} = \hbar\begin{pmatrix}-\frac{\Delta}{2} & \Omega\\ \Omega & \frac{\Delta}{2}\end{pmatrix} \tag{1.112}$$

$$H_{2nd} = \hbar\begin{pmatrix}-\frac{\Delta}{2} & \Omega\\ \Omega & \frac{\Delta}{2}\end{pmatrix} \tag{1.113}$$

Now the time dependence has been completely removed. The second round modified form of Schrodinger's equation is now gives:

$$i\hbar\frac{\partial\Theta}{\partial t} = H_{2nd}\Theta \tag{1.114}$$

$$i\hbar\frac{\partial\Theta}{\partial t} = \hbar\begin{pmatrix}-\frac{\Delta}{2} & \Omega\\ \Omega & \frac{\Delta}{2}\end{pmatrix}\Theta \tag{1.115}$$

Where:

$$\Theta = P^{-1}\Phi = \begin{pmatrix}e^{\frac{i\Delta t}{2}} & 0\\ 0 & e^{\frac{-i\Delta t}{2}}\end{pmatrix}\Phi = \begin{pmatrix}e^{\frac{i\Delta t}{2}} & 0\\ 0 & e^{\frac{-i\Delta t}{2}}\end{pmatrix}\begin{pmatrix}\exp\left(\frac{i\omega_0 t}{2}\right) & 0\\ 0 & \exp\left(-\frac{i\omega_0 t}{2}\right)\end{pmatrix}\Psi \tag{1.116}$$

$$\Theta = \begin{pmatrix}e^{\frac{i(\Delta+\omega_0)t}{2}} & 0\\ 0 & e^{\frac{-i(\Delta+\omega_0)t}{2}}\end{pmatrix}\Psi \tag{1.117}$$

$$\Theta = \begin{pmatrix}e^{\frac{i\omega t}{2}} & 0\\ 0 & e^{\frac{-i\omega t}{2}}\end{pmatrix}\Psi \tag{1.118}$$

We now have a more familiar situation, as the time-dependence in the Hamiltonian has been removed. We can proceed "normally" and get the eigenvalues and eigenvectors of this time-independent H:

$$\lambda_1 = -\frac{\hbar}{2}\sqrt{\Delta^2 + 4\Omega^2}, \qquad v_1 = \begin{pmatrix} \frac{\Delta - \sqrt{\Delta^2 + 4\Omega^2}}{2\Omega} \\ 1 \end{pmatrix} \tag{1.119}$$

$$\lambda_2 = \frac{\hbar}{2}\sqrt{\Delta^2 + 4\Omega^2}, \qquad v_2 = \begin{pmatrix} \frac{\Delta + \sqrt{\Delta^2 + \Omega^2}}{2\Omega} \\ 1 \end{pmatrix} \tag{1.120}$$

This tells us the stationary basis for the function Θ, which we can then relate to Ψ. The general evolution of a state can then be found if it is written in terms of these eigenstates.

$$\Psi(0) = \Phi(0) = \Theta(0) = c_1 \begin{pmatrix} \frac{\Delta - \sqrt{\Delta^2 + 4\Omega^2}}{2\Omega} \\ 1 \end{pmatrix} + c_2 \begin{pmatrix} \frac{\Delta + \sqrt{\Delta^2 + \Omega^2}}{2\Omega} \\ 1 \end{pmatrix} \tag{1.121}$$

We can use the time-evolution operator with definite energies to evolve the Θ state:

$$\Theta(t) = c_1 \begin{pmatrix} \frac{\Delta - \sqrt{\Delta^2 + 4\Omega^2}}{2\Omega} \\ 1 \end{pmatrix} e^{-\frac{iE_1 t}{\hbar}} + c_2 \begin{pmatrix} \frac{\Delta + \sqrt{\Delta^2 + \Omega^2}}{2\Omega} \\ 1 \end{pmatrix} e^{-\frac{iE_2 t}{\hbar}} \tag{1.122}$$

For E_1 and E_2 we use the eigenvalues we just solved for to give:

$$\Theta(t) = c_1 \begin{pmatrix} \frac{\Delta - \sqrt{\Delta^2 + 4\Omega^2}}{2\Omega} \\ 1 \end{pmatrix} e^{i\sqrt{\frac{\Delta^2}{4} + \Omega^2}t} + c_2 \begin{pmatrix} \frac{\Delta + \sqrt{\Delta^2 + \Omega^2}}{2\Omega} \\ 1 \end{pmatrix} e^{-i\sqrt{\frac{\Delta^2}{4} + \Omega^2}t} \tag{1.123}$$

Then to convert back to $\Psi(t)$:

$$\Psi(t) = \begin{pmatrix} e^{\frac{-i\omega t}{2}} & 0 \\ 0 & e^{\frac{i\omega t}{2}} \end{pmatrix} \Theta(t) \tag{1.124}$$

We plug in to get:

$$\Psi(t) = c_1 \begin{pmatrix} e^{\frac{-i\omega t}{2}} \dfrac{\Delta - \sqrt{\Delta^2 + 4\Omega^2}}{2\Omega} \\ e^{\frac{i\omega t}{2}} \end{pmatrix} e^{i\sqrt{\frac{\Delta^2}{4}+\Omega^2}t} + c_2 \begin{pmatrix} e^{\frac{-i\omega t}{2}} \dfrac{\Delta + \sqrt{\Delta^2 + \Omega^2}}{2\Omega} \\ e^{\frac{i\omega t}{2}} \end{pmatrix} e^{-i\sqrt{\frac{\Delta^2}{4}+\Omega^2}t} \tag{1.125}$$

Simplifying and removing the global phase gives:

$$\Psi(t) = c_1 \begin{pmatrix} \dfrac{\Delta}{2\Omega} - \dfrac{\sqrt{\frac{\Delta^2}{4} + \Omega^2}}{\Omega} \\ e^{i\omega t} \end{pmatrix} e^{i\left(\sqrt{\frac{\Delta^2}{4}+\Omega^2}\right)t} + c_2 \begin{pmatrix} \dfrac{\Delta}{2\Omega} + \dfrac{\sqrt{\frac{\Delta^2}{4} + \Omega^2}}{\Omega} \\ e^{i\omega t} \end{pmatrix} e^{-i\left(\sqrt{\frac{\Delta^2}{4}+\Omega^2}\right)t} \tag{1.126}$$

If the phase of the drive is nonzero (i.e., $\cos(\omega t + \phi)$ instead of $\cos(\omega t)$), the solution gets modified slightly to:

$$\Psi(t) = c_1 \begin{pmatrix} \dfrac{\Delta}{2\Omega} - \dfrac{\sqrt{\frac{\Delta^2}{4} + \Omega^2}}{\Omega} \\ e^{i(\omega t+\phi)} \end{pmatrix} e^{i\left(\sqrt{\frac{\Delta^2}{4}+\Omega^2}\right)t} + c_2 \begin{pmatrix} \dfrac{\Delta}{2\Omega} + \dfrac{\sqrt{\frac{\Delta^2}{4} + \Omega^2}}{\Omega} \\ e^{i(\omega t+\phi)} \end{pmatrix} e^{-i\left(\sqrt{\frac{\Delta^2}{4}+\Omega^2}\right)t} \tag{1.127}$$

We can simplify slightly by defining the variable:

$$r \equiv \sqrt{\frac{\Delta^2}{4} + \Omega^2} \tag{1.128}$$

To give the final result:

$$\Psi(t) = \begin{pmatrix} c_1 \dfrac{1}{\Omega}\left(\dfrac{\Delta}{2} - r\right) e^{irt} + c_2 \dfrac{1}{\Omega}\left(\dfrac{\Delta}{2} + r\right) e^{-irt} \\ \left(c_1 e^{irt} + c_2 e^{-irt}\right) e^{i(\omega t+\phi)} \end{pmatrix}, \qquad r \equiv \sqrt{\frac{\Delta^2}{4} + \Omega^2} \tag{1.129}$$

Some solutions of this equation in comparison to QuTiP models are shown below, and there is excellent agreement.

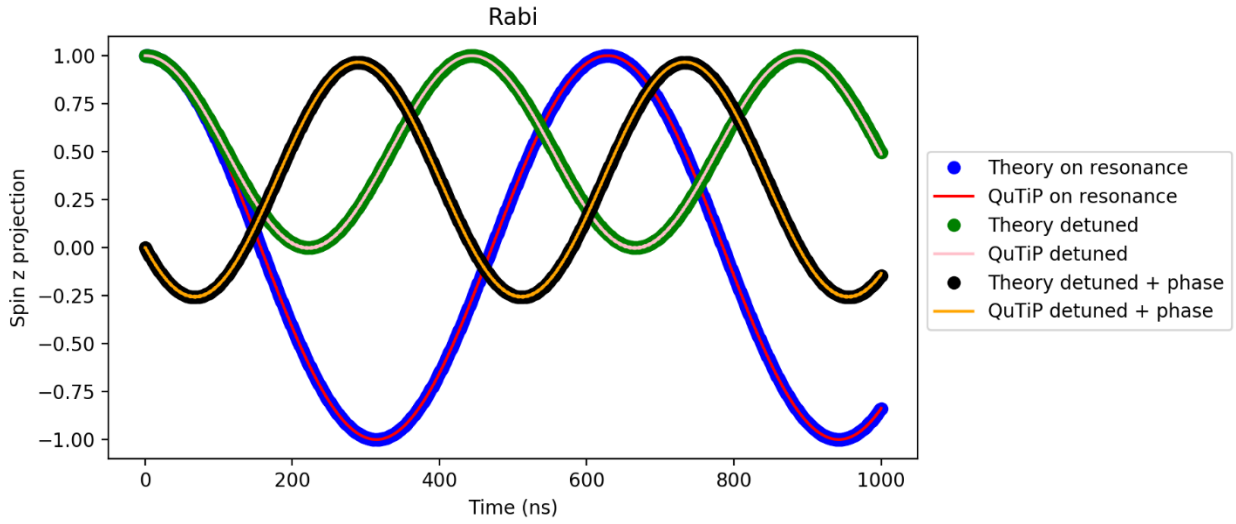

Figure 1.3 | Rabi oscillations from QuTiP and theoretical results. The theoretical result in equation 1.129 shows excellent agreement with QuTiP models for various conditions. For the detuned + phase plots, the initial state is $|+x\rangle$ instead of $|+z\rangle$ in order to avoid repeating the graphs from the detuned + no phase plots.

As one specific example, it is worth looking at the following case to get an intuition for Ω. The solution with zero detuning and zero phase is given by:

$$\Psi(t) = c_1 \begin{pmatrix} -1 \\ e^{i\omega t} \end{pmatrix} e^{i\Omega t} + c_2 \begin{pmatrix} 1 \\ e^{i\omega t} \end{pmatrix} e^{-i\Omega t} \tag{1.130}$$

Starting in the state $\Psi(0) = \begin{pmatrix} 1 \\ 0 \end{pmatrix}$ then gives:

$$\Psi(t) = -\frac{1}{2} \begin{pmatrix} -1 \\ e^{i\omega t} \end{pmatrix} e^{i\Omega t} + \frac{1}{2} \begin{pmatrix} 1 \\ e^{i\omega t} \end{pmatrix} e^{-i\Omega t} \tag{1.131}$$

$$\Psi(t) = \begin{pmatrix} \frac{1}{2}\left(e^{i\Omega t} + e^{-i\Omega t}\right) \\ \frac{1}{2} e^{i\omega t}\left(e^{-i\Omega t} - e^{i\Omega t}\right) \end{pmatrix} \tag{1.132}$$

Rewriting:

$$\Psi(t) = \begin{pmatrix} \cos(\Omega t) \\ -ie^{i\omega t}\sin(\Omega t) \end{pmatrix} \tag{1.133}$$

In this context, we see that Ω is the Rabi freuqnency:

$$\Omega = 2\pi f = \frac{2\pi}{T} = \text{Rabi frequency} \tag{1.134}$$

This is why the term Ω is called the Rabi frequency even though it appears as amplitude in the original field Hamiltonian:

$$H_{field} = -\begin{pmatrix} 0 & 2\hbar\Omega\cos\omega t \\ 2\hbar\Omega\cos\omega t & 0 \end{pmatrix}, \qquad \hbar\Omega \equiv \frac{d_{eg}E_0}{2} \tag{1.135}$$

1.5.3 Microwave rotations on the Bloch sphere

Returning to the Bloch sphere, it turns out that *any* oscillating field drive on a state in a two-level system can be mapped to a rotation on the Bloch sphere around a rotation axis $\vec{u}$. This must be framed with the slight caveat that we must be in the rotating frame for this to hold true. But once this transformation is made, the axis of rotation is solely determined by the frequency of detuning and the phase on the field drive. More specifically, the detuning frequency determines the polar angle of the rotation axis ($\theta = 90^o$ for no detuning), while the phase on the drive gives the azimuthal angle of the rotation axis ($\phi = 0$ for no phase). In the simplest case with no detuning and no phase on the drive, the rotation axis is along the x-axis. This is sometimes referred to as an "X gate". A schematic of this rotation is shown in the figure below:

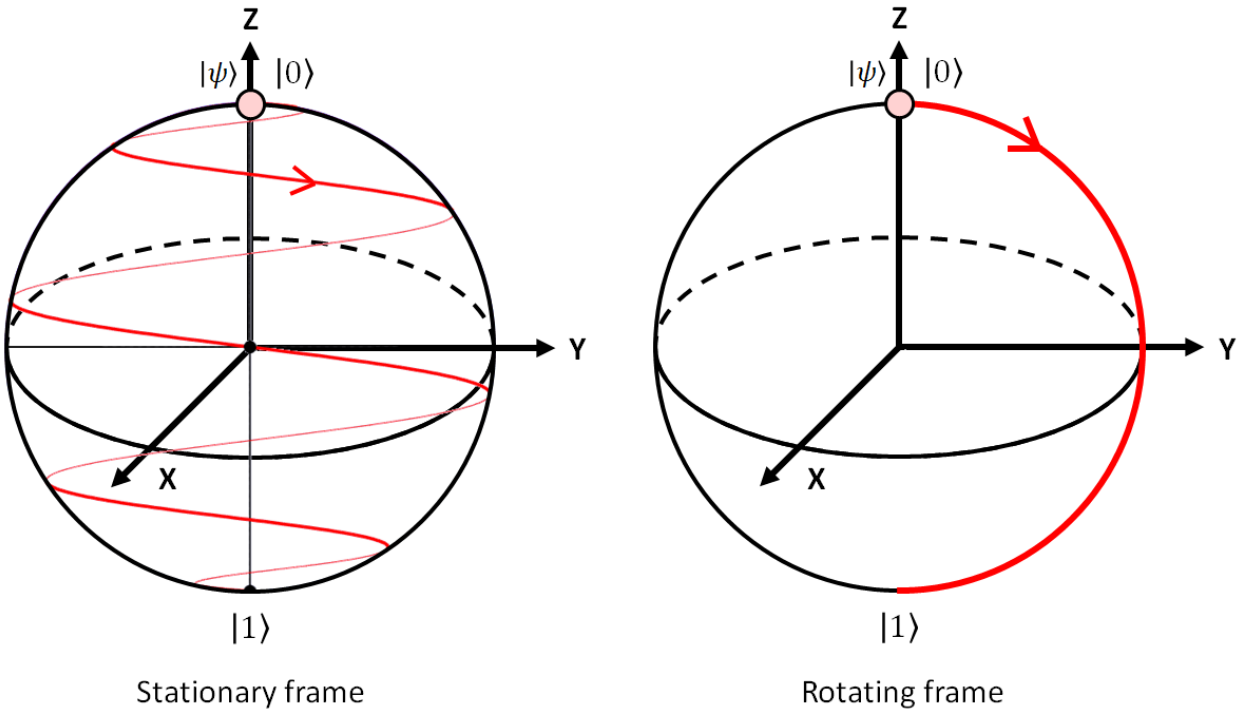

Figure 1.4 | State rotation on the Bloch sphere. In both pictures, an off-axis oscillating field drive causes a rotation from the $|0\rangle$ state to the $|1\rangle$ state. In the left picture, the Bloch sphere coordinate system is stationary, which results in a spherical spiral path. In the right picture, the coordinates rotate around the z-axis to match the Larmor precession of the system. In this "rotating frame" the field drive is a rotation around the x-axis for the case of no detuning or additional phase on the drive.

Before delving into more general rotations, we must first lay some mathematical groundwork on rotation matrices. General three-dimensional rotations can be described by a set of 3x3 rotation matrices defined as follows:

$$R_x(\theta) = \begin{pmatrix} 1 & 0 & 0 \\ 0 & \cos\theta & -\sin\theta \\ 0 & \sin\theta & \cos\theta \end{pmatrix} \tag{1.136}$$

$$R_y(\theta) = \begin{pmatrix} \cos\theta & 0 & \sin\theta \\ 0 & 1 & 0 \\ -\sin\theta & 0 & \cos\theta \end{pmatrix} \tag{1.137}$$

$$R_z(\theta) = \begin{pmatrix} \cos\theta & -\sin\theta & 0 \\ \sin\theta & \cos\theta & 0 \\ 0 & 0 & 1 \end{pmatrix} \tag{1.138}$$

Here the axis of rotation is given in the subscript, with the direction of rotation defined by the right-hand rule using that axis. A rotation matrix is multiplied by an initial vector to determine a new vector after the rotation. Mathematically this looks like:

$$R_n(\theta)v_{old} = v_{new}, \qquad v = \begin{pmatrix} x \\ y \\ z \end{pmatrix} \tag{1.139}$$

So for example, an "x" rotation would look like:

$$R_x(\theta) \cdot v = \begin{pmatrix} 1 & 0 & 0 \\ 0 & \cos\theta & -\sin\theta \\ 0 & \sin\theta & \cos\theta \end{pmatrix} \begin{pmatrix} x \\ y \\ z \end{pmatrix} = \begin{pmatrix} x \\ y\cos\theta - z\sin\theta \\ y\sin\theta + z\cos\theta \end{pmatrix} \tag{1.140}$$

More generally, the rotation does not have to about a Cartesian axis, but can be about any axis defined by a vector $\vec{u}$. If we write the most general rotation matrix as:

$$R = \begin{pmatrix} a & b & c \\ d & e & f \\ g & h & i \end{pmatrix} \tag{1.141}$$

Then the axis of rotation is given by:

$$\vec{u} = \begin{pmatrix} h - f \\ c - g \\ d - b \end{pmatrix} \tag{1.142}$$

And the angle of rotation is:

$$\theta = \sin^{-1}\left(\frac{|\vec{u}|}{2}\right) \tag{1.143}$$

With this in mind, there are two main cases to go through for the two-level system:

1) **Bloch sphere rotation with nonzero phase and zero detuning on drive**
2) **Bloch sphere rotation with nonzero detuning and zero phase on drive**

Nonzero phase and zero detuning

The rotation matrix works out to be:

$$R_n = \begin{pmatrix} \cos^2(\Omega t) + \cos(2\phi)\sin^2(\Omega t) & \sin 2\phi \sin^2(\Omega t) & \sin(\phi)\sin(2\Omega t) \\ \sin(2\phi)\sin^2(\Omega t) & \cos^2(\Omega t) - \cos(2\phi)\sin^2(\Omega t) & -\cos(\phi)\sin(2\Omega t) \\ -\sin\phi \sin(2\Omega t) & \cos\phi \sin(2\Omega t) & \cos(2\Omega t) \end{pmatrix} \quad (1.144)$$

Which gives the axis of rotation as:

$$\vec{u} = \begin{pmatrix} 2\cos\phi \sin(2\Omega t) \\ 2\sin\phi \sin(2\Omega t) \\ 0 \end{pmatrix} = \begin{pmatrix} \cos\phi \\ \sin\phi \\ 0 \end{pmatrix} 2\sin(2\Omega t) \quad (1.145)$$

And the angle of rotation as:

$$\theta = \sin^{-1}\left(\frac{|\vec{u}|}{2}\right) = \sin^{-1}\left(\frac{2\sin(2\Omega t)}{2}\right) = \sin^{-1}(\sin(2\Omega t)) = 2\Omega t \quad (1.146)$$

Here, we see that the rotation angle is directly proportional to the amplitude and duration of the field drive. In the case of no detuning, the axis of rotation is always in the xy plane with an angle set by the phase of the drive.

Nonzero detuning and zero phase

$$R_n = \begin{pmatrix} \cos^2(rt) - \frac{\Delta^2 - 4\Omega^2}{\Delta^2 + 4\Omega^2}\sin^2(rt) & -\frac{\Delta}{2r}\sin(2rt) & \frac{\Omega\Delta}{r^2}\sin^2(rt) \\ \frac{\Delta}{2r}\sin(2rt) & \cos(2rt) & -\frac{\Omega}{r}\sin(2rt) \\ \frac{4\Delta\Omega}{\Delta^2 + 4\Omega^2}\sin^2(rt) & \frac{\Omega}{r}\sin(2rt) & \cos(2rt) + \frac{2\Delta^2}{\Delta^2 + 4\Omega^2}\sin^2(rt) \end{pmatrix} \quad (1.147)$$

Where, as before,

$$r \equiv \sqrt{\frac{\Delta^2}{4} + \Omega^2} \quad (1.148)$$

This gives the axis of rotation as:

$$\vec{u} = \begin{pmatrix} \frac{2\Omega}{r}\sin(2rt) \\ 0 \\ \frac{\Delta}{r}\sin(2rt) \end{pmatrix} = \begin{pmatrix} 2\Omega \\ 0 \\ \Delta \end{pmatrix}\frac{\sin(2rt)}{r} \quad (1.149)$$

And the angle of rotation as:

$$\theta = \sin^{-1}\left(\frac{|\vec{u}|}{2}\right) = \sin^{-1}\left(\frac{\sqrt{4\Omega^2 + \Delta^2}\frac{\sin(2rt)}{r}}{2}\right) = \sin^{-1}\left(\frac{2\sin(2rt)}{2}\right) = 2rt \quad (1.150)$$

$$\theta = 2rt, \qquad r = \sqrt{\frac{\Delta^2}{4} + \Omega^2} \quad (1.151)$$

While the rotation angle is still directly proportional to the duration of the field drive, it now depends on both the drive detuning and amplitude. As the detuning increases, the rotation angle will also increase, effectively increasing the Rabi rate. This is why detuned Rabi is observed to oscillate faster. In the case of no detuning, the axis of rotation is always in the xy plane with an angle set by the phase of the drive. With detuning, the rotation axis gains a polar angle proportional to the detuning, as can be seen in the expression for $\vec{u}$. This also explains why detuned Rabi does

not reach full contrast, since a rotation around a non-azimuthal axis will not span the poles of the z-axis.

Experimentally, we can control the phase of the drive through IQ modulation of our signal generator and adjust the detuning by straightforwardly shifting the frequency of the drive, which gives full control over the desired rotation of the quantum state. For external fields inherent to the system, we can use the above results to help understand their effect on the state.

Chapter 2

The Divacancy in Silicon Carbide

2.1 Introduction

With the foundational tools built up in chapter 1, we are now ready to approach the main quantum system of interest for this thesis: the neutral divacancy in silicon carbide. Notationally we will use the word "divacancy" and the shorthand "VV^0" interchangeably. Here the "VV^0" represents a silicon vacancy (V), a carbon vacancy (V), and a neutral charge state (0). The divacancy collectively localizes two unpaired electrons in the band gap, which together form an electronic spin state as the foundation of the VV^0 qubit. [1-6]

As a material, silicon carbide serves as an excellent host for electron spin qubits [7]. Most importantly, silicon carbide is a wide-band gap semiconductor which means that the relevant energy levels are well isolated in the band gap from thermal fluctuations. The nuclear spins of both naturally abundant ^{12}C and ^{28}Si are zero, meaning that coherence-limiting nuclear coupling is minimized for electronic spins. The relatively high index of refraction of SiC ($n \approx 2.6$) also allows for the formation of photonic structures, which will be explored in later chapters. The relative technological maturity of SiC also allows for commercial growth of 4-inch single-crystalline wafers with capabilities of both P-type and N-type doping. Outside of quantum information, silicon

carbide has also already been developed for MEMS and NEMS applications [8-9]. Lastly, the divacancy itself is optically active in the near infrared (NIR) regime, which transmits through SiC with low losses and is also amenable to long-distance telecom fibers.

In this chapter we will focus on the physics of the divacancy, although many other promising spin defects have been explored in silicon carbide such as the silicon vacancy, the nitrogen-vacancy center, vanadium ions, and chromium ions [10-20]. Many of the results presented here have parallels with the NV^- center in diamond [21-23]. We will see that the spin state of the VV^0 can be optically addressed with near-infrared light and coherently controlled with electromagnetic fields. To work towards these results, we will outline the VV^0 ground and excited state Hamiltonians and map out the effects of external fields on the spin state energies and time evolution.

2.2 Structure of silicon carbide and the divacancy

The silicon carbide lattice comes in over 250 distinct configurations, which are referred to as polytypes. The most common ones are labeled 2H, 3C, 4H, 6H. For the purpose of this thesis we'll mainly be focusing on the 4H polytype. In this notation, the number refers to the number of atomic bilayers needed for the lattice to repeat itself, and the letter refers to either a hexagonal (H) or cubic (C) structure. A silicon carbide bilayer consists of one layer of silicon and carbon atoms that are bonded to each other. As bilayers are stacked on top of each other, they can be differentiated into three types as "A", "B", or "C" depending on the orientation relative to the [0001] *c*-axis. An "A"

and "B" layer are identical within a translation, whereas a "C" layer is rotated by 60 degrees around the *c*-axis. In this way, a C layer is sometimes referred to as a twist and a B layer as no twist. With these definitions, the 4H-SiC polytype then features the stacking pattern of ABCB. This can equivalently be represented by either BCBA, CBAB, or BABC. Similarly, 2H-SiC has AB pattern, 3C-SiC has ABC, and 6H-SiC has ABCACB. A schematic of the 4H silicon carbide lattice and the twist/no twist convention is shown in figures 2.1 and 2.2.

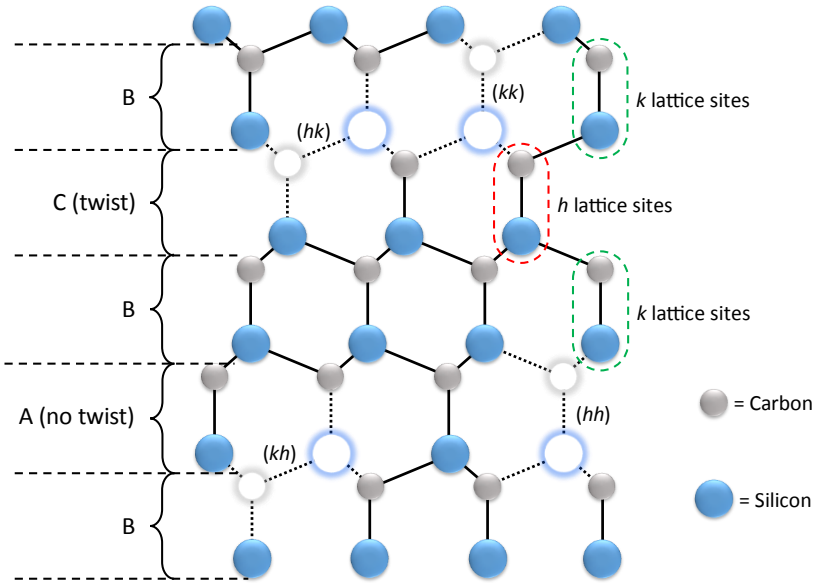

Figure 2.1 | 4H-SiC lattice and VV^0 orientation. In this two-dimensional view of the 4H-SiC lattice, the bilayers are labeled on the left using the ABC convention. A single bilayer contains a silicon and carbon atom connected by *c*-axis oriented bond. In the 4H polytype, the "B" bilayer alternates between "A" and "C" bilayers. Also featured are the four possible orientations of the divacancy, which are distinguished by their lattice sites. Here the *h* lattice sites are found in A and C bilayers and the *k* lattice sites are found in B bilayers.

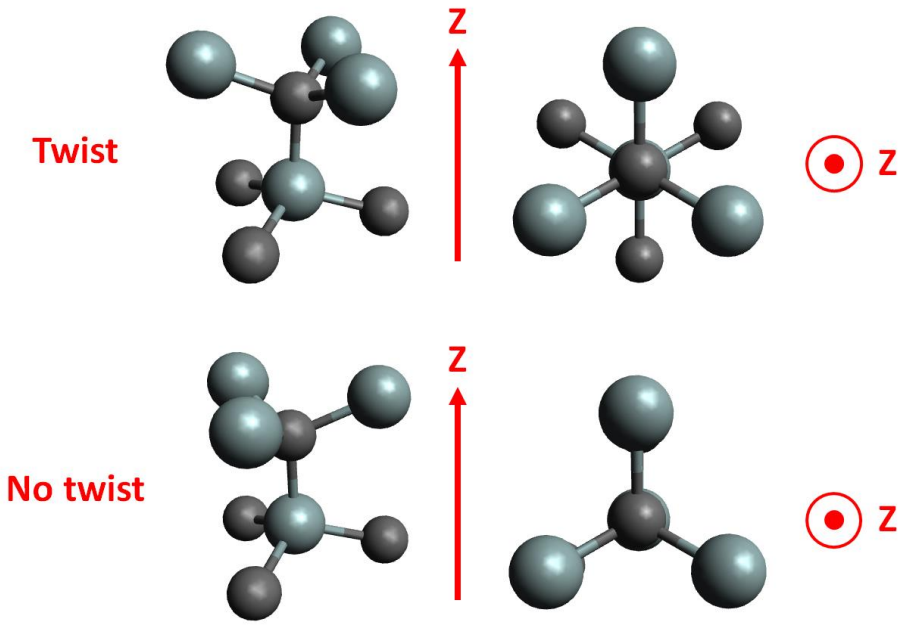

Figure 2.2 | Twist vs. no twist in the SiC lattice. Here, a twist refers to a rotation around the Si – C bond. Under a twist there is a 60^{o} rotation around the z-axis ([0001] *c*-axis) and the mirror symmetry of the local structure is broken.

Structurally, the divacancy consists of an adjacent silicon and carbon vacancy in the SiC lattice. For each SiC polytype, the number of possible divacancy orientations is given by the polytype number. For 4H-SiC, for example, there are four possible orientations. To distinguish them, each divacancy is typically labeled by two letters which denote to the local crystal structure. Here "h" refers to a local hexagonal structure and "k" refers to a local quasicubic structure. The first letter is used for the carbon vacancy and the second letter is used for the silicon vacancy. In this manner, we have the four possible orientations of (*hh*), (*kk*), (*hk*), and (*kh*). Early work with VV^{0} referred to these as PL1, PL2, PL3, and PL4, respectively. [4] The defects labeled PL5 and PL6 are also featured in past work [4], although instead of divacancies they are believed to be stacking faults in the SiC lattice. For the purposes of this thesis we will not go into detail about the PL5/PL6 defects, although they are notable for their room temperature operation [24]. The four divacancies can be further distinguished as either lying parallel to the *c*-axis as in (*hh*) and (*kk*), or along another lattice

direction in the "basal" (*hk*) and (*kh*) defects. An outline of the divacancy structures in given in figure 2.2 above.

2.3 Electron spin-1 ground state of the VV^0

The neutral divacancy traps six electrons which form isolated energy levels (orbitals) in the SiC band gap. Two of the electrons remain unpaired in their respective orbitals, leading to a spin-1 ground state. Thus, when we talk about the "spin" of the VV^0 center, we are referring to the combined spin of these two electrons in the two excited state orbitals. A schematic of this orbital occupation is shown in the figure below:

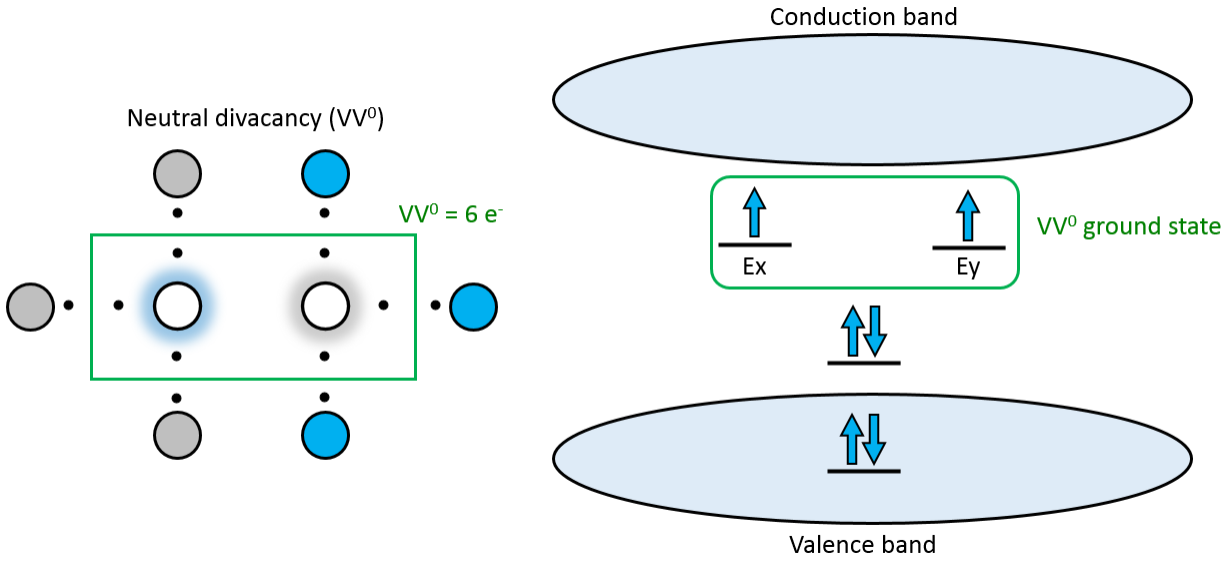

Figure 2.3 | Divacancy electrons and band gap energy levels. The adjacent silicon and carbon vacancies trap six electrons in the silicon carbide lattice. These electrons occupy energy levels both in the valence band and in the band gap. The presence of unpaired electrons leads to the spin-1 ground state.

The two unpaired electrons form the spin triplet and singlet states, which can be mathematically represented by:

$$\left.\begin{array}{c} |1,1\rangle = \uparrow\uparrow \\ |1,0\rangle = \dfrac{\uparrow\downarrow + \downarrow\uparrow}{\sqrt{2}} \\ |1,-1\rangle = \downarrow\downarrow \end{array}\right\}, \qquad s_{total} = 1, \qquad \text{triplet states} \tag{2.1}$$

$$\left.|0,0\rangle = \frac{\uparrow\downarrow - \downarrow\uparrow}{\sqrt{2}}\right\}, \qquad s_{total} = 0, \qquad \text{singlet state} \tag{2.2}$$

Here the notation follows $|s_{total}, m_s\rangle$. For this thesis (and in the literature in general) we use the shorthand $m_s = 0, \pm 1$ to refer to the spin triplet states. It is these states that are optically addressed and controlled in divacancy experiments. In the excited state, one of the excited state orbitals becomes occupied with a second electron, but the system as a whole still forms a spin triplet. This will be discussed in more detail in section 2.8.

2.4 Ground state Hamiltonian

Both the stationary behavior and the time evolution of the VV^0 ground state are governed by its ground state Hamiltonian. The two unpaired electrons in the ground state form the spin triplet states, which in turn form a 3-dimensional Hilbert space of possible spin states. Practically speaking, for qubit applications we usually select two of these states to be our qubit basis, such as $m_s = \{|0\rangle, |+1\rangle\}$ or $m_s = \{|0\rangle, |-1\rangle\}$. In later chapters we will see that these spin states can be initialized, coherently controlled, and optically readout. For the purposes of this chapter, we will focus on the form of the Hamiltonian, the influence of external fields, and implications for time evolution.

2.4.1 Zero-field Hamiltonian

Without the presence of any external field, strain, or nuclear spin, the VV^0 ground state spin Hamiltonian is dictated solely by spin-orbit and spin-spin interactions. We can write the Hamiltonian as:

$$H_{gs} = \frac{1}{\hbar}\left(\vec{S} \cdot \vec{D} \cdot \vec{S}\right) \tag{2.3}$$

Where:

$$\vec{S} = \left(S_x, S_y, S_z\right) = \text{spin 1 operators} \tag{2.4}$$

$$\vec{D} = \begin{pmatrix} D_{xx} & 0 & 0 \\ 0 & D_{yy} & 0 \\ 0 & 0 & D_{zz} \end{pmatrix} = \text{zero field splitting tensor} \tag{2.5}$$

And:

$$S_x = \frac{\hbar}{\sqrt{2}}\begin{pmatrix} 0 & 1 & 0 \\ 1 & 0 & 1 \\ 0 & 1 & 0 \end{pmatrix}, \qquad S_y = \frac{\hbar}{\sqrt{2}}\begin{pmatrix} 0 & -i & 0 \\ i & 0 & -i \\ 0 & i & 0 \end{pmatrix}, \qquad S_z = \hbar\begin{pmatrix} 1 & 0 & 0 \\ 0 & 0 & 0 \\ 0 & 0 & -1 \end{pmatrix} \tag{2.6}$$

It is important to note that many sources do not include the $1/\hbar$ prefactor for H_{gs}, but it is necessary in order to make the Hamiltonian have the correct units of energy. Expanding the product in H_{gs} gives:

$$H_{gs} = \frac{1}{\hbar}\begin{pmatrix} S_x & S_y & S_z \end{pmatrix}\begin{pmatrix} D_{xx} & D_{xy} & D_{xz} \\ D_{yx} & D_{yy} & D_{yz} \\ D_{zx} & D_{zy} & D_{zz} \end{pmatrix}\begin{pmatrix} S_x \\ S_y \\ S_z \end{pmatrix} \tag{2.7}$$

$$H_{gs} = \frac{1}{\hbar}\begin{pmatrix} S_xD_{xx} + S_yD_{yx} + S_zD_{zx} & S_xD_{xy} + S_yD_{yy} + S_yD_{zy} & S_xD_{xz} + S_yD_{yz} + S_zD_{zz} \end{pmatrix}\begin{pmatrix} S_x \\ S_y \\ S_z \end{pmatrix} \tag{2.8}$$

$$H_{gs} = \frac{1}{\hbar}\begin{pmatrix}(S_x D_{xx} + S_y D_{yx} + S_z D_{zx})S_x + (S_x D_{xy} + S_y D_{yy} + S_y D_{zy})S_y \\ +(S_x D_{xz} + S_y D_{yz} + S_z D_{zz})S_z\end{pmatrix} \tag{2.9}$$

$$H_{gs} = \frac{1}{\hbar}\begin{pmatrix}S_x D_{xx} S_x + S_x D_{xy} S_y + S_x D_{xz} S_z + S_y D_{yx} S_x + S_y D_{yy} S_y + S_y D_{yz} S_z \\ +S_z D_{zx} S_x + S_z D_{zy} S_y + S_z D_{zz} S_z\end{pmatrix} \tag{2.10}$$

Alternatively, this can be expressed as:

$$H_{gs} = \frac{1}{\hbar}\sum_{ij} S_i D_{ij} S_j \tag{2.11}$$

Since the off-diagonal terms of the zero-field splitting tensor are zero, this simplifies to:

$$H_{gs} = \frac{1}{\hbar}(S_x D_{xx} S_x + S_y D_{yy} S_y + S_z D_{zz} S_z) \tag{2.12}$$

Notationally we define:

$$D_j \equiv D_{jj} \tag{2.13}$$

These D terms are constants, not tensors, so we can say:

$$H_{gs} = \frac{1}{\hbar}(D_x S_x^2 + D_y S_y^2 + D_z S_z^2) \tag{2.14}$$

Which, using the definitions for S_x, S_y, S_z, gives:

$$H_{gs} = \frac{1}{\hbar}\left(D_x \frac{\hbar^2}{2}\begin{pmatrix}1 & 0 & 1\\ 0 & 2 & 0\\ 1 & 0 & 1\end{pmatrix} - D_y \frac{\hbar^2}{2}\begin{pmatrix}-1 & 0 & 1\\ 0 & -2 & 0\\ 1 & 0 & -1\end{pmatrix} + D_z \hbar^2 \begin{pmatrix}1 & 0 & 0\\ 0 & 0 & 0\\ 0 & 0 & 1\end{pmatrix}\right) \tag{2.15}$$

$$H_{gs} = \hbar\left(\begin{pmatrix}\frac{D_x}{2} & 0 & \frac{D_x}{2}\\ 0 & D_x & 0\\ \frac{D_x}{2} & 0 & \frac{D_x}{2}\end{pmatrix} + \begin{pmatrix}\frac{D_y}{2} & 0 & -\frac{D_y}{2}\\ 0 & D_y & 0\\ -\frac{D_y}{2} & 0 & \frac{D_y}{2}\end{pmatrix} + \begin{pmatrix}D_z & 0 & 0\\ 0 & 0 & 0\\ 0 & 0 & D_z\end{pmatrix}\right) \tag{2.16}$$

$$H_{gs} = \hbar \begin{pmatrix} \frac{D_x}{2} + \frac{D_y}{2} + D_z & 0 & \frac{D_x}{2} - \frac{D_y}{2} \\ 0 & D_x + D_y & 0 \\ \frac{D_x}{2} - \frac{D_y}{2} & 0 & \frac{D_x}{2} + \frac{D_y}{2} + D_z \end{pmatrix} \tag{2.17}$$

At this point we make the following substitutions to obtain the familiar D and E terms:

$$D \equiv \frac{3}{2} D_z, \qquad E \equiv \frac{1}{2}\left(D_x - D_y\right) \tag{2.18}$$

Which gives:

$$H_{gs} = \hbar \begin{pmatrix} \frac{D_x}{2} + \frac{D_y}{2} - \frac{D_z}{2} + D & 0 & E \\ 0 & D_x + D_y & 0 \\ E & 0 & \frac{D_x}{2} + \frac{D_y}{2} - \frac{D_z}{2} + D \end{pmatrix} \tag{2.19}$$

$$H_{gs} = \hbar \begin{pmatrix} \frac{1}{2}\left(D_x + D_y - D_z\right) + D & 0 & E \\ 0 & D_x + D_y + D_z - D_z & 0 \\ E & 0 & \frac{1}{2}\left(D_x + D_y - D_z\right) + D \end{pmatrix} \tag{2.20}$$

The $\vec{D}$ tensor is traceless, meaning the sum of the diagonal terms is zero:

$$D_x + D_y + D_z = 0 \tag{2.21}$$

Substituting this result gives:

$$H_{gs} = \hbar \begin{pmatrix} D - D_z & 0 & E \\ 0 & -D_z & 0 \\ E & 0 & D - D_z \end{pmatrix} = \hbar \begin{pmatrix} \frac{1}{3} D & 0 & E \\ 0 & -\frac{2}{3}\left(\frac{3}{2} D_z\right) & 0 \\ E & 0 & \frac{1}{3} D \end{pmatrix} \tag{2.22}$$

$$H_{gs} = \hbar \begin{pmatrix} \frac{1}{3}D & 0 & E \\ 0 & -\frac{2}{3}D & 0 \\ E & 0 & \frac{1}{3}D \end{pmatrix} \tag{2.23}$$

This is the main result for the zero-field VV^0 ground state Hamiltonian. At this point, it is popular to add a 2/3 D along the main diagonal. However, this addition leads to a non-invertible matrix which can cause potential mathematical issues, so here we will use the Hamiltonian form above. The eigenvalues and eigenvectors of H_{gs} are:

$$\{\lambda_1, v_1\} = \left\{\hbar\left(-\frac{2}{3}D\right), \begin{pmatrix} 0 \\ 1 \\ 0 \end{pmatrix}\right\}, \qquad \{\lambda_2, v_2\} = \left\{\hbar\left(\frac{D}{3} - E\right), \begin{pmatrix} -1 \\ 0 \\ 1 \end{pmatrix}\right\}, \qquad \{\lambda_3, v_3\} = \left\{\hbar\left(\frac{D}{3} + E\right), \begin{pmatrix} 1 \\ 0 \\ 1 \end{pmatrix}\right\} \tag{2.24}$$

The eigenstates presented here are the stable stationary states of the system. The vector v_1 is the $m_s = 0$ state. For the other two states, we frequently use the following definitions for the "plus" and "minus" states:

$$|+\rangle \equiv \begin{pmatrix} 1 \\ 0 \\ 1 \end{pmatrix}, \qquad |-\rangle \equiv \begin{pmatrix} -1 \\ 0 \\ 1 \end{pmatrix} \tag{2.25}$$

As with the two-level system, we can combine these eigenstates with the time-evolution operator to write the general state $\Psi(t)$ at any given time:

$$\Psi(t) = \sum_n c_n \psi_n e^{-\frac{iE_n t}{\hbar}} \tag{2.26}$$

In this case, we have:

$$\Psi(t) = c_0\psi_0 e^{-\frac{iE_0 t}{\hbar}} + c_-\psi_- e^{-\frac{iE_- t}{\hbar}} + c_+\psi_n e^{-\frac{iE_+ t}{\hbar}} \tag{2.27}$$

$$\Psi(t) = c_0 \begin{pmatrix} 0 \\ 1 \\ 0 \end{pmatrix} e^{-i\left(-\frac{2}{3}D\right)t} + c_- \begin{pmatrix} -1 \\ 0 \\ 1 \end{pmatrix} e^{-i\left(\frac{D}{3}-E\right)t} + c_+ \begin{pmatrix} 1 \\ 0 \\ 1 \end{pmatrix} e^{-i\left(\frac{D}{3}+E\right)t} \tag{2.28}$$

$$\Psi(t) = \begin{pmatrix} 0 \\ c_0 e^{i\left(\frac{2}{3}D\right)t} \\ 0 \end{pmatrix} + \begin{pmatrix} -c_- e^{-i\left(\frac{D}{3}-E\right)t} \\ 0 \\ c_- e^{-i\left(\frac{D}{3}-E\right)t} \end{pmatrix} + \begin{pmatrix} c_+ e^{-i\left(\frac{D}{3}+E\right)t} \\ 0 \\ c_+ e^{-i\left(\frac{D}{3}+E\right)t} \end{pmatrix} \tag{2.29}$$

$$\Psi(t) = \begin{pmatrix} c_+ e^{-i\left(\frac{D}{3}+E\right)t} - c_- e^{-i\left(\frac{D}{3}-E\right)t} \\ c_0 e^{i\left(\frac{2}{3}D\right)t} \\ c_+ e^{-i\left(\frac{D}{3}+E\right)t} + c_- e^{-i\left(\frac{D}{3}-E\right)t} \end{pmatrix} \tag{2.30}$$

This can be useful when trying to determine the time evolution of a superposition of eigenstates, as given by the coefficients c_0, c_+, c_-. For the (*hh*) and (*kk*) *c*-axis oriented defects, the E term vanishes, giving:

$$H_{gs} = \hbar \begin{pmatrix} \frac{1}{3}D & 0 & 0 \\ 0 & -\frac{2}{3}D & 0 \\ 0 & 0 & \frac{1}{3}D \end{pmatrix}, \qquad \text{c axis VV}^0 \tag{2.31}$$

With differing eigenvalues and eigenvectors of:

$$\{\lambda_1, v_1\} = \left\{\hbar\left(\frac{D}{3}\right), \begin{pmatrix} 1 \\ 0 \\ 0 \end{pmatrix}\right\}, \qquad \{\lambda_2, v_2\} = \left\{\hbar\left(-\frac{2}{3}D\right), \begin{pmatrix} 0 \\ 1 \\ 0 \end{pmatrix}\right\}, \qquad \{\lambda_3, v_3\} = \left\{\hbar\left(\frac{D}{3}\right), \begin{pmatrix} 0 \\ 0 \\ 1 \end{pmatrix}\right\} \tag{2.32}$$

Note that with no E term, two of the eigenstates are degenerate. These are the $m_s = \pm 1$ states. Normally, we apply a small B-field along the z-axis (the *c*-axis direction) to Zeeman split these states and lift the degeneracy. Plugging in $E = 0$ into eq. () gives a general state $\Psi(t)$ of:

$$\Psi(t) = \begin{pmatrix} c_1 e^{-i\left(\frac{D}{3}\right)t} \\ c_2 e^{-i\left(-\frac{2}{3}D\right)t} \\ c_3 e^{-i\left(\frac{D}{3}\right)t} \end{pmatrix} \tag{2.33}$$

2.4.2 Effect of static magnetic field

The contribution of static magnetic field to the ground state Hamiltonian can be written as:

$$V_B = \mu_B g_{gs}^{\parallel} \hat{S}_z B_z + \mu_B g_{gs}^{\perp} \left(\hat{S}_x B_x + \hat{S}_y B_y\right) \tag{2.34}$$

Where μ_B is the Bohr magneton:

$$\mu_B = \frac{e\hbar}{2m_e} = 9.274 \cdot 10^{-24} \tag{2.35}$$

The variables $g_{gs}^{\parallel}, g_{gs}^{\perp}$ are the components of the ground state electronic g-factor tensor, and are both very close to 2. The matrices S_x, S_y, S_z take the same form as before. Putting V_B in matrix form gives:

$$V_B = \mu_B \begin{pmatrix} g_{gs}^{\parallel} B_z & \frac{g_{gs}^{\perp}}{\sqrt{2}}\left(B_x - iB_y\right) & 0 \\ \frac{g_{gs}^{\perp}}{\sqrt{2}}\left(B_x + iB_y\right) & 0 & \frac{g_{gs}^{\perp}}{\sqrt{2}}\left(B_x - iB_y\right) \\ 0 & \frac{g_{gs}^{\perp}}{\sqrt{2}}\left(B_x + iB_y\right) & -g_{gs}^{\parallel} B_z \end{pmatrix} \tag{2.36}$$

It should be noted here that an addition of B_z magnetic field will Zeeman split the energy levels according to the relation 2.8 MHz/G. This is commonly used as a gauge of magnetic field strength (or conversely expected splitting under a known B-field) in divacancy experiments.

2.4.3 Effect of static electric field and strain

The effect of both static electric field $E_{x,y,z}$ and static strain $\delta_{x,y,z}$ can be expressed by the following terms, which are added to the zero-field Hamiltonian.

$$V_E = \left(d_{gs}^{\parallel}E_z + \epsilon_{gs}^{\parallel}\delta_z\right)\left(\hat{S}_z^2 - \frac{S(S+1)}{3}\right) + \left(d_{gs}^{\perp}E_x + \epsilon_{gs}^{\perp}\delta_x\right)\left(\hat{S}_y^2 - \hat{S}_x^2\right) + \left(d_{gs}^{\perp}E_y + \epsilon_{gs}^{\perp}\delta_y\right)\left(\hat{S}_x\hat{S}_y + \hat{S}_y\hat{S}_x\right) \tag{2.37}$$

Where $\left\{d_{gs}^{\parallel}, d_{gs}^{\perp}\right\}$ are the spin-electric field coupling constants and $\left\{\epsilon_{gs}^{\parallel}, \epsilon_{gs}^{\perp}\right\}$ are the spin-strain coupling constants. For the matrix components, we have:

$$\hat{S}_z^2 - \frac{S(S+1)}{3} = \begin{pmatrix} \frac{1}{3} & 0 & 0 \\ 0 & -\frac{2}{3} & 0 \\ 0 & 0 & \frac{1}{3} \end{pmatrix}, \qquad \hat{S}_y^2 - \hat{S}_x^2 = \begin{pmatrix} 0 & 0 & -1 \\ 0 & 0 & 0 \\ -1 & 0 & 0 \end{pmatrix},$$
$$\hat{S}_x\hat{S}_y + \hat{S}_y\hat{S}_x = \begin{pmatrix} 0 & 0 & -i \\ 0 & 0 & 0 \\ i & 0 & 0 \end{pmatrix} \tag{2.38}$$

So writing out the components gives:

$$V_E = \left(d_{gs}^{\parallel}E_z + \epsilon_{gs}^{\parallel}\delta_z\right)\begin{pmatrix} \frac{1}{3} & 0 & 0 \\ 0 & -\frac{2}{3} & 0 \\ 0 & 0 & \frac{1}{3} \end{pmatrix} + \left(d_{gs}^{\perp}E_x + \epsilon_{gs}^{\perp}\delta_x\right)\begin{pmatrix} 0 & 0 & -1 \\ 0 & 0 & 0 \\ -1 & 0 & 0 \end{pmatrix} + \left(d_{gs}^{\perp}E_y + \epsilon_{gs}^{\perp}\delta_y\right)\begin{pmatrix} 0 & 0 & -i \\ 0 & 0 & 0 \\ i & 0 & 0 \end{pmatrix} \tag{2.39}$$

And combining gives:

$$V_E = \begin{pmatrix} \frac{1}{3}\left(d_{gs}^{\parallel}E_z + \epsilon_{gs}^{\parallel}\delta_z\right) & 0 & \begin{pmatrix} d_{gs}^{\perp}\left(-E_x - iE_y\right) \\ + \epsilon_{gs}^{\perp}\left(-\delta_x - i\delta_y\right) \end{pmatrix} \\ 0 & -\frac{2}{3}\left(d_{gs}^{\parallel}E_z + \epsilon_{gs}^{\parallel}\delta_z\right) & 0 \\ \begin{pmatrix} d_{gs}^{\perp}\left(-E_x + iE_y\right) \\ + \epsilon_{gs}^{\perp}\left(-\delta_x + i\delta_y\right) \end{pmatrix} & 0 & \frac{1}{3}\left(d_{gs}^{\parallel}E_z + \epsilon_{gs}^{\parallel}\delta_z\right) \end{pmatrix} \quad (2.40)$$

The effect of E_z, δ_z is to shift the $m_s = 0$ energy down and shift the $m_s = \pm 1$ energies up. Broadly speaking, the presence of $E_x, E_y, \delta_x, \delta_y$ will introduce off-diagonal coupling between the $m_s = \pm 1$ states. In the case of E_x, δ_x, this is equivalent to modifying the E term that appears in the zero-field Hamiltonian. Investigations of the divacancy spin strain and electric field coupling are presented in [25-28].

2.4.4 Effect of nuclear spins and local paramagnetic spins

The ground state Hamiltonian can also be affected by the nuclear spin environment. Similar to single electrons, the protons and neutrons that compose any nucleus each have a spin of ½ and a comparatively small magnetic moment. In an entire nucleus, the atomic number (the number of protons) and mass number (number of protons + neutrons) both play an important role in the overall spin of the nuclear magnetic moment. If the mass number is even, there will be an integer spin, whereas if the mass number is odd, there will be a half-integer spin. More specifically, if both the mass number and the atomic number are even (i.e. an even number of both protons and

neutrons), then the nuclear spin will be zero. Nuclear spin is commonly represented by the letter I. The examples of naturally abundant ^{12}C and ^{28}Si both have $I = 0$ and thus no coupling to the neutral divacancy in the SiC lattice. Meanwhile the most common isotopes of ^{13}C and ^{29}Si both have $I = 1/2$. When a nonzero nuclear spin couples to the VV^0, the Hamiltonian is modified by the addition of the following terms:

$$V_{nuclear} = \begin{matrix} A_{gs}^{\parallel}\hat{S}_z \otimes \hat{I}_z + A_{gs}^{\perp}\left(\hat{S}_x \otimes \hat{I}_x + \hat{S}_y \otimes \hat{I}_y\right) \\ + P_{gs}\left(S_I \otimes \hat{I}_z^2 - \frac{I(I+1)}{3}\right) + \mu_N g_N S_I \otimes \left(\vec{I} \cdot \vec{B}\right) \end{matrix} \quad (2.41)$$

Where $\otimes$ denotes a tensor product, S_I is the 3x3 identity matrix, $\left\{A_{gs}^{\parallel}, A_{gs}^{\perp}\right\}$ are the magnetic hyperfine parameters, P_{gs} is the nuclear electric quadrupole parameter, μ_N is the nuclear magneton, and g_N is the nuclear g-factor of the relevant nuclear isotope. The scalar I is the nuclear spin (e.g. $I = 1/2$ for ^{13}C). The nuclear spin matrices $\left\{\hat{I}_x, \hat{I}_y, \hat{I}_z\right\}$ take the same form as the "regular" spin matrices with spin I. For example, for the case of 13C which has $I = 1/2$, we would use the Pauli matrices with $\left\{\hat{I}_x, \hat{I}_y, \hat{I}_z\right\} = \left\{\sigma_x, \sigma_y, \sigma_z\right\}$. Practically speaking we will only see nuclear isotopes with either $I = 1/2$ or $I = 0$ in the SiC lattice. If $I = 0$, the nuclear Hamiltonian $\widehat{H}_{nuclear}$ simply becomes zero. So for nuclear spins in SiC, the nuclear Hamiltonian gets modified to:

$$V_{nuclear}^{SiC} = \begin{matrix} A_{gs}^{\parallel}\hat{S}_z \otimes \hat{\sigma}_z + A_{gs}^{\perp}\left(\hat{S}_x \otimes \hat{\sigma}_x + \hat{S}_y \otimes \hat{\sigma}_y\right) \\ + P_{gs}\left(S_I \otimes \hat{\sigma}_z^2 - \frac{1}{4}\right) + \mu_N g_N S_I \otimes \left(\vec{\sigma} \cdot \vec{B}\right) \end{matrix} \quad (2.42)$$

The presence of the nuclear spin bath in the SiC has important effects on the VV^0 decoherence and dephasing times, as is explored in [29]. Meanwhile, local paramagnetic spins from lattice

defects and impurities can also couple to the divacancy electron spin. Usually this is the result of dipolar coupling between electrons. This interaction can be broadly written as:

$$V_{dipole} = \sum_i \sum_{j>i} \widehat{\boldsymbol{S}}_i \cdot \boldsymbol{P}^e_{i,j} \cdot \widehat{\boldsymbol{S}}_j \tag{2.43}$$

Where we are summing over all paramagnetic spins. Here $\widehat{\boldsymbol{S}}_i$ represents the electronic spin of defect i and $\boldsymbol{P}^e_{i,j}$ represents the electronic diole-dipole coupling term for each spin.

2.4.5 Total combined Hamiltonian

In total then, the ground state VV^0 Hamiltonian can be written as:

$$H^{total}_{gs} = H_{gs} + V_B + V_E + V^{SiC}_{nuclear} + V_{dipole} \tag{2.44}$$

The zero-field Hamiltonian and magnetic/electric/strain effects can be combined into one matrix to give:

$$H_{gs} + V_B + V_E = \begin{pmatrix} \begin{pmatrix} \frac{1}{3}\hbar D + \mu_B g^{\parallel}_{gs} B_z \\ +\frac{1}{3}\left(d^{\parallel}_{gs} E_z + \epsilon^{\parallel}_{gs}\delta_z\right) \end{pmatrix} & \mu_B \frac{g^{\perp}_{gs}}{\sqrt{2}}\left(B_x - iB_y\right) & \begin{pmatrix} \hbar E \\ +d^{\perp}_{gs}\left(-E_x - iE_y\right) \\ +\epsilon^{\perp}_{gs}\left(-\delta_x - i\delta_y\right) \end{pmatrix} \\ \mu_B \frac{g^{\perp}_{gs}}{\sqrt{2}}\left(B_x + iB_y\right) & -\frac{2}{3}\hbar D - \frac{2}{3}\left(d^{\parallel}_{gs} E_z + \epsilon^{\parallel}_{gs}\delta_z\right) & \mu_B \frac{g^{\perp}_{gs}}{\sqrt{2}}\left(B_x - iB_y\right) \\ \begin{pmatrix} \hbar E \\ +d^{\perp}_{gs}\left(-E_x + iE_y\right) \\ +\epsilon^{\perp}_{gs}\left(-\delta_x + i\delta_y\right) \end{pmatrix} & \mu_B \frac{g^{\perp}_{gs}}{\sqrt{2}}\left(B_x + iB_y\right) & \begin{pmatrix} \frac{1}{3}\hbar D - \mu_B g^{\parallel}_{gs} B_z \\ +\frac{1}{3}\left(d^{\parallel}_{gs} E_z + \epsilon^{\parallel}_{gs}\delta_z\right) \end{pmatrix} \end{pmatrix} \tag{2.45}$$

If one just wants to focus on the general field/strain dependence without prefactors, then this can be simplified to:

$$H_{gs} + V_B + V_E \approx \begin{pmatrix} \frac{1}{3}D + B_z + E_z + \delta_z & B_x - iB_y & E - E_x - iE_y - \delta_x - i\delta_y \\ B_x + iB_y & -\frac{2}{3}D - E_z - \delta_z & B_x - iB_y \\ E - E_x + iE_y - \delta_x + i\delta_y & B_x + iB_y & \frac{1}{3}D - B_z + E_z + \delta_z \end{pmatrix} \quad (2.46)$$

The additional terms $V_{nuclear}^{SiC}$ and V_{dipole} cannot be cast into matrix form easily, and they would likely be 6x6 dimensional for coupling to spin ½ particles.

2.5 The benefits of a diagonal Hamiltonian

When presented with a Hamiltonian in any system, one is generally interested in the stationary eigenstates and the effects of external fields on time-evolution of a starting state. In the case of a diagonal zero-field Hamiltonian, the basis that the Hamiltonian is expressed in already composes the eigenstates of the system. Additionally, the placement of off-diagonal external field entries immediately provides information for which transitions will be driven by sinusoidally varying magnitudes of these fields. In the case of the *c*-axis divacancy with a Bz Zeeman splitting, the Hamiltonian takes the general form:

$$H_{gs} = \hbar \begin{pmatrix} \frac{1}{3}D + B_z & 0 & 0 \\ 0 & -\frac{2}{3}D & 0 \\ 0 & 0 & \frac{1}{3}D - B_z \end{pmatrix} \quad (2.47)$$

As outlined in figure 2.4, the diagonal elements give the energies of the eigenstates and the off-diagonal elements dictate coupling between the eigenstates.

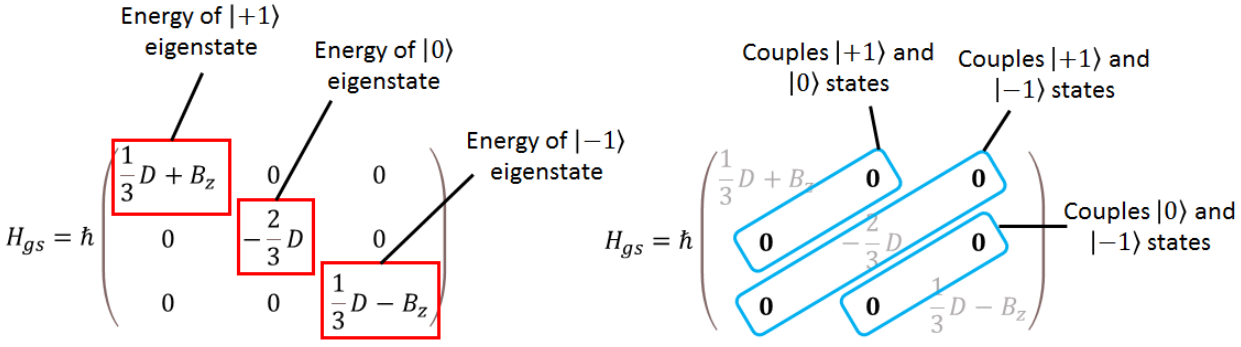

Figure 2.4 | Interpretation of a diagonal Hamiltonian. For a diagonal Hamiltonian, the diagonal entries (red boxes) directly give the energies of the eigenstates. The off-diagonal elements (blue boxes) provide coupling between the different eigenstates.

Alternatively, we can look at the row and column indices of an off-diagonal entry to see which states it will couple. Entry H_{ij} in row i and column j will couple eigenstates i and j, and likewise H_{ji} will couple the same two eigenstates j and i. For example, a Bx field in the *c*-axis Hamiltonian will couple the $|0\rangle \leftrightarrow |+1\rangle$ states and the $|0\rangle \leftrightarrow |-1\rangle$ states, as shown in figure 2.5.

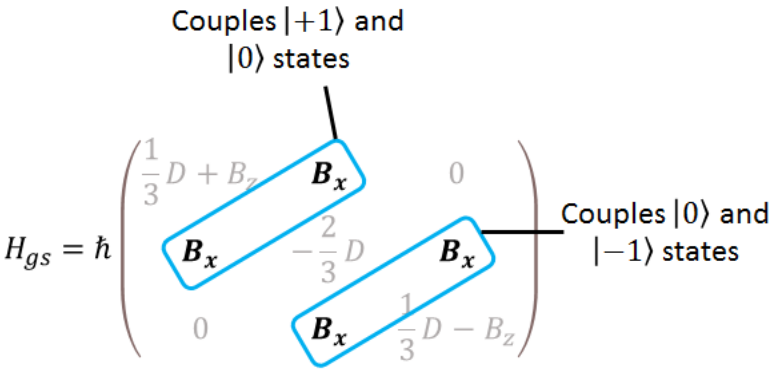

Figure 2.5 | Diagonal Hamiltonian effect of B_x magnetic field. An off-diagonal B_x element in the *c*-axis VV^0 Hamiltonian provides direct coupling between the $m_s = 0$ ($|0\rangle$) eigenstate and the $m_s = \pm 1$ eigenstates ($|\pm 1\rangle$).

The upshot of this argument is that it is beneficial to have a diagonal zero-field Hamiltonian in order to make these statements about eigenenergies and coupling behavior. If the zero-field Hamiltonian is not diagonal, then we will have to apply a transformation to diagonalize it. The key point is that this same transformation will have to be applied to any external field terms to see what their effect is. This will be discussed in more detail in the next two sections.

2.5.1 Hamiltonian diagonalization and change of basis

To determine the effects of drive fields on a non-diagonal Hamiltonian, we will follow two steps:

1) Diagonalize the Hamiltonian and get the new basis corresponding to the diagonalization.
2) Use this new basis to transform the drive fields

We will do the first step in this section and the second step in the next section and summarize the results. It is worth noting that the second step can also be applied more generally, as any Hamiltonian can be transformed under any new basis regardless of whether or not the end result is diagonal. As an example of a non-diagonal Hamiltonian to work with, we can examine the zero-field basal VV^0, which has a nonzero E term:

$$H_{basal} = \hbar \begin{pmatrix} \frac{1}{3}D & 0 & E \\ 0 & -\frac{2}{3}D & 0 \\ E & 0 & \frac{1}{3}D \end{pmatrix} \tag{2.48}$$

This matrix is diagonalizable, meaning that

$$A = PDP^{-1} \tag{2.49}$$

For a given matrix A and a diagonal matrix D. The diagonalization can be performed either analytically or programmatically (e.g. using the python sympy package). The matrix P is composed of column vectors that represent the new basis of the diagonalized Hamiltonian. In this case, diagonalization on H_{basal} gives:

$$P = \begin{pmatrix} -\frac{1}{\sqrt{2}} & 0 & \frac{1}{\sqrt{2}} \\ 0 & 1 & 0 \\ \frac{1}{\sqrt{2}} & 0 & \frac{1}{\sqrt{2}} \end{pmatrix}, \quad D = \begin{pmatrix} \frac{1}{3}D - E & 0 & 0 \\ 0 & -\frac{2}{3}D & 0 \\ 0 & 0 & \frac{1}{3}D + E \end{pmatrix}, \quad P^{-1} = \begin{pmatrix} -\frac{1}{\sqrt{2}} & 0 & \frac{1}{\sqrt{2}} \\ 0 & 1 & 0 \\ \frac{1}{\sqrt{2}} & 0 & \frac{1}{\sqrt{2}} \end{pmatrix} \tag{2.50}$$

The columns of P give the basis that results in a diagonal Hamiltonian. This is the "plus/minus" basis, expressed as:

$$|-\rangle = \frac{1}{\sqrt{2}}\begin{pmatrix} -1 \\ 0 \\ 1 \end{pmatrix}, \quad |0\rangle = \begin{pmatrix} 0 \\ 1 \\ 0 \end{pmatrix}, \quad |+\rangle = \frac{1}{\sqrt{2}}\begin{pmatrix} 1 \\ 0 \\ 1 \end{pmatrix}, \quad \text{plus minus basis} \tag{2.51}$$

In this basis, the new Hamiltonian takes the form of D:

$$H_{basal} = D = \begin{pmatrix} \frac{1}{3}D - E & 0 & 0 \\ 0 & -\frac{2}{3}D & 0 \\ 0 & 0 & \frac{1}{3}D + E \end{pmatrix}_{\substack{\text{plus minus} \\ \text{basis}}} \tag{2.52}$$

With energy eigenvalues equal to the diagonal entries $\frac{1}{3}D - E$, $-\frac{2}{3}D$, and $\frac{1}{3}D + E$.

This completes the first step of our procedure. We have identified a new basis that diagonalizes the Hamiltonian and gives the stationary eigenstates and eigenenergies of the system. The next step is to use this basis in the matrix P to transform drive fields from the old basis (the integer basis) to the new basis (the plus-minus basis). With this in mind, we can give P the more informative name of the change of basis matrix COB:

$$P = COB = (|-\rangle \quad |0\rangle \quad |+\rangle), \qquad \text{change of basis matrix} \tag{2.53}$$

So a general transformation of a matrix A to a matrix B in this new basis will look like:

$$B = COB^{-1} \cdot A \cdot COB \tag{2.54}$$

We will see how this works in the next section and use the results to state the transitions rules for the VV^0 ground state.

2.5.2 Transition rules for the VV^0 ground state

We can apply the transformation from the previous section:

$$B = COB^{-1} \cdot A \cdot COB \tag{2.55}$$

To individual drive fields to examine their behavior in the new basis. We will start with the transformation of Bx field, which gives:

$$H_{Bx} = \begin{pmatrix} -\frac{1}{\sqrt{2}} & 0 & \frac{1}{\sqrt{2}} \\ 0 & 1 & 0 \\ \frac{1}{\sqrt{2}} & 0 & \frac{1}{\sqrt{2}} \end{pmatrix} \begin{pmatrix} 0 & B_x & 0 \\ B_x & 0 & B_x \\ 0 & B_x & 0 \end{pmatrix} \begin{pmatrix} -\frac{1}{\sqrt{2}} & 0 & \frac{1}{\sqrt{2}} \\ 0 & 1 & 0 \\ \frac{1}{\sqrt{2}} & 0 & \frac{1}{\sqrt{2}} \end{pmatrix} = \begin{pmatrix} 0 & 0 & 0 \\ 0 & 0 & \sqrt{2}B_x \\ 0 & \sqrt{2}B_x & 0 \end{pmatrix} \quad (2.56)$$

This result means that in the case of a basal VV^0 with an E term, an alternating Bx drive will only cause transitions between the $|0\rangle$ and $|+\rangle$ states. The states are determined through the formalism outlined in the previous section, with the $|0\rangle$ and $|+\rangle$ eigenenergies appearing in row/column 2 and 3, respectively.

Carrying this out this same transformation for the other drive fields gives the following:

$$H_{By} = \begin{pmatrix} -\frac{1}{\sqrt{2}} & 0 & \frac{1}{\sqrt{2}} \\ 0 & 1 & 0 \\ \frac{1}{\sqrt{2}} & 0 & \frac{1}{\sqrt{2}} \end{pmatrix} \begin{pmatrix} 0 & -iB_y & 0 \\ iB_y & 0 & -iB_y \\ 0 & iB_y & 0 \end{pmatrix} \begin{pmatrix} -\frac{1}{\sqrt{2}} & 0 & \frac{1}{\sqrt{2}} \\ 0 & 1 & 0 \\ \frac{1}{\sqrt{2}} & 0 & \frac{1}{\sqrt{2}} \end{pmatrix} = \begin{pmatrix} 0 & \sqrt{2}iB_y & 0 \\ -\sqrt{2}iB_y & 0 & 0 \\ 0 & 0 & 0 \end{pmatrix} \quad (2.57)$$

$$H_{Bz} = \begin{pmatrix} -\frac{1}{\sqrt{2}} & 0 & \frac{1}{\sqrt{2}} \\ 0 & 1 & 0 \\ \frac{1}{\sqrt{2}} & 0 & \frac{1}{\sqrt{2}} \end{pmatrix} \begin{pmatrix} B_z & 0 & 0 \\ 0 & 0 & 0 \\ 0 & 0 & -B_z \end{pmatrix} \begin{pmatrix} -\frac{1}{\sqrt{2}} & 0 & \frac{1}{\sqrt{2}} \\ 0 & 1 & 0 \\ \frac{1}{\sqrt{2}} & 0 & \frac{1}{\sqrt{2}} \end{pmatrix} = \begin{pmatrix} 0 & 0 & -B_z \\ 0 & 0 & 0 \\ -B_z & 0 & 0 \end{pmatrix} \quad (2.58)$$

$$H_{Ex} = \begin{pmatrix} -\frac{1}{\sqrt{2}} & 0 & \frac{1}{\sqrt{2}} \\ 0 & 1 & 0 \\ \frac{1}{\sqrt{2}} & 0 & \frac{1}{\sqrt{2}} \end{pmatrix} \begin{pmatrix} 0 & 0 & -E_x \\ 0 & 0 & 0 \\ -E_x & 0 & 0 \end{pmatrix} \begin{pmatrix} -\frac{1}{\sqrt{2}} & 0 & \frac{1}{\sqrt{2}} \\ 0 & 1 & 0 \\ \frac{1}{\sqrt{2}} & 0 & \frac{1}{\sqrt{2}} \end{pmatrix} = \begin{pmatrix} E_x & 0 & 0 \\ 0 & 0 & 0 \\ 0 & 0 & -E_x \end{pmatrix} \quad (2.59)$$

$$H_{Ey} = \begin{pmatrix} -\frac{1}{\sqrt{2}} & 0 & \frac{1}{\sqrt{2}} \\ 0 & 1 & 0 \\ \frac{1}{\sqrt{2}} & 0 & \frac{1}{\sqrt{2}} \end{pmatrix} \begin{pmatrix} 0 & 0 & -iE_y \\ 0 & 0 & 0 \\ iE_y & 0 & 0 \end{pmatrix} \begin{pmatrix} -\frac{1}{\sqrt{2}} & 0 & \frac{1}{\sqrt{2}} \\ 0 & 1 & 0 \\ \frac{1}{\sqrt{2}} & 0 & \frac{1}{\sqrt{2}} \end{pmatrix} = \begin{pmatrix} 0 & 0 & iE_y \\ 0 & 0 & 0 \\ -iE_y & 0 & 0 \end{pmatrix} \quad (2.60)$$

$$H_{Ez} = \begin{pmatrix} -\frac{1}{\sqrt{2}} & 0 & \frac{1}{\sqrt{2}} \\ 0 & 1 & 0 \\ \frac{1}{\sqrt{2}} & 0 & \frac{1}{\sqrt{2}} \end{pmatrix} \begin{pmatrix} E_z & 0 & 0 \\ 0 & -E_z & 0 \\ 0 & 0 & E_z \end{pmatrix} \begin{pmatrix} -\frac{1}{\sqrt{2}} & 0 & \frac{1}{\sqrt{2}} \\ 0 & 1 & 0 \\ \frac{1}{\sqrt{2}} & 0 & \frac{1}{\sqrt{2}} \end{pmatrix} = \begin{pmatrix} E_z & 0 & 0 \\ 0 & -E_z & 0 \\ 0 & 0 & E_z \end{pmatrix} \quad (2.61)$$

Following the same convention of the previous section, the effects of these fields are summarized table 2.1:

Type of AC drive	Transitions	
	c-axis VV^0 with static Bz	Basal VV^0, no static field
Bx drive	$\|0\rangle \leftrightarrow \|+1\rangle$, $\|0\rangle \leftrightarrow \|-1\rangle$	$\|0\rangle \leftrightarrow \|+\rangle$
By drive	$\|0\rangle \leftrightarrow \|+1\rangle$, $\|0\rangle \leftrightarrow \|-1\rangle$	$\|0\rangle \leftrightarrow \|-\rangle$
Bz drive	No transition	$\|+\rangle \leftrightarrow \|-\rangle$
Ex drive	$\|+1\rangle \leftrightarrow \|-1\rangle$	No transition
Ey drive	$\|+1\rangle \leftrightarrow \|-1\rangle$	$\|+\rangle \leftrightarrow \|-\rangle$
Ez drive	No transition	No transition

Table 2.1 | Transition rules for *c*-axis and basal divacancies under sinusoidally varying magnetic and electric fields. As an example, B_x and B_y magnetic fields are commonly used to drive spin transitions in the *c*-axis VV^0 ($|0\rangle \leftrightarrow |\pm 1\rangle$), while B_z has no effect ("No transition").

This table gives some background why it is sometimes said that $\Delta m_s = \pm 2$ transitions are "magnetically forbidden" for *c*-axis VV^0s, as no combination of magnetic fields will drive a $|+1\rangle \leftrightarrow |-1\rangle$ transition. Instead, an alternating electric field must be used for such a transition [25]. However, with the E term present in basal VV^0s (or an artificially induced E term with a static Ex applied to a *c*-axis VV^0s), the transition rules change and a magnetic field can cause transitions between the two nonzero spin eigenstates $|+\rangle$ and $|-\rangle$. [31] Therefore, the rules of what is or is not "allowed" for magnetic/electric driving depends entirely on the context of the undriven Hamiltonian, which is sometimes directly controllable with the application of static fields or strains. [31]

2.6 An analytical approach to the magnetically driven VV^0 system

In this section we will attempt to obtain full analytical solutions to the wavefunction for the *c*-axis VV^0 ground state (i.e. no E term) under an alternating transverse microwave field (Bx). The exclusion the E term is not out of laziness, but necessity. We will see that even this "simple" system poses immensely complicated solutions. Indeed, we will not be able to write out the final closed form solution, mostly because the solution would not reasonably fit on a page! However the analysis up until that point follows the same approach as the two-level system, with many parallels between the two derivations.

The simplest case is a *c*-axis defect with a Zeeman splitting, in which case we have:

$$H_{gs} = \hbar \begin{pmatrix} \frac{1}{3}D + \frac{\mu_B g_{gs}^{\parallel} B_z}{\hbar} & \frac{\mu_B g_{gs}^{\perp}}{\hbar\sqrt{2}} B_x & 0 \\ \frac{\mu_B g_{gs}^{\perp}}{\hbar\sqrt{2}} B_x & -\frac{2}{3}D & \frac{\mu_B g_{gs}^{\perp}}{\hbar\sqrt{2}} B_x \\ 0 & \frac{\mu_B g_{gs}^{\perp}}{\hbar\sqrt{2}} B_x & \frac{1}{3}D - \frac{\mu_B g_{gs}^{\parallel} B_z}{\hbar} \end{pmatrix} \tag{2.62}$$

For notational simplicity we will define:

$$B_z \equiv \frac{\mu_B g_{gs}^{\parallel}}{\hbar} B_z, \qquad B_x \equiv \frac{\mu_B g_{gs}^{\perp}}{\hbar\sqrt{2}} B_x \tag{2.63}$$

So we simply have:

$$H_{gs} = \hbar \begin{pmatrix} \frac{1}{3}D + B_z & B_x & 0 \\ B_x & -\frac{2}{3}D & B_x \\ 0 & B_x & \frac{1}{3}D - B_z \end{pmatrix} \tag{2.64}$$

To turn this to a sinusoidal B-field drive, we write:

$$H_{gs} = \hbar \begin{pmatrix} \frac{1}{3}D + B_z & B_x \cos\omega t & 0 \\ B_x \cos\omega t & -\frac{2}{3}D & B_x \cos\omega t \\ 0 & B_x \cos\omega t & \frac{1}{3}D - B_z \end{pmatrix} \tag{2.65}$$

$$H_{gs} = \hbar \begin{pmatrix} \frac{1}{3}D + B_z & \frac{B_x}{2}\left(e^{i\omega t} + e^{-i\omega t}\right) & 0 \\ \frac{B_x}{2}\left(e^{i\omega t} + e^{-i\omega t}\right) & -\frac{2}{3}D & \frac{B_x}{2}\left(e^{i\omega t} + e^{-i\omega t}\right) \\ 0 & \frac{B_x}{2}\left(e^{i\omega t} + e^{-i\omega t}\right) & \frac{1}{3}D - B_z \end{pmatrix} \tag{2.66}$$

To simplify this, we redefine the B_x field as:

$$B_x \equiv \frac{B_x}{2} \tag{2.67}$$

Which gives:

$$H_{gs} = \hbar \begin{pmatrix} \frac{1}{3}D + B_z & B_x\left(e^{i\omega t} + e^{-i\omega t}\right) & 0 \\ B_x\left(e^{i\omega t} + e^{-i\omega t}\right) & -\frac{2}{3}D & B_x\left(e^{i\omega t} + e^{-i\omega t}\right) \\ 0 & B_x\left(e^{i\omega t} + e^{-i\omega t}\right) & \frac{1}{3}D - B_z \end{pmatrix} \tag{2.68}$$

Continuing with the interaction picture approach, we have the equation:

$$i\hbar \frac{\partial \Phi}{\partial t} = \left(P^{-1}HP - i\hbar P^{-1}\frac{\partial P}{\partial t}\right)\Phi \tag{2.69}$$

Our first choice for P will be given as follows, by convention:

$$P^{-1} = \exp\left(\frac{iH_{0,S}t}{\hbar}\right) \tag{2.70}$$

Here $H_{0,S}$ represents the time-independent part of the Hamiltonian, so:

$$H_{0,S} = \hbar\begin{pmatrix} \frac{1}{3}D + B_z & 0 & 0 \\ 0 & -\frac{2}{3}D & 0 \\ 0 & 0 & \frac{1}{3}D - B_z \end{pmatrix} \tag{2.71}$$

This gives:

$$P^{-1} = \begin{pmatrix} \exp\left(i\left(\frac{1}{3}D + B_z\right)t\right) & 0 & 0 \\ 0 & \exp\left(i\left(-\frac{2}{3}D\right)t\right) & 0 \\ 0 & 0 & \exp\left(i\left(\frac{1}{3}D - B_z\right)t\right) \end{pmatrix} \tag{2.72}$$

Inverting is straightforward since this is a diagonal matrix:

$$P = \begin{pmatrix} \exp\left(-i\left(\frac{1}{3}D + B_z\right)t\right) & 0 & 0 \\ 0 & \exp\left(i\left(\frac{2}{3}D\right)t\right) & 0 \\ 0 & 0 & \exp\left(-i\left(\frac{1}{3}D - B_z\right)t\right) \end{pmatrix} \tag{2.73}$$

Now we can write $P^{-1}HP$:

$$P^{-1}HP = \hbar\begin{pmatrix} \frac{1}{3}D + B_z & B_x(e^{i\omega t} + e^{-i\omega t})e^{(D+B_z)it} & 0 \\ B_x(e^{i\omega t} + e^{-i\omega t})e^{-(D+B_z)it} & -\frac{2}{3}D & B_x(e^{i\omega t} + e^{-i\omega t})e^{-(D-B_z)it} \\ 0 & B_x(e^{i\omega t} + e^{-i\omega t})e^{(D-B_z)it} & \frac{1}{3}D - B_z \end{pmatrix} \quad (2.74)$$

Now time for the derivative portion, $i\hbar P^{-1}\frac{\partial P}{\partial t}$:

$$\frac{\partial P}{\partial t} = \begin{pmatrix} -i\left(\frac{1}{3}D + B_z\right)\exp\left(-i\left(\frac{1}{3}D + B_z\right)t\right) & 0 & 0 \\ 0 & i\left(\frac{2}{3}D\right)\exp\left(i\left(\frac{2}{3}D\right)t\right) & 0 \\ 0 & 0 & -i\left(\frac{1}{3}D - B_z\right)\exp\left(-i\left(\frac{1}{3}D - B_z\right)t\right) \end{pmatrix} \quad (2.75)$$

$$P^{-1}\frac{\partial P}{\partial t} = \begin{pmatrix} -i\left(\frac{1}{3}D + B_z\right) & 0 & 0 \\ 0 & i\left(\frac{2}{3}D\right) & 0 \\ 0 & 0 & -i\left(\frac{1}{3}D - B_z\right) \end{pmatrix} \quad (2.76)$$

$$i\hbar P^{-1}\frac{\partial P}{\partial t} = \hbar\begin{pmatrix} \left(\frac{1}{3}D + B_z\right) & 0 & 0 \\ 0 & -\left(\frac{2}{3}D\right) & 0 \\ 0 & 0 & \left(\frac{1}{3}D - B_z\right) \end{pmatrix} \quad (2.77)$$

Combining these components gives:

$$H_{new} = P^{-1}HP - i\hbar P^{-1}\frac{\partial P}{\partial t} \quad (2.78)$$

$$H_{new} = \hbar\begin{pmatrix} 0 & B_x(e^{i\omega t} + e^{-i\omega t})e^{(D+B_z)it} & 0 \\ B_x(e^{i\omega t} + e^{-i\omega t})e^{-(D+B_z)it} & 0 & B_x(e^{i\omega t} + e^{-i\omega t})e^{-(D-B_z)it} \\ 0 & B_x(e^{i\omega t} + e^{-i\omega t})e^{(D-B_z)it} & 0 \end{pmatrix} \quad (2.79)$$

Applying the rotating wave approximation here, the quickly varying terms are dropped:

$$H_{new} = \hbar \begin{pmatrix} 0 & B_x\left(e^{-i\omega t}\right)e^{(D+B_z)it} & 0 \\ B_x\left(e^{i\omega t}\right)e^{-(D+B_z)it} & 0 & B_x\left(e^{i\omega t}\right)e^{-(D-B_z)it} \\ 0 & B_x\left(e^{-i\omega t}\right)e^{(D-B_z)it} & 0 \end{pmatrix} \quad (2.80)$$

$$H_{new} = \hbar \begin{pmatrix} 0 & B_x e^{i\left(-\omega+(D+B_z)\right)t} & 0 \\ B_x e^{i\left(\omega-(D+B_z)\right)t} & 0 & B_x e^{i\left(\omega-(D-B_z)\right)t} \\ 0 & B_x e^{i\left(-\omega+(D-B_z)\right)t} & 0 \end{pmatrix} \quad (2.81)$$

Previously for the two-level system we introduced a single detuning. Now there are two detunings, defined as:

$$\Delta_+ \equiv \omega - (D + B_z), \qquad \Delta_- \equiv \omega - (D - B_z) \quad (2.82)$$

So:

$$H_{new} = \hbar \begin{pmatrix} 0 & B_x e^{-i\Delta_+ t} & 0 \\ B_x e^{i\Delta_+ t} & 0 & B_x e^{i\Delta_- t} \\ 0 & B_x e^{-i\Delta_- t} & 0 \end{pmatrix} \quad (2.83)$$

As before, this satisfies the equation:

$$i\hbar \frac{\partial \Phi}{\partial t} = H_{new}\Phi \quad (2.84)$$

Where the modified wave function is:

$$\Phi = P^{-1}\Psi = \begin{pmatrix} \exp\left(i\left(\frac{1}{3}D + B_z\right)t\right) & 0 & 0 \\ 0 & \exp\left(i\left(-\frac{2}{3}D\right)t\right) & 0 \\ 0 & 0 & \exp\left(i\left(\frac{1}{3}D - B_z\right)t\right) \end{pmatrix}\Psi \quad (2.85)$$

As before, we will now repeat the interaction picture procedure. We have:

$$i\hbar \frac{\partial \Theta}{\partial t} = \left(P^{-1}H_{new}P - i\hbar P^{-1}\frac{\partial P}{\partial t}\right)\Theta \quad (2.86)$$

Where:

$$\Theta \equiv P^{-1}\Phi \tag{2.87}$$

First we have to diagonalize H_{new}:

$$H_{new} = \hbar B_x \begin{pmatrix} 0 & e^{-i\Delta_+ t} & 0 \\ e^{i\Delta_+ t} & 0 & e^{i\Delta_- t} \\ 0 & e^{-i\Delta_- t} & 0 \end{pmatrix} \tag{2.88}$$

$$H_{new} = \hbar B_x \left(\begin{pmatrix} -e^{i(\Delta_- - \Delta_+)t} & e^{i(\Delta_- - \Delta_+)t} & e^{i(\Delta_- - \Delta_+)t} \\ 0 & -\sqrt{2}e^{i\Delta_- t} & \sqrt{2}e^{i\Delta_- t} \\ 1 & 1 & 1 \end{pmatrix} \begin{pmatrix} 0 & 0 & 0 \\ 0 & -\sqrt{2} & 0 \\ 0 & 0 & \sqrt{2} \end{pmatrix} \right) \cdot \begin{pmatrix} -\frac{1}{2}e^{i(-\Delta_- + \Delta_+)t} & 0 & \frac{1}{2} \\ \frac{1}{4}e^{i(-\Delta_- + \Delta_+)t} & -\frac{\sqrt{2}}{4}e^{-i\Delta_- t} & \frac{1}{4} \\ \frac{1}{4}e^{i(-\Delta_- + \Delta_+)t} & \frac{\sqrt{2}}{4}e^{-i\Delta_- t} & \frac{1}{4} \end{pmatrix} \tag{2.89}$$

Noting that:

$$\Delta_- - \Delta_+ = 2B_z \tag{2.90}$$

This can be rewritten as:

$$H_{new} = \hbar B_x \begin{pmatrix} -e^{2iB_z t} & e^{2iB_z t} & e^{2iB_z t} \\ 0 & -\sqrt{2}e^{i\Delta_- t} & \sqrt{2}e^{i\Delta_- t} \\ 1 & 1 & 1 \end{pmatrix} \begin{pmatrix} 0 & 0 & 0 \\ 0 & -\sqrt{2} & 0 \\ 0 & 0 & \sqrt{2} \end{pmatrix} \begin{pmatrix} -\frac{1}{2}e^{-2iB_z t} & 0 & \frac{1}{2} \\ \frac{1}{4}e^{-2iB_z t} & -\frac{\sqrt{2}}{4}e^{-i\Delta_- t} & \frac{1}{4} \\ \frac{1}{4}e^{-2iB_z t} & \frac{\sqrt{2}}{4}e^{-i\Delta_- t} & \frac{1}{4} \end{pmatrix} \tag{2.91}$$

Rearranging this gives:

$$\begin{pmatrix} -\frac{1}{2}e^{-2iB_z t} & 0 & \frac{1}{2} \\ \frac{1}{4}e^{-2iB_z t} & -\frac{\sqrt{2}}{4}e^{-i\Delta_- t} & \frac{1}{4} \\ \frac{1}{4}e^{-2iB_z t} & \frac{\sqrt{2}}{4}e^{-i\Delta_- t} & \frac{1}{4} \end{pmatrix} H_{new} \begin{pmatrix} -e^{2iB_z t} & e^{2iB_z t} & e^{2iB_z t} \\ 0 & -\sqrt{2}e^{i\Delta_- t} & \sqrt{2}e^{i\Delta_- t} \\ 1 & 1 & 1 \end{pmatrix} = \hbar B_x \begin{pmatrix} 0 & 0 & 0 \\ 0 & -\sqrt{2} & 0 \\ 0 & 0 & \sqrt{2} \end{pmatrix} \tag{2.92}$$

This immediately provides us with our P^{-1} and P for the second round:

$$P^{-1} = \begin{pmatrix} -\frac{1}{2}e^{-2iB_z t} & 0 & \frac{1}{2} \\ \frac{1}{4}e^{-2iB_z t} & -\frac{\sqrt{2}}{4}e^{-i\Delta_- t} & \frac{1}{4} \\ \frac{1}{4}e^{-2iB_z t} & \frac{\sqrt{2}}{4}e^{-i\Delta_- t} & \frac{1}{4} \end{pmatrix}, \qquad P = \begin{pmatrix} -e^{2iB_z t} & e^{2iB_z t} & e^{2iB_z t} \\ 0 & -\sqrt{2}e^{i\Delta_- t} & \sqrt{2}e^{i\Delta_- t} \\ 1 & 1 & 1 \end{pmatrix} \quad (2.93)$$

Giving:

$$P^{-1}H_{new}P = \hbar B_x \begin{pmatrix} 0 & 0 & 0 \\ 0 & -\sqrt{2} & 0 \\ 0 & 0 & \sqrt{2} \end{pmatrix} \quad (2.94)$$

For the time derivative part, $i\hbar P^{-1}\frac{\partial P}{\partial t}$:

$$\frac{\partial P}{\partial t} = \begin{pmatrix} -2iB_z e^{2iB_z t} & 2iB_z e^{2iB_z t} & 2iB_z e^{2iB_z t} \\ 0 & -i\Delta_-\sqrt{2}e^{i\Delta_- t} & i\Delta_-\sqrt{2}e^{i\Delta_- t} \\ 0 & 0 & 0 \end{pmatrix} \quad (2.95)$$

$$P^{-1}\frac{\partial P}{\partial t} = \begin{pmatrix} -\frac{1}{2}e^{-2iB_z t} & 0 & \frac{1}{2} \\ \frac{1}{4}e^{-2iB_z t} & -\frac{\sqrt{2}}{4}e^{-i\Delta_- t} & \frac{1}{4} \\ \frac{1}{4}e^{-2iB_z t} & \frac{\sqrt{2}}{4}e^{-i\Delta_- t} & \frac{1}{4} \end{pmatrix} \begin{pmatrix} -2iB_z e^{2iB_z t} & 2iB_z e^{2iB_z t} & 2iB_z e^{2iB_z t} \\ 0 & -i\Delta_-\sqrt{2}e^{i\Delta_- t} & i\Delta_-\sqrt{2}e^{i\Delta_- t} \\ 0 & 0 & 0 \end{pmatrix} \quad (2.96)$$

$$P^{-1}\frac{\partial P}{\partial t} = \begin{pmatrix} iB_z & -iB_z & -iB_z \\ -\frac{1}{2}iB_z & \frac{1}{2}iB_z + \frac{1}{2}i\Delta_- & \frac{1}{2}iB_z - \frac{1}{2}i\Delta_- \\ -\frac{1}{2}iB_z & \frac{1}{2}iB_z - \frac{1}{2}i\Delta_- & \frac{1}{2}iB_z + \frac{1}{2}i\Delta_- \end{pmatrix} \quad (2.97)$$

Rewriting:

$$P^{-1}\frac{\partial P}{\partial t} = \begin{pmatrix} iB_z & -iB_z & -iB_z \\ -\frac{1}{2}iB_z & \frac{1}{2}i(B_z + \Delta_-) & \frac{1}{2}i(B_z - \Delta_-) \\ -\frac{1}{2}iB_z & \frac{1}{2}i(B_z - \Delta_-) & \frac{1}{2}i(B_z + \Delta_-) \end{pmatrix} \quad (2.98)$$

So:

$$i\hbar P^{-1}\frac{\partial P}{\partial t} = \hbar\begin{pmatrix} -B_z & B_z & B_z \\ \frac{1}{2}B_z & -\frac{1}{2}(B_z+\Delta_-) & -\frac{1}{2}(B_z-\Delta_-) \\ \frac{1}{2}B_z & -\frac{1}{2}(B_z-\Delta_-) & -\frac{1}{2}(B_z+\Delta_-) \end{pmatrix} \tag{2.99}$$

So combining:

$$H_{2nd} = P^{-1}H_{new}P - i\hbar P^{-1}\frac{\partial P}{\partial t} \tag{2.100}$$

$$H_{2nd} = \hbar\begin{pmatrix} B_z & -B_z & -B_z \\ -\frac{1}{2}B_z & -\sqrt{2}B_x + \frac{1}{2}(B_z+\Delta_-) & \frac{1}{2}(B_z-\Delta_-) \\ -\frac{1}{2}B_z & \frac{1}{2}(B_z-\Delta_-) & \sqrt{2}B_x + \frac{1}{2}(B_z+\Delta_-) \end{pmatrix} \tag{2.101}$$

The second round modified Schrodinger's equation is now:

$$i\hbar\frac{\partial \Theta}{\partial t} = H_{2nd}\Theta \tag{2.102}$$

$$i\hbar\frac{\partial \Theta}{\partial t} = \hbar\begin{pmatrix} B_z & -B_z & -B_z \\ -\frac{1}{2}B_z & -\sqrt{2}B_x + \frac{1}{2}(B_z+\Delta_-) & \frac{1}{2}(B_z-\Delta_-) \\ -\frac{1}{2}B_z & \frac{1}{2}(B_z-\Delta_-) & \sqrt{2}B_x + \frac{1}{2}(B_z+\Delta_-) \end{pmatrix}\Theta \tag{2.103}$$

As before, as the time-dependence in the Hamiltonian has been entirely removed after two interaction picture transformations.

The work thus far has been laborious and correct, but at this point it is not reasonable to proceed further. If we were to follow our normal procedure, then the next step would be to get the eigenvalues and eigenvectors of this time-independent Hamiltonian in order to write the general time evolution. However, the diagonalization of H_{2nd} gives eigenvalues and eigenvectors that are far too lengthy to put into this thesis. Shockingly, the first entry of the first eigenvector contains over 40 terms! As a middle ground it is possible to programmatically diagonalize this matrix and

output the wavefunction Ψ for particular numerical values of B_z, B_x, and ω at each time of interest t. In this way we can still compare the analytical result from the above equation with the QuTiP model of the same initial Hamiltonian. Fortunately there is excellent agreement between these two models under both resonant and detuned microwave regimes.

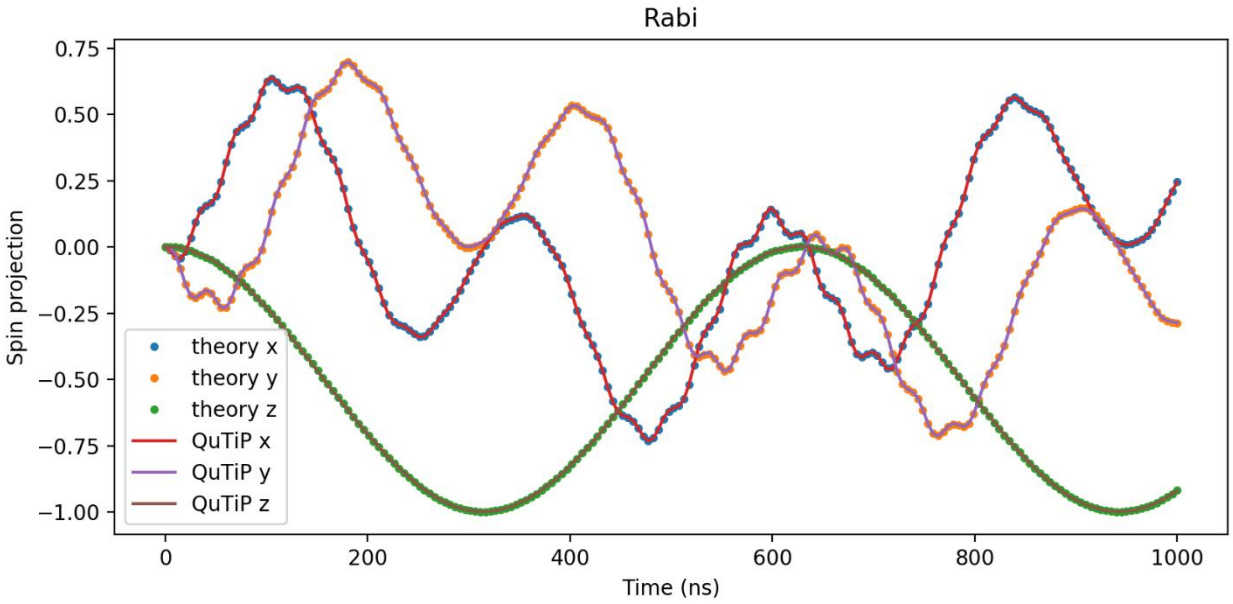

Figure 2.6 | Simulated Rabi oscillations between $m_s = 0 \leftrightarrow -1$ for the 3-level VV^0 ground state. Here there is a B_z Zeeman splitting and a B_x drive with no detuning or phase. The "theory" curves are obtained with the matrix equation in 2.103. The "QuTiP" curves are obtained using the python QuTiP package with the Hamiltonian in equation 2.68. The simulation starts in $m_s = 0$ in both cases.

In this case, the z-projection of spin follows a simple sinusoid as it is driven between $m_s = 0$ and $m_s = -1$. The x and y projections of spin follow more complicated behavior, but feature excellent agreement between the two models. This shows that the double interaction picture approach is somewhat generalizable for obtaining analytical solutions to Schrodinger's equation under sinusoidal drives, but these solutions can quickly become intractable for relatively simple 3x3 Hamiltonians. QuTiP is still able to easily handle 3x3 systems, but one can imagine how the

model could break down for much higher dimensions (i.e., 100 or 1000). Extrapolating this idea perhaps gives some insight as to why the physical quantum systems built into quantum processors are a promising route to simulate quantum dynamics once the dimensionality passes a certain threshold. The inclusion of multiqubit gates and entangled states would only muddy the waters further, reinforcing the necessity for quantum processors to accurately model complex quantum systems.

We have shown the possibility of driving magnetic transitions between integer spin states such as $m_s = 0 \leftrightarrow +1$ and $m_s = 0 \leftrightarrow -1$. This was possible due to the presence of magnetic field terms in the off-diagonal entries of the Hamiltonian linking these states together. If we examine the electric field terms in the Hamiltonian, we can see that electric field is driving is also possible. The allowed transitions were outlined in table 2.1 in section "Transition rules for the VV^0 ground state". The same derivation that we just performed could also be carried out for AC electric field transitions with the same overall end result.

Lastly, we can perform a quick calculation to get an idea of what magnetic field amplitudes are necessary to drive spin transitions. The transverse magnetic field term in the ground state Hamiltonian is:

$$\frac{\mu_B g_{gs}^{\perp}}{\sqrt{2}}\left(B_x - iB_y\right), \qquad \mu_B = \text{Bohr magneton} = \frac{e\hbar}{2m_e}, \qquad g_{gs}^{\perp} \approx 2 \tag{2.104}$$

During microwave driving, we have a sinusoidally varying term:

$$\frac{\mu_B g_{gs}^{\perp}}{\sqrt{2}} B_x \cos(\omega t) = 2\hbar\Omega \cos(\omega t) \tag{2.105}$$

With zero detuning and zero phase, the frequency of the Rabi oscillations will be given by Ω. Plugging in 2 for the g-factor and isolating Ω gives:

$$\Omega = \frac{\mu_B}{\sqrt{2}\hbar} B_x = (1.575 \cdot 10^9) B_x \tag{2.106}$$

Relating this to the period T of a Rabi oscillation gives:

$$\frac{2\pi}{T} = (1.575 \cdot 10^9) B_x, \qquad T = \frac{4 \cdot 10^{-9}}{B_x} \tag{2.107}$$

To obtain ~100 ns period Rabi oscillations commonly observed, we need a B-field amplitude of:

$$B_x = \frac{4 \cdot 10^{-9}}{100 \cdot 10^{-9}} = \frac{4}{100} = 0.025\, T = 250\, G \tag{2.108}$$

2.7 The two-level subspace assumption

Even for quantum systems containing many states, it is usually possible to select a pair of states to treat as an isolated two-level system. For example, if we were dealing with the *c*-axis VV^0 with a Bz field, we could select the $m_s = 0$ and $m_s = +1$ states as our qubit basis. To do this, we start with the ground state Hamiltonian:

$$H_{gs} = \hbar \begin{pmatrix} \frac{1}{3}D + B_z & B_x & 0 \\ B_x & -\frac{2}{3}D & B_x \\ 0 & B_x & \frac{1}{3}D - B_z \end{pmatrix} \tag{2.109}$$

Where again "B_z" and "B_x" are simplified magnetic field terms that drop other multiplicative factors. Now we only focus on the entries corresponding to the $m_s = 0$ and $m_s = +1$ states. Or phrased another way, we seek to drop the $m_s = -1$ state from this system. Looking at the diagonal entries, the $m_s = -1$ state's energy appears in the 3rd row/column. We then drop this entire 3rd row/column to give:

$$H_{gs} = \hbar \begin{pmatrix} \frac{1}{3}D + B_z & B_x & \cancel{0} \\ B_x & -\frac{2}{3}D & \cancel{B_x} \\ \cancel{0} & \cancel{B_x} & \cancel{\frac{1}{3}D - B_z} \end{pmatrix} = \hbar \begin{pmatrix} \frac{1}{3}D + B_z & B_x \\ B_x & -\frac{2}{3}D \end{pmatrix} \tag{2.110}$$

This implies that the states of interest (and the ones to be eliminated) must be eigenstates whose energies appear along the main diagonal of the zero field Hamiltonian. With this reduced Hamiltonian at hand, we can now treat the dynamics of the $\{m_s = 0, m_s = +1\}$ subspace as a two-level system with the same dynamics outlined in the first chapter of this thesis.

In general, this assumption holds when there is not significant "crosstalk" between the eigenstates. In the *c*-axis VV^0 example with Zeeman splitting, the $m_s = \pm 1$ states must be sufficiently split such that a transition between $m_s = 0$ to either $m_s = \pm 1$ does not inadvertently cause transitions to the other integer spin state $m_s = \mp 1$. Similarly, the eigenstates $m_s = -1, 0, +1$ should each be stationary without unwanted mixing caused by, for example, off-diagonal entries in the Hamiltonian.

As an example of mixing, the E term appears naturally in off-diagonal entries of the Hamiltonian for basal VV^0 defects [31]. This means that the integer states $\{m_s = 0, m_s = +1\}$ would be an inappropriate choice for a two-level system subspace. After diagonalizing this

Hamiltonian to remove this mixing behavior, however, we could then select the more natural states $\{|0\rangle, |+\rangle\}$ which are stationary in this Hamiltonian.

While this selection of a subspace may seem pedantic, it is in fact a cornerstone of engineering and understanding quantum systems. In the example of magnetic driving of the VV^0, we just saw that analytical solutions are intractable if all three levels are included but greatly simplify if only two levels are considered. More generally, typical measurements to characterize a quantum system (Rabi oscillations, decoherence and dephasing times, etc.) are most easily understood in a two-level system setting. The building blocks of quantum computing and communication protocols also often assume two-level systems and simple one or two-qubit gates. Thus, this subspace assumption is often implicitly made across various quantum platforms including the VV^0. Two suitably isolated and stable states are chosen as the "qubit" and characterization measurements are built from this selection.

In some cases, the nontrivial interplay between multiple eigenstates may be a desired effect. In stimulated Raman adiabatic passage, for example, an excited state $|e\rangle$ serves as an intermediary level to facilitate population transfer between two ground states $|g_1\rangle$ and $|g_2\rangle$ that are not directly coupled in a Λ system. [32] In most cases, however, considering the dynamics of all possible levels quickly becomes prohibitive. Indeed, the complexity of classically simulating an n-dimensional quantum system grows exponentially as n increases.

2.8 Excited state Hamiltonian

From the previous sections we have seen that the 3x3 ground state Hamiltonian of the divacancy can be quite complicated. Unfortunately the situation does not get any simpler in the excited state, which now features a 6x6 Hamiltonian. For a 6-dimensional system we must immediately abandon any hopes of writing analytical solutions for state evolutions or making geometric parallels to Bloch spheres or rotations. The excited state Hamiltonian is also not diagonalizable in the general case, meaning the idea of stable stationary states is on tenuous ground. Finally, the presence of spontaneous emission means that any pseudo-stable states we are able to discern will quickly decay to the ground state. Quantifying this decay rate is also quite complicated and is revisited in chapter 5 on cavity QED.

Given these roadblocks, our description of the excited state will not go into as much detail as the previous sections. Nevertheless, an intuition of the excited state can be developed by examining its Hamiltonian and the energies it predicts. We will start with a description of the excited state orbitals and the possible basis states used to describe the system. We will then use these bases to express the zero-field Hamiltonian and outline the energy level structure. Finally, we'll see how the addition of electric field, strain, and magnetic field modifies the Hamiltonian in a similar fashion to the ground state Hamiltonian in section 2.4.

2.8.1 Excited state orbitals

The electron orbitals outlined in section 2.3 still hold for the excited state, with the difference being the occupation of the higher energy orbitals. Since there are two excited state orbitals, there are two general configurations of the unpaired electrons, each of which then gives a spin triplet. The excited state orbitals are sometimes referred to as the e_x and e_y orbitals [33-34]. The decay from

the excited state to the ground state results in the emission of an infrared wavelength photon. Depending on the vacancy type the zero-phonon emission of this decay is in the range of ~1040-1140 nm, although emissions at longer wavelengths are possible if phonons are involved. Either way, the overall spin state of the system is generally preserving during these decays. The properties of the emission spectrum are discussed in more detail in the section in chapter 3 titled "VV^0 emission spectrum".

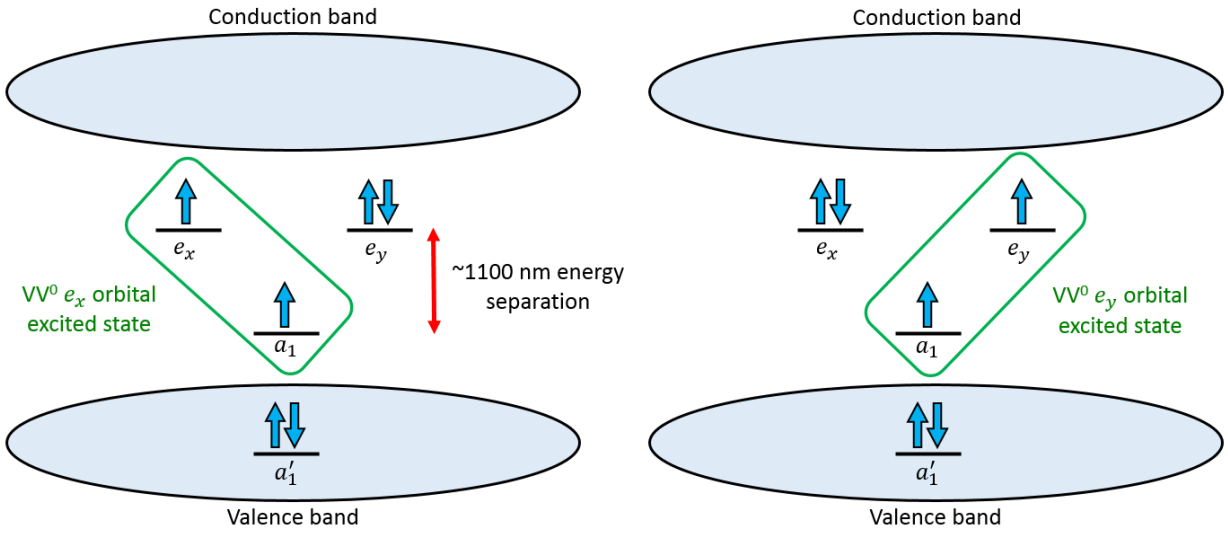

Figure 2.7 | Orbitals in the band gap. The six electrons of the neutral divacancy occupy four orbitals, three of which are in the SiC band gap. In the excited state, one of the electrons in the a_1 orbital gets excited to either the e_x or e_y orbital. Both possible configurations of the orbital occupations are shown here. The green box highlights the unpaired electrons that form the spin-1 state of the excited state.

Figure 2.7 provides two specific examples of excited state configurations. Given that there are two excited state orbitals and each contains a spin triplet, this results in six possible excited states. [3] However, the direct pairing of the spin triplet states with the Ex/Ey orbital occupation does not directly give the eigenstates of the excited state. This leads to the questions of what are the excited state eigenstates and what is an appropriate basis for the excited state? This decision was made

naturally in the ground state, as the spin triplet states there are exactly the eigenstates of the ground state Hamiltonian. However, in the excited state the picture is not as clear, so this warrants some additional discussion of basis states.

2.8.2 Defining basis states

Continuing with the idea presented in the previous section, one definition of basis states could be to categorize the state by its excited state orbital occupation and the spin state of the unpaired electrons. Just as with the ground state, we can represent the ms = -1/0/+1 states as:

$$|+1\rangle = \begin{pmatrix}1\\0\\0\end{pmatrix}, \qquad |0\rangle = \begin{pmatrix}0\\1\\0\end{pmatrix}, \qquad |-1\rangle = \begin{pmatrix}0\\0\\1\end{pmatrix} \tag{2.111}$$

Meanwhile we can label the two excited state orbitals as "X" and "Y" such that:

$$|X\rangle = \text{in } e_x \text{ orbital}, \qquad |Y\rangle = \text{in } e_y \text{ orbital} \tag{2.112}$$

Or, as vectors:

$$|X\rangle = \begin{pmatrix}1\\0\end{pmatrix}, \qquad |Y\rangle = \begin{pmatrix}0\\1\end{pmatrix} \tag{2.113}$$

Therefore, there are six combinations in the excited state, depending on which orbital you are in and what spin state you are in. These form the basis states:

$$|X\rangle \otimes |+1\rangle = \begin{pmatrix}1\\0\\0\\0\\0\\0\end{pmatrix}, \qquad |X\rangle \otimes |0\rangle = \begin{pmatrix}0\\1\\0\\0\\0\\0\end{pmatrix}, \qquad |X\rangle \otimes |-1\rangle = \begin{pmatrix}0\\0\\1\\0\\0\\0\end{pmatrix} \tag{2.114}$$

$$|Y\rangle \otimes |+1\rangle = \begin{pmatrix} 0 \\ 0 \\ 0 \\ 1 \\ 0 \\ 0 \end{pmatrix}, \qquad |Y\rangle \otimes |0\rangle = \begin{pmatrix} 0 \\ 0 \\ 0 \\ 0 \\ 1 \\ 0 \end{pmatrix}, \qquad |Y\rangle \otimes |-1\rangle = \begin{pmatrix} 0 \\ 0 \\ 0 \\ 0 \\ 0 \\ 1 \end{pmatrix} \tag{2.115}$$

This is the basis used in reference [21] for the NV^- center in diamond, which shares an identical excited state structure with *c*-axis divacancies. This basis is complete and spans the Hilbert space of all possible excited states, so any state can be represented as a linear combination of these vectors. For this thesis, we will refer to this basis as the "Doherty basis" since it is built off of his work in reference [21].

Unfortunately, however, these basis states are not the stationary states of the excited state Hamiltonian. In an attempt to use basis states that more closely resemble eigenstates, we can instead use another basis as in [29,30]. These basis states are denoted as $\{|A_1\rangle, |A_2\rangle, |E_x\rangle, |E_y\rangle, |E_1\rangle, |E_2\rangle\}$ and can be written in terms of the orbtial/spin basis states as:

$$\begin{gathered} |A_1\rangle = |E_-\rangle \otimes |+1\rangle - |E_+\rangle \otimes |-1\rangle \\ |A_2\rangle = |E_-\rangle \otimes |+1\rangle + |E_+\rangle \otimes |-1\rangle \\ |E_x\rangle = |X\rangle \otimes |0\rangle \\ |E_y\rangle = |Y\rangle \otimes |0\rangle \\ |E_1\rangle = |E_-\rangle \otimes |-1\rangle - |E_+\rangle \otimes |+1\rangle \\ |E_2\rangle = |E_-\rangle \otimes |-1\rangle + |E_+\rangle \otimes |+1\rangle \end{gathered} \tag{2.116}$$

This basis will be referred to as the "Maze basis" since it is built off of his work in reference [33]. Here, the $|E_\pm\rangle$ states are defined as:

$$|E_+\rangle = -|X\rangle - i|Y\rangle \tag{2.117}$$

$$|E_-\rangle = |X\rangle - i|Y\rangle \tag{2.118}$$

Which are sometimes referred to as the states of definite orbital angular momentum [33,34]. Distributing the terms in eq 2.116, we can write the Maze basis states in the Doherty basis explicitly as:

$$|A_1\rangle = \frac{1}{2}\begin{pmatrix} 1 \\ 0 \\ 1 \\ -i \\ 0 \\ i \end{pmatrix}_{\text{Doherty}} \quad , \quad |A_2\rangle = \frac{1}{2}\begin{pmatrix} 1 \\ 0 \\ -1 \\ -i \\ 0 \\ -i \end{pmatrix}_{\text{Doherty}} \tag{2.119}$$

$$|E_1\rangle = \frac{1}{2}\begin{pmatrix} 1 \\ 0 \\ 1 \\ i \\ 0 \\ -i \end{pmatrix}_{\text{Doherty}} \quad , \quad |E_2\rangle = \frac{1}{2}\begin{pmatrix} -1 \\ 0 \\ 1 \\ -i \\ 0 \\ -i \end{pmatrix}_{\text{Doherty}} \tag{2.120}$$

$$|E_x\rangle = |X\rangle \otimes |0\rangle = \begin{pmatrix} 0 \\ 1 \\ 0 \\ 0 \\ 0 \\ 0 \end{pmatrix}_{\text{Doherty or Maze}} \quad , \quad |E_y\rangle = |Y\rangle \otimes |0\rangle = \begin{pmatrix} 0 \\ 0 \\ 0 \\ 0 \\ 1 \\ 0 \end{pmatrix}_{\text{Doherty or Maze}} \tag{2.121}$$

The "Doherty" subscript is there as a reminder that these vectors are written using the Doherty basis vectors. Note that a factor of ½ has been included for $|A_1\rangle, |A_2\rangle, |E_1\rangle, |E_2\rangle$ for normalization.

2.8.3 The zero-field *c*-axis VV^0 excited state Hamiltonian

It would be possible to write the excited state Hamiltonian entirely in terms of a linear combination of the 36 possible outer products between the Doherty basis vectors. Since this would be quite

verbose, instead the excited state Hamiltonian is represented using tensor products of the 2x2 Pauli matrices to represent the X/Y orbitals and the 3x3 spin-1 matrices to represent the spin state. This is written as [21]:

$$\begin{aligned}\hat{H}_{es}^{LT} = D_{es}^{\parallel}\left[\hat{S}_z^2 - \frac{S(S+1)}{3}\right] - \lambda_{es}^{\parallel}\hat{\sigma}_y \otimes \hat{S}_z + D_{es}^{\perp}\left[\hat{\sigma}_z \otimes \left(\hat{S}_y^2 - \hat{S}_x^2\right) - \hat{\sigma}_x \otimes \left(\hat{S}_y\hat{S}_x + \hat{S}_x\hat{S}_y\right)\right] \\ + \lambda_{es}^{\perp}\left[\hat{\sigma}_z \otimes \left(\hat{S}_x\hat{S}_z + \hat{S}_z\hat{S}_x\right) - \hat{\sigma}_x \otimes \left(\hat{S}_y\hat{S}_z + \hat{S}_z\hat{S}_y\right)\right]\end{aligned} \tag{2.122}$$

Where $\hat{\sigma}_x, \hat{\sigma}_y, \hat{\sigma}_z$ are the Pauli matrices, $\hat{S}_x, \hat{S}_y, \hat{S}_z$ are the $S = 1$ spin operators, and $D_{es}^{\parallel}, D_{es}^{\perp}, \lambda_{es}^{\parallel}, \lambda_{es}^{\perp}$ are scalar fine structure parameters that will be discussed in more detail in the next section. As a reminder, we have:

$$\sigma_x = \begin{pmatrix} 0 & 1 \\ 1 & 0 \end{pmatrix}, \qquad \sigma_y = \begin{pmatrix} 0 & -i \\ i & 0 \end{pmatrix}, \qquad \sigma_z = \begin{pmatrix} 1 & 0 \\ 0 & -1 \end{pmatrix} \tag{2.123}$$

And the spin-1 operators are:

$$S_x = \frac{\hbar}{\sqrt{2}}\begin{pmatrix} 0 & 1 & 0 \\ 1 & 0 & 1 \\ 0 & 1 & 0 \end{pmatrix}, \qquad S_y = \frac{\hbar}{\sqrt{2}}\begin{pmatrix} 0 & -i & 0 \\ i & 0 & -i \\ 0 & i & 0 \end{pmatrix}, \qquad S_z = \hbar\begin{pmatrix} 1 & 0 & 0 \\ 0 & 0 & 0 \\ 0 & 0 & -1 \end{pmatrix} \tag{2.124}$$

As an example of tensor products, we can write the following term in matrix form:

$$\hat{\sigma}_y \otimes \hat{S}_z = \begin{pmatrix} 0 & -i \\ i & 0 \end{pmatrix} \otimes \begin{pmatrix} 1 & 0 & 0 \\ 0 & 0 & 0 \\ 0 & 0 & -1 \end{pmatrix} \tag{2.125}$$

In general, for tensor products are computed with the following pattern:

$$A = \begin{pmatrix} a_{11} & a_{12} \\ a_{21} & a_{22} \end{pmatrix}, \qquad B = \begin{pmatrix} b_{11} & b_{12} \\ b_{21} & b_{22} \end{pmatrix} \tag{2.126}$$

$$A \otimes B = \begin{pmatrix} a_{11}\begin{pmatrix} b_{11} & b_{12} \\ b_{21} & b_{22} \end{pmatrix} & a_{12}\begin{pmatrix} b_{11} & b_{12} \\ b_{21} & b_{22} \end{pmatrix} \\ a_{21}\begin{pmatrix} b_{11} & b_{12} \\ b_{21} & b_{22} \end{pmatrix} & a_{22}\begin{pmatrix} b_{11} & b_{12} \\ b_{21} & b_{22} \end{pmatrix} \end{pmatrix} = \begin{pmatrix} a_{11}b_{11} & a_{11}b_{12} & a_{12}b_{11} & a_{12}b_{12} \\ a_{11}b_{21} & a_{11}b_{22} & a_{12}b_{21} & a_{12}b_{22} \\ a_{21}b_{11} & a_{21}b_{12} & a_{22}b_{11} & a_{22}b_{12} \\ a_{21}b_{21} & a_{21}b_{22} & a_{22}b_{21} & a_{22}b_{22} \end{pmatrix} \quad (2.127)$$

With this in mind, the example product becomes:

$$\hat{\sigma}_y \otimes \hat{S}_z = \begin{pmatrix} 0 & -i \\ i & 0 \end{pmatrix} \otimes \begin{pmatrix} 1 & 0 & 0 \\ 0 & 0 & 0 \\ 0 & 0 & -1 \end{pmatrix} = \begin{pmatrix} 0 & 0 & 0 & -i & 0 & 0 \\ 0 & 0 & 0 & 0 & 0 & 0 \\ 0 & 0 & 0 & 0 & 0 & i \\ i & 0 & 0 & 0 & 0 & 0 \\ 0 & 0 & 0 & 0 & 0 & 0 \\ 0 & 0 & -i & 0 & 0 & 0 \end{pmatrix}_{\text{Doherty}} \quad (2.128)$$

The "Doherty" subscript is there to remind us that this matrix is written assuming the Doherty basis vectors. Applying this same methodology with all of the other tensor products and combining the results gives:

$$H_{ES} = \begin{pmatrix} \frac{1}{3}D_{es}^{\parallel} & \frac{1}{\sqrt{2}}\lambda_{es}^{\perp} & -D_{es}^{\perp} & i\lambda_{es}^{\parallel} & i\frac{1}{\sqrt{2}}\lambda_{es}^{\perp} & iD_{es}^{\perp} \\ \frac{1}{\sqrt{2}}\lambda_{es}^{\perp} & -\frac{2}{3}D_{es}^{\parallel} & -\frac{1}{\sqrt{2}}\lambda_{es}^{\perp} & -i\frac{1}{\sqrt{2}}\lambda_{es}^{\perp} & 0 & -i\frac{1}{\sqrt{2}}\lambda_{es}^{\perp} \\ -D_{es}^{\perp} & -\frac{1}{\sqrt{2}}\lambda_{es}^{\perp} & \frac{1}{3}D_{es}^{\parallel} & -iD_{es}^{\perp} & i\frac{1}{\sqrt{2}}\lambda_{es}^{\perp} & -i\lambda_{es}^{\parallel} \\ -i\lambda_{es}^{\parallel} & i\frac{1}{\sqrt{2}}\lambda_{es}^{\perp} & iD_{es}^{\perp} & \frac{1}{3}D_{es}^{\parallel} & -\frac{1}{\sqrt{2}}\lambda_{es}^{\perp} & D_{es}^{\perp} \\ -i\frac{1}{\sqrt{2}}\lambda_{es}^{\perp} & 0 & -i\frac{1}{\sqrt{2}}\lambda_{es}^{\perp} & -\frac{1}{\sqrt{2}}\lambda_{es}^{\perp} & -\frac{2}{3}D_{es}^{\parallel} & \frac{1}{\sqrt{2}}\lambda_{es}^{\perp} \\ -iD_{es}^{\perp} & i\frac{1}{\sqrt{2}}\lambda_{es}^{\perp} & i\lambda_{es}^{\parallel} & D_{es}^{\perp} & \frac{1}{\sqrt{2}}\lambda_{es}^{\perp} & \frac{1}{3}D_{es}^{\parallel} \end{pmatrix}_{Doherty} \quad (2.129)$$

This can be used to model the energies and dynamics within the excited state. The numerous off-diagonal entries indicate that these basis states are not stationary and will rapidly mix into each other. In this form, it is difficult to gain an intuition for the dynamics at play in the excited state.

In an attempt to gain a more diagonal form, we can instead write the zero-field zero-strain Hamiltonian in the "Maze" basis of $\{|A_1\rangle, |A_2\rangle, |E_x\rangle, |E_y\rangle, |E_1\rangle, |E_2\rangle\}$, which gives:

$$H_{ES} = \begin{pmatrix} \Delta - \Delta' + \lambda_z & 0 & 0 & 0 & 0 & 0 \\ 0 & \Delta + \Delta' + \lambda_z & 0 & 0 & 0 & 0 \\ 0 & 0 & -2\Delta & 0 & 0 & i\Delta'' \\ 0 & 0 & 0 & -2\Delta & \Delta'' & 0 \\ 0 & 0 & 0 & \Delta'' & \Delta - \lambda_z & 0 \\ 0 & 0 & -i\Delta'' & 0 & 0 & \Delta - \lambda_z \end{pmatrix} \tag{2.130}$$

As can be seen, this matrix is almost diagonal, except for the off-diagonal entries involving Δ''. With this form we can make some observations about the excited state at zero strain. Because the first two rows/column are only occupied on the main diagonal, we can say that the states corresponding to these rows/columns are truly stationary. In this case, the higher energy $|A_1\rangle$ and $|A_2\rangle$ states are stationary. Meanwhile, the zero spin $|E_x\rangle$ and $|E_y\rangle$ states will mix with the lower energy $|E_1\rangle$ and $|E_2\rangle$ states and vice versa. This mixing is dictated by the magnitude of Δ'' and is built into the system. Realistically the strain is almost never zero for a divacancy, but before we examine those effects we need to consolidate the numerous parameters that appears in these Hamiltonians. This is the subject of the next section.

2.8.4 Relations between excited state parameters

Unfortunately, the variables used for the excited state parameters is somewhat inconsistent in the literature. As a summary we have the following sets of variables: [3,21,32]

$$\text{Doherty } (\text{NV}^-) = \{\lambda_{es}^{\parallel}, D_{es}^{\parallel}, D_{es}^{\perp}, \lambda_{es}^{\perp}\} \tag{2.131}$$

$$\text{Maze } (\text{NV}^-) = \{\lambda_z, \Delta, \Delta', \Delta''\} \tag{2.132}$$

$$\text{Christle } (\text{VV}^0) = \{\lambda_z, D_{es}, \Delta_1, \Delta_2\} \tag{2.133}$$

Where the variables have been listed in corresponding order. For the NV^- center in diamond, the following values result in matching zero-strain energy eigenvalues for the excited state Hamiltonian:

$$\text{Doherty } (\text{NV}^-), \quad \begin{matrix} \lambda_{es}^{\parallel} = 5.3\ GHz, & D_{es}^{\parallel} = 1.42\ GHz, \\ D_{es}^{\perp} = \dfrac{1.55}{2}\ GHz, & \lambda_{es}^{\perp} = \dfrac{0.2}{\sqrt{2}}\ GHz \end{matrix} \tag{2.134}$$

In the Maze basis we have:

$$\text{Maze } (\text{NV}^-), \quad \begin{matrix} \lambda_z = 5.3\ GHz, & \Delta = \dfrac{1.42}{3}\ GHz, \\ \Delta' = 1.55\ GHz, & \Delta'' = 0.2\ GHz \end{matrix} \tag{2.135}$$

From these NV^- values we can infer the initial relations:

$$\lambda_{es}^{\parallel} = \lambda_z, \qquad D_{es}^{\parallel} = 3\Delta, \qquad D_{es}^{\perp} = \frac{\Delta'}{2}, \qquad \lambda_{es}^{\perp} = \frac{\Delta''}{\sqrt{2}} \tag{2.136}$$

As we move to the VV^0 in silicon carbide, the following values are obtained from the work in [3]:

$$(hh)\ \text{VV}^0, \quad \begin{matrix} \lambda_z = 3.538 \pm 0.052\ GHz, & D_{es} = 0.855 \pm 0.017\ GHz, \\ \Delta_1 = 0.577 \pm 0.019\ GHz, & \Delta_2 = 0.031 \pm (+0.050 - 0.031)\ GHz \\ \text{95\% intervals} & \end{matrix} \tag{2.137}$$

$$(kk)\ \text{VV}^0, \quad \begin{matrix} \lambda_z = 6.090 \pm 0.052\ GHz, & D_{es} = 0.852 \pm 0.012\ GHz, \\ \Delta_1 = 0.584 \pm 0.012\ GHz, & \Delta_2 = 0.044 \pm (+0.046 - 0.044)\ GHz \\ \text{95\% intervals} & \end{matrix} \tag{2.138}$$

Although it is a different system, these variables correspond to those presented by Doherty and Maze in the following way:

$$\lambda_{es}^{\parallel} = \lambda_z = \lambda_z, \qquad D_{es}^{\parallel} = 3\Delta = D_{es}, \qquad D_{es}^{\perp} = \frac{\Delta'}{2} = \frac{\Delta_1}{2}, \qquad \lambda_{es}^{\perp} = \frac{\Delta''}{\sqrt{2}} = \frac{\Delta_2}{\sqrt{2}} \qquad (2.139)$$

The physical interpretation of these variables is tied to spin-spin and spin-orbit interactions usually without much further elaboration. The work by Doherty *et al.*, perhaps wisely, avoids venturing into explanations and simply calls them "parameters". In the work by Maze *et al.*, λ_z is referred to as the axial part of the spin-orbit interaction (with λ_{xy} the non-axial part), Δ, Δ' are parameters that have to do with the spin-spin interactions and zero-field splittings, Δ'' is a "mixing" term between spin states. Here "mixing" refers to the fact that the Maze basis Hamiltonian is diagonal except for the presence of the Δ'' terms which cause interactions between the $\{|A_1\rangle, |A_2\rangle, |E_x\rangle, |E_y\rangle, |E_1\rangle, |E_2\rangle\}$ basis states. Since we are dealing with the VV^0 in SiC, moving forward we will use the variables $\{\lambda_z, D_{es}, \Delta_1, \Delta_2\}$ featured in [3].

2.8.5 Excited state level structure

With the Hamiltonian established and excited state parameters chosen, we can now map out the energy levels of the excited state as given in the figure below:

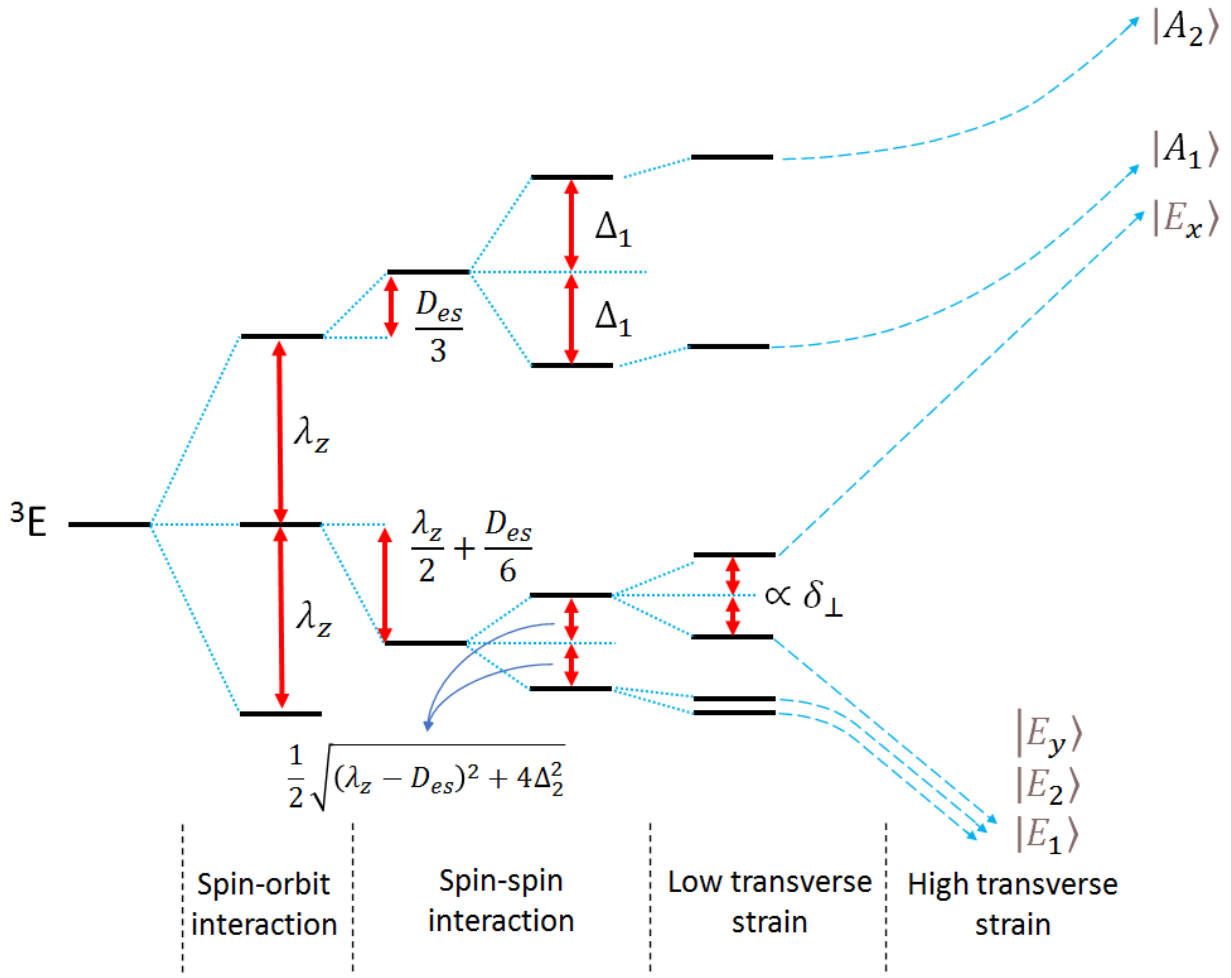

Figure 2.8 | VV^0 excited state level structure. The energy levels are generally split into four regimes as labeled at the bottom of the figure. The addition of transverse strain breaks the final degeneracy of the Hamiltonian from four energy levels to six, which then separate into two branches with additional strain. The excited state parameters $\{\lambda_z, D_{es}, \Delta_1, \Delta_2, \delta_\perp\}$ adapted from [3] are used here.

The general effect of transverse strain is apparent in the figure above, but is demonstrated more explicitly in the figure below:

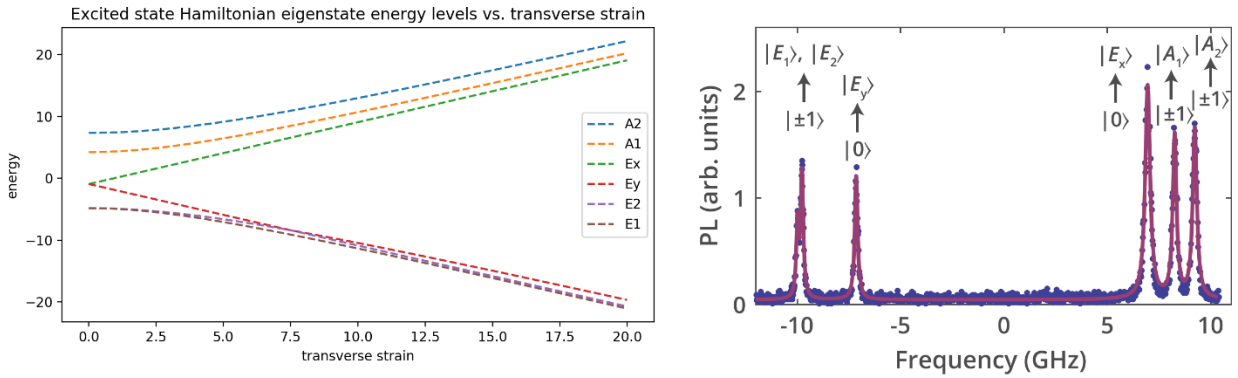

Figure 2.9 | VV^0 Excited state energy levels. On the left is the analytical result from the (*hh*) VV^0 Hamiltonian showing the energy eigenstates as a function of transverse strain. On the right is a photoluminescence excitation (PLE) spectrum of a single (*hh*) VV^0 in SiC adapted from [3].

Before we more precisely quantify the effects of strain and other external fields, we will first establish a conversion between the Doherty and Maze bases in the next section.

2.8.6 Transforming between bases

Similar to the approach in section 2.5, a transition between these two bases can be achieved through the change of basis matrix (COB). This matrix can be written as:

$$COB = (A_1 \quad A_2 \quad -E_y \quad -E_x \quad E_2 \quad E_1) \tag{2.140}$$

$$COB = \left(\begin{pmatrix} \frac{1}{2} \\ 0 \\ \frac{1}{2} \\ -\frac{i}{2} \\ 0 \\ \frac{i}{2} \end{pmatrix} \quad \begin{pmatrix} \frac{1}{2} \\ 0 \\ -\frac{1}{2} \\ -\frac{i}{2} \\ 0 \\ -\frac{i}{2} \end{pmatrix} - \begin{pmatrix} 0 \\ 0 \\ 0 \\ 1 \\ 0 \end{pmatrix} - \begin{pmatrix} 0 \\ 1 \\ 0 \\ 0 \\ 0 \\ 0 \end{pmatrix} \quad \begin{pmatrix} -\frac{1}{2} \\ 0 \\ \frac{1}{2} \\ -\frac{i}{2} \\ 0 \\ -\frac{i}{2} \end{pmatrix} \quad \begin{pmatrix} \frac{1}{2} \\ 0 \\ \frac{1}{2} \\ \frac{i}{2} \\ 0 \\ -\frac{i}{2} \end{pmatrix}\right) \tag{2.141}$$

Which gives:

$$COB = \begin{pmatrix} \frac{1}{2} & \frac{1}{2} & 0 & 0 & -\frac{1}{2} & \frac{1}{2} \\ 0 & 0 & 0 & -1 & 0 & 0 \\ \frac{1}{2} & -\frac{1}{2} & 0 & 0 & \frac{1}{2} & \frac{1}{2} \\ -\frac{i}{2} & -\frac{i}{2} & 0 & 0 & -\frac{i}{2} & \frac{i}{2} \\ 0 & 0 & -1 & 0 & 0 & 0 \\ \frac{i}{2} & -\frac{i}{2} & 0 & 0 & -\frac{i}{2} & -\frac{i}{2} \end{pmatrix}, \quad COB^{-1} = \begin{pmatrix} \frac{1}{2} & 0 & \frac{1}{2} & \frac{i}{2} & 0 & -\frac{i}{2} \\ \frac{1}{2} & 0 & -\frac{1}{2} & \frac{i}{2} & 0 & \frac{i}{2} \\ 0 & 0 & 0 & 0 & -1 & 0 \\ 0 & -1 & 0 & 0 & 0 & 0 \\ -\frac{1}{2} & 0 & \frac{1}{2} & \frac{i}{2} & 0 & \frac{i}{2} \\ \frac{1}{2} & 0 & \frac{1}{2} & -\frac{i}{2} & 0 & \frac{i}{2} \end{pmatrix} \tag{2.142}$$

With this matrix, we can convert the excited state Hamiltonian (or any field or strain term in the Hamiltonian) using the relations

$$H_{Doherty} = COB \cdot H_{Maze} \cdot COB^{-1} \tag{2.143}$$

$$COB^{-1} \cdot H_{Doherty} \cdot COB = H_{Maze} \tag{2.144}$$

We will use these conversions in the upcoming sections.

2.8.7 Effect of electric field and strain

The presence of electric field or strain corresponds to adding the following terms to the zero-field Hamiltonian [21]:

$$V_E^{es} = d_{es}^{\parallel}(E_z + \delta_z)I_2 \otimes I_3 + d_{es}^{\perp}(E_x + \delta_x)\hat{\sigma}_z \otimes I_3 - d_{es}^{\perp}(E_y + \delta_y)\hat{\sigma}_x \otimes I_3 \tag{2.145}$$

Where $\{E_x, E_y, E_z\}$ is electric field, $\{\delta_x, \delta_y, \delta_z\}$ is strain, $\{\sigma_x, \sigma_y, \sigma_z\}$ are the 2D Pauli matrices, $\{S_x, S_y, S_z\}$ are the 3D spin-1 matrices, $\{I_2, I_3\}$ are 2x2 or 3x3 identity matrices, and $\{d_{es}^{\parallel}, d_{es}^{\perp}\}$ are electric dipole moment components. This equation is written using the Doherty basis. It is important to put the Pauli matrices σ_i first in the tensor products and the 3-dimensional spin

matrices S_i second, so we generally have $\sigma_i \otimes S_i$ for each term. Carrying out these tensor products and combining terms can give the Hamiltonian in matrix form. For simplicity we include the strain terms here with no prefactors. Note that the electric field will have the same dependence:

$$V_E^{es} \approx \begin{pmatrix} \delta_z + \delta_x & 0 & 0 & -\delta_y & 0 & 0 \\ 0 & \delta_z + \delta_x & 0 & 0 & -\delta_y & 0 \\ 0 & 0 & \delta_z + \delta_x & 0 & 0 & -\delta_y \\ -\delta_y & 0 & 0 & \delta_z - \delta_x & 0 & 0 \\ 0 & -\delta_y & 0 & 0 & \delta_z - \delta_x & 0 \\ 0 & 0 & -\delta_y & 0 & 0 & \delta_z - \delta_x \end{pmatrix}_{Doherty} \tag{2.146}$$

Using the COB conversion outlined in the previous section, we can write this in the Maze basis as [33,34]:

$$V_E^{es} \approx \begin{pmatrix} \delta_z & 0 & 0 & 0 & \delta_x & -i\delta_y \\ 0 & \delta_z & 0 & 0 & i\delta_y & -\delta_x \\ 0 & 0 & \delta_z + \delta_x & \delta_y & 0 & 0 \\ 0 & 0 & \delta_y & \delta_z - \delta_x & 0 & 0 \\ \delta_x & -i\delta_y & 0 & 0 & \delta_z & 0 \\ i\delta_x & -\delta_y & 0 & 0 & 0 & \delta_z \end{pmatrix}_{Maze} \tag{2.147}$$

Note that in both cases δ_z gets added along the main diagonal, which has the effect of uniformly shifting all the energies.

2.8.8 Effect of magnetic field

The presence of magnetic field corresponds to adding the following terms to the zero-field Hamiltonian [21]:

$$V_B^{es} = \mu_B\left(l_{es}^{\parallel}\hat{\sigma}_y \otimes \hat{S}_I + g_{es}^{\parallel}\hat{\sigma}_I \otimes \hat{S}_z\right)B_z + \mu_B g_{es}^{\perp}\hat{\sigma}_I \otimes \left(\hat{S}_x B_x + \hat{S}_y B_y\right) \tag{2.148}$$

Where $\{B_x, B_y, B_z\}$ is magnetic field, $\{\sigma_x, \sigma_y, \sigma_z\}$ are the 2D Pauli matrices, $\{S_x, S_y, S_z\}$ are the 3D spin-1 matrices, $\{\sigma_I, S_I\}$ are 2x2 or 3x3 identity matrices, μ_B is the Bohr magneton, $l_{es}^{\parallel}$ is the orbital magnetic moment, and $\{g_{es}^{\parallel}, g_{es}^{\perp}\}$ are electronic g-factors. This equation is written using the Doherty basis. Here, again it is important preserve the order $\sigma_i \otimes S_i$ for each tensor product. Carrying out these products and combining into matrix form gives the following dependence, with prefactors dropped for simplicity:

$$V_B^{es} \approx \begin{pmatrix} B_z & B_x - iB_y & 0 & -iB_z & 0 & 0 \\ B_x + iB_y & 0 & B_x - iB_y & 0 & -iB_z & 0 \\ 0 & B_x + iB_y & -B_z & 0 & 0 & -iB_z \\ iB_z & 0 & 0 & B_z & B_x - iB_y & 0 \\ 0 & iB_z & 0 & B_x + iB_y & 0 & B_x - iB_y \\ 0 & 0 & iB_z & 0 & B_x + iB_y & -B_z \end{pmatrix}_{Doherty} \tag{2.149}$$

Using the COB conversion, in the Maze basis this becomes:

$$V_B^{es} \approx \begin{pmatrix} 0 & B_z & B_x & B_y & 0 & 0 \\ B_z & 0 & -iB_y & iB_x & 0 & 0 \\ B_x & iB_y & 0 & -iB_z & B_x & -iB_y \\ B_y & -iB_x & iB_z & 0 & -B_y & -iB_x \\ 0 & 0 & B_x & -B_y & 0 & -B_z \\ 0 & 0 & iB_y & iB_x & -B_z & 0 \end{pmatrix}_{Maze} \tag{2.150}$$

2.9 Excited state polarization rules

The transitions between the ground and excited states of the VV^0 follow polarization selectivity rules for both absorption and emission of photons. Generally speaking, the polarization state of a photon can be denoted as a complex linear combination of horizontal and vertical polarizations, which can be expressed as:

$$|H\rangle, \quad \text{Horizontally polarized light} \tag{2.151}$$

$$|V\rangle, \quad \text{Vertically polarized light} \tag{2.152}$$

Combining these polarization basis states leads to the other four states of:

$$|L\rangle = \frac{1}{\sqrt{2}}(|H\rangle + i|V\rangle), \quad \text{Left circularly polarized light} \tag{2.153}$$

$$|R\rangle = \frac{1}{\sqrt{2}}(|H\rangle - i|V\rangle), \quad \text{Right circularly polarized light} \tag{2.154}$$

$$|D\rangle = \frac{1}{\sqrt{2}}(|H\rangle + |V\rangle), \quad \text{Diagonally polarized light} \tag{2.155}$$

$$|A\rangle = \frac{1}{\sqrt{2}}(|H\rangle - |V\rangle), \quad \text{Antidiagonally polarized light} \tag{2.156}$$

With this notation in hand, we can represent the absorption/emission of photons between the ground and excited states of the *c*-axis VV^0 in the following table, which follows the same rules as the NV^- center in diamond [33-35]:

	$\|A_1\rangle$	$\|A_2\rangle$	$\|E_1\rangle$	$\|E_2\rangle$	$\|E_x\rangle$	$\|E_y\rangle$
$\|m_s = -1\rangle$	$\|L\rangle$	$\|L\rangle$	$\|R\rangle$	$\|R\rangle$	-	-
$\|m_s = 0\rangle$	-	-	-	-	$\|V\rangle$	$\|H\rangle$
$\|m_s = +1\rangle$	$\|R\rangle$	$\|R\rangle$	$\|L\rangle$	$\|L\rangle$	-	-

Table 2.2 | Polarization selectivity of transitions between ground and excited states of the divacancy. As an example, left circularly polarized light ($|L\rangle$) will couple the $|A_1\rangle$ and $|A_2\rangle$ excited states to the $|m_s = -1\rangle$ ground state. This coupling applies for both optical absorption and emission.

As an example, when the VV^0 is in the $|A_2\rangle$ excited state, it can either decay to the $|m_s = +1\rangle$ ground state and emit a right circularly polarized photon $|R\rangle$ or decay to the $|m_s = -1\rangle$ ground state and emit a left circularly polarized photon $|L\rangle$. This is shown schematically in figure 2.10.

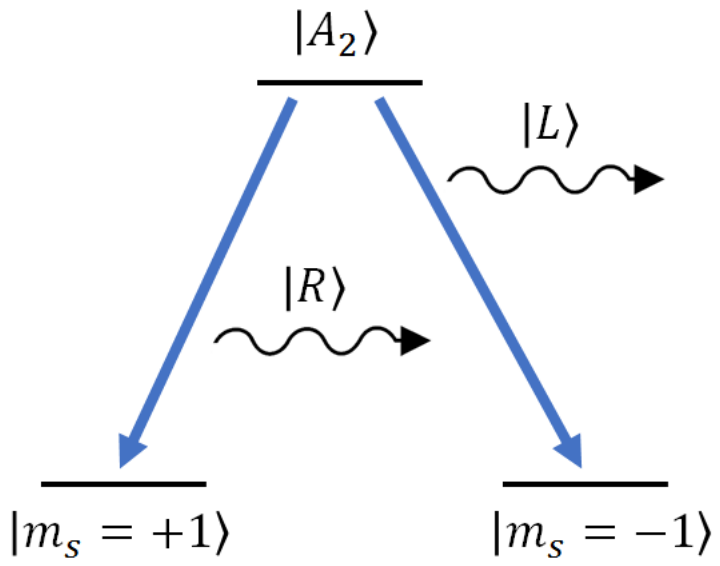

Figure 2.10 | Polarization of emitted light when decaying from the VV^0 $|A_2\rangle$ excited state. A *c*-axis VV^0 prepared in the $|A_2\rangle$ excited state will have an equal probability of emitting a right circularly polarized photon ($|R\rangle$) and decaying to the $|m_s = +1\rangle$ ground state or emitting a left circularly polarized photon ($|L\rangle$) and decaying to the $|m_s = -1\rangle$ ground state.

The pairs of photon states $\{|H\rangle, |V\rangle\}$, $\{|L\rangle, |R\rangle\}$, and $\{|A\rangle, |D\rangle\}$ are completely orthogonal to each other, which provides a potential selectivity when collecting or exciting with polarized light. For example, pumping with $|R\rangle$ light will in principle only excite the $|m_s = +1\rangle \rightarrow \{|A_1\rangle, |A_2\rangle\}$ transitions, even if the energies of these transitions are overlapping with the $|m_s = +1\rangle \rightarrow \{|E_1\rangle, |E_2\rangle\}$ transitions. Conversely, excitation with diagonal light $|D\rangle$ will not provide any selectivity for any transition, as $|D\rangle$ is not orthogonal to any of the polarization states $\{|H\rangle, |V\rangle, |L\rangle, |R\rangle\}$ featured in table 2.2.

2.10 The intersystem crossing

In addition to the ground state and excited state manifolds, the VV^0 also contains an intermediary singlet state commonly referred to as the intersystem crossing (ISC). This intermediate state provides a non-radiative decay pathway from the excited state that competes with the ES → GS transition. This state also appears in the NV^- center in diamond and is well documented in the NV^- literature [36,37]. An energy level schematic of the ISC is included in the figure below:

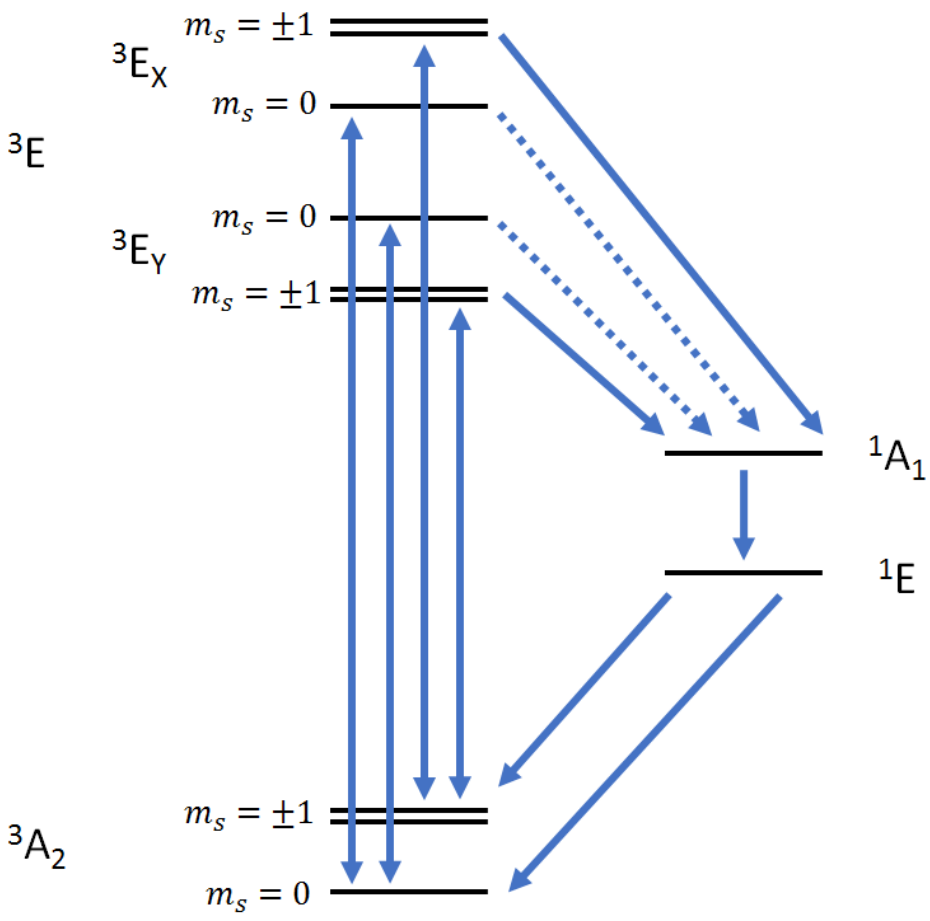

Figure 2.11 | Energy level schematic of the intersystem crossing. The ISC connects the excited state to the ground state through a competing nonradiative decay pathway. The dotted lines indicate the comparatively weaker rates to the ISC from $m_s = 0$ excited states.

Each excited state has its own rate to the ISC which can affect the cyclicity of a transition used for readout. Generally the $m_s = 0$ excited states have the lowest relative rates, which is why they are selected as the cycling resonant readout states for both the NV^- center and the VV^0. Once in the state is in ISC, any time spent will not result in detected photons, so this decay pathway results in an overall lower count rate. Decay from the ISC to the ground state also randomizes the spin state despite a preference towards $m_s = 0$ in most cases. On the bright side, this does allow for off-resonant initialization and readout through this mechanism. While the quantitative measures of ISC rates are not well explored in for the VV^0 in SiC, the dynamics at play are quantifiable and share many parallels to the NV^- center in diamond.

Broadly speaking, the ISC is like the training wheels for solid-state color centers. For initial experiments an ISC is a quick and easy way to demonstrate optical initialization and readout and serves as a great benefit to the system. For high-fidelity single defect experiments, however, the ISC ultimately limits the ability to achieve single-shot readout and entanglement. Because there is no easy way to "remove" the ISC from the system, it sours into an undesirable feature. Nevertheless, we will explore the impact of the ISC level in a Markov chain model in chapter 4 and consider its relationship with Purcell enhancement in chapter 7.

Chapter 3

Figures of Merit

3.1 Decoherence of a quantum state

In nearly all experiments, the ability of a quantum state to remain stable is an important figure of merit that determines the eventual fidelity of quantum computing, communication, and metrology protocols. This state stability is generally termed the "coherence" of a state, and the loss of this stability to referred to as "decoherence". More specifically, the decoherence of a quantum state means the loss of information about the amplitude and phase of the basis states that compose the quantum state. In the long-time limit, any state will eventually reach an equilibrium where all information is lost and no definitive statements can be made about the state. At intermediate time scales, there may be uncertainty attached to individual components but the overall state is still known. In the example of a two-level system, the most general state at $t = 0$ can be written as:

$$|\psi\rangle(0) = c_0|0\rangle + c_1 e^{i\phi}|1\rangle \tag{3.1}$$

Where here c_0, c_1 are the amplitudes and ϕ is the phase between the states. After a certain amount of time has elapsed, this state may become:

$$|\psi\rangle(t) = (c_0(t) \pm \Delta c_0)|0\rangle + (c_1(t) \pm \Delta c_1)e^{i(\phi(t)\pm\Delta\phi)}|1\rangle \tag{3.2}$$

Where here the uncertainties in the variables are represented by $\Delta c_0, \Delta c_1, \Delta\phi$. How quickly this uncertainty grows with time is called the decoherence time of the qubit. Its specific value can set restraints on the time scale of experiments and the amount of time a qubit is allowed to be "idle" before its quantum information is lost. The time scale of decoherence can also vary dramatically between systems, spanning the full gamut from single nanoseconds to multiple hours. An important caveat to this time scale is the speed with which operations can be performed on the qubit. In some contexts, it is the ratio of the decoherence time over the qubit gate time that truly matters for applications. In most cases the two time scales trend in the same direction; exceedingly long coherence times usually come at the cost of slower operation speeds (although this is not always the case, see ref [38]).

The cause of decoherence in solid-state qubits is generally attributed to stochastic fluctuations of electric and magnetic fields in the environment. These fluctuations can come from nuclear spins, paramagnetic impurities, and other defect species. More directly, thermal fluctuations and phonons directly limit the coherence of most systems, which is why cryogenic cooling is nearly ubiquitous for quantum information experiments.

In this section, we will examine some of the common ways decoherence is measured and quantified in the context of the divacancy in silicon carbide.

3.2 T_2^* – The spin dephasing time

The T_2^* time refers to the time scale associated with dephasing of a qubit, where we are interested in the phase between the eigenstates that compose the state. In a completely dephased state, this

phase information is completely lost, even though the qubit may still be in a pure state. For a two-level system, precession of a superposition state is normally given by:

$$\Psi(t) = e^{\frac{i\omega_0 t}{2}}\left(c_g|g\rangle + c_e|e\rangle e^{-i\omega_0 t}\right) \tag{3.3}$$

Dropping global phase gives:

$$\Psi(t) = c_g|g\rangle + c_e|e\rangle e^{-i\omega_0 t} \tag{3.4}$$

Here the excited state $|e\rangle$ accumulates phase, which we are interested in tracking, relative to the ground state $|g\rangle$. The phase accumulation rate is given by ω_0 in the above equation, such that the accumulated phase after a time t is simply given by $\omega_0 t$. This means that a differential phase accumulation $d\phi$ is given by $d\phi = \omega_0 dt$. However, we may not always be able to rely on a uniform rate. If it is instead a function of time $\omega(t)$, then we must integrate the differential phase with respect to time to obtain a total phase accumulation:

$$\phi = \int d\phi = \int \omega(t)dt \tag{3.5}$$

The frequency may change with time due to fluctuations in the environment that cause shifted energy splittings between the two levels. We can make these fluctuations explicit by defining the time-varying frequency as:

$$\omega(t) \equiv \omega_0 + \delta(t) \tag{3.6}$$

In which case the total accumulated phase is:

$$\phi_{total} = \int \big(\omega_0 + \delta(t)\big)dt = \omega_0 t + \int \delta(t)dt \tag{3.7}$$

Or:

$$\phi_{total} = \omega_0 t + \phi_{noise}, \qquad \phi_{noise} = \int \delta(t) dt \tag{3.8}$$

The quantity $\omega_0 t$ is the "normal" accumulated phase, while $\int \delta(t) dt$ represents a deviation from this value due to the fluctuating environment. Note that the state is always on the Bloch sphere equator even with this noise term but its phase is now variable. Typically, $\delta(t)$ is a stochastic function that cannot be predicted.

To measure the overall loss of phase information due to noise, we perform an ensemble of identically prepared Ramsey interferometry experiments and average their results. Since $\delta(t)$ varies from experiment to experiment, its presence manifests as an averaging out of signal. The Ramsey sequence in outlined below in figure 3.1:

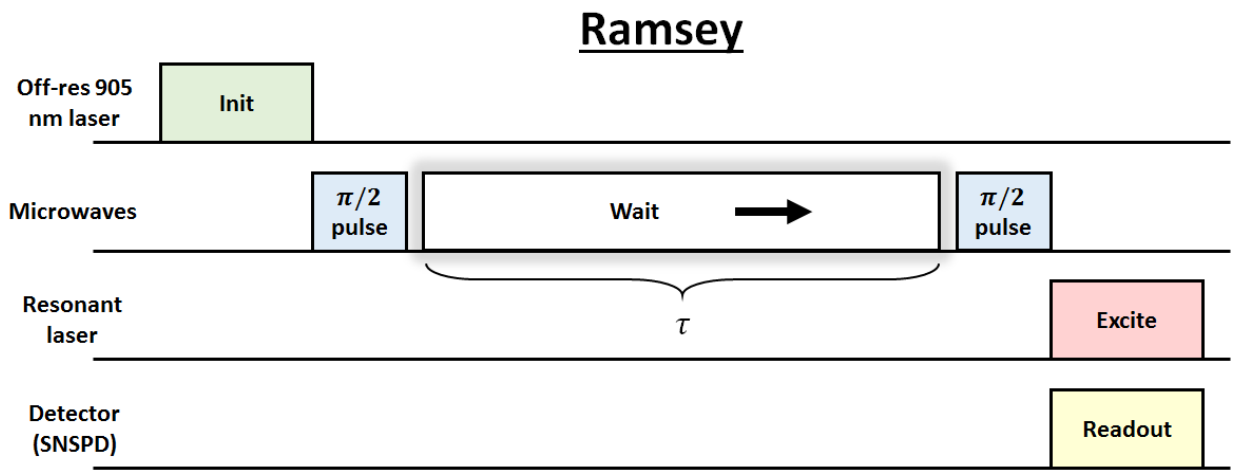

Figure 3.1 | Ramsey pulse sequence. The wait time τ between $\pi/2$ pulses is varied between experiments to determine when dephasing naturally occurs for a superposition state.

We can describe each part of this sequence in the context of VV^0 experiments. Initialization can be done optically with either resonant or off-resonant laser light. Microwave rotations of $\pi/2$

are applied with AC signal passing through nearby striplines or wire bonds. The phase ϕ_{total}, which we are interested in measuring, accumulates during the free evolution time τ between the two microwave pulses. During the readout sequence, we optically excite the defect and read out photoluminescence (PL) either in the form of voltage for a photoreceiver or quantized photon counts for a superconducting nanowire detector (SNSPD). Throughout this thesis we will use "counts" to represent PL, as most experiments were performed on single defects with an SNSPD. More details on the initialization, microwave rotation, and readout steps are discussed in sections 3.7, 3.8 of this chapter and chapter 4.

To work towards a mathematical understanding, it is useful to think of photoluminescence as a z-projection of the quantum state on the Bloch sphere. A higher z-projection gives more counts (on average), and vice versa. In other words, the $m_s = 0$ spin state is on average brighter than the $m_s = \pm 1$ state. The reasons for this are discussed in more detail in section 3.8, but for now we take this at face value. In terms of Bloch sphere coordinates, the z-projection is then given by the sine of the polar angle:

$$\text{z projection on Bloch sphere,} \qquad z = \sin(\theta) \tag{3.9}$$

Keeping with the Bloch sphere picture, each $\pi/2$ pulse corresponds to a 90-degree rotation around either the x-axis or y-axis. In reality, any azimuthal axis of rotation can be chosen as long as they are consistent (or exactly opposite) between the two microwave pulses, but here we will assume each rotation is around the negative y-axis. With this convention, the second $\pi/2$ pulse maps the azimuthal phase ϕ directly to the polar angle θ:

$$\text{polar angle after } \frac{\pi}{2} \text{ MW pulse,} \qquad \theta = \phi \tag{3.10}$$

We can now combine these results to get an expression for the photoluminescence PL. The PL is proportional to the magnitude of the z projection, but to be precise both the baseline of PL counts and the full range of counts between the $m_s = 0, \pm 1$ states must be incorporated into the sine as an additive and multiplicative factor, respectively. In total this gives:

$$\text{Photoluminescence (PL)}, \qquad PL = a\sin(\phi) + b \tag{3.11}$$

Where ϕ has been substituted for θ, "a" is related to the contrast between the bright $m_s = 0$ state and the dark $m_s = \pm 1$ state, and "b" is related to the baseline level of counts when in the dark $m_s = \pm 1$ state. For the sake of capturing the effects of dephasing without getting hindered by imperfect contrast, however, we will drop these factors and simply say:

$$PL \approx \sin(\phi) \tag{3.12}$$

Of course this relation cannot be taken too literally since photoluminescence cannot be negative, but making this step will simplify our analysis.

We are now interested in quantifying the effect of the phase noise term $\phi_{noise} = \int \delta(t)dt$ as we average the PL from many experiments. In a perfect world, the energy splitting between the eigenstates is fixed for all times and $\delta(t) = 0$. In this case the phase accumulation would be identical across all experiments, and the uniform Larmor precession would give an exact sinusoidal dependence for the phase. In terms of variables, ϕ_{total} would simply be $\omega_0 t$, meaning the PL would be given by $PL = \sin(\theta) = \sin(\omega_0 t)$ with no decay envelope. This is the case for "infinite coherence" as the PL would never decay with time.

Realistically, however, the noise term $\delta(t)$ is nonzero and varies both within a single experiment and from experiment to experiment. Using the direct mapping of azimuthal phase ϕ to polar angle θ, we can use eq. 3.12 to write the PL function as

$$PL = \sin(\phi_{total}) = \sin\left(\omega_0 t + \int \delta(t)dt\right) \tag{3.13}$$

The integral of the stochastic function $\int \delta(t)dt$ cannot be simplified until we make additional assumptions. For simplicity let us assume that $\delta(t)$ is a a normally distributed variable with a standard deviation of σ:

$$\delta(t) = \mathcal{N}(0, \sigma) \tag{3.14}$$

Where $\mathcal{N}(0, \sigma)$ denotes a sample from a normal distribution with mean 0 and standard deviation σ. How often the environment will "switch" its configuration is subject to several variables such as the density/stability of impurities and the presence of external static fields or laser radiation. We will assume that the environment switches (i.e. a sample from this normal distribution) with a frequency f, such that the number of switches in a time t is given by:

$$n = ft, \qquad \text{number of switches in time } t \tag{3.15}$$

Therefore, an elapsed time of t will correspond to sampling n times from a normal distribution $\mathcal{N}(0, \sigma)$. Each of these samples will contribute to the total accumulated phase. We can represent the additional phase (which can be positive or negative) accumulated at each time step due to the noise as a list:

$$\phi_{list} = [\mathcal{N}(0, \sigma),\ \mathcal{N}(0, \sigma),\ \mathcal{N}(0, \sigma),\ \ldots n \text{ times}] \tag{3.16}$$

Since this list will have many entries, we can use the central limit theorem to characterize the list mean:

$$\bar{x}_{\phi} = 0 \pm \frac{\sigma}{\sqrt{n}} \tag{3.17}$$

The total phase from this noise is obtained by multiplying this average by the n entries in the list:

$$\phi_{noise} = n\bar{x}_{\phi} = 0 \pm \frac{\sigma}{\sqrt{n}} n = 0 \pm \sigma\sqrt{n} \tag{3.18}$$

This is equivalent to the integral of the noise term, meaning:

$$\int \delta(t)dt = \mathcal{N}\left(0, \sigma\sqrt{ft}\right) \tag{3.19}$$

With this more explicit expression for the phase gained due to noise, the total accumulated phase (including the natural Larmor precession) then becomes:

$$\phi_{total} = \omega_0 t + \phi_{noise} = \omega_0 t + \left(0 \pm \sigma\sqrt{n}\right) = \omega_0 t \pm \sigma\sqrt{n} \tag{3.20}$$

As before, we take the sine of this total phase to map to a z-projection on the Bloch sphere after the $\pi/2$ rotation:

$$z = \sin(\phi_{total}) = \sin\left(\omega_0 t \pm \sigma\sqrt{n}\right) \tag{3.21}$$

As we perform many experiments and average them, the result for any particular time t will be given by:

$$z_{avg}(t) = \mu(z) = \mu\left(\sin\left(\omega_0 t \pm \sigma\sqrt{n}\right)\right) \tag{3.22}$$

Where $\mu(\ \ )$ denotes the average after many experiments. Substituting our earlier equation $n = ft$ and equating $PL_{avg}(t) = z_{avg}(t)$ gives:

$$PL_{avg}(t) = \mu\left(\sin\left(\omega_0 t \pm \sigma\sqrt{ft}\right)\right) \tag{3.23}$$

$$PL_{avg}(t) = \mu\left(\sin\left(\omega_0 t \pm \left(\sigma\sqrt{f}\right)\sqrt{t}\right)\right) \tag{3.24}$$

So after many accumulated experiments, the averaged PL represents the average of the sine of a normally distributed variable. Whereas a regular normally distributed variable is centered on its mean regardless of the standard deviation, this symmetry is broken when the variable is fed into a sine function.

This behavior is demonstrated in figure 3.2. The sine of a random normal variable is plotted for multiple standard deviations σ. Whereas the mean μ of the variable remains the same as the standard deviation increases, the mean of the *sine* of the variable changes and trends towards zero. This trend towards zero is what is responsible for the exponential decay to zero signal that we observe in an averaged Ramsey sequence. As the acquisition time in the Ramsey sequence increases, the noise term is integrated over an increasing time interval, which results in a greater standard deviation. This behavior is similar to the increase standard deviation of a random walk as the number of steps increases.

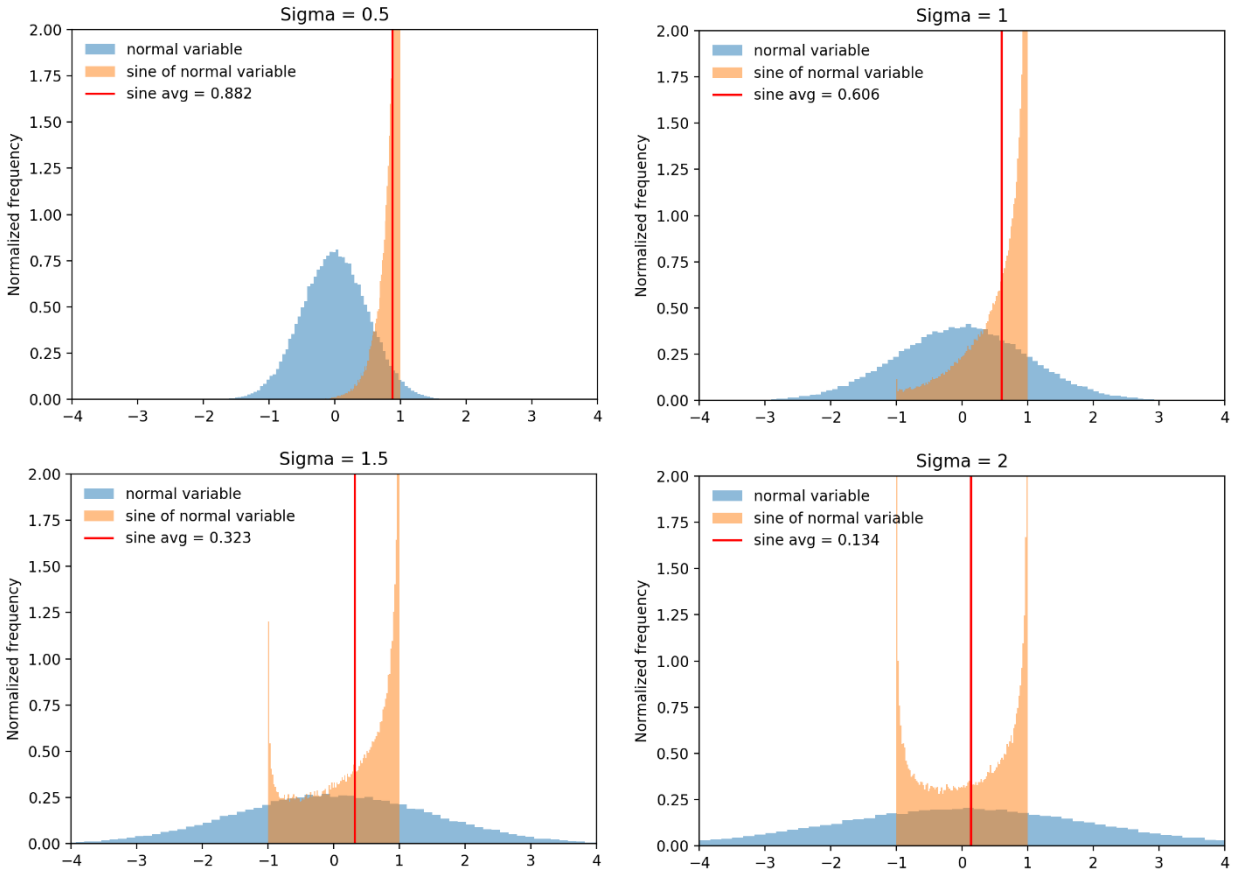

Figure 3.2 | Sine of normal distribution for various standard deviations σ. All graphs are using $\sin\left(\mathcal{N}(0,\sigma)+\frac{\pi}{2}\right)$, where $\mathcal{N}(0,\sigma)$ is a normally distributed variable with mean 0 and standard deviation σ. The phase of $\pi/2$ is included to showcase the asymmetric sine distributions. As the standard deviation increases, the mean of the sine distribution approaches zero. This parallels the T_2^* signal approaching zero for long wait times.

In experiments, we quantify T_2^* by fitting an exponential to a decaying PL envelope. To corroborate that this sine behavior gives an exponentially decaying Ramsey signal, we can run Mote Carlo simulations of the average PL over time, using the result of equation 3.24. This gives the following figure:

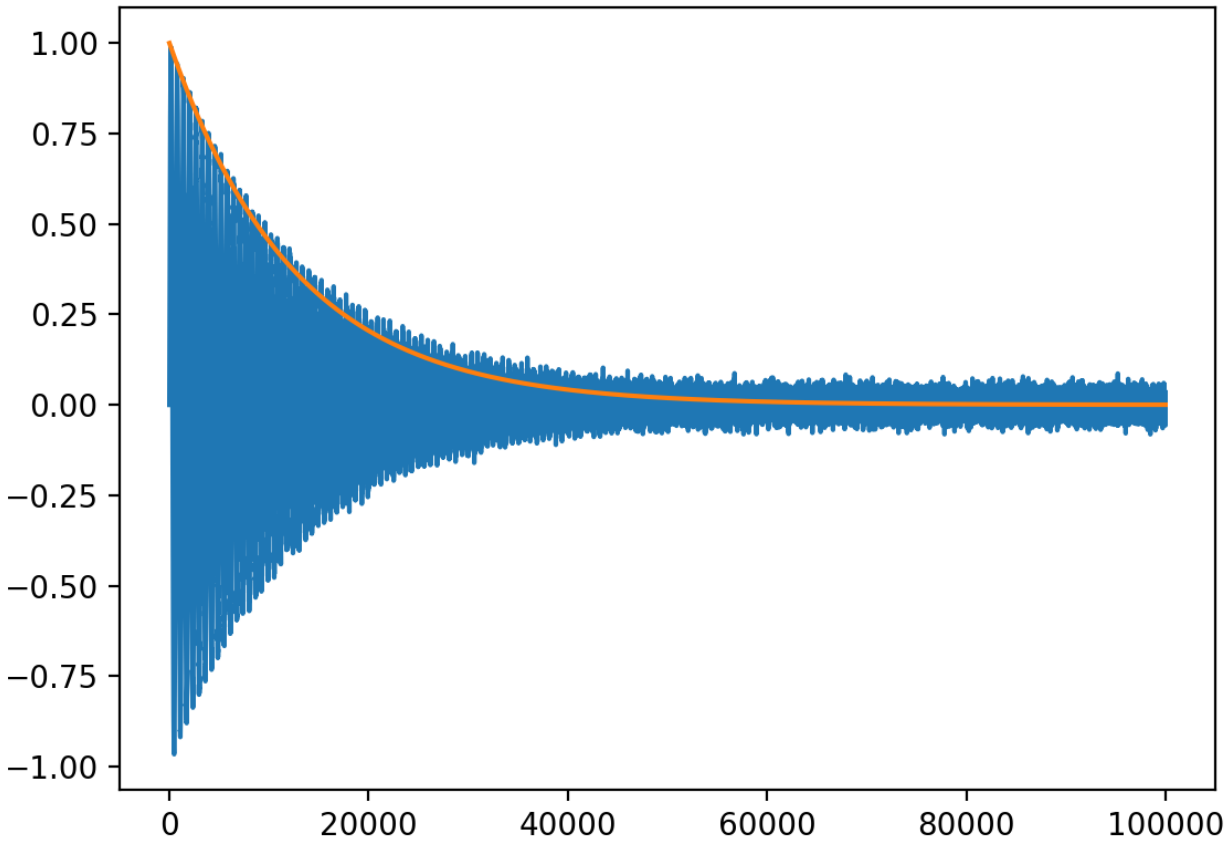

Figure 3.3 | Simulated Ramsey decay. The blue curve (which appears solid due to the high frequency of oscillations) is from a Monte Carlo model with repeated random sampling of equation 3.24, whereas the orange curve is $\exp(-t/T_2^*)$, where $T_2^* = 2/\sigma^2 f$. Here the x-axis is arbitrary time units and the y-axis is arbitrary units of photoluminescence (PL) relative to some baseline PL level at y = 0.

As can be seen in the figure, the averaged PL exponentially decreases as the readout time increases. This exponential approach is well-modeled by a T_2^* time of:

$$T_2^* = \frac{2}{\sigma^2 f}, \qquad PL_{avg} = \exp\left(-\frac{t}{T_2^*}\right) \tag{3.25}$$

As either the standard deviation or the frequency of the noise increases, the dephasing time T_2^* increases. As expected, T_2^* becomes infinite when there is no noise ($\sigma = 0$) or the external field is static ($f = 0$). In practice, we use the following function to fit Ramsey decays:

$$\exp\left(-\left(\frac{t}{T_2^*}\right)^n\right) \tag{3.26}$$

Where n is a free parameter that is related to the frequency of the noise sources. For a SiC VV^0 the T_2^* is usually on the order of a microsecond, but can be slightly shorter or longer depending on the sample [3,38,39].

Physically, a short T_2^* or a short dephasing time is correlated with electric and magnetic field noise in the vicinity of the defect, both of which appear in the VV^0 Hamiltonian. However, the dephasing time alone does not determine exactly *which* noise sources are present. Similar to how a weight of an object does not tell you its composition, the T_2^* of a qubit alone does not tell you details about the local environment. Instead, it tells you the level of uncertainty in the phase between the two eigenstates of an arbitrary state Ψ, which in turn will inhibit the operation of quantum gates and protocols.

As mentioned, dephasing generally occurs from noise sources in the environment which cause stochastically varying fields. Typically these noise sources are dominated by the nuclear spins from naturally abundant ^{13}C (1.1%) and ^{29}Si (4.7%). However, the ~10^3-10^4 higher magnetic moment of a single electron compared to a ^{13}C or ^{29}Si isotope means that dipolar coupling to stray electrons at concentrations 10^3-10^4 more dilute that the ~1-4% nuclear abundance can still have a significant effect. This can most notably come from high levels of nearby doping, which is used for photonic and electronic SiC devices. Beyond this, other defects in the sample such as other vacancies, divacancies, interstitial defects, and dangling bonds at surfaces can also couple and cause dephasing. Some of these defects are naturally occurring, and some are induced by the lattice damage from electron irradiation or ion implantation used to create divacancies in the first place.

3.3 T_2 – The spin decoherence time

The T_2 is generally called the spin decoherence time, but it also referred as the transverse relaxation time or spin-spin relaxation time. In a way, it also measures the dephasing of a quantum state, but with cancelling of quasistatic fields. To gain an intuition for this, we will immediately turn to the Hahn echo sequence is used to measure T_2, which is shown in the figure below:

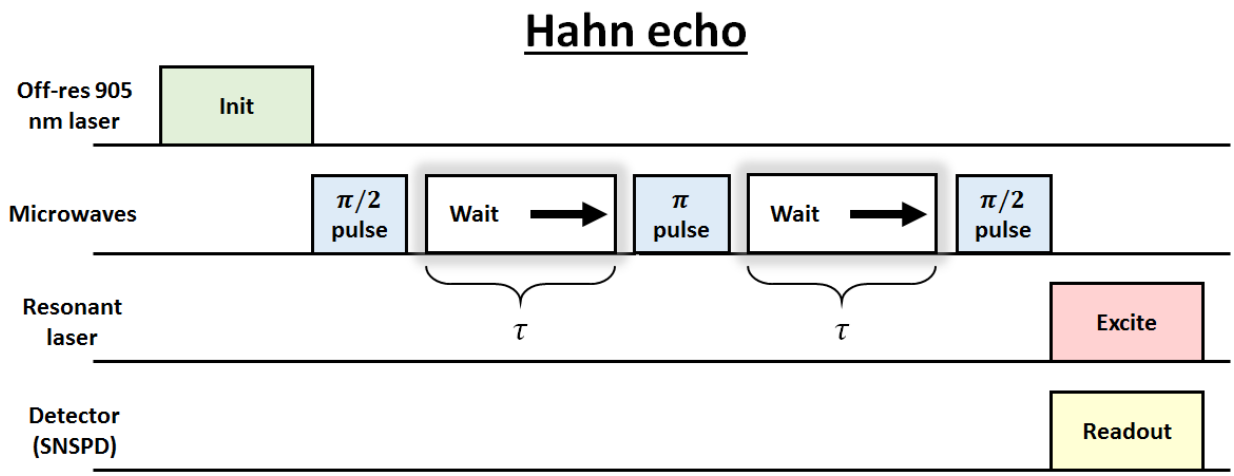

Figure 3.4 | Hahn echo pulse sequence used to measure T_2. Here the time τ between the "refocusing" π pulse and the adjacent $\pi/2$ pulses is increased until the state loses coherence.

In principle the T_2 time will always be longer than the T_2^* time. This is because the π pulse in the Hahn echo sequence has the effect of "undoing" unwanted dephasing caused by external fields. For this reason the π pulse is sometimes referred to as a refocusing pulse. The "echo" terminology stems from the fact that state after the second waiting period there should be a resurgence of the original starting state due to the mirror symmetry of the sequence. To see how the Hahn echo

works, we can break the two waiting periods into one where phase is accumulated and one where phase is "unaccumulated". This can be represented by:

Accumulate phase:

$$\Psi(t_1) = c_g|g\rangle + c_e|e\rangle \exp\left(-i\int_0^{\tau}\big(\omega_0 + \delta(t)\big)dt\right) \tag{3.27}$$

Unaccumulate phase:

$$\Psi(t_2) = c_g|g\rangle + c_e|e\rangle \exp\left(-i\int_{\tau}^{2\tau}\big(\omega_0 + \delta(t)\big)dt\right) \tag{3.28}$$

Combining these expressions then gives the total accumulated phase:

$$\phi_{final} = \int_0^{\tau}\big(\omega_0 + \delta(t)\big)dt - \int_{\tau}^{2\tau}\big(\omega_0 + \delta(t)\big)dt \tag{3.29}$$

If the Hahn echo works perfectly, then these two integrals cancel and no phase information is lost. This has the immediate implication that the noise term $\delta(t)$ was simply never a function of time in the first place, or at least on the time scale of the wait period τ. In this context, the noise would be referred to as "quasistatic" – stationary on the time scale of a single experiment but varying on the time scale of multiple averaged experiments. At some point as τ lengthens, we reach the time scale of $\delta(t)$ varying, which then means that the accumulated and unaccumulated phases will no longer be equal. This manifests as an imperfect Hahn echo and a nonzero total accumulated phase. As we saw in the previous section, this then corresponds to a drop in PL over many averaged experiments.

In this sense, a T_2 measurement filters out low-frequency noise in the experiment and thus extends your dephasing time. Extrapolating this idea, including many refocusing π pulses with

short waiting times would filter out high-frequency noise. This is indeed the idea behind dynamical decoupling [30], which is commonly used to extend the coherence time of various qubit systems. There is a limit to dynamical decoupling, of course, as T_2 cannot extend beyond T_1. T_1 is referred to as the spin relaxation time and is the subject of the next section.

For a Hahn echo decay, we use the same exponential fit as for a Ramsey decay, given by:

$$\exp\left(-\left(\frac{t}{T_2}\right)^n\right) \tag{3.30}$$

Where $T_2 > T_2^*$. For a VV^0 in SiC the T_2 is on the order of ~1 ms [3], but can be shorter in the presence of extra noise sources. The noise sources responsible for T_2 decay are identical to those for T_2^* decay: nuclear spins from naturally abundant isotopes, electron spins from other defects, and dangling bonds from nearby surfaces.

3.4 T_1 – The spin relaxation time

The last relevant time scale for generalized decoherence is T_1, the spin relaxation time or spin-lattice relaxation time. In contrast to the T_2^* and T_2 decay mechanisms, spin relaxation is completely unrelated to the phase of the quantum state. On the contrary, spin relaxation measures how long a completely polarized eigenstate of the system will remain in the same state. A schematic of a T_1 measurement is given below:

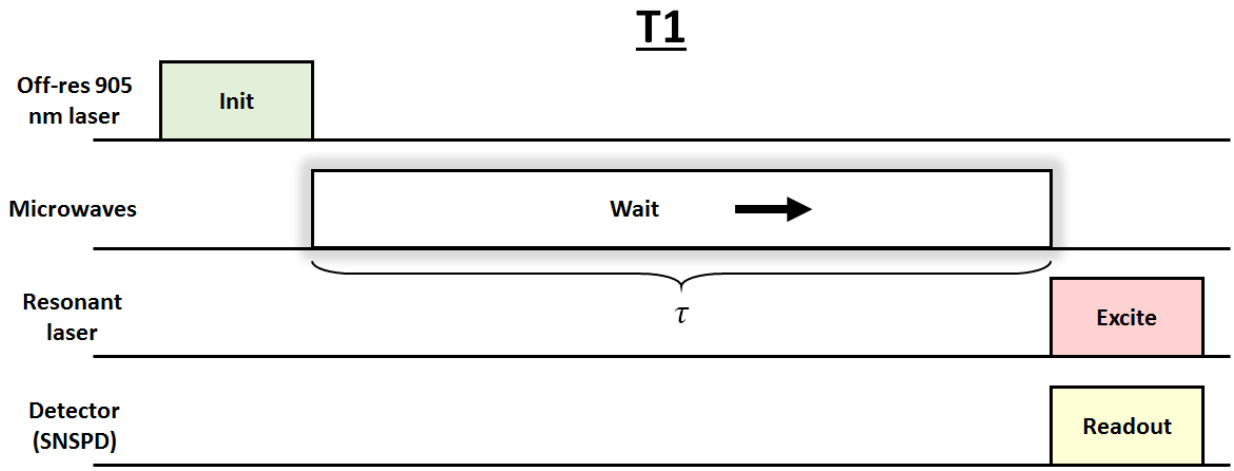

Figure 3.5 | Pulse sequence for measuring T_1. In this sequence, the spin is initialized into $|0\rangle$ and no microwaves are applied. The wait time τ between initialization and readout is increased until the initially prepared state loses coherence.

The only way for an initialized eigenstate to show decay over an ensemble of experiments is if for some fraction of experiments, the state completely flips to the other eigenstate. Since this is an energy nonconserving processing, this is most commonly achieved through the interaction with lattice phonons. By extension then, T_1 times are generally the longest under cryogenic temperatures, and usually quickly decay when approaching room temperature.

Any other process that results in an energy exchange with the qubit can also lead to T_1 decay. In the case of the VV^0, this can occur with spin flipping processes such as interacting with a fluctuating magnetic field matched with the Larmor frequency of the defect. Any process that leads to a T_1 decay will also lead to a T_2 decay, which leads to the inequality:

$$T_2 \leq 2T_1 \tag{3.31}$$

For the VV^0, the T_1 times at cryogenic temperatures are beyond 1 ms and perhaps even beyond one second, but it has not yet been fully characterized. Unfortunately these times can lead to

prohibitively long averaging of experiments. When these measurements are collected, however, a simple exponential fit of $\exp(-t/T_1)$ gives the spin relaxation time.

3.5 Divacancy optical spectrum and Debye-Waller factor

Emission and absorption spectrum

When the VV^0 is optically excited, the radiative decay back to the ground state spans a wide range of near-infrared wavelengths. The emission spectrum can generally be categorized into a sharp zero-phonon line (ZPL) and a broad phonon side band (PSB). When no phonons are involved (i.e. zero-phonon), the emission is narrowly centered around a ZPL wavelength that varies among defect types. For divacancies in silicon carbide, the ZPL emission takes values between ~1040 nm and ~1132 nm. When phonons are also emitted with the radiative decay, the photon's energy is lowered due to conservation of energy. This results in redshifted optical emission in a continuous range of ~1100-1400 nm, although most of this emission is focused in the ~150 nm beyond the ZPL. Measuring spectra with a spectrometer is an important diagnostic tool to identify defect types in a SiC sample and to distinguish from other point emitters. A typical spectrum of a VV^0 is shown in figure 3.6 which features both the ZPL and PSB [31].

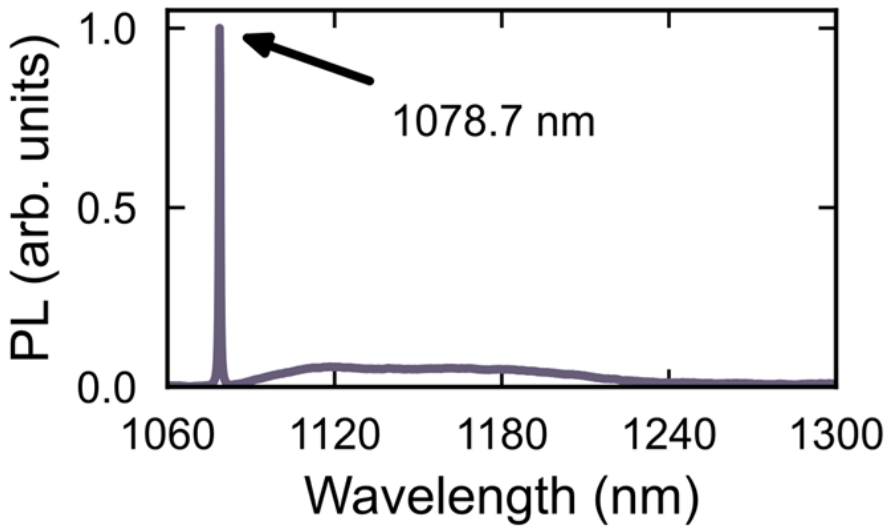

Figure 3.6 | Emission spectrum from a (*kh*) divacancy in silicon carbide. Spectrum adapted from [31]. Roughly ~10% of the (*kh*) divacancy's optical emission is in the zero-phonon line at ~1078 nm, while the rest of the emission is in the phonon sideband at longer wavelengths.

When the emission spectrum is mirrored over the ZPL, one obtains the absorption spectrum, which provides possible wavelengths to off-resonantly excite the defect with. In a similar fashion to the PSB, wavelengths ~100-150 nm away from the ZPL are most efficient for pumping. Therefore, we typically use either 975 nm or 905 nm diode lasers for excitation. It is worth noting that phonons are involved in this process as well, as the ground state "overshoots" the excited state energy and then decays to the excited state through the emission of phonons. The entire process is spin-preserving, meaning that a $m_s = 0$ ground state will be pumped to a $m_s = 0$ excited state, for example. After the mirroring of the spectrum the ZPL still remains in the same place, acting as either a resonant absorption or resonant emission wavelength. A schematic of absorption/emission in shown in figure 3.7.

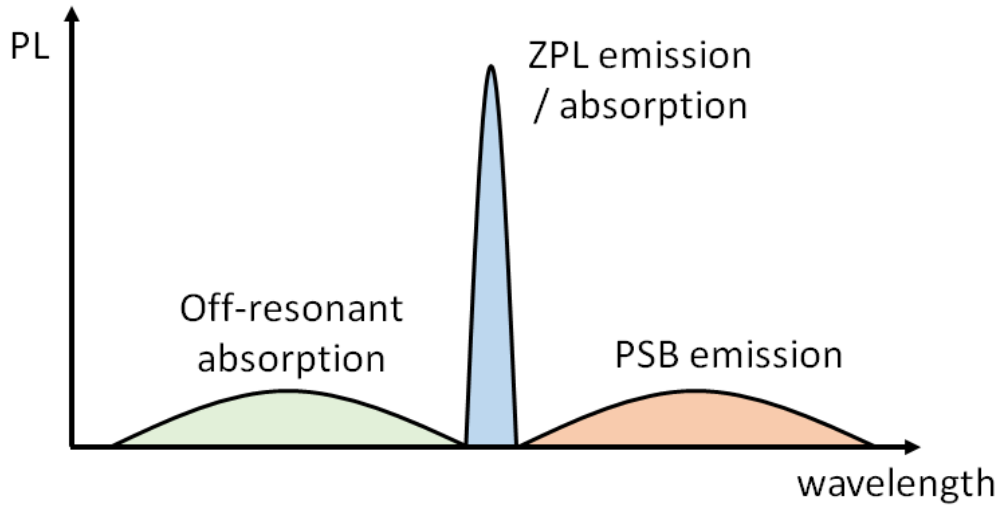

Figure 3.7 | Photon absorption and emission spectrum. Here, the sharp blue peak represents the zero-phonon line (ZPL) transition that can be used for either absorption or emission. The broad red hump is the phonon sideband (PSB) that is exclusive for emission. Mirroring this over the ZPL gives a broad absorption hump (green) that can be used for off-resonant excitation of the VV^0.

Lastly, the features of the spectrum are highly dependent on temperature. Generally at temperatures below 20K the peaks will be reasonably sharp. At higher temperatures, the spectrum and most notably the ZPL will significantly broaden. At 200K and above, the spectrum essentially becomes featureless. This behavior is shown in figure 3.8, adapted from the seminal SiC divacancy work that first identified these defects experimentally [1].

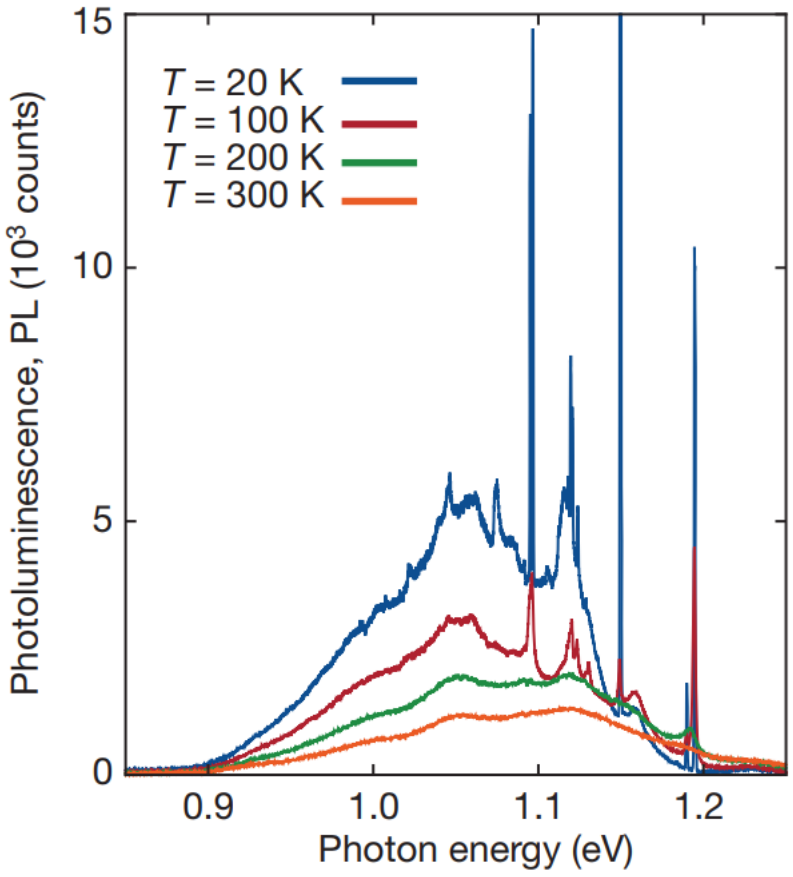

Figure 3.8 | Optical spectrum of divacancy ensembles at various temperatures. Plot adapted from [1]. Photoluminescence from a SiC sample containing an ensemble of divacancies. The sharp peaks at low temperature correspond to the zero-phonon lines of different divacancies. These peaks disappear as the sample approaches room temperature.

The main upshot of this temperature dependence is that SiC samples must be cryogenically cooled in order to resolve individual optical transitions. Although some defects are optically active at room temperature (most notably PL5 and PL6) [4], zero-phonon transitions are practically infeasible to address. In our experiments we typically cool samples to ~5K with helium cryostats (more on this in chapter 4).

The Debye-Waller factor

An important figure of merit for this system is the percentage of emission that is emitted into the zero-phonon line. This is termed the Debye-Waller factor (DWF), defined as:

$$\alpha \equiv \%\ \text{emission into ZPL} = \frac{\tau_{ZPL} + \tau_{PSB}}{\tau_{ZPL}} \tag{3.32}$$

Where τ_{ZPL}, τ_{PSB} are the radiative lifetimes of the ZPL and PSB transitions. The emission of ZPL photons is critical for the formation of spin-photon entanglement [35], as the polarization of the photon will only correlate with the spin state if there are no emitted phonons. Additionally, long distance spin-spin entanglement protocols that rely on the interference of indistinguishable photons must also use the ZPL for photon interference [40]. Phonon emission in this context would also be detrimental, as it would "leak" spin information to the environment interacting with these phonons.

For divacancies in silicon carbide, the Debye-Waller factor is typically ~5-10% depending on the defect type [3, 30]. The aspects that determine a Debye-Waller factor are nontrivial and beyond the scope of this thesis, but the factor is fairly consistent from defect to defect. It also means that PSB emission is 90-95% of all emitted photons, which is partially why we readout photoluminescence in the sideband. For the purposes of scaling spin-spin entanglement protocols, however, it is crucial to increase this Debye-Waller factor. Luckily, it is possible to modify the DWF through nanophotonic structures around the defect, which will be discussed in chapter 7.

3.6 Charge instability

In the ideal scenario, the VV^0 is electrically neutral and contains six electrons. We have assumed this charge neutrality in all of the spin physics of the ground and excited states so far. However, it

is possible for the VV^0 to become ionized into either the VV^+ or VV^- state [41-46]. This is usually caused by fluctuations in the local electric field, which destabilizes the neutral form of the divacancy. This is generally an undesirable effect, as the defect is no longer optically active and any spin information is lost. The electric field fluctuations are in turn caused by photoionization of nearby charge traps, which occurs across a wide range of excitation wavelengths [41]. Since divacancies in our experiments are optically initialized and read out, this means that every experiment will have a chance to ionize the divacancy. By the same token, exposure to off-resonant light in the broad range of ~300-1000nm will "recharge" an ionized divacancy to its neutral charge state. The exact time scale of ionizing and recharging is not well characterized, but it can happen slow enough to be noticeable on the ~ms time scale when reading out photoluminescence. To a certain degree, proximity to SiC surfaces also appears to increase the effects of ionization, which is an important consideration for nanostructures. A schematic of the "charge scrambling" induced by laser light is shown in the figure below.

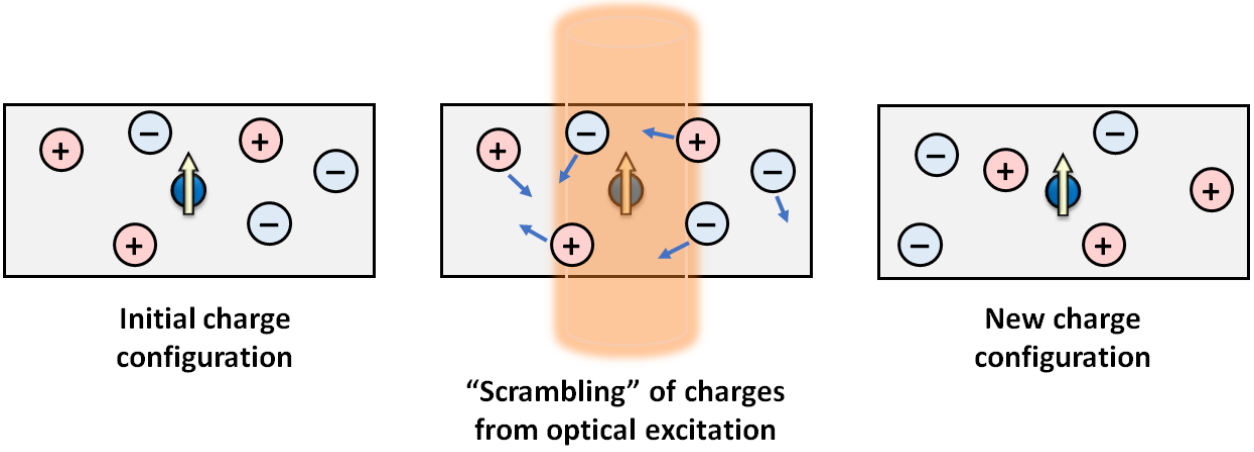

Figure 3.9 | Randomization of charge traps from photoexcitation. Laser light causes local charges in traps (light red "+", light blue "–") around the defect (blue circle with yellow arrow) to become "scrambled", before becoming "frozen" in a fixed configuration once the laser light is turned off. This can induce either an ionized charge state or a neutral state. Additionally, this laser-induced charge noise is the main culprit behind spectral diffusion.

In the context of energy levels within the SiC band gap, VV^0 ionization can occur either through the transfer of charges to or from the valence and conduction bands. Intermediary charge traps can capture electrons from the conduction band or photoemit electrons into the conduction band [45]. The same mechanisms are in place for capture/photoexcitation of holes to and from the valence band. These processes then result in an ionized divacancy state, either VV^+ or VV^-, although based on the results of [41] the negative charge state VV^- is more likely. An outline of energy levels in the band gap is shown in the figure below, adapted from [41,46].

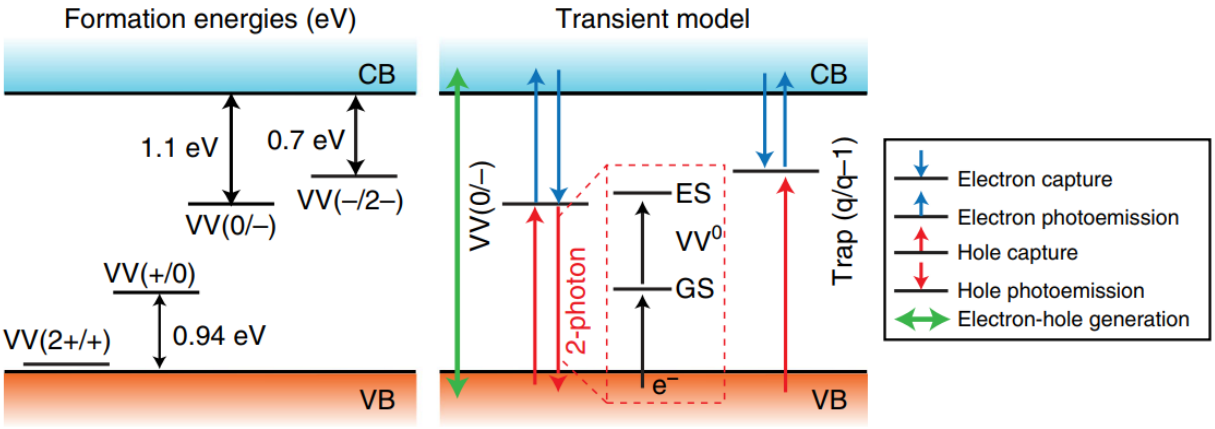

Figure 3.10 | Theoretical energy levels of difference charge states of the VV^0 in silicon carbide. Figure adapted from reference [41], which builds on the study in [46]. Different charge states of the divacancy occupy different energies within the SiC band gap. Electron/hole capture and photoemission processes facilitate transitions between charge states.

In addition to laser-induced recharging, another way to limit the effects of divacancy ionization is to place the divacancy into a built-in PIN diode. This is the subject of the study in [42]. The main idea of this geometry is that the built-in electric field from the PIN diode will evacuate and stabilize the charge traps even under optical excitation. Lastly, it would be possible to model the charge state as a separate nonradiative state in a Markov model to be discussed shortly, although such models would require complicated measurements to determine ionization and recharge rates

with high precision. More information on the dynamics of the divacancy charge states can be found in references [41-46].

3.7 Three-level model for the divacancy

A variety of measurements that we use to characterize the VV^0 system can be understood in the context of competing rates between the divacancy's isolated energy levels. For example, an excited state lifetime measurement is determined by a balance between the radiative decay from the excited state and the nonradiative decay to either the intersystem crossing or a charged state. Since these measurements place important bounds on the speed and fidelity of quantum protocols, it is fruitful to develop a model to capture these dynamics. By understanding the underlying components of the model, we can then identify the limiting factors for different protocols and potentially engineer the system to improve its performance.

A basic model to start with involves three levels: The ground state, the excited state, and an intermediate state that allows nonradiative decays. These can be labeled as n_1, n_2, and n_3, respectively. For simplicity we will refer to the intermediate level n_3 as the ISC, but more broadly it can also encompass other nonradiative states such as an ionized VV^- or VV^+. Rates of transitions between these levels are represented by the variables r_{ij}, where i is the initial level and j is the final level. An outline of this system is given in figure 3.11.

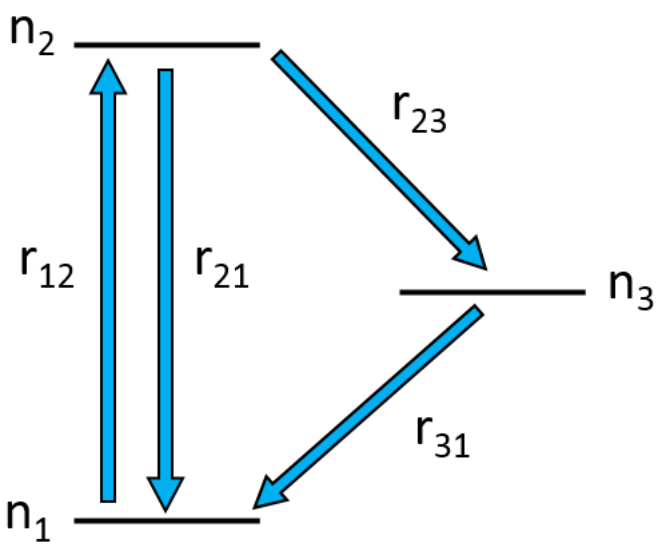

Figure 3.11 | Three-level model of VV^0 optical transitions. In this diagram, n_1 represents the ground state, n_2 represents the excited state, and n_3 represents an overall nonradiative state, which in practice is a combination of the inter-system crossing singlet state and ionized states of the VV^0. Rates between these levels are denoted by r_{12}, r_{21}, r_{23}, and r_{31}.

It is important to note that each transition rate r_{ij} corresponds to a physical process and not all rates are allowed in this system. For example, the ground state will not excite to ISC ($r_{13} = 0$), and the ISC will not excite to the excited state ($r_{32} = 0$). All other processes are allowed, and their physical interpretations are given below:

$$r_{12} = \text{laser pumping rate} \tag{3.33}$$

$$r_{21} = \text{radiative decay rate} \tag{3.34}$$

$$r_{23} = \text{decay rate from excited state to ISC} \tag{3.35}$$

$$r_{32} = \text{decay rate from ISC to ground state} \tag{3.36}$$

The reader may recognize this system as a Markov chain. Indeed, the decision to use rates to describe transitions between levels implies that this is a continuous-time Markov chain. The

discrete-time analog of this would be to describe transitions as a probability per time step. We will cover both versions here, starting with the continuous Markov chain.

3.7.1 Continuous-time Markov chain

The centerpiece of all Markov chains (continuous or discrete) is to obtain the transition matrix, which allows the system's dynamics to be fully modeled. For a continuous-time Markov chain, this matrix is typically represented by Q. Since this system contains three levels, Q will be a 3x3 square matrix:

$$Q = \begin{pmatrix} q_{11} & q_{12} & q_{13} \\ q_{21} & q_{22} & q_{23} \\ q_{31} & q_{32} & q_{33} \end{pmatrix} \tag{3.37}$$

Here, the entries q_{ij} generally represent transition rates. To fill out the individual entries, we can focus on the transitions *out* of each level. The diagonal entries q_{ii} should represent the total summed rate out of level i (and are negative), whereas off-diagonal entries q_{ij} represent the transition out of level i to level j. Note that the sums of each row will be zero by design. Each row i of the matrix Q will then represent the rates leaving the level i. Using figure [___] as a reference, we can focus on each level and fill out each row of the matrix based on the rates provided. This gives the matrix:

$$Q = \begin{pmatrix} -r_{12} & r_{12} & 0 \\ r_{21} & -r_{21} - r_{23} & r_{23} \\ r_{31} & 0 & -r_{31} \end{pmatrix} \tag{3.38}$$

Once we have obtained this transition matrix, we can use it to relate the current state of the system to the state at future times. Here, the "state of the system" can be represented as a vector $\vec{n}(t)$:

$$\vec{n}(t) = \begin{pmatrix} n_1(t) \\ n_2(t) \\ n_3(t) \end{pmatrix} \tag{3.39}$$

Where $n_i(t)$ represents each level's occupation as a function of time. With this vector, we can immediately write the differential equation that governs the system's evolution:

$$\left(\overrightarrow{n'}(t)\right)^T = \left(\vec{n}(t)\right)^T Q \tag{3.40}$$

Where v^T represents the transpose of vector v. Expanding this equation for the system as hand gives:

$$\begin{pmatrix} n_1'(t) & n_2'(t) & n_3'(t) \end{pmatrix} = \begin{pmatrix} n_1(t) & n_2(t) & n_3(t) \end{pmatrix} \begin{pmatrix} -r_{12} & r_{12} & 0 \\ r_{21} & -r_{21} - r_{23} & r_{23} \\ r_{31} & 0 & -r_{31} \end{pmatrix} \tag{3.41}$$

Or, multiplying this out:

$$n_1'(t) = -r_{12}n_1(t) + r_{21}n_2(t) + r_{31}n_3(t) \tag{3.42}$$

$$n_2'(t) = r_{12}n_1(t) - r_{21}n_2(t) - r_{23}n_2(t) \tag{3.43}$$

$$n_3'(t) = r_{23}n_2(t) - r_{31}n_3(t) \tag{3.44}$$

This system of coupled differential equations fully describes the occupation of each level as a function of time, subject to initial conditions. Despite the fact that we have chosen a relatively simple 3-level system as an initial model, the solutions of these equations are generally nontrivial.

We will look at examples of how these equations can be applied to actual measurements, but first we will examine the discrete-time version of this same Markov chain.

3.7.2 Discrete-time Markov chain

Just as in the continuous case, our initial goal for the discrete-time Markov chain is to obtain the transition matrix. In the discrete setting it is typically represented by P instead of Q. The system still contains three levels, so P will still be a 3x3 square matrix:

$$P = \begin{pmatrix} p_{11} & p_{12} & p_{13} \\ p_{21} & p_{22} & p_{23} \\ p_{31} & p_{32} & p_{33} \end{pmatrix} \tag{3.45}$$

Here, each entry p_{ij} now represents a *probability* instead of a rate. This is given by:

$$p_{ij} = \text{transition probability from state } i \text{ to state } j \text{ after time step } \Delta t$$

Meanwhile, the diagonal entries p_{ii} represent the probability per time unit that the state will remain in the same level. In the VV^0 system each level can remain stable for a nonzero amount of time, so the diagonal entries will all be nonzero. The p_{13} and p_{32} entries will be zero by design, similar to the continuous case. This gives:

$$P = \begin{pmatrix} p_{11} & p_{12} & 0 \\ p_{21} & p_{22} & p_{23} \\ p_{31} & 0 & p_{33} \end{pmatrix} \tag{3.46}$$

If we want to use the rates in figure 3.11 to fill out these entries, we have to be careful in translating a rate to a probability. If we had a two-level system with only an excited state and a ground state, the rate of decay from the excited state would be defined as:

$$r \equiv \frac{\lim_{t \to 0} \left(P_{decay}(0 \to t) \right)}{t} = \frac{P_{decay}(0 \to dt)}{dt} \tag{3.47}$$

Where $P_{decay}(0 \to t)$ represents probability of decay in the time window from 0 to t. This is the exact scenario for a Poisson process, which follows an exponential distribution. More specifically, the probability density function (PDF) representing the probability of decay is an exponential distribution with a single parameter λ:

$$\text{exponential PDF} = \lambda e^{-\lambda t} \tag{3.48}$$

The parameter λ, by definition, is the probability per differential time that the decay will occur. Put more simply, λ is our rate r.

$$\lambda = r \tag{3.49}$$

If we want to express p_{ij} in terms of r_{ij} for a discrete model, we must make the time step infinitesimally small (dt). Under these conditions, we can then treat eq. () as a fraction and say:

$$p_{ij} = P_{decay}(0 \to dt) = r_{ij} \cdot dt \tag{3.50}$$

This then gives the off-diagonal elements of the discrete transition matrix as:

$$P = \begin{pmatrix} p_{11} & r_{12}dt & 0 \\ r_{21}dt & p_{22} & r_{23}dt \\ r_{31}dt & 0 & p_{33} \end{pmatrix} \tag{3.51}$$

To fill the diagonal entries, we use the convention that the rows of the discrete transition matrix must add to one (for a probability of one). This gives:

$$P = \begin{pmatrix} 1 - r_{12}dt & r_{12}dt & 0 \\ r_{21}dt & 1 - r_{21}dt - r_{23}dt & r_{23}dt \\ r_{31}dt & 0 & 1 - r_{31}dt \end{pmatrix} \tag{3.52}$$

Or:

$$P = \begin{pmatrix} -r_{12} & r_{12} & 0 \\ r_{21} & -r_{21} - r_{23} & r_{23} \\ r_{31} & 0 & -r_{31} \end{pmatrix} dt + I \tag{3.53}$$

And since Q is given by:

$$Q = \begin{pmatrix} -r_{12} & r_{12} & 0 \\ r_{21} & -r_{21} - r_{23} & r_{23} \\ r_{31} & 0 & -r_{31} \end{pmatrix} \tag{3.54}$$

We have the relation:

$$P = Qdt + I \tag{3.55}$$

Taking one time step in the discrete Markov chain corresponds to multiplying the state of the system by P on the right. This can be represented as:

$$\left(\vec{n}(t + dt)\right)^T = \left(\vec{n}(t)\right)^T P \tag{3.56}$$

In the continuous Markov chain, the next step was to obtain differential equations to describe the system's dynamics. For the discrete case, we can instead use python to incrementally evolve the state of the system according to the equation above.

3.7.3 Monte Carlo model of the divacancy

A third way to approach the modeling of the VV^0 system is to use a Monte Carlo model. This method relies on random sampling to simulate the dynamics of the VV^0 system at each time step. At each moment in time, we are interested in the state of the system after a time step Δt. As an example (with arbitrary numbers), when the system is currently in its excited state we could assign a 95% chance of staying, a 4.5% chance of radiatively decaying to the ground state, and a 0.5% chance of decaying to the ISC. These probabilities can be set up for each state of the system and the time evolution from any starting point can be obtained by iteratively applying these rules. The use of probabilities of transitions per unit time mirrors the concepts of a discrete Markov chain very closely, and indeed the two models are almost identical. The key difference is that since the Monte Carlo model uses repeated random sampling, the system's dynamics will not be deterministic like they are in the Markov chain. In the limit of infinite averaging, however, the two results should converge. This comes with a drawback of needing to perform time-intensive averaging of many Monte Carlo results to see the similarity to the Markov chain. We will avoid delving too much into which model is "superior" and show the more important result that they predict the same behavior for the VV^0 in various scenarios. We will apply both the continuous and discrete Markov chain and the Monte Carlo model to some example scenarios.

3.7.4 Lifetime measurement

In a lifetime measurement, the system is initialized into its excited state and then is released, resulting in exponentially decaying counts over time. For this experiment we set the initial conditions set at the excited state:

$$n_0(0) = 0, \qquad n_1(0) = 1, \qquad n_2(0) = 0 \tag{3.57}$$

In this experiment there is no direct pumping rate because the system always starts in its excited state. This means that:

$$r_{12} = \text{laser pumping rate} = 0 \tag{3.58}$$

In the continuous Markov chain, the differential equations describing the system then simplify to

$$n_1'(t) = r_{21}n_2(t) + r_{31}n_3(t) \tag{3.59}$$

$$n_2'(t) = -r_{21}n_2(t) - r_{23}n_2(t) \tag{3.60}$$

$$n_3'(t) = r_{23}n_2(t) - r_{31}n_3(t) \tag{3.61}$$

And we are interested in obtaining the excited state population $n_2(t)$ as a function of time. Focusing on the differential equation for $n_2(t)$ directly gives:

$$n_2'(t) = -(r_{21} + r_{23})n_2(t) \tag{3.62}$$

$$n_2(t) = \exp(-(r_{21} + r_{23})t) \tag{3.63}$$

Interestingly, the rate r_{31} from the ISC to the ground state plays no role in this lifetime measurement. Instead the decay is dictated by a combination of the radiative and nonradiative rates to the ground state and ISC, respectively. This equation is an analytical result for the excited state population from the continuous Markov chain, and we will compare it to the results of a discrete Markov chain.

In the discrete Markov chain with $r_{12} = 0$, we have the stochastic matrix as:

$$P = \begin{pmatrix} 1 & 0 & 0 \\ r_{21}dt & 1 - r_{21}dt - r_{23}dt & r_{23}dt \\ r_{31}dt & 0 & 1 - r_{31}dt \end{pmatrix} \tag{3.64}$$

Once this matrix is obtained, it is enough to fully describe the time dynamics of the system. As an example we can set the rates as the following for both the discrete Markov and Monte Carlo models:

$$r_{21} = \frac{0.05}{ns}, \qquad r_{23} = \frac{0.01}{ns}, \qquad r_{31} = \frac{0.01}{ns} \tag{3.65}$$

This gives an excited state population vs. time as outlined in figure 3.12

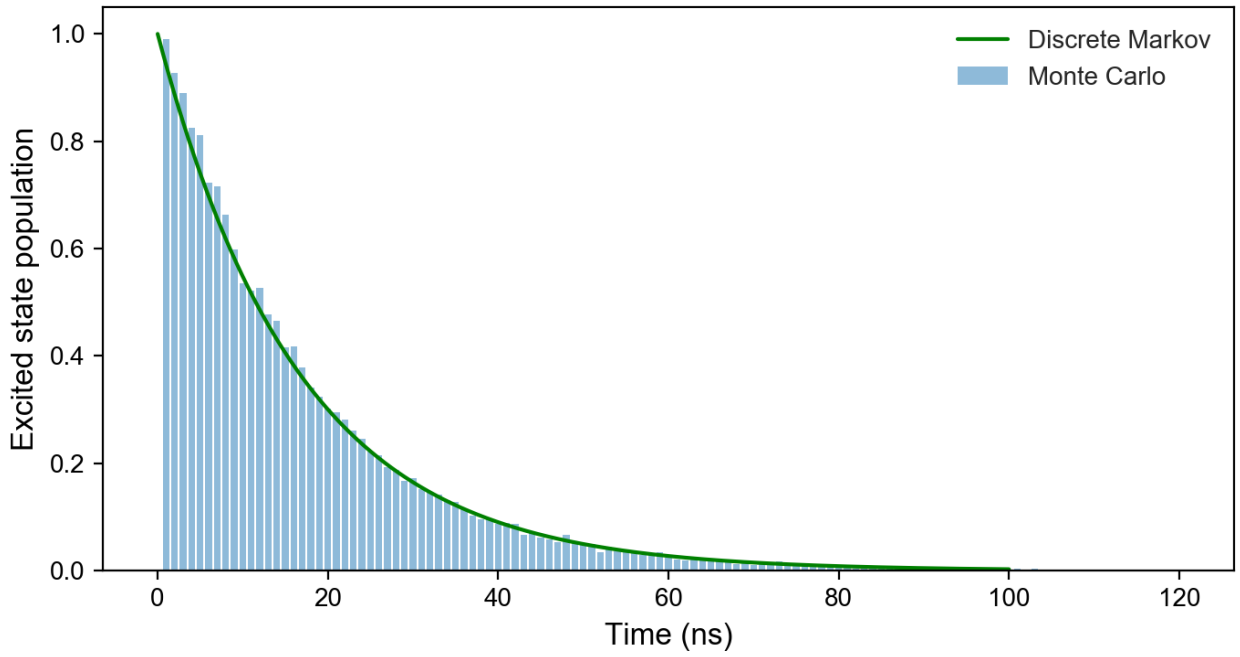

Figure 3.12 | Simulated lifetime measurement according to a 3-level model. When the state of the 3-level system is initially prepared in the excited state, competing decays to the other two levels cause an exponential decay of the excited state population.

As can be seen, there is excellent agreement between the Monte Carlo result and the discrete Markov chain prediction. The slight noise in the Monte Carlo data is a natural result of the random sampling that it is built upon; in this case there were 50,000 averaged simulated experiments. To see the effect that the excited state to ISC rate r_{23} can have on this curve, we can also run a simulation with the following parameters:

$$r_{21} = \frac{0.05}{ns}, \qquad r_{23} = \frac{0.05}{ns}, \qquad r_{31} = \frac{0.01}{ns} \tag{3.66}$$

Where again, r_{31} has no effect and is arbitrarily set to 0.01. Under these conditions with a fivefold increase in the r_{23} rate, there is a noticeable effect on the lifetime decay which is shown in figure 3.13.

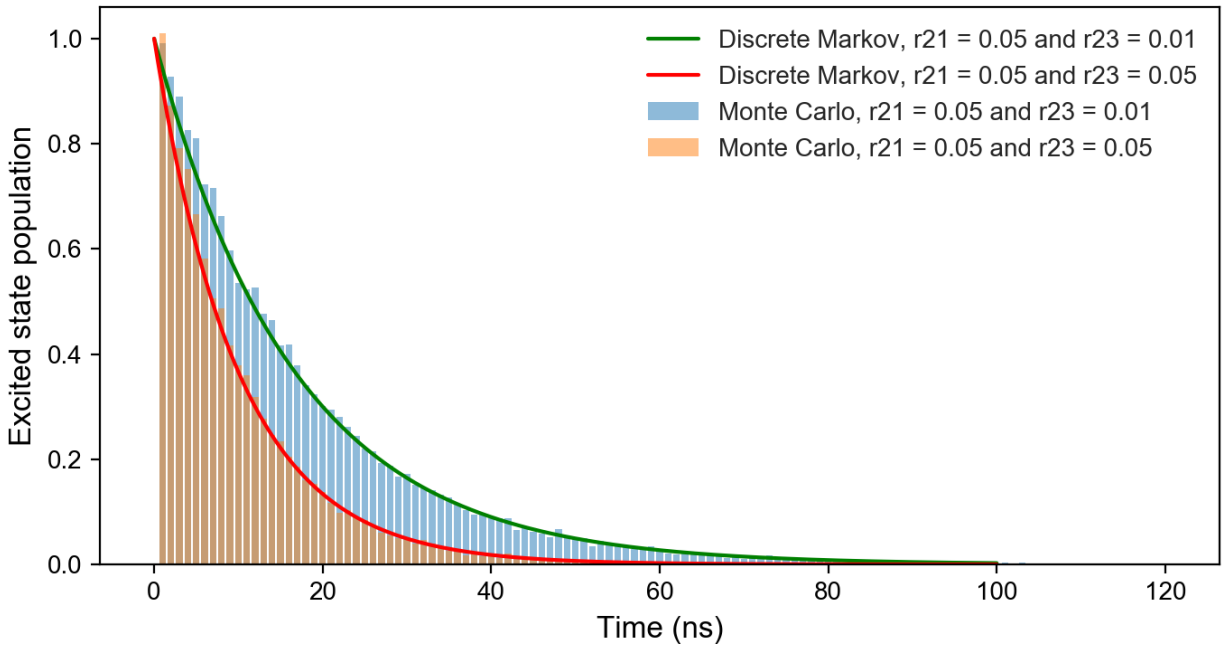

Figure 3.13 | Effect of increased r_{23} rate on lifetime decay curve. Increasing the rate to the nonradiative state n_3 causes an overall faster decay of the excited state population. This holds true even as transitions to and from n_3 are not directly measured through photon emission.

Here there is still excellent agreement between the Monte Carlo and discrete Markov models, which both show a significant speedup in the measured decay from the excited state. While this result is mathematically predicted from the continuous Markov result in equation 3.63, there is also an intuitive understanding of this effect. With a higher r_{23} the radiative decay pathway will more frequently go to the nonradiative ISC decay pathway instead, which does not result in detectable photons. This means that the photons that *are* detected are more heavily weighted towards faster decays, which explains why the decay curve is steeper with a higher r_{23} rate.

While the models appear to work very well here, there is an ambiguity in how the rates are determined. Namely, only the value of $(r_{21} + r_{23})$ is constrained. For example, we can see in figure 3.12 that the rates $r_{21} = \frac{0.05}{ns}$ and $r_{23} = \frac{0.01}{ns}$ provide a good fit to the blue bars which we can treat as a data set. However, *any* combination of r_{21} and r_{23} that gives the same combined value of $r_{21} + r_{23} = \frac{0.06}{ns}$ would give the exact same fit. This means that the rates of $\left\{r_{21} = \frac{0.04}{ns}, r_{23} = \frac{0.02}{ns}\right\}$ or $\left\{r_{21} = \frac{0.03}{ns}, r_{23} = \frac{0.03}{ns}\right\}$ would be equally valid fits to the data with no way of discerning how the rates should be distributed. The ambiguity is even more dire for the r_{31} rate, which for this measurement simply has no effect at all! This means that in practice, we would have to combine a lifetime decay with one or multiple other measurements (for example, a count rate with a known collection efficiency) in order to discern the individual rates.

The upshot of this exercise is that Monte Carlo and Markov chains can both robustly model the behavior of an excited state decay according to a three-level model, but the free parameters in the model allow for ambiguity to enter the attempted fits to data. Ideally a model should then be built with as few free parameters (or in this case levels) as possible, but an oversimplified model may miss out on key physics that is at play in the real system. This is ultimately a delicate balance, and we will see how this scenario plays out for other example measurements in the upcoming sections.

3.7.5 $g^{(2)}$ autocorrelation measurement

A $g^{(2)}$ autocorrelation measurement is a common way to confirm to presence of a single defect. The measurement is performed by tracking the arrival times of all collected photons and then computing the *differences* of the times Δt. Then, the frequency of each Δt occurring is plotted for various values of Δt. For example, a $\Delta t = 5\ ns$ means that a second photon arrived exactly 5 ns after the arrival of a first photon. If the $\Delta t = 5\ ns$ value of the $g^{(2)}$ curve was very high, this would mean that photons very frequently arrive 5 ns apart. If only one optical emitter is present, then it is impossible to emit two photons at the exact same time at $\Delta t = 0\ ns$. Therefore, the $g^{(2)}$ measurement serves as a reliable tool to check for single emitters, provided that the background signal is low or averaged enough to be subtracted away. Generally, we say that if the dip of the $g^{(2)}$ curve at t = 0 goes below 0.5, then there is only one optical emitter, whereas a dip above 0.5 indicates multiple emitters. Since each photon count means that the system was *just* in the excited state, the $g^{(2)}$ curve is also equivalent to mapping out the excited state population versus time. This value can be readily simulated using the 3-level model, and we will show the continuous and discrete Markov chain results here. Although using a Monte Carlo simulation is also entirely possible, it does not add to the discussion so we will forgo it here.

Continuous Markov chain

When using the differential equations from the continuous Markov chain, this time we cannot set r_{12} to zero. This means that we use the equations in their original form:

$$n_1'(t) = -r_{12}n_1(t) + r_{21}n_2(t) + r_{31}n_3(t) \tag{3.67}$$

$$n_2'(t) = r_{12}n_1(t) - r_{21}n_2(t) - r_{23}n_2(t) \tag{3.68}$$

$$n_3'(t) = r_{23}n_2(t) - r_{31}n_3(t) \tag{3.69}$$

By setting the initial conditions set at the ground state:

$$n_1(0) = 1, \qquad n_2(0) = 0, \qquad n_3(0) = 0 \tag{3.70}$$

We can obtain a solution to the excited state population $n_2(t)$ using *Wolfram Mathematica*, which gives:

$$n_2(t) = \frac{r_{12}\exp\left(-\frac{1}{2}(a_1+b)t\right)\left(a_3(-1+\exp(bt)) + r_{31}b\left(-1-\exp(bt)+2\exp\left(\frac{1}{2}(a_1+b)t\right)\right)\right)}{2a_2b} \tag{3.71}$$

Where:

$$a_1 = r_{12} + r_{21} + r_{23} + r_{31} \tag{3.72}$$

$$a_2 = r_{12}r_{23} + r_{31}(r_{12} + r_{21} + r_{23}) \tag{3.73}$$

$$a_3 = r_{31}(r_{21} + r_{23} - r_{31}) + r_{12}(2r_{23} + r_{31}) \tag{3.74}$$

$$b = \sqrt{a_1^2 - 4a_2} \tag{3.75}$$

Even though we are still only using a 3-level model, we see that the introduction of a pumping rate results in much more complicated behavior!

Discrete Markov chain

Similarly in the discrete case, we must leave the r_{12} rate in, meaning the stochastic matrix is:

$$P = \begin{pmatrix} 1 - r_{12}dt & r_{12}dt & 0 \\ r_{21}dt & 1 - r_{21}dt - r_{23}dt & r_{23}dt \\ r_{31}dt & 0 & 1 - r_{31}dt \end{pmatrix} \tag{3.76}$$

For demonstration purposes, we will use this matrix to show the behavior of the excited state population for various pumping powers. We can use the same rates as in the lifetime section:

$$r_{21} = \frac{0.05}{ns}, \qquad r_{23} = \frac{0.01}{ns}, \qquad r_{31} = \frac{0.01}{ns} \tag{3.77}$$

For the pumping rate r_{12}, we can select a large range of rates to show the limiting behavior. In this case we will sweep over the following rates:

$$r_{12} = \frac{10^{-7}}{ns} \leftrightarrow \frac{10^{1}}{ns} \tag{3.78}$$

The result of this sweep is shown in figure 3.14.

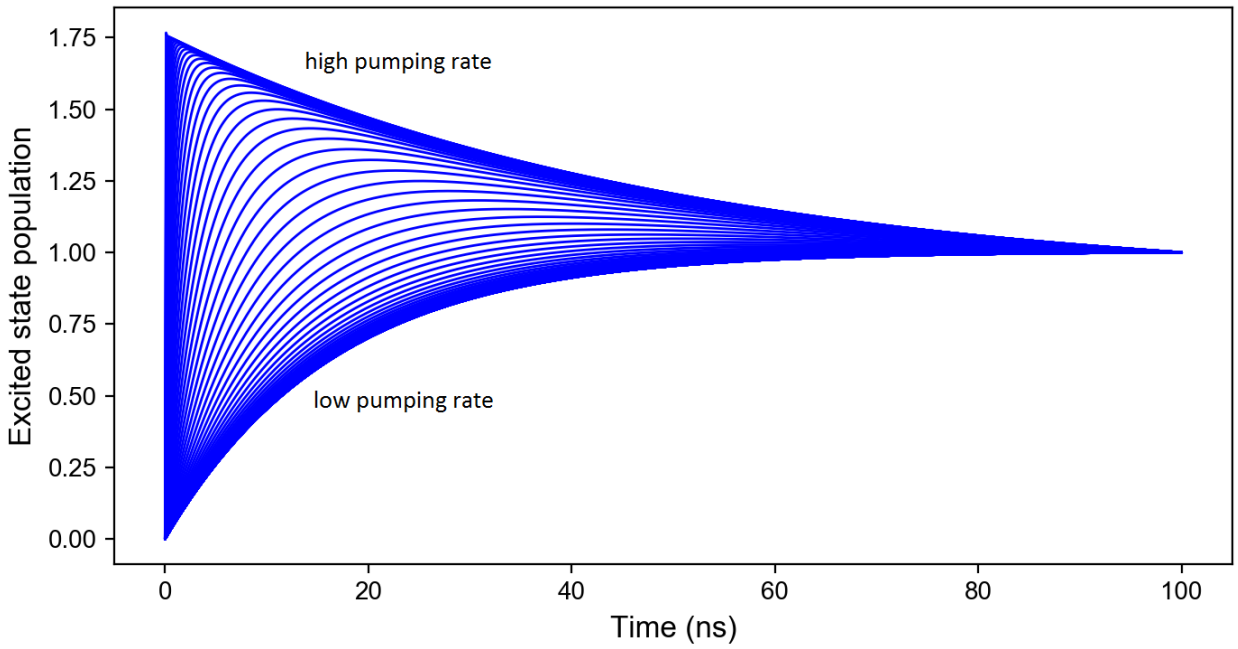

Figure 3.14 | $g^{(2)}$ curve for a variety of pumping powers. Each blue curve represents a different pumping rate ranging from 10^{-7}/ns to 10/ns. Each curve is normalized to the y-axis value at t = 100 ns. Equations 3.76 and 3.77 are used for this model.

In the high-power limit, the excited state population n_2 becomes populated immediately and then decays exponentially. In the low power limit, the excited state population steadily grows until it reaches its equilibrium level. In between, it is possible for n_1 to first reach a local maximum and then decay from there. When this local maximum is observed experimentally, we refer to it as a "bunching" of the $g^{(2)}$ curve. In this model it is induced by the high pumping power, but it can also be due to significant rates into the intersystem crossing level n_3.

It is worth noting that in experimental measurements negative values of t are also included, which corresponds to taking the graph in figure 3.14 and reflecting it over the y-axis. When this mirrored graph is obtained, the full-width half maximum of the $g^{(2)}$ curve should approximately correspond to the excited state lifetime, although there is no simple relation and the width can be varied significantly by the pumping power. In figure 3.14, for example, the low power y = 0.5 value is at ~11.5 ns, which does not have a clear relation to the radiative excited state lifetime of 20 ns nor the total lifetime of 16.7 ns.

Lastly, the addition of the pumping rate r_{12} as a free parameter in this model will significantly increase the uncertainty of the four individual rates. This means that while the best fit curve from the continuous Markov chain result will likely fit a measured $g^{(2)}$ curve quite well, the rates cannot be determined confidently from this measurement alone. This effect was also seen in the lifetime model, and in a similar fashion a combination of multiple independent measurements would be needed to determine the system's rates uniquely.

3.8 Five-level model for the divacancy

Given the complexity of the previous section's results, it seems the last thing we would want to do is add more levels to our 3-level model. However, if we want to incorporate spin-dependent phenomenon, it is necessary to include spin sublevels in the ground and excited states. At a bare minimum this results in two added levels to give a 5-level model. The rate picture for this model is shown in figure 3.15.

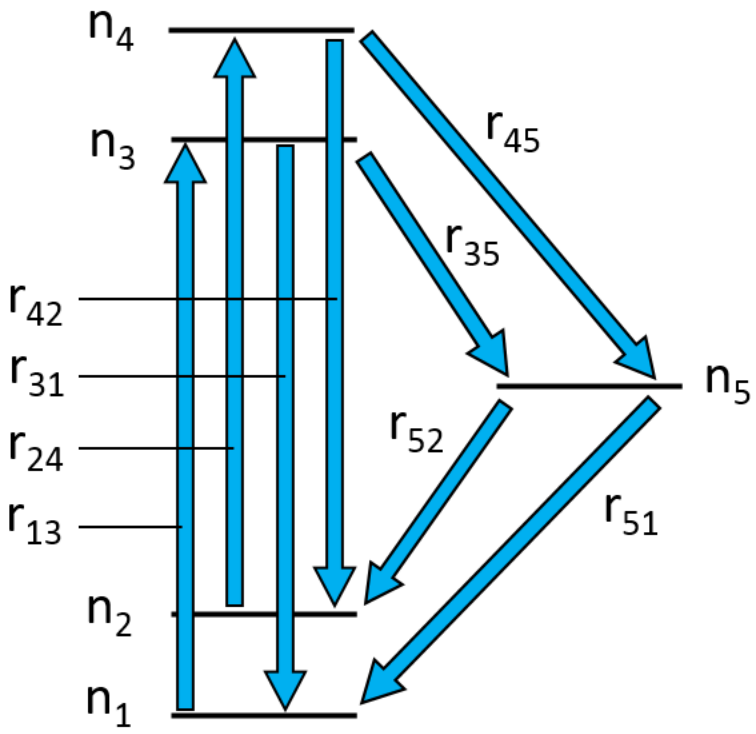

Figure 3.15 | 5-level model of the VV^0. In this diagram, n_1 and n_2 represent ground states with differing spin character, n_3 and n_4 represent corresponding excited states, and n_5 represents an overall nonradiative state as a combination of the inter-system crossing singlet state and ionized states of the VV^0. Rates between these levels are denoted by r_{ij}.

Here, n_1 and n_2 are meant to represent spin states in the ground state, with $n_1 = \{m_s = 0\}$ and $n_2 = \{m_s = \pm 1\}$ as one possible assignment for the VV^0 system. The states n_3 and n_4 are then

the corresponding spin states in the excited state. The state n_5 is again an intermediate state for nonradiative decay, which in most cases refers to the ISC.

With a 5-level system, the differential equations from a continuous Markov chain would be cumbersome. Likewise the Monte Carlo model takes much longer to simulate dynamics. So for the following discussion, we will rely solely on the discrete Markov chain. As before, the probabilities in the stochastic matrix of the discrete Markov chain will follow the relation $p_{ij} = r_{ij} \cdot dt$. This then gives the off-diagonal elements of the discrete transition matrix as:

$$P = \begin{pmatrix} p_{11} & r_{12}dt & r_{13}dt & r_{14}dt & r_{15}dt \\ r_{21}dt & p_{22} & r_{23}dt & r_{24}dt & r_{25}dt \\ r_{31}dt & r_{32}dt & p_{33} & r_{34}dt & r_{35}dt \\ r_{41}dt & r_{42}dt & r_{43}dt & p_{44} & r_{45}dt \\ r_{51}dt & r_{52}dt & r_{53}dt & r_{54}dt & p_{55} \end{pmatrix} \tag{3.79}$$

According to the picture in figure 3.15, many of these rates can be set to zero:

$$P = \begin{pmatrix} p_{11} & 0 & r_{13}dt & 0 & 0 \\ 0 & p_{22} & 0 & r_{24}dt & 0 \\ r_{31}dt & 0 & p_{33} & 0 & r_{35}dt \\ 0 & r_{42}dt & 0 & p_{44} & r_{45}dt \\ r_{51}dt & r_{52}dt & 0 & 0 & p_{55} \end{pmatrix} \tag{3.80}$$

Filling out the diagonal elements by imposing that each row sums to 1 then gives:

$$P = \begin{pmatrix} 1 - r_{13}dt & 0 & r_{13}dt & 0 & 0 \\ 0 & 1 - r_{24}dt & 0 & r_{24}dt & 0 \\ r_{31}dt & 0 & 1 - (r_{31} + r_{35})dt & 0 & r_{35}dt \\ 0 & r_{42}dt & 0 & 1 - (r_{42} + r_{45})dt & r_{45}dt \\ r_{51}dt & r_{52}dt & 0 & 0 & 1 - (r_{51} + r_{52})dt \end{pmatrix} \tag{3.81}$$

Lastly, we can make some simplifications to the model by saying that the excitation rate will be the same regardless of the spin state. This means that $r_{13} = r_{24}$. We can also assume that the

radiative decay rate will be approximately the same regardless of spin state, so $r_{31} = r_{42}$. With these assumptions we now have 6 rates in a 5-level system.

$$P = \begin{pmatrix} 1 - r_{13}dt & 0 & r_{13}dt & 0 & 0 \\ 0 & 1 - r_{13}dt & 0 & r_{13}dt & 0 \\ r_{31}dt & 0 & 1 - (r_{31} + r_{35})dt & 0 & r_{35}dt \\ 0 & r_{31}dt & 0 & 1 - (r_{31} + r_{45})dt & r_{45}dt \\ r_{51}dt & r_{52}dt & 0 & 0 & 1 - (r_{51} + r_{52})dt \end{pmatrix} \quad (3.82)$$

With this model, we further lose the ability to infer each individual rate with low uncertainty, but we gain the flexibility to describe more phenomenon. For example, the addition of the rates r_{35}, r_{45} and r_{52}, r_{51} allows for an asymmetric decay from the excited state to the ground state through the ISC. It is this asymmetry that allows for effects like off-resonant spin initialization and readout. We will examine these examples in the following sections.

3.8.1 Spin initialization

In optical spin initialization, an off-resonant laser pumps the ground state spin levels continuously until an equilibrium of spin population is reached. Due to the asymmetric branching of spin states both to and from the ISC, this results in a predominantly $m_s = 0$ spin population. Typically, spin initialization fidelities are in the range of ~95% for the VV^0. To see how this could be the case, we can use the stochastic matrix above to directly to simulate the "n_1" ($m_s = 0$) and "n_2" $m_s = \pm 1$) levels over time. The caveat to this is that the equilibrium levels will also have partially occupied n_3, n_4, n_5 levels. To translate these levels to the ground state once the pumping laser is switched off, we can simulate the system for a given time with laser excitation, then remove the pumping

rate r_{13} and continue to time evolve the system. As example parameters that give a high initialization fidelity, we can use:

$$r_{13} = \frac{0.01}{ns}, \quad r_{31} = \frac{0.05}{ns}, \quad r_{35} = \frac{0.001}{ns}, \quad r_{45} = \frac{0.005}{ns}, \quad r_{51} = \frac{0.05}{ns}, \quad r_{52} = \frac{0.01}{ns} \tag{3.83}$$

The result of this simulation is given in figure 3.16.

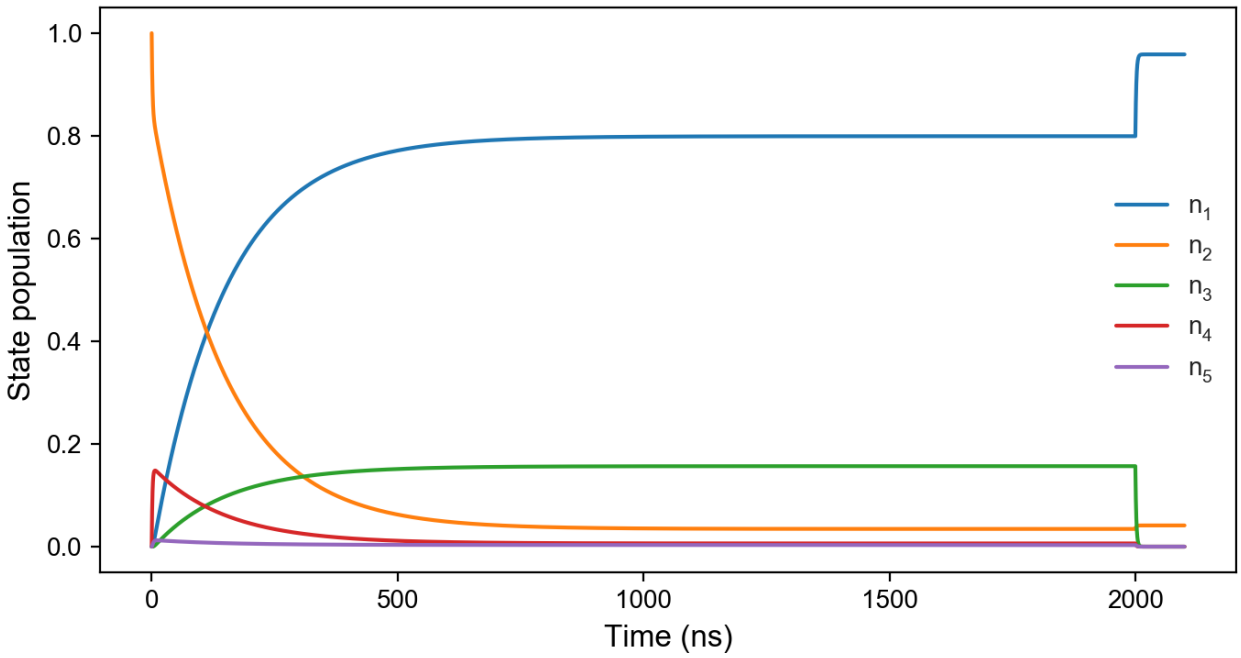

Figure 3.16 | Simulated spin initialization in 5-level model. The 5-level system is evolved with the stochastic matrix in equation 3.82 and rates in equation 3.83. The pumping rate is turned off at t = 2000 ns. After this initialization pulse, most of the population is in the n_1 state.

The majority of the model's time is spent pumping the defect, then the "kink" at t = 2000 ns corresponds turning off the pumping rate and letting the system relax. The spin initialization fidelity is then given by the final population of the $m_s = 0$ state n_1. In this case, we start with a $m_s = \pm 1$ state and reach a $m_s = 0$ initialization of ~96%, which is close to what is observed experimentally. This high initialization was possible through the 5x larger branching of the $m_s =$

± 1 excited state to the ISC (r_{45}) and the 5x larger preferential decay to $m_s = 0$ from the ISC (r_{51}). Incidentally, the time scale of the initialization is also the right order of magnitude, as we typically pump anywhere from 3 to 10 microseconds for off-resonant spin initialization. While this set of parameters gives the correct results, it is by no means a unique solution the rate dynamics. With 6 free parameters at play, there are many ways to achieve this same end result. As with the lifetime and $g^{(2)}$ examples, we would need to combine this result with many other measurements if we wanted to truly fit the rate parameters. Nevertheless, this result is a demonstration of how spin initialization can arise due to the dynamics of the ISC.

3.8.2 Spin readout

The complement to off-resonant spin initialization is off-resonant optical spin readout. The idea of spin-dependent readout contrast is that under off-resonant pumping, the $m_s = 0$ state will usually give more total counts in a given readout window than the $m_s = \pm 1$ state. In reality this difference is only ~5% based on optically detected magnetic resonance (ODMR) scans, but is readily observed with averaging of experiments. The reasons for this contrast are founded in spin-dependent ISC dynamics, similar to spin initialization. Another important point is that after a very long readout time, the relative differences in total counts will shrink due to spin initialization effects with off-resonant excitation. This means that in practice the readout window should be truncated to maximize contrast. This is sometimes at odds with collecting as many photons as possible to lower averaging time, so a balance must be struck based on the timing of the experimental sequence and the time available to run experiments. However, the upshot of this

measurement is that it allows for optical readout of spin states, which is used nearly in all experiments.

To map the photon counts from a defect to the Markov model, we focus on the cumulative total excited state populations over time. Here we are using a cumulative sum of populations since a constant excited state population implies a constant stream of photon counts and an increasing overall count. The key point to this measurement is to see a noticeable difference in counts when starting in the $m_s = 0$ state as opposed to the $m_s = \pm 1$ state. Here we can observe this effect using the same rates as the previous section:

$$r_{31} = \frac{0.05}{ns}, \qquad r_{35} = \frac{0.001}{ns}, \qquad r_{45} = \frac{0.005}{ns}, \qquad r_{51} = \frac{0.05}{ns}, \qquad r_{52} = \frac{0.01}{ns} \tag{3.84}$$

In figure 3.17, we plot the "readout contrast" vs readout time. Here readout contrast is defined as the total counts collected with a $m_s = 0$ start (here n_1) divided by the total counts collected with a $m_s = \pm 1$ start (here n_2), where again counts are mapped to the total excited state population $n_3 + n_4$. So a y-value of 1.05, for example, means 5% more counts from $m_s = 0$. Lastly, similar to the model of the $g^{(2)}$ measurement in section 3.7.5, we can perform this simulation over various pumping rates r_{13}. In this case we use:

$$r_{13} = \frac{10^{-3}}{ns} \leftrightarrow \frac{10^{-1}}{ns} \tag{3.85}$$

This gives the following result:

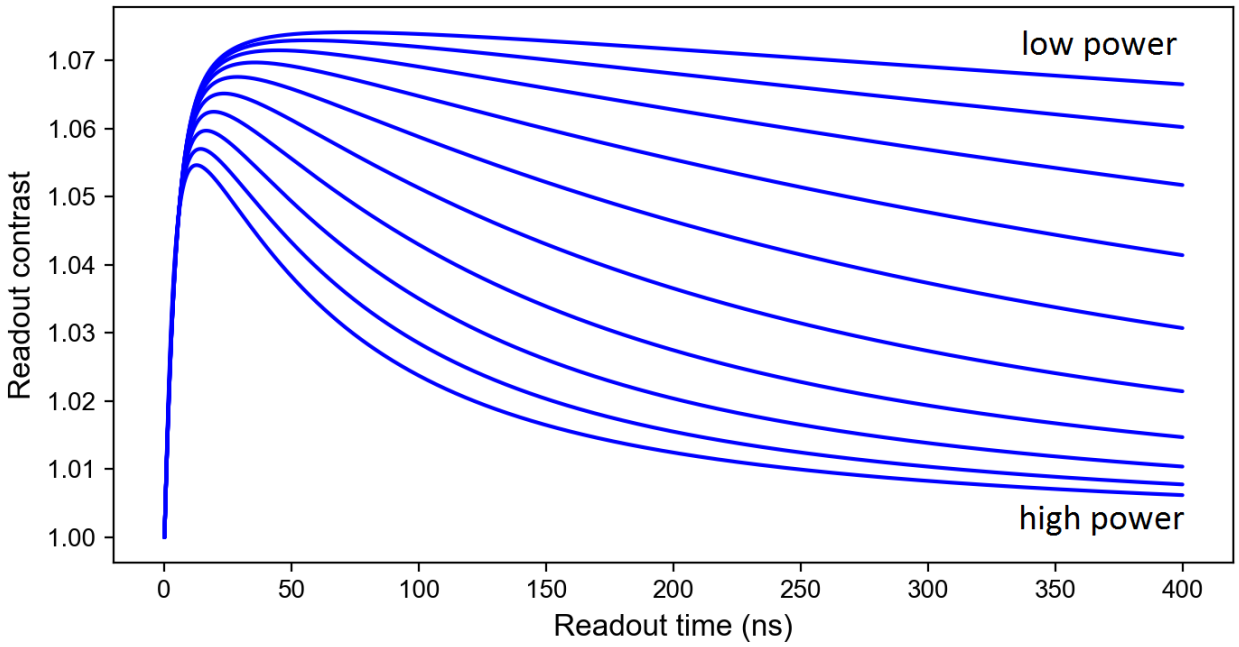

Figure 3.17 | Spin readout contrast with off-resonant optical excitation as a function of readout time. Readout contrast is determined by the ratio of excited state population when starting in n_1 ($m_s = 0$) compared to n_2 ($m_s = \pm 1$). Pumping rates between 10^{-3}/ns and 10^{-1}/ns are shown here. The readout contrast is highest for a low optical pumping power, which must be weighed against the lower photon counts obtained.

In this model, we can see that it is actually beneficial to use a lower pumping power in order to maximize readout contrast, which here peaks around ~7%. This would come at the cost of increased averaging since the counts would not be as high. In the high-power limit, a smaller readout contrast of ~1-5% is still observed. At short readout times, the contrast "bunches" at a maximum value before decaying. This slight peak in counts is also observed experimentally, see for example figure 4 in reference [3]. Thus, in general this model agrees well with experimental results. Similar to spin initialization, the mechanism for readout contrast lies in the asymmetric branching of spin states to and from the ISC level.

If desired, we could add even more levels to this Markov model. In reality the VV^0 has 3 ground state spin levels, 6 excited states, 2 ISC states, and 2 charge states for a total of 13 levels. However, the rates from such a model would be nearly impossible to determine even with many

measurements, or at the very least many assumptions would need to be made. Perhaps more importantly, including all levels is not even necessary to describe experimental results. We've seen that relatively simple 3- and 5-level models are enough to accurately simulate lifetime decays, $g^{(2)}$ autocorrelation measurements, and off-resonant spin initialization and readout. Thus, the Markov model is a powerful tool that lends itself naturally to the isolated electronic levels of the VV^0.

3.9 Collection efficiency calculation

It cannot be overemphasized how important photon collection efficiency is for nearly all experiments performed in our lab. As single VV^0 experiments have developed in the past ~5 years, so has the need for higher collection efficiencies. This becomes crucial for both single-shot readout experiments and the scalability/feasibility of remote spin-spin entanglement.

In this section, we will work through a calculation for the free-space collection efficiency from a *c*-axis divacancy in silicon carbide. This calculation should also be generalizable to objectives with other NA's and to the NV center in diamond.

3.9.1 Initial setup

When using a free-space objective for collection, it is important to keep in mind the definition of numerical aperture NA for a lens. Using figure 3.18 as a reference, the NA is defined as the sine of the angle θ that is formed with the focal length and radius of the lens. This NA will be left as a

free variable in the upcoming calculations, but generally takes values of ~0.6-0.9 depending on the objective.

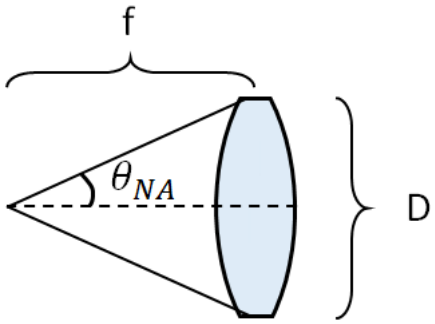

Figure 3.18 | Definition of angle θ_{NA} for a lens or objective. The angle θ_{NA} directly determines the numerical aperture, NA, of the lens or objective. Here f is the focal length and D is the diameter of the lens or objective.

The equation for NA is:

$$NA = n_{air} \sin \theta_{NA} = \sin \theta_{NA} \tag{3.86}$$

Some example NA's for objectives used in active setups are:

$$100x \text{ objective}, \quad 0.85 = \sin \theta_{NA}, \quad \theta_{NA} = 58.2^o \tag{3.87}$$

$$50x \text{ objective}, \quad 0.65 = \sin \theta_{NA}, \quad \theta_{NA} = 40.5^o \tag{3.88}$$

For the purposes of this calculation we will refer to this angle as θ_{NA}. With this, the general ray optics picture is as follows:

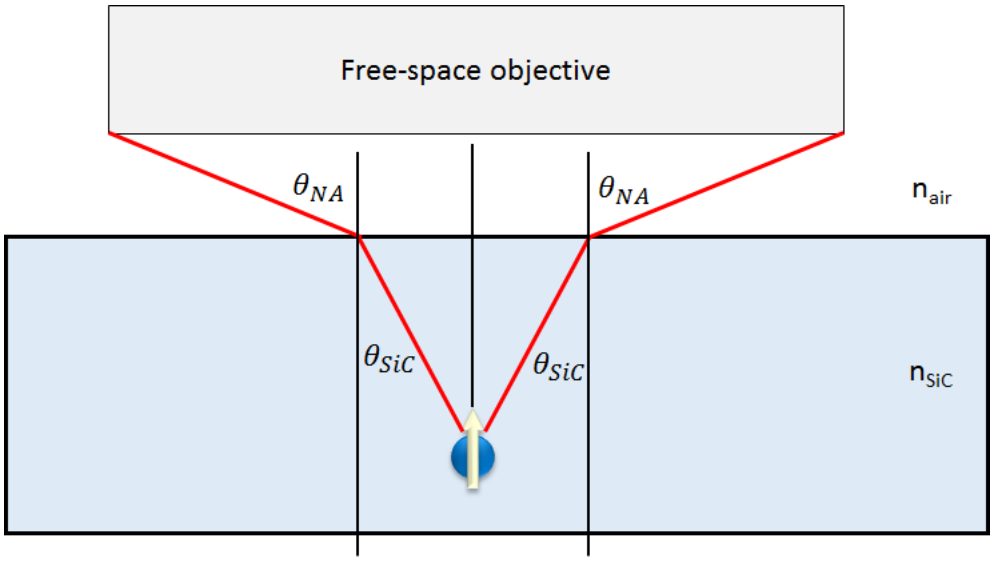

Figure 3.19 | General ray optics picture of collection of light from a point source emitter in silicon carbide. The angles θ_{SiC} and θ_{NA} obey Snell's law. Only light that is emitted into the solid angle of the objective will be collected.

Snell's law gives the relation between θ_{NA} and θ_{SiC}:

$$n_{air} \sin \theta_{NA} = n_{SiC} \sin \theta_{SiC} \tag{3.89}$$

Where the indices of refraction are $n_{SiC} = 2.58$ at ~1100 nm and $n_{air} = 1$. To get the collection efficiency, we want the ratio of two powers:

1) The power emitted by a dipole emitter in a full sphere around the emitter in the SiC (i.e. 100% collection efficiency).
2) The power emitted by a dipole emitter in the collection cone within the objective NA, after accounting for reflection/refraction at the SiC/air interface.

We will start with a basic calculation and then add corrections until the full picture is obtained.

3.9.2 Collection efficiency for an isotropic emitter in free space

Here we are assuming a uniform emitter in free space. Without any refraction, the collection efficiency will be given by the ratio of the solid angle subtended by the emission cone to the solid angle subtended by full emission (4π for a full sphere):

$$CE = \frac{\text{solid angle of cone with } \theta_{NA}}{4\pi} \tag{3.90}$$

We can substitute the solid angle from a cone as:

$$\text{solid angle of cone with } \theta = 2\pi(1 - \cos\theta) \tag{3.91}$$

So:

$$CE = \frac{2\pi(1 - \cos\theta_{NA})}{4\pi} = \frac{1 - \cos\theta_{NA}}{2} = \sin^2\left(\frac{\theta_{NA}}{2}\right) \tag{3.92}$$

$$CE = \sin^2\left(\frac{\theta_{NA}}{2}\right) \tag{3.93}$$

Note that in the limiting case of $\theta_{NA} = 90^o$ this gives the correct CE = 0.5 since we would be collecting from the top half of the defect.

3.9.3 Dipole emission in free space

The divacancy is not an isotropic emitter, but rather a combination of two emission dipoles. For a *c*-axis VV^0 which this calculation is based upon, the two emission dipoles are oriented along the x

and y directions perpendicular to the *c*-axis (z-axis). We will ultimately find that there is in fact no modification to the collection efficiency due to this emission profile, but it is still worth verifying. For this situation it is useful to recall the time-averaged Poynting vector for a dipole oriented along the z-direction:

$$\langle \vec{S} \rangle_z = \left(\frac{\mu_0 p_0^2 \omega^4}{32\pi^2 c} \right) \frac{\sin^2 \theta}{r^2} \hat{r}, \qquad [S] = \frac{W}{m^2} = \frac{\text{energy transfer}}{\text{unit area} \cdot \text{unit time}} \tag{3.94}$$

To determine a collection efficiency, we will be integrating the appropriately defined Poynting vector over the angles defined by the collection cone of the objective. In this case, since we are integrating over all azimuthal angles, the two VV^0 dipoles can be treated as a single dipole in the xy plane due to rotational symmetry. A sketch of dipole orientations is given in figure 3.20.

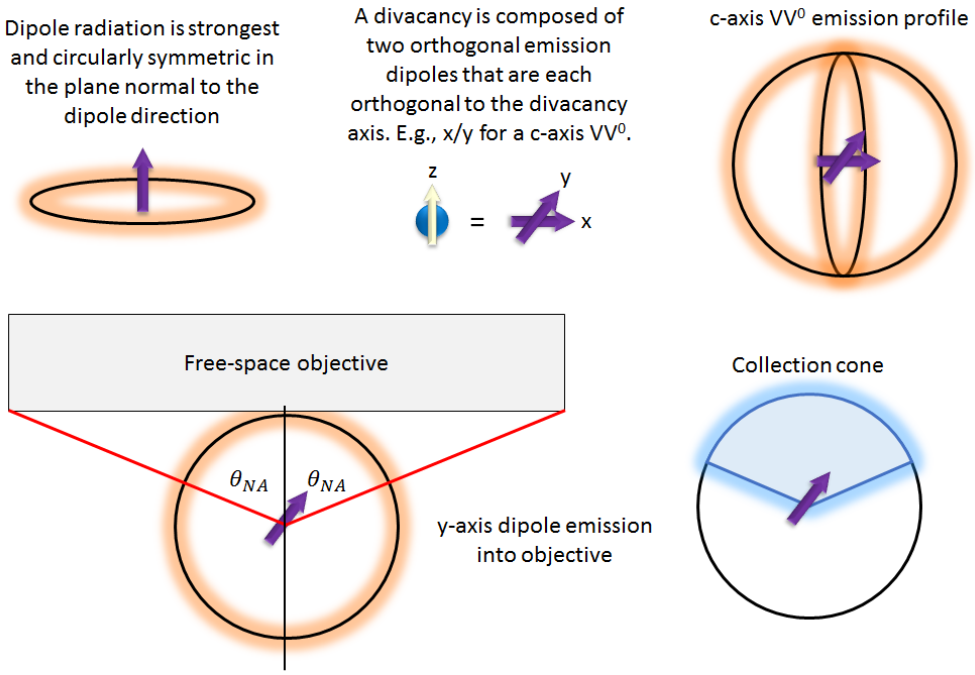

Figure 3.20 | Sketch of dipole orientations. A dipole optical emitter will have a rotationally symmetric emission profile. The VV^0 emission consists of two orthogonal dipole emission profiles. For a *c*-axis VV^0, these dipoles are both parallel to the top SiC surface. Any photons emitted outside of the solid angle of the objective will be not collected.

The simplest orientation for a single dipole in the xy plane would be along the y-axis. In this case the y-axis Poynting vector gets modified by changing the $\sin^2\theta$ to a $\cos^2\phi$:

$$\langle\vec{S}\rangle_y = \left(\frac{\mu_0 p_0^2 \omega^4}{32\pi^2 c}\right)\frac{\cos^2\phi}{r^2}\hat{r} \tag{3.95}$$

To get a power from the Poynting vector, we must integrate it over an area. We will integrate over all azimuthal angles (0 to 2π) but only integrate the polar angle from 0 to θ_{NA} since this is what is encapsulated by the objective. This represents the power emitted into the upwards cone with angle θ_{NA} without accounting for refraction:

$$P_{dipole} = \int_0^{2\pi}\int_0^{\theta_{NA}}\left(\langle\vec{S}\rangle_y \cdot d\vec{A}\right) = \int_0^{2\pi}\int_0^{\theta_{NA}}\left|\langle\vec{S}\rangle_y\right| r^2 \sin\theta \, d\theta d\phi \tag{3.96}$$

The prefactors in $\langle\vec{S}\rangle_y$ will be dropped since we are ultimately after a relative power compared to the collection over all angles, so:

$$P_{dipole} \propto \int_0^{2\pi}\int_0^{\theta_{NA}}(\cos^2\phi)\sin\theta \, d\theta d\phi = \int_0^{2\pi}\cos^2\phi \, d\phi \int_0^{\theta_{NA}}\sin\theta \, d\theta = \pi(1-\cos\theta_{NA}) \tag{3.97}$$

Meanwhile a "full" integral encapsulating all polar angles for dipole emission from 0 to π would give:

$$P_{dipole,full} \propto \int_0^{2\pi}\int_0^{\pi}(\cos^2\phi)\sin\theta \, d\theta d\phi = \pi(1-\cos\pi) = 2\pi \tag{3.98}$$

So the fractional power within the collection cone of the objective is:

$$\text{Fractional power} = \frac{P_{dipole}}{P_{dipole,full}} = \frac{\pi(1-\cos\theta_{NA})}{2\pi} = \frac{1-\cos\theta_{NA}}{2}, \qquad \text{xy dipole emission} \qquad (3.99)$$

Which is exactly our collection efficiency:

$$CE = \frac{1-\cos\theta_{NA}}{2} = \sin^2\left(\frac{\theta_{NA}}{2}\right), \qquad \text{xy dipole emission} \qquad (3.100)$$

Note that this result is identical to the collection efficiency for isotropic emission. In the isotropic case, the fractional power would be given by the same procedure except without the factor of $\cos^2\phi$ from the dipole Poynting vector:

$$\text{Fractional power} = \frac{P_{isotropic}}{P_{isotropic,full}} = \frac{\int_0^{2\pi} d\phi \int_0^{\theta_{NA}} \sin\theta \, d\theta}{\int_0^{2\pi} d\phi \int_0^{\pi} \sin\theta \, d\theta} = \frac{1-\cos\theta_{NA}}{2} = \sin^2\left(\frac{\theta_{NA}}{2}\right) \qquad (3.101)$$

$$CE = \sin^2\left(\frac{\theta_{NA}}{2}\right), \qquad \text{isotropic emission} \qquad (3.102)$$

Which again matches the result from equation (3.93), as expected. Evidently the emission from a *c*-axis VV^0 is sufficiently symmetric that the collection efficiency does not change from an isotropic emitter. This is almost certainly not the case for a basal VV^0 where symmetry is broken, but we will continue to focus on the *c*-axis case for this calculation.

3.9.4 Effect of refraction

To incorporate the losses from refraction, we use Snell's law to rewrite the smaller angle θ_{SiC} in terms of the large angle θ_{NA}:

$$\theta_{SiC} = \sin^{-1}\left(\frac{\sin\theta_{NA}}{n_{SiC}}\right) \tag{3.103}$$

When accounting for refraction, this is the angle we want to use instead of the θ_{NA} used previously. Substituting this in for θ_{NA} in eq. (2) then immediately gives:

$$CE = \sin^2\left(\frac{\theta_{NA}}{2}\right) = \sin^2\left(\frac{\sin^{-1}\left(\frac{\sin\theta_{NA}}{n_{SiC}}\right)}{2}\right) \tag{3.104}$$

$$CE = \frac{1}{2}\left(1 - \sqrt{1 - \left(\frac{\sin\theta_{NA}}{n_{SiC}}\right)^2}\right) \tag{3.105}$$

3.9.5 Effect of Fresnel reflection

For reflection at the SiC/air interface, we need to incorporate the Fresnel equations. Modifying our earlier picture to include transmission T and reflection R, we now have:

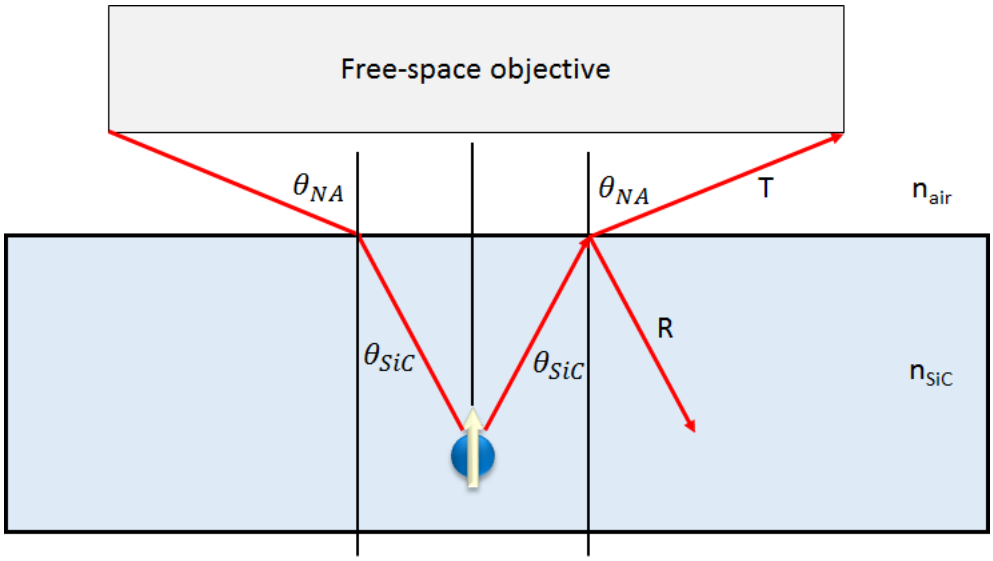

Figure 3.21 | Ray optics picture with Fresnel transmission T and reflection R. The angles θ_{SiC} and θ_{NA} are determined by Snell's law. A fraction of the light at the SiC/air interface will be transmitted while the rest will be reflected, denoted here by T and R.

The Fresnel equations then give:

$$R_s = \left|\frac{n_{SiC}\cos\theta_{SiC} - \sqrt{1-(n_{SiC}\sin\theta_{SiC})^2}}{n_{SiC}\cos\theta_{SiC} + \sqrt{1-(n_{SiC}\sin\theta_{SiC})^2}}\right|^2, \qquad R_p = \left|\frac{n_{SiC}\sqrt{1-(n_{SiC}\sin\theta_{SiC})^2} - \cos\theta_{SiC}}{n_{SiC}\sqrt{1-(n_{SiC}\sin\theta_{SiC})^2} + \cos\theta_{SiC}}\right|^2 \tag{3.106}$$

$$T_s = 1 - R_s, \qquad T_p = 1 - R_p \tag{3.107}$$

Where R_s, R_p represent the reflectance for s-polarized or p-polarized light and T_s, T_p represent the transmission for s-polarized or p-polarized light. Here we are interested in the transmission. Assuming 50/50 polarization, we have:

$$T_{avg}(\theta) = \frac{T_s + T_p}{2} = 1 - \frac{R_s + R_p}{2} \tag{3.108}$$

$$T_{avg}(\theta) = 1 - \frac{1}{2}\left(\left|\frac{n_{SiC}\cos\theta - \sqrt{1-(n_{SiC}\sin\theta)^2}}{n_{SiC}\cos\theta + \sqrt{1-(n_{SiC}\sin\theta)^2}}\right|^2 + \left|\frac{n_{SiC}\sqrt{1-(n_{SiC}\sin\theta)^2} - \cos\theta}{n_{SiC}\sqrt{1-(n_{SiC}\sin\theta)^2} + \cos\theta}\right|^2\right) \tag{3.109}$$

We will repeat the integrals done in section above, except now we will include this angle-dependent average transmission factor. We will also only integrate up to θ_{SiC} (instead of θ_{NA}) in order to account for refraction. This gives:

$$P_{dipole} = \int_0^{2\pi}\int_0^{\theta_{SiC}} \left|\langle \vec{S} \rangle_y\right| T_{avg}(\theta) dA = \int_0^{2\pi}\int_0^{\theta_{SiC}} \left|\langle \vec{S} \rangle_y\right| T_{avg}(\theta) r^2 \sin\theta \, d\theta d\phi \qquad (3.110)$$

The prefactors in $\langle \vec{S} \rangle_y$ will be dropped again:

$$P_{dipole} \propto \int_0^{2\pi}\int_0^{\theta_{SiC}} (\cos^2\phi) T_{avg}(\theta) \sin\theta \, d\theta d\phi = \int_0^{2\pi} \cos^2\phi \, d\phi \int_0^{\theta_{SiC}} T_{avg}(\theta) \sin\theta \, d\theta \qquad (3.111)$$

$$P_{dipole} \propto \pi \int_0^{\theta_{SiC}} T_{avg}(\theta) \sin\theta \, d\theta \qquad (3.112)$$

And as before, we will divide this result by 2π from $P_{dipole,full}$ (which does not change) to give the collection efficiency:

$$CE = \frac{1}{2}\int_0^{\theta_{SiC}} T_{avg}(\theta) \sin\theta \, d\theta \,, \qquad \text{xy dipole emission} \qquad (3.113)$$

In the isotropic emitter case, we now have:

$$\text{Fractional power} = \frac{P_{isotropic}}{P_{isotropic,full}} = \frac{\int_0^{2\pi} d\phi \int_0^{\theta_{SiC}} T_{avg}(\theta) \sin\theta \, d\theta}{\int_0^{2\pi} d\phi \int_0^{\pi} \sin\theta \, d\theta} = \frac{\int_0^{\theta_{SiC}} T_{avg}(\theta) \sin\theta \, d\theta}{2} \qquad (3.114)$$

$$CE = \frac{1}{2}\int_0^{\theta_{SiC}} T_{avg}(\theta) \sin\theta \, d\theta \,, \qquad \text{isotropic emission} \qquad (3.115)$$

Here the two collection efficiencies are still identical. Analytically solving this integral with $T_{avg}(\theta)$ is complicated, so we have to turn to numerical results. Using the more common 100x objective, we have:

$$100x \text{ objective}, \qquad 0.85 = \sin\theta_{NA}, \qquad \theta_{NA} = 58.2^{o} \tag{3.116}$$

And:

$$\theta_{SiC} = \sin^{-1}\left(\frac{\sin\theta_{NA}}{n_{SiC}}\right) = 19.2^{o} \tag{3.117}$$

This gives the result:

$$CE = 1.6\%, \qquad \text{for 0.85 NA objective} \tag{3.118}$$

3.9.6 Addition of a solid immersion lens

A solid immersion lens (SIL) is a popular option to increase collection efficiency by eliminating the effects of refraction at the SiC/air interface. The silicon carbide (or any refractive material) is molded into a hemisphere with the optical emitter at its center. In this geometry, every emitted ray is at exact 90^{o} to the surface. At this normal incidence for a SIL, we have $\theta_{SiC} = 0$, so the Fresnel coefficients become:

$$R_s = R_p = \left|\frac{n_{SiC} - 1}{n_{SiC} + 1}\right|^2, \qquad T_s = T_p = 1 - R_s = 1 - R_p \tag{3.119}$$

Which evaluates to:

$$R_s = R_p = 0.1948 \tag{3.120}$$

$$T_s = T_p = 0.8052 \tag{3.121}$$

This is now a constant factor. We also raise the upper bound of the integral from θ_{SiC} to θ_{NA} since there is no refraction due to the normal incidence at the SiC/air interface. This gives the improved collection efficiency of:

$$CE = 19.1\%, \quad \text{enhancement} \approx 12\ x, \quad \text{for 0.85 NA objective} \tag{3.122}$$

Note that this improvement assumes perfect positioning of the emitter at the center of the SIL. In real life, the improvement might only be a factor of ~5-8.

3.9.7 Summary of results

A summary of these results is presented in the plots below, which plot collection efficiency as a function of collection angle.

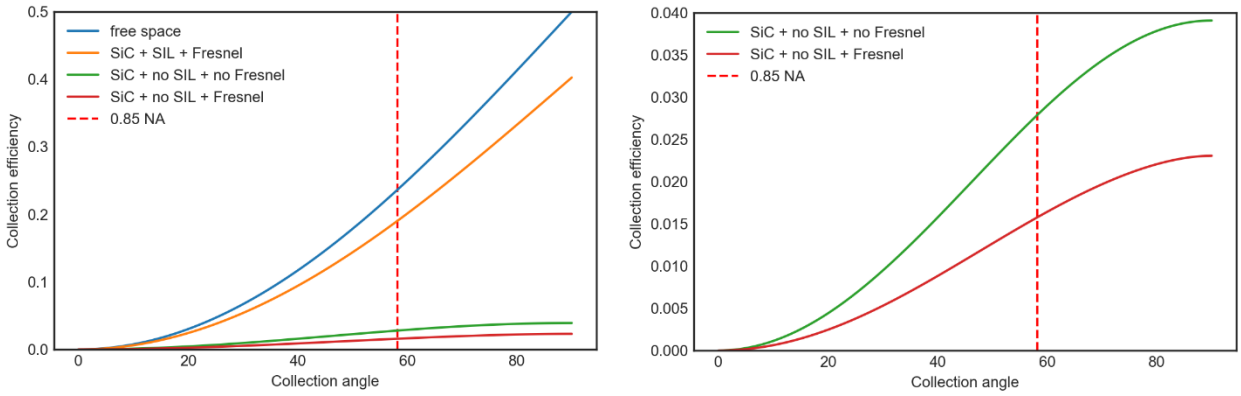

Figure 3.22 | Collection efficiencies as a function of collection angle for different geometries and assumptions. Note that for all of these graphs, the result is equivalent regardless of whether the emitter is isotropic or a dipole. The graph on the right is the same as on the left, except with a rescaled y-axis to get a better sense of scale for the non-SIL geometries.

The main upshot of this calculation is that the relatively low collection efficiency of an optical emitter in silicon carbide can be significantly improved through a SIL, the NA of the objective, or even anti-reflection coatings at the surface.

Further collection efficiency losses in current silicon carbide setups are tabulated below. Note that the exact loss of many of these factors is not known and so can only be approximated.

Source of loss	% of light transmitted
Ray optics losses from VV^0 to objective (0.85 NA)	1.6% (from above calculation)
Transmission through objective	~90%
All optics (mirrors + dichroics + etc.) between objective and single mode fiber	~80%
Coupling into single mode fiber	~50%
SNSPD baseline efficiency at PSB (~1200-1250 nm)	~70%
SNSPD loss collecting unpolarized vs. polarized light	~75% (assuming PSB emission is unpolarized)

Table 3.1 | Sources of optical collection loss. Collection efficiency losses are approximated from various sources.

$$\text{Total transmission} = 1.6\% \cdot 90\% \cdot 80\% \cdot 50\% \cdot 70\% \cdot 75\% = 0.30\% \tag{3.123}$$

Also listed below are possible sources of improvement:

Source of improvement	Improvement (200% means 2x improvement)
SIL	1200% (with perfect alignment)
Adaptive optics system	~150%
Higher 0.9 NA objective	~120% (if SIL is already included)
MW mixing of $m_s = -1$ into 0	200%
Anti-reflection (AR) coatings	~125% (from equation 3.121, assuming + SIL)

Table 3.2 | Sources of optical collection gain. Potential collection efficiency gains are approximated from various sources.

$$\text{Total posisble improvement} = 12 \cdot 1.5 \cdot 1.2 \cdot 2 \cdot 1.25 = 54 \tag{3.124}$$

Thus, with a highly engineered SIL-based system, the collection efficiency could improve from ~0.3% to ~15%. Further improvements from here would have to employ integrated optics components (on-chip waveguides, tapered fibers, grating couplers, etc.).

Chapter 4

Equipment and software

Now that we have outlined many of the theoretical foundations for the divacancy, it's time to discuss the hardware and software that goes into actual experiments. This chapter will be organized into hardware, software, and a discussion of pulses sequences which are used to run actual experiments. Optical diffusion and curve fitting are discussed at the end of the chapter.

4.1 Hardware

In order to provide full control over a divacancy spin, it is necessary to interweave multiple systems at once. Microwave application requires GHz frequency electronics with nanosecond timing control. Optical addressability necessitates the use of multiple lasers carefully aligned on an optical table with specialized wavelength-dependent mirrors, lenses, and filters. Readout of infrared single photons employs the use of a superconducting nanowire detector. Low sample temperatures require the use of helium-based cryogenics while maintaining optical and microwave access. There is a tremendous amount of physical hardware that goes into each of these systems. In this section, we will broadly categorize them into electronics, optics, and cryogenics, and cover the salient features and connectivity that allows experiments to happen.

4.1.1 Electronics

In our lab the main goal of electronics equipment is to create synchronized experiments with optical and microwave signals on nanosecond time scales. A typical configuration of equipment is shown in figure 4.1.

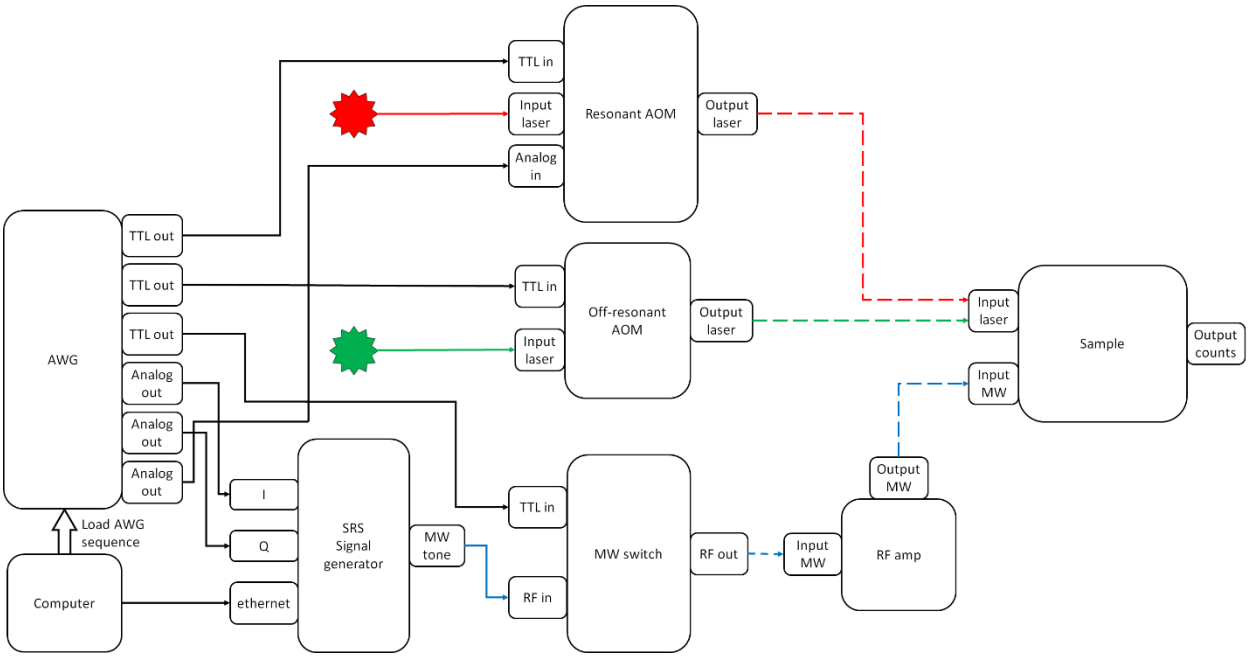

Figure 4.1 | Electronic block diagram of a typical VV^0 setup. Signals from the AWG gate microwave output from the SRS signal generator and the excitation lasers through the AOMs. The gating of these components is synchronized through a collective pulse sequence that is uploaded from a lab computer and run on the AWG.

We use an arbitrary wave generator (AWG) for timing control of experiments. Depending on the setup we use either a Tektronix 5014c or a Zurich HDAWG, although both are fully capable

of running our experiments. In either case the AWG outputs either digital TTL voltages or continuous analog voltages. TTL is typical used for on/off gating, whereas analog signal is using for control of IQ modulation and resonant AOM control as shown in the figure. The Stanford Research Systems (SRS) signal generator is used as our source of MW signal. It has a variable output power up to 16.5 dBm (~4.5 mW) in a frequency range of DC to ~6 GHz. The I and Q quadratures of the signal are controlled with the AWG and the output power is controlled with direct commands from a computer. Microwave switches are gated by TTL pulses and selectively turn signals on or off. The amplifiers we use are typically designed for signals in the ~1 GHz to 4 GHz range, although lower frequency amplifiers in the 1-1000 MHz range are also used for nuclear spin experiments. The power gain is up to 37 dBm with a max input of 0 dBm. Amplifiers with less gain (which are much less expensive) are available but may result in insufficient powers to effectively drive spin rotations.

As an aside on power units, the conversion between Watts and dBm is given by:

$$P_{(W)} = 10^{\left(\frac{P_{(dBm)}-30}{10}\right)} \tag{4.1}$$

Where dBm can be positive or negative or even zero. The units of dBm are commonly used because gains and losses can be calculated quickly as additive or subtractive factors. Some common examples of power are:

$$1\ mW = 0\ dBm, \qquad 1\ W = 30\ dBm \tag{4.2}$$

From any starting power, each ±10 dBm corresponds to a factor of 10x gain or loss in power. So, a 30 dB gain from an amplifier would be factor of 10^3 increase in power. Under max power for our model, a 0 dBm input signal would go to 37 dBm which is ~5W. Microwave signals travel

along either SMA or BNC cables. BNC is typically used for longer distance transmissions, whereas SMA is typically used after the amplifier close to the sample.

Acousto-optic modulators (AOM) and electro-optic modulators (EOM) are used to gate off-resonant and resonant lasers, respectively. The EOMs are used for resonant lasers due to their generally faster rise and fall times on the nanosecond time scale, which becomes relevant when exploring excited state dynamics. The general operating principle of an AOM/EOM is that it uses acoustic waves or electric fields to induce a change in index of refraction in the device material, which in turn forms a sort of diffraction pattern for outgoing light. In practice this means that the incoming beam is deflected to a first order beam with the AOM/EOM on, which is used to address the sample. In this manner, gating the AOM/EOM on or off with gate the laser reaching the sample as on/off.

For readout, photons from the sample are fed to an SNSPD which outputs small voltage spikes to eventually be read out by data acquisition device (DAQ). A schematic of the relevant readout electronics is given in figure 4.2.

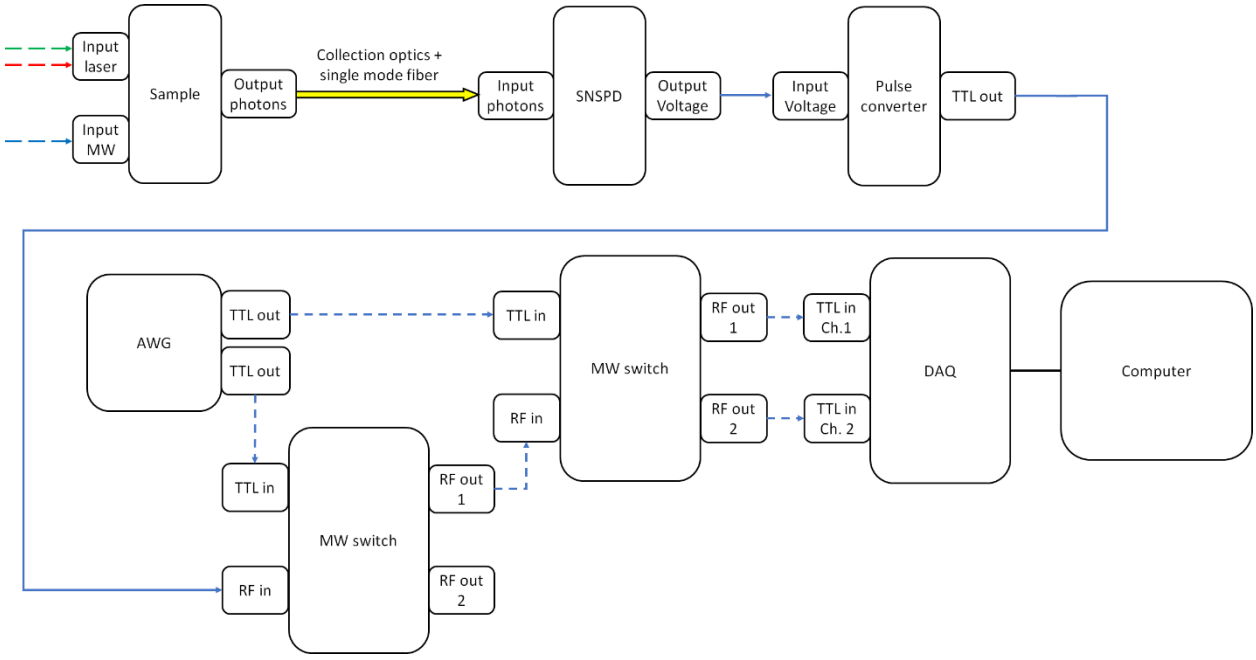

Figure 4.2 | Schematic of readout electronics. The photons from the sample travel through a single-mode fiber to the SNSPD, which outputs small mV voltage spikes. These pulses are converted to TTL and sent to the DAQ, which is queried by a computer to obtain the photon counts.

Here, a pulse converter turns the SNSPD output to TTL pulses that can be read by the DAQ. The intermediary MW switches are used to selectively gate which channels of the DAQ receive counts, with the option of receiving none at all (e.g., during spin initialization).

4.1.2 Optics

A simplified schematic of how lasers and dichroic mirrors can be configured in a VV^0 optical setup is shown below.

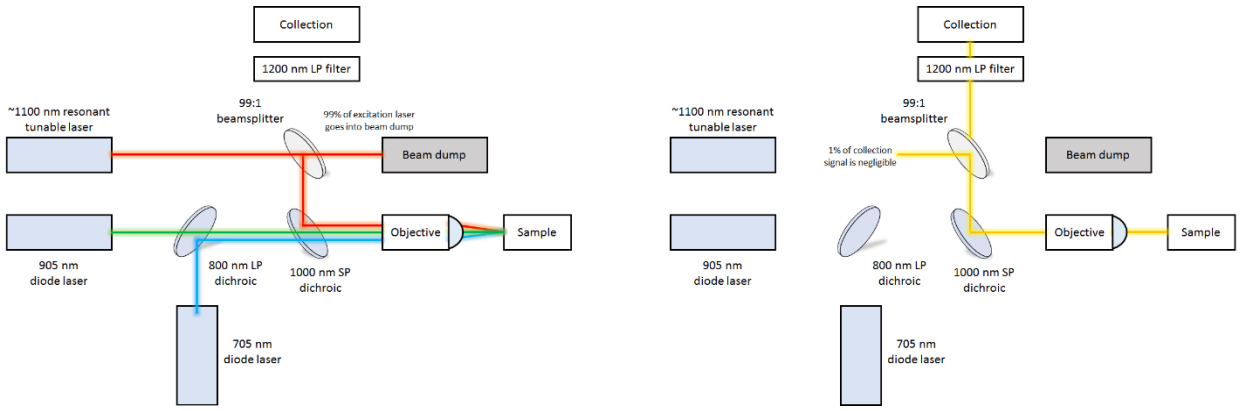

Figure 4.3 | Optical excitation and collection paths for a basic VV^0 setup. The left figure represents excitation, while the right figure represents collection. Here blue represents the charge reset 705 nm laser light, green represents 905 (or 975) nm off-resonant excitation laser light, red represents resonant laser light, and yellow represents photoluminescence from the defect.

For alignment purposes, it is often useful to work with only 90-degree angles that are aligned with the holes of the optical table. Generally the beam is constrained to be at a constant height throughout the path, which allows for fine tuning to be limited to the x/y directions. The choice of mirrors can be important to minimize reflection losses, so should be checked based on the wavelengths of interest (especially for collection). In practice there are multiple options that allow for 95+% reflection. We typically use 1-inch diameter mirrors mounted on manual two-axis kinetic mounts. Two mirrors can direct a beam angle and displacement. A pair of mirrors is sometimes called "bow-tie" configuration due to the crossing of the laser in some geometries. Translating a beam without changing its angle is referred to as "beam walking" and involves deterring the beam angle with the first bow-tie mirror, then compensating for this deflection by adjusting the second bow-tie mirror. Generally speaking, greater separation between mirrors allows for finer control of the beam, at the cost of occupying more space on the optical table. The collection path is usually optimized with photoluminescence with a high density VV^0 ensemble control sample. Then finer tuning is done with a less dense ensemble, and then again with a single defect control chip. During

this process, it is important to properly filter out the excitation laser (often with multiple filters) to ensure one is not simply maximizing laser scatter.

The choice of dichroic mirrors is very important and determines what wavelengths will reach the sample and what wavelengths will reach the collection path. Spectral filters can be used to select which wavelengths of light to be detected. Typically, we collect photons in the phonon sideband (PSB) of the VV^0, which is roughly in the wavelength range of 1200-1500 nm. Thus, a 1200 nm longpass filter is sufficient. Off-resonant lasers are diode lasers typically either at 905 nm or 975 nm. The use of a tunable resonant laser requires a wavemeter for precise measurement of the laser frequency and a Fabry-Perot cavity to diagnose if the laser is single-mode or multimode.

To gain automated spatial control of the beam over the sample, we use either a fast-steering mirror (FSM) with a pair of lenses or two motorized translational stages for x/y control. In either case, a motorized stage is used for focus control in the z-direction. The FSM offers the advantage of faster spatial scans, but has the drawbacks of slight collection losses and difficulty of alignment and imaging due to the two extra lenses involved. Visual imaging of the sample is done with a white light source and two flip mount pellicles that reflect light into a camera. Usually the imaging optics are as close to the sample as possible in order to maximize the field of view. Most (if not all) of our optical setups employ a periscope configuration of mirrors right before reaching the sample. This is to allow for 3-axis translational control with the motorized stages, and also allows for an adjustable beam height right before the laser reaches the sample. Our setups currently employ a near-infrared (NIR) 100x free space objective for both excitation and collection. Here, the important figures of merit are a large numerical aperture (NA) and a large enough working distance to image a cryogenically cooled sample through the cryostat window.

The collection path ends with focusing the free space PL into a single-mode fiber to be fed into the SNSPD. Fiber coupling can also be used for AOMs and EOMs, either as direct fiber coupled units or by branching the excitation laser into an "AOM box" and then fiber coupling back to the main excitation path.

4.1.3 Cryogenics

To obtain the low-temperatures needed for most experiments, we currently use closed-cycle helium cryostats from Montana instruments. These cryostats come in different model types which are primarily distinguished by the size of the sample stage. In general, a larger sample stage allows for more/larger samples at the cost of a longer cooldown period. Regardless of the model, we are able to typically reach steady temperatures of ~4-5 K for weeks or months at a time. The closed-cycle design offers a significant advantage over flow cryostats, which must be frequently replenished (every ~3-4 days) with liquid helium in order to stay operational.

In addition to reaching low temperatures, there are multiple crucial aspects of any cryostat in our experiments:

1) Optical access for excitation/collection
2) DC and Microwave access
3) Low vibrational noise to mitigate interference with optical focus onto a sample.

All three of these benchmarks are achieved by the Cryostation standard (S) series, which are used frequently in our labs. A figure of the s50 model and sample chamber is shown in the figure below:

Figure 4.4 | Montana Instruments closed-cycle cryostat. Pictured here is the Montana Instruments Cryostation s50 model. The upper left is the unit as a whole, the upper right is the exposed sample chamber, and the bottom image shows optical access through windows in the sample chamber and microwave access through customizable patch panels. Not shown here are custom vacuum attachments that are used to connect to external turbo pumps.

The basic idea of operation is that a closed-cycle helium condensation/vaporization cycle is used to cool a platform stage, which in turn cools "stage 2" and "stage 1" of the sample chamber before ultimately cooling the sample itself. Luckily, silicon carbide has a high thermal conductivity so direct contact with a copper mount is sufficient to provide cooling. The sample chamber must be operated under high vacuum (~1e-5-1e-6 Torr), which is achieved through an external turbo pump at the beginning of cooldowns supplemented by natural cryopumping as the system cools. The unit comes separate liquid helium hosing and a compressor in order to complete the closed cycle. We typically store the compressors in a separate cooling closet, although in principle they could also be located in the lab itself.

4.2 Software – Nspyre

For divacancy experiments, instrument control and experimental algorithms are largely implemented by a custom-made python package termed "Nspyre". This stands for "Networked Scientific Python Research Environment". In earlier iterations the package was simply "Spyre", but a networked capability was later added to allow for remote control by lab computers that are not directly connected to the instruments in use.

In a broad view, Nspyre builds upon the Lantz package in python, which offers "driver" modules to connect to instruments from many companies (NI, Newport, etc.) through various physical connections (USB, ethernet, GPIB, etc.). Beyond simply connecting to individual instruments and issuing commands, however, Nspyre facilitates the synchronization between multiple instruments needed for real experiments. Individual experiments like ODMR or PLE can be run through separate "spyrelets" and collected data can be viewed in real time. Live plotting, data viewing, and a basic GUI are achieved through the pyqtgraph and pyQt5 packages. Remote control (the "networked" part of Nspyre) is implemented using the pymongo package.

The general use of Nspyre will be presented in somewhat chronological order based on the steps one takes when running an experiment, with the exception of the "Designing an experiment" section. In practice, experiments are coded in python before Nspyre is launched, although it is possible to run basic instrument commands in a built-in command line.

4.2.1 Launching Nspyre – Widgets.main.py

The module to launch the main menu GUI is currently located under nspyre\nspyre\widgets as the module "main.py". Running this file from a command terminal (under the appropriate conda environment) will bring up the following menu:

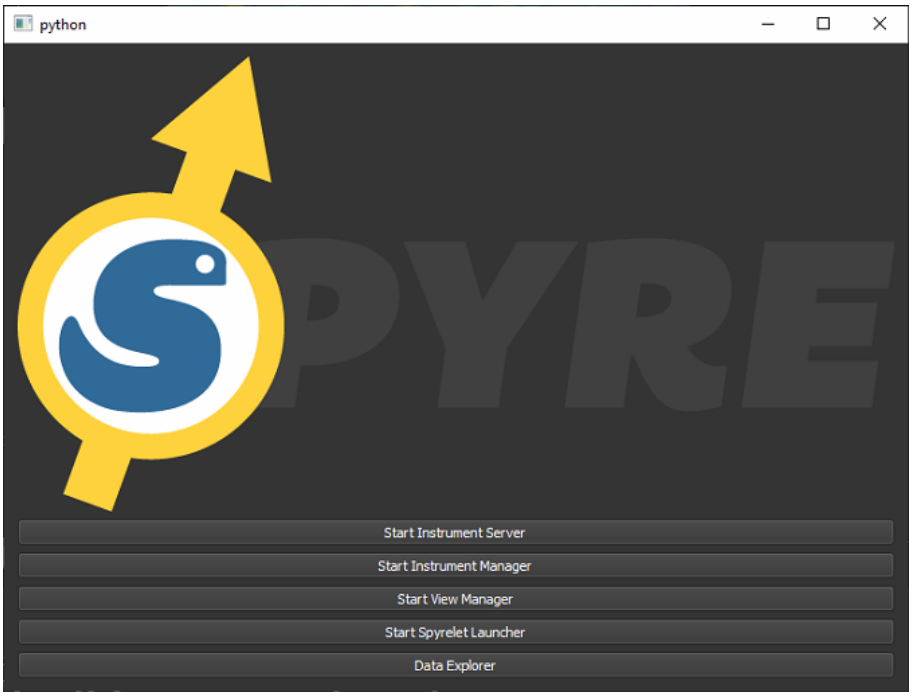

Figure 4.5 | The "main menu" of Nspyre as of July 2021. The five options from this main menu are used to launch experiments, control instruments, and view data.

It is from this menu that all experiments and instrument commands are run. The pymongo server is launched from a separate command terminal with the command "mongo". We will assume the remote server is operating as intended and focus on the five options of the Nspyre main menu and the creation of spyrelet experiment files.

4.2.2 Connecting to instruments – Instrument Server

The first option on the main menu is "Start Instrument Server". Clicking on this button will cause a separate command line terminal to open and display text for each loaded instrument. Which instruments the program attempts to connect to is determined by the configuration file "config.yaml", which contains key information for setting Nspyre parameters. As a basic demonstration, the configuration file stores the devices in a list where each entry contains the appropriate the Lantz driver class for the instrument and the physical connection mechanism, as shown below:

```
device_list:
  sg1:
    - lantz.drivers.stanford.SG396
    - [tcpip::xxx.xxx.x.xxx]
  daq:
    - lantz.drivers.ni.simple_daq.Read_DAQ
    - [Dev1]
  solar_mot:
    - lantz.drivers.toptica.MotDLpro
    - ['COM5', 1]
```

Certain instruments will require additional steps to enable connection before running Nspyre. For example, we use a USB server that must be launched manually on startup and separate software to connect to the Toptica tunable laser and wavemeter.

4.2.3 Viewing instruments – Instrument Manager

Provided that the instrument server has successfully connected to all desired instruments, one can view these instruments in the Nspyre GUI by clicking the "Start Instrument Manager" button on the main menu. This will pull up a menu similar to the one shown below:

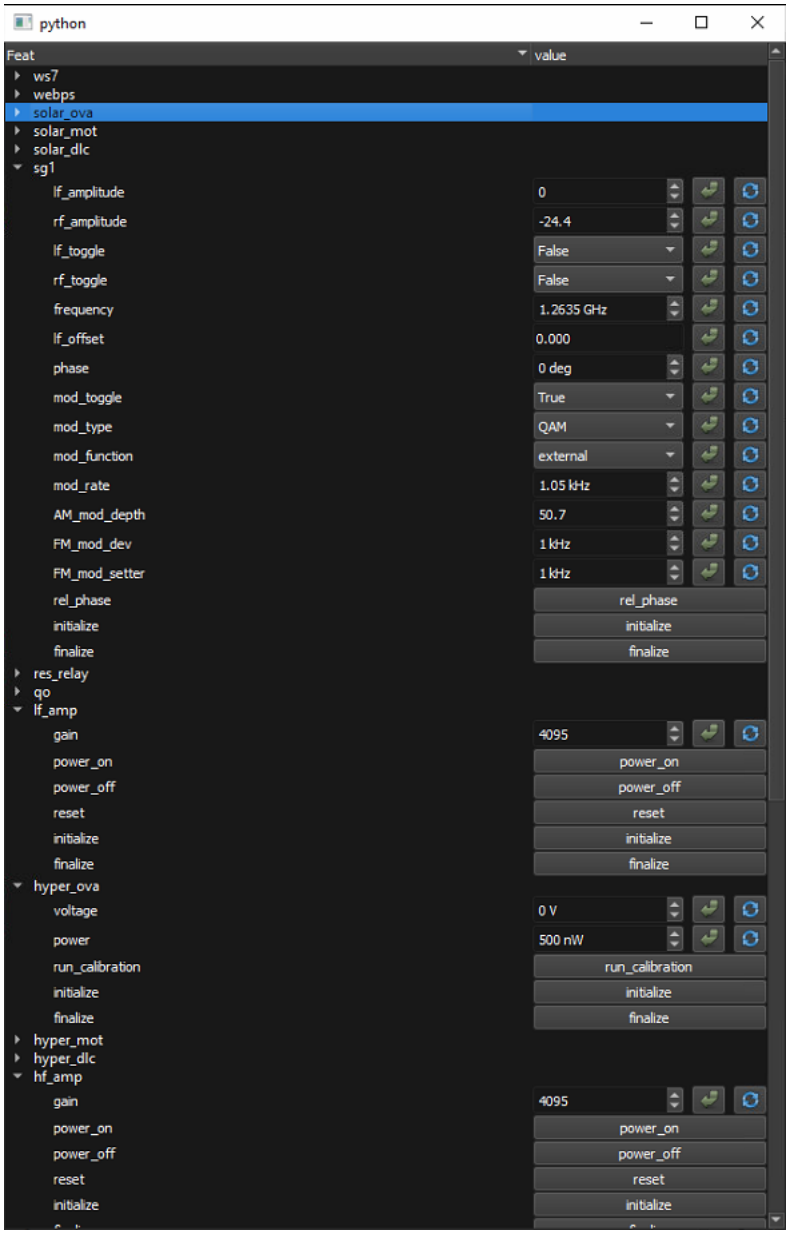

Figure 4.6 | Instrument Manager menu. Various instruments and parameters are displayed in an interactive GUI. Parameters values can be set using the green return arrow and refreshed using the blue circular arrows.

The parameters of a particular instrument can generally be categorized into float values and Boolean values, both of which can be set and toggled in the GUI. Setting values on instruments directly can be used to explore different conditions when running experiments. For example, one may be interested in running the same ODMR experiment under a variety of microwave powers.

4.2.4 Designing an experiment – Spyrelets

The structure of each experiment is determined by user-defined classes called "spyrelets" to be run in the spyrelet launcher. Each class is inherited from a parent Spyrelet class located in the spyrelet.py module. Important elements to be filled in or overwritten are shown below with comments:

```
class Spyrelet():
    # A dict with the names and associated class of the devices
    # required to run this spyrelet
    REQUIRED_DEVICES = dict()

    # A dict with the name and associated class of the sub-spyrelet
    # required to run this spyrelet
    REQUIRED_SPYRELETS = dict()

    # A definition of the parameters that are used as arguments
    # to the main/initialize/finalize functions.
    # These are used both to generate a launcher GUI and to enforce
    # units at call time.
    PARAMS = dict()
```

```
# An extra dictionary, which can be defined by the user at
# initialization time. This can store anything the users want
CONSTS = dict()

"""
A few notes about the spyrelet class:
    - This is the class you need to subclass for making
      experiments.
    - All devices used in the spyrelet must be listed in the
      REQURIRED_DEVICES dict
    - All sub-spyrelet must also be listed in the
      REQUIRED_SPYRELETS dict
    - Upon instantiation the class will check the __init__
      arguments devices and spyrelets to make sure they
      satisfy these requirements
    - For higher performance we will store the data internally
      as a list instead of a dataframe.  Quicker to append to
      a list.
"""

def main(self, *args, **kwargs):
    """This is the method that will contain the user main
      logic. Should be overwritten"""
    raise NotImplementedError
```

```
    def initialize(self, *args, **kwargs):
        """This is the method that will contain the user initialize
          logic. Should be overwritten"""
        pass

    def finalize(self, *args, **kwargs):
        """This is the method that will contain the user finalize
          logic. Should be overwritten
        This will run even if the initialize or main errors out
        """
        pass
```

The functions that must be overwritten are the main, initialize, and finalize functions, although other functions can be included. As an example, the TaskVsTime spyrelet is used to measure photoluminescence counts vs time and has some of the shortest code among the different spyrelets. The relevant code is included below:

```
class TaskVsTime(Spyrelet):
    REQUIRED_DEVICES = {
        'daq': Read_DAQ,
    }

    PARAMS = {
```

```
    'channel':          {'type':str, 'default': 'DAQ1/ctr2'},
    'time_per_point':   {'type':float, 'units': 's',},
    'iterations':       {'type':int, 'positive':True},
}

def read(self, time_per_point):
    if self.ttype == 'CI':
        cnt = self.daq.read(self.tname, 1)
        time.sleep(time_per_point)
        val = self.daq.read(self.tname, 1)[0] - cnt[0]
        return val/time_per_point
    if self.ttype == 'AI':
        clock_rate = 8000
        samples = int(time_per_point*clock_rate)
        return np.mean(self.daq.read(self.tname,samples)[0])

def main(self, channel, time_per_point, iterations=100):
    start_t = time.time()
    iterator = count() if iterations == 'inf' else
    range(iterations)
    for i in self.progress(iterator):
        val = self.read(time_per_point.to('s').m)
        self.acquire({
            't': time.time()-start_t,
```

```
            'val': val,
        })

    def initialize(self, channel, time_per_point,
        iterations=100):
        self.tname = self.name + '_task'
        self.daq.new_task(self.tname, [channel])
        self.ttype = self.daq.get_task_type(self.tname)
        self.daq.start(self.tname)

    def finalize(self, channel, time_per_point, iterations=100):
        self.daq.stop(self.tname)
        self.daq.clear_task(self.tname)
```

Here, the main/initialize/finalize functions are properly overwritten, and there is an additional read function defined and used in the main function. Of course, more complicated experiments that interface with more equipment will have much longer spyrelet classes, but the basic structure remains the same. In this way any experiment can be designed with user-defined logic and loaded into the spyrelet launcher menu, which will be discussed in the next section.

4.2.5 Running an experiment – Spyrelet Launcher

Clicking the "Spyrelet Launcher" button on the main menu will bring up a new GUI window with all spyrelets loaded. The dropdown menu at the top of this window can be used to select which spyrelet to view. An example for the FSM scan is shown in the figure below:

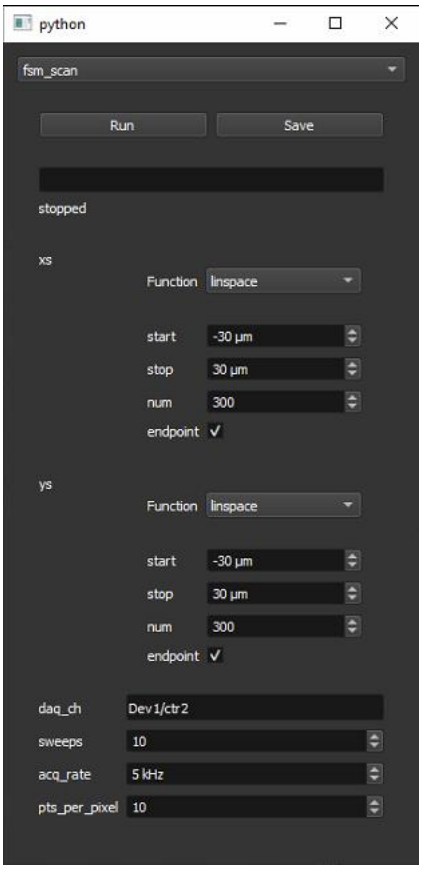

Figure 4.7 | Spyrelet launcher window. Shown here is the fast-steering mirror (FSM) scan experiment, which rasters the laser across the sample and collects photoluminescence from each point. The top drop-down menu is used to toggle between different spyrelets. Experimental parameters are set in the GUI and the experiment is initiated with the run button. For example, here the start/stop indicates the size of the raster window and num gives the number of points to collect on that axis.

The different parameters of the particular experiment can be set by the options in the spyrelet menu. The run button will start the experiment, after which the button toggles to "stop" to terminate the experiment. After an experiment has been run, the save button can be used to save the collected

data. Lastly, in the configuration file the elements of the experiment_list collection determine which spyrelets to load, as sampled below:

```
experiment_list:
  taskvtime:
    class: nspyre.user.taskvstime.TaskVsTime
    args: {device_alias: {daq: daq}}
  taskvline:
    class: nspyre.user.taskvsline.TaskVsLine
    args: {device_alias: {'sg':'sg1'}}
  taskvfreq:
    class: nspyre.user.taskvsfreq.TaskVsFreq
    args: {device_alias: {'sg':'sg1'}}
  fsm_scan:
    class: nspyre.user.taskvsfsm.TaskVsFSM
```

4.2.6 Viewing data – View Manager and Data Explorer

The last two options in the Nspyre main menu are "Start view manager" and "Data explorer". Both of these options will bring forth a data viewing window, with the view manager for current live data and the data explorer for past saved data. In both instances, an interactive graph is displayed as demonstrated in the figure below:

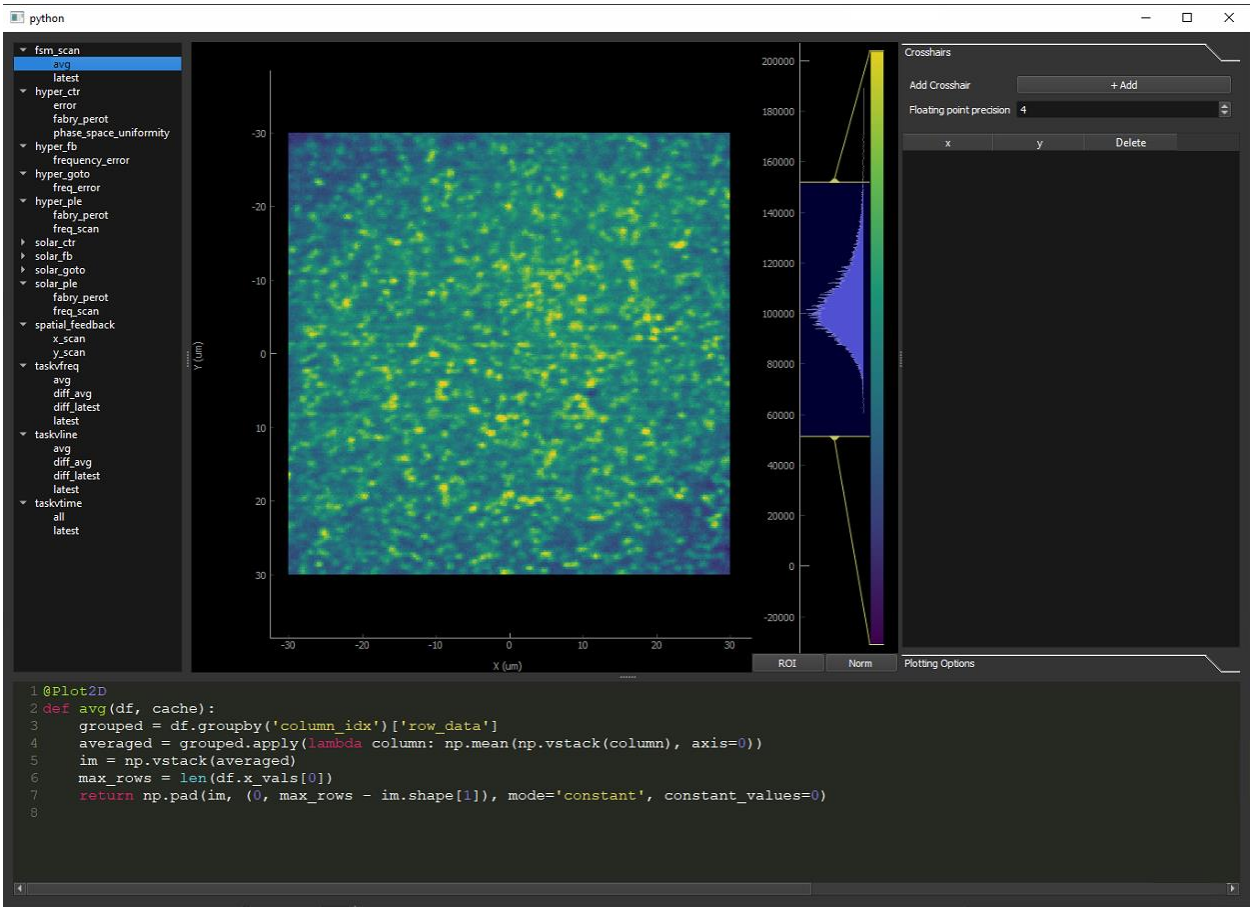

Figure 4.8 | Viewing window for the Nspyre view manager. An example spatial scan from a fast-steering mirror (FSM) raster is shown here, with defect identifiable bright spots corresponding to one or multiple divacancies.

In the viewing window it is possible to interactively scale the graph and set markers for coordinates of interest. After an experiment is initiated by hitting the "run" button in the spyrelet launcher, the view manager will show the accumulation and averaging of data in real time.

4.3 Pulse sequences

The structure of each experiment is determined by the specific "pulse sequence" that is run on the AWG. Here, the pulses refer to the periods of on/off behavior for various instruments. For the majority of experiments, the variables of interest are optical initialization, spin manipulation, resonant excitation, and optical readout. Each of these variables corresponds with a physical instrument which is gated according to the pulse sequence. Optical initialization is typically performed with off-resonant lasers, spin manipulation with AC microwave fields generated from a stripline or wire bond, resonant excitation with a resonant tunable laser, and readout with an SNSPD.

There are several distinguishing factors that make a pulse sequence unique. As a first step, generally sequences can be either "continuous wave" (CW) or pulsed. A CW sequence has all of its components in a fixed state of on or off without any switching with time. Additionally, when microwaves are involved the sequences can either be "two-trace" to compare signal with/without microwaves or "single-trace" if only signal with microwaves is being measured. A single trace sequence corresponds to one curve being plotted and a two-trace sequence corresponds to two curves being plotted, after which we may be interested in taking a difference for comparison. When two traces are involved the sequence can be split into two "halves" for comparison, whereas the second half is simply repeated in a single-trace sequence. Finally, the variable that is being swept in the sequence is a fundamental factor that determines what type of measurement is being taken.

Regardless of the sequence structure, we always have photon counts as the dependent variable on the y-axis. The x-axis is the independent variable that is being swept in the pulse sequence. Generally speaking, if microwave frequency is being swept then the sequence is some sort of ODMR measurement (run with the Taskvsfreq spyrelet). If laser frequency is being swept, the sequence is most likely some sort of PLE measurement (run with the Taskvslaserfreq spyrelet). As

we will see, some sequences are identically constructed with the only difference being what variable is swept. Lastly, the pulse sequences outlined here are by no means a comprehensive collection of all possibilities, but hopefully they give an intuition for the key factors in designing an experiment.

4.3.1 Measuring microwave transitions – ODMR

Optically detected magnetic resonance (ODMR) combines optical initialization and readout with microwave rotations into a single measurement that allows us to experimentally characterize the microwave transitions of the ground state. It is a tremendously powerful technique for characterizing defects and identifying defect type, and is often the first step towards more in-depth measurements. The central idea is to measure either an increase or decrease in photoluminescence (PL) from a defect or ensemble defects when applied microwaves are on resonance with a ground state magnetic transition (e.g., $m_s = 0 \leftrightarrow m_s = \pm 1$). In this way, one can obtain the exact microwave frequencies that cause these transitions to occur.

We will review three types of ODMR in this section:

- Off-res CW ODMR
- CW resonant ODMR
- Pulsed resonant ODMR

There are different types of ODMR measurements that can be run, but we'll start with the most basic, and in some respects, the most informative measurement: Off-res CW ODMR. An outline of the pulse sequence is given below:

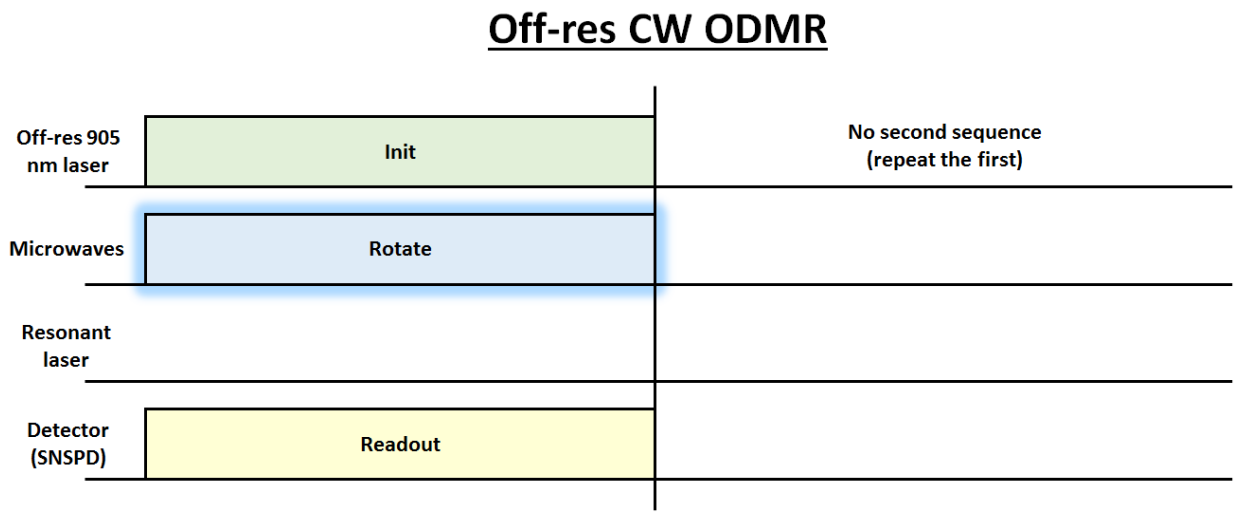

Figure 4.9 | Off-res CW ODMR pulse sequence. The highlight on the blue "rotate" portion indicates that the microwave frequency is being swept as the independent variable. Note that this sequence can be run either as above or as two separate traces with and without microwaves.

Due to the continuous nature of this sequence, it technically is not necessary to have gating components like an AOM or MW switch to run this experiment. In fact, loading a pulse sequence onto an AWG is not necessary either, as no actual gating is occurring. The off-resonant excitation is constantly on, microwaves are constantly being delivered to the sample, and the detector is constantly reading out PL/photons (with a longpass filter to filter out laser scatter). The only experimental control that is truly required is to sweep the microwave frequencies that are being output from the signal generator. This sweeping is denoted in the figure by the blue highlight surrounding the "rotate" pulse.

The lower experimental requirements for CW sequences make them appealing options for setups that are not fully built. Additionally, the simplicity of this measurement makes debugging

issues more straightforward if the results are not as expected. At the cost of this experimental simplicity comes conceptual complexity. For instance, if the spin is constantly being initialized, why would we ever expect to measure a spin rotation? The answer is that initialization does not happen instantaneously, even under constant illumination. In the periods between optical excitation and ISC decay that cause initialization, the spin is being uniformly rotated due to the presence of microwaves. This competition between spin initialization and spin rotation results in a steady state equilibrium spin orientation. The closer the microwaves are to being on resonance, the more this equilibrium shifts towards a rotated spin state. For detuned microwaves, the equilibrium will be closer to the polarized spin state.

How the spin state maps to a photoluminescence contrast depends on the divacancy in question. For the (*hh*) VV^0, the $m_s = 0$ state serves as the "bright" state, meaning that microwave rotations to $m_s = \pm 1$ will manifest as less PL. For the (*kk*) VV^0 the situation is reversed, where the $m_s = 0$ state is in fact the "dark state" and more PL is measured in the $m_s = \pm 1$ states. In the (*kh*) VV^0, a mixture of both behavior is seen. The $|-\rangle$ state is the brighests, followed by the $|0\rangle$ state, and then the $|+\rangle$ state as the darkest. A figure of off-res ODMR for single VV^0's displayed this behavior is shown below in figure 4.10 [2]. Note that due the constant signal from the off-resonant laser, the contrast is this measurement is typically only ~5-10% and so more averaging is required.

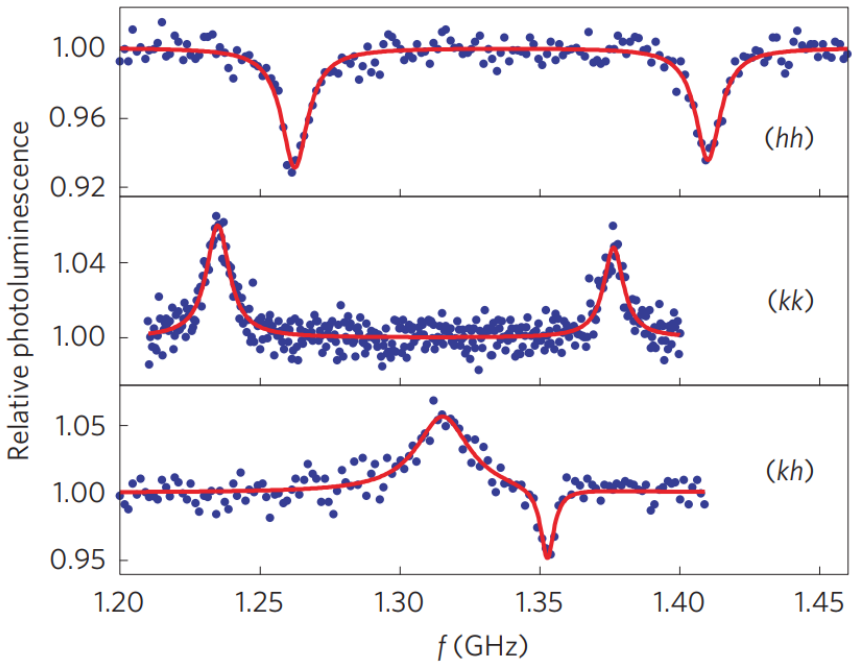

Figure 4.10 | Off-res ODMR contrast for single VV^0 defects. Adapted from [2]. When off-resonant excitation is used, the (*hh*) VV^0 displays a negative ODMR contrast, the (*kk*) VV^0 displays a positive ODMR contrast, and the (*kh*) VV^0 displays both positive and negative ODMR contrast. Contrast levels are typically ~5-10%.

The next sequence, CW resonant ODMR, is still a continuous sequence but employs the use of a resonant laser + a red 705 nm laser in place of the 905/975 nm off-resonant excitation laser. A schematic of the pulse sequence is shown below:

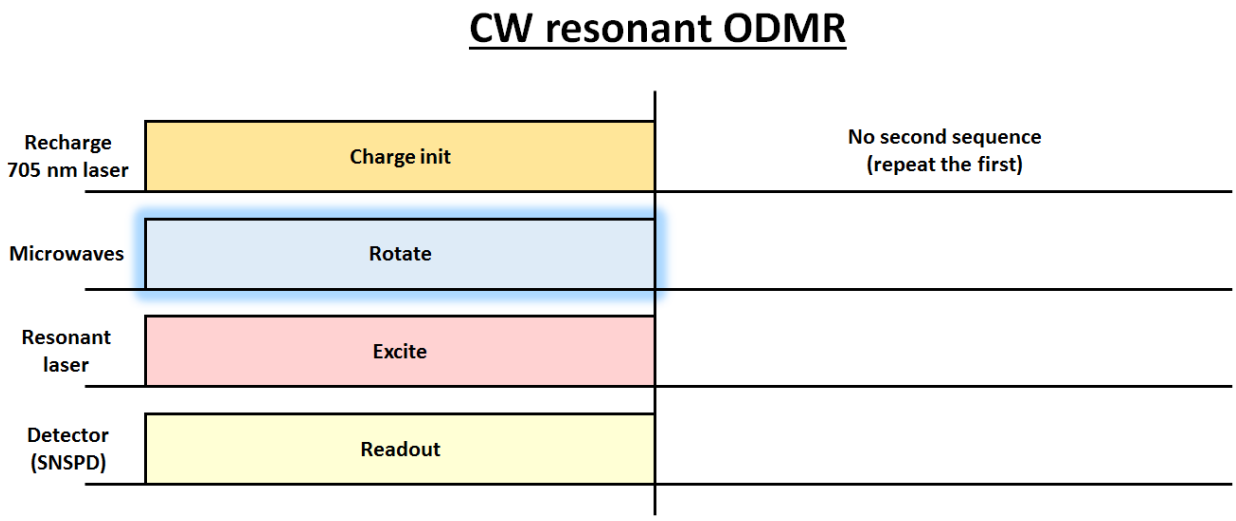

Figure 4.11 | Pulse sequence for CW resonant ODMR. The blue highlight on the "rotate" pulse indicates that microwave frequency is being swept as the independent variable. Note that this sequence can be run either as above or as two separate traces with and without microwaves.

The role of the 705 nm red laser is to "recharge" the divacancy to its neutral charge state in the event that the resonant laser ionizes the divacancy. This mechanism is also in place for the 905/975 nm laser, but the added benefit of 705 nm (besides more efficient recharging) is that its contribution to optical excitation is negligible. This means that any photon counts collected can be attributed to excitation from the resonant laser. This ultimately provides a much higher contrast signal than off-res ODMR, as there is no longer a constant background signal from the off-resonant laser being continuously on. In this way, the many purposes of the single 905/975 nm laser have been separated into two lasers.

Here, the resonant laser is tuned to the (mostly) cycling transition of $|0\rangle \rightarrow |E_x\rangle$ or $|0\rangle \rightarrow |E_y\rangle$. Without microwave mixing between the $|0\rangle$ and $|\pm 1\rangle$ (or $|\pm\rangle$) ground states, this continuous excitation will eventually pump the defect into a nonzero spin state and photoluminescence will stop. When applied microwaves approach a transition frequency, the spin states become mixed and photoluminescence is observed. With this mechanism, the use of a resonant laser ensures that

the counts are always higher on microwave resonance. This means that the defect-dependent contrast signal seen with off-res ODMR is lost, with the benefit of significantly higher contrast levels.

The last type of ODMR frequently used in experiments is the pulsed version of resonant ODMR. Here it is necessary to have a well-calibrated microwave pi pulse (which will be discussed in the next section) in order to run the sequence most efficiently. This can sometimes result in a chicken-or-egg scenario. Calibrating a pi pulse requires the correct MW frequency, which can be obtained through pulsed ODMR, which in turn needs a calibrated pi pulse, leading to circular requirements. This is usually resolved either by using an off-resonant ODMR sequence or simply iterating between pi pulse calibration and pulsed ODMR to dial in the parameters. A schematic of the pulsed resonant ODMR sequence is shown below:

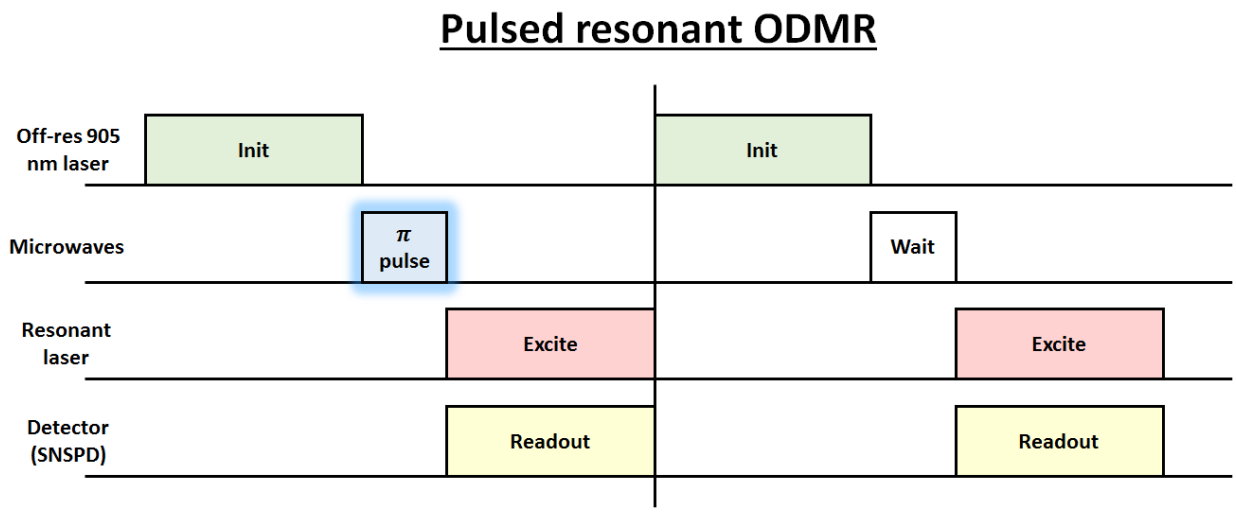

Figure 4.12 | Pulse sequence for pulsed resonant ODMR. The blue highlight on the π pulse indicates that microwave frequency is being swept as the independent variable. This sequence can alternatively be run as a single trace where only the first half of the sequence is repeated, which would provide a 2x speedup for data acquisition at the cost of losing the no-MW comparison signal.

Here, the initialization, rotation, and readout portions of the sequence have now been separated. This means that the SNSPD can be gated to collect photons only during the resonant excitation period, which helps aid with contrast. MW rotation is now no longer competing with a simultaneous initialization pulse, meaning that an initialized $|0\rangle$ state should fully rotate to either $|\pm 1\rangle$ for *c*-axis VV^0's or $|\pm\rangle$ for basal VV^0's. Pulsed resonant ODMR may take longer to collect due to less overall collection time, but it boasts the highest contrast levels of all sequences. When off-resonant initialization is used, the contrast is ~95%. When resonant initialization is used (not shown here) the contrast is ~99% [39,43]. When the $|0\rangle \rightarrow |E_x\rangle$ or $|0\rangle \rightarrow |E_y\rangle$ resonant transition is used, the pi pulse will rotate into a non-cycling spin state and thus result in a loss of counts. This means the contrast sign will be negative, regardless of defect type. Due to the high contrast levels, pulsed ODMR is usually reserved for high-precision measurements or paper-quality data.

4.3.2 Measuring optical transitions – PLE

Photoluminescence excitation (PLE) measurements involve sweeping the frequency of a narrowline excitation laser on an optically active defect. When the defect photoluminesces, the laser is in resonance with an excited state optical transition. Therefore, this measurement can be used to map out the transition frequencies between the ground and excited states. PLE, in combination with ODMR, provides clear evidence of a color center defect and also helps categorize the defect type. In contrast with ODMR, however, PLE is usually only performed with single defects. When an ensemble of defects is present, the excited state's high sensitivity to local strain and electric field results in the overlap of many PLE lines which combine to give a featureless "hump" of signal that does not provide much information [1]. Similar to ODMR, there

are CW and pulsed version of PLE. It can also be run with or without the presence of microwaves, which are used to reveal the optical transitions of the nonzero spin sublevels.

We will review three types of PLE in this section:

- Pulsed PLE (no MW)
- CW PLE
- Pulsed MW PLE

The simplest version of PLE involves no microwave application, although it is still a pulsed measurement so timing electronics are necessary. An outline of this pulse sequence is given below:

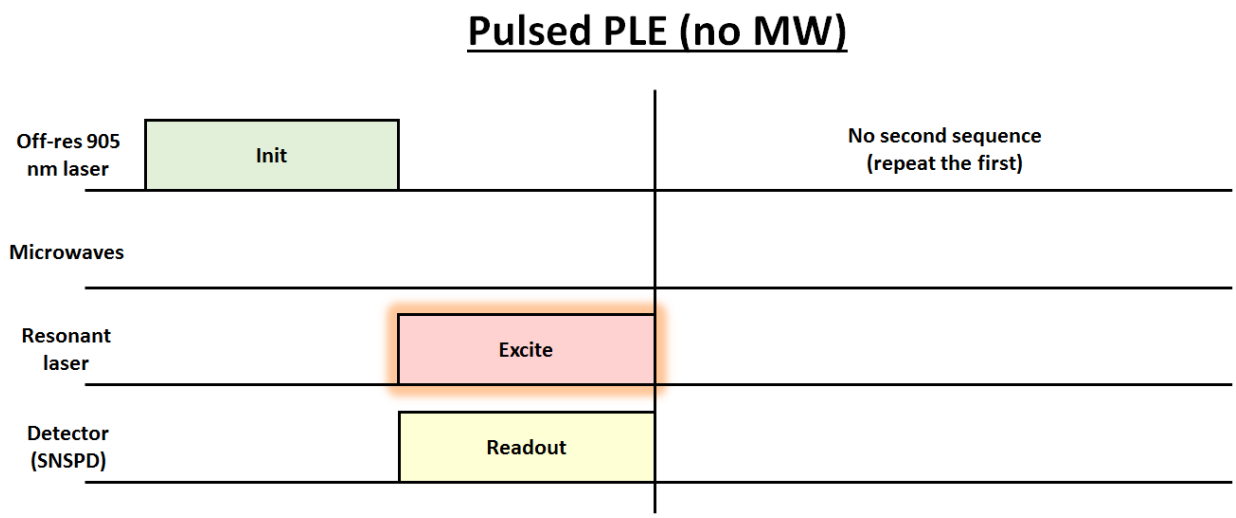

Figure 4.13 | Pulse sequence for pulsed PLE with no microwaves. The sweeping of the resonant laser frequency is denoted by the red highlight surrounding the "excite" pulse.

Here, sweeping the resonant laser frequency will result in counts only when it is on resonance with an optical transition. Since there are six excited states, one may expect there to be six PLE peaks. However, this is not the case for this sequence. Spin initialization polarizes the spin state to

$m_s = 0$, for which there are only two excited state transitions to $|E_x\rangle$ (higher energy) or $|E_y\rangle$ (lower energy). Since these spin zero transitions can vary widely with local strain, this sequence is frequently used as an initial characterization of the excited state transitions.

A continuous version of this sequence is possible, but the off-res 905/975 nm laser must be replaced with a charge init laser of 705 nm light to limit background counts in a similar fashion to CW resonant ODMR. In fact, the pulse sequences for CW PLE and CW resonant ODMR are identical! The key difference is that the laser frequency is being swept for PLE as opposed to microwave frequency for ODMR. The CW PLE pulse sequence is shown below:

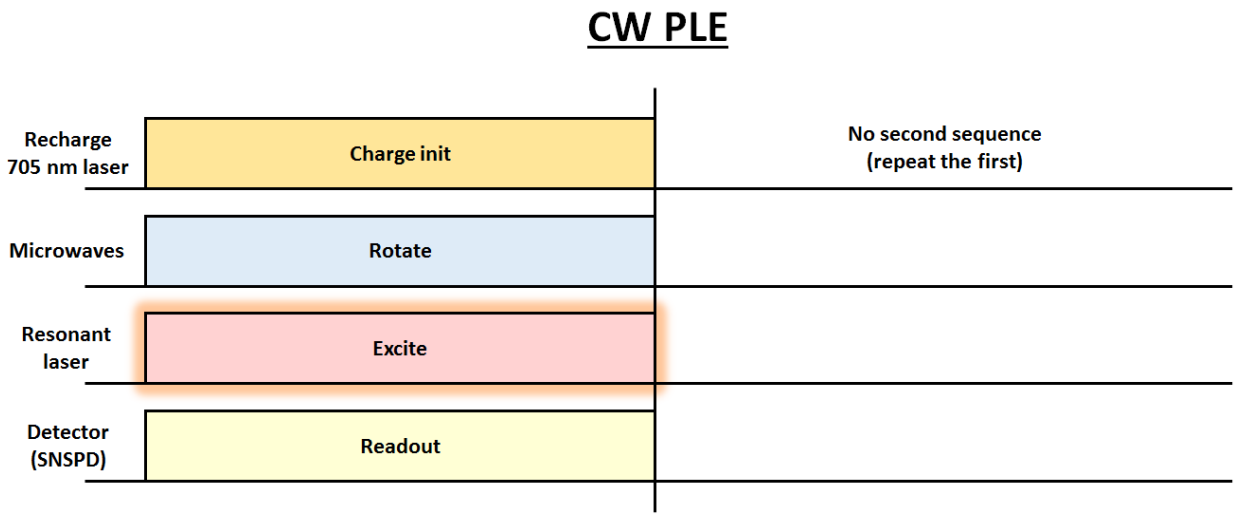

Figure 4.14 | Pulse sequence for CW PLE. The red highlight on the "excite" pulse indicates that optical frequency is being swept as the independent variable. Note that this sequence can be run either as above or as two separate traces with and without microwaves.

Similar to CW resonant ODMR, running this sequence technically does not require timing components such as the AWG, AOM, or MW switches. In practice, however, these components are usually well established before one attempts to do single defect experiments. Since this

sequence does not feature any explicit spin initialization and constantly rotates the spin state, it is possible to detect all six excited state transitions outlined in chapter 2.

Lastly, PLE can be run as a pulsed sequence, as given below:

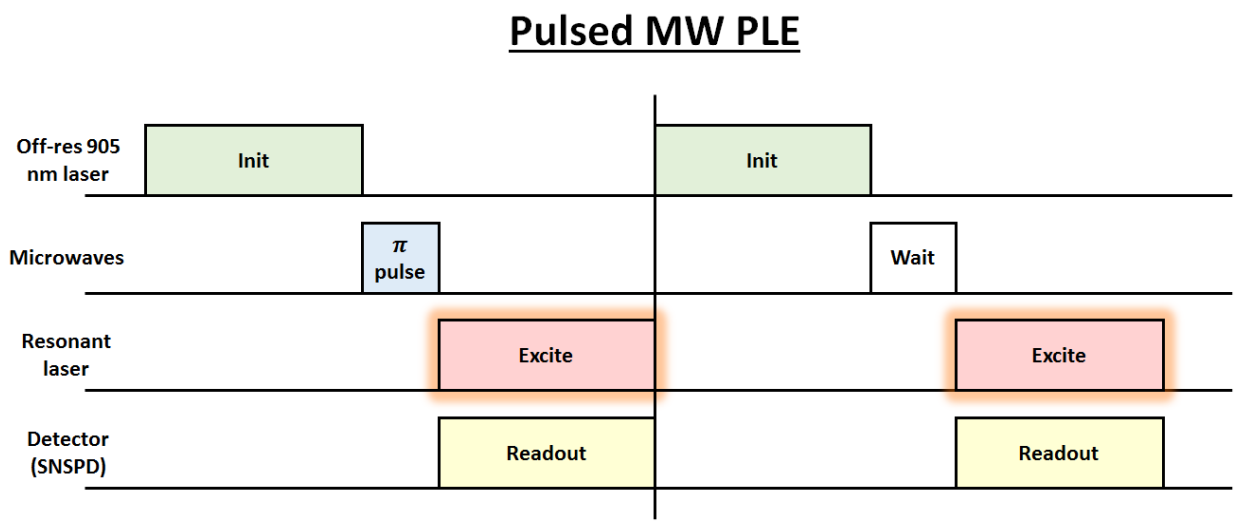

Figure 4.15 | Pulse sequence for microwave-assisted pulsed PLE. The red highlights on the "excite" pulses indicate that optical frequency is being swept as the independent variable. This sequence can alternatively be run as a single trace where only the first half of the sequence is repeated, which would provide a 2x speedup for data acquisition at the cost of losing the no-MW comparison signal.

Here, the spin initialization and subsequent pi pulse combines to initialize the spin into either $|\pm 1\rangle$ for a *c*-axis VV^0 or $|\pm\rangle$ for a basal VV^0. In this way, the first trace directly compares signal from nonzero spin states to signal in the second trace from spin zero states [3]. Since the $\{|A_1\rangle, |A_2\rangle, |E_1\rangle, |E_2\rangle\}$ states are not cycling and thus do not emit many photons, their PLE peaks will be comparatively very weak. In practice this sequence is sometimes forgone in favor of CW PLE due to these low counts, but it is still frequently used when there is not access to a gated 705 nm laser.

4.3.3 Pi pulse calibration

Lastly, pulse sequences can be designed to calibrate certain elements of an experiment to be used as parts of other sequences. The most common calibration is that of a pi pulse between spin states, which for the VV^0 usually means $|0\rangle \leftrightarrow |\pm 1\rangle$ or $|0\rangle \leftrightarrow |\pm\rangle$. We will review the two main types of pi pulse calibration in this section:

- Power pi pulse calibration
- Time pi pulse calibration

The sequence for power pi pulse calibration is shown below:

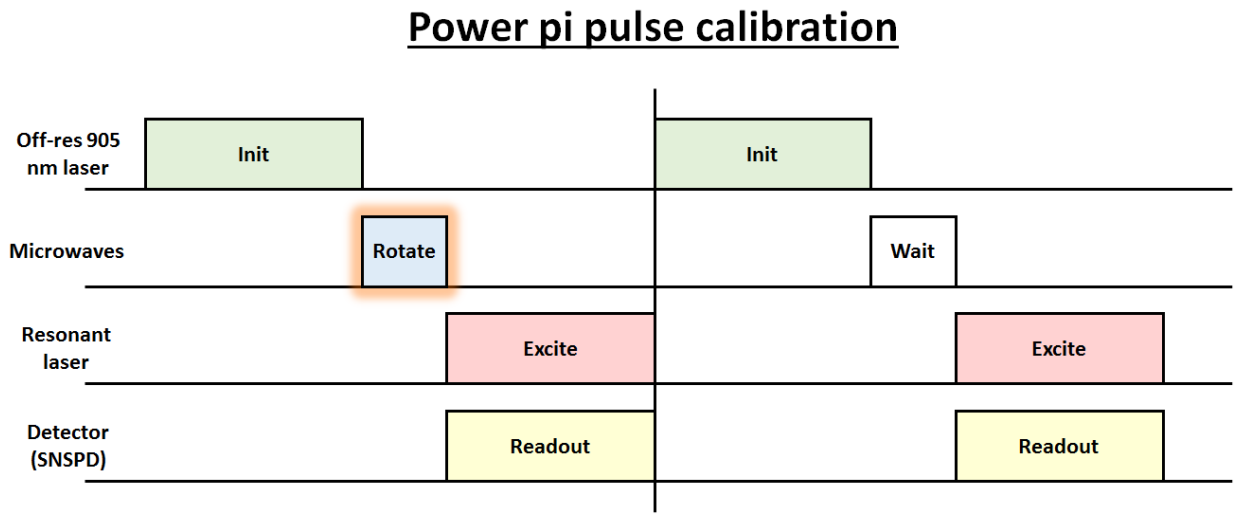

Figure 4.16 | Pulse sequence used for calibrating a power pi pulse. The variation of power is represented by the red highlight on the microwave "rotate" pulse. This sequence can alternatively be run as a single trace where only the first half of the sequence is repeated, which would provide a 2x speedup for data acquisition at the cost of losing the no-MW comparison signal.

Here, a "power pi pulse" refers to a spin rotation where the duration of the microwave pulse is kept constant but the power the microwaves are increased until a full pi rotation is achieved. This can be convenient as the total length of the pulse sequence can be kept fixed, which makes the AWG sequence simpler to design. The resonant laser is set to a cycling transition at either $|0\rangle \rightarrow |E_x\rangle$ or $|0\rangle \rightarrow |E_y\rangle$. Note that this sequence is nearly identical to pulsed resonant ODMR, with the key difference of sweeping microwave power instead of microwave frequency. The calibration of the pi pulse is achieved by selecting the power that results in maximum photoluminescence contrast, which is negative in sign here.

Conversely, the sequence for time pi pulse calibration is shown below:

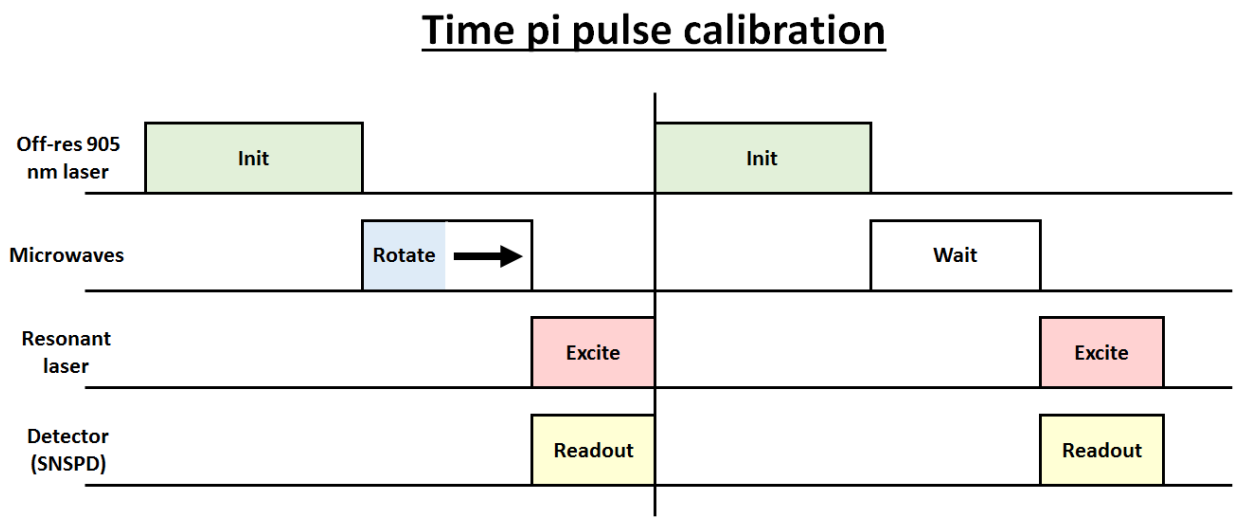

Figure 4.17 | Pulse sequence used for calibrating a time pi pulse. The varying time duration of the microwave rotation is represented by the black arrow. This sequence can alternatively be run as a single trace where only the first half of the sequence is repeated, which would provide a 2x speedup for data acquisition at the cost of losing the no-MW comparison signal.

In a time-based pi pulse, the microwave pulse is kept at a fixed power and varied in duration. This time-based measurement is the more "traditional" form that is used to demonstrate, for

example, Rabi oscillations. It is otherwise identical to the power pi pulse calibration, so both forms are used interchangeably.

4.4 Optical linewidths and spectral diffusion

When collecting PLE scans, the full-width half-maximum of each excitation peak is an indication of the divacancy's local environment. In an ideal case, these optical linewidths are sufficiently narrow to individually address the spin sublevel transitions. In many cases, however, broadened linewidths cause the transition frequencies to overlap and excitation selectivity is lost. The other consequence is that the generation of indistinguishable ZPL photons for remote spin-spin entanglement becomes greatly limited. [40]

The main culprit for broadening is a fluctuating charge environment that causes Stark shifting of the excited state energies. We refer to this effect as "spectral diffusion". Since the excited state is much more strongly affected by electric field than the ground state [25], local charge fluctuations result in changes in transition energies. As these stochastic changes are averaged over many experiments, the excitation frequency will appear to have a broad range, even if it remains narrow for any one particular experiment. The fluctuating charges are in turn caused by optical excitation, which allows for charge traps in the silicon carbide to become photoionized and collectively "scramble" to a new configuration and this a new electric field at the defect. The time scale of this effect is not well characterized, but it becomes faster (and thus broader) under higher laser powers and is present under a wide range of off-resonant wavelengths from ~300-1000 nm.

The measured PLE linewidth has a broad range of values depending on the SiC sample and divacancy preparation procedure. The narrowest possible linewidth is set by the lifetime of the divacancy of $\tau \approx 15\ ns$, which corresponds to $f_{FWHM} = \frac{1}{2\pi\tau} \approx 10\ MHz$. In practice the linewidth is usually in the range of ~100's of MHz for intrinsically doped SiC with divacancies >1 micron below the surface. Generally speaking, divacancies created with electron irradiation give narrower linewidths than those created with ion implantation, which we attribute to the lessened crystal damage (and thus formation of charge traps) from electron irradiation. When ion implantation is used, the linewidths are usually broadened by another 200-300 MHz. As long as the linewidth remains below ~1 GHz then the optical transitions are usually resolved.

Naturally, we wish to limit the effects of spectral diffusion as much as possible. One recent approach to this problem is to incorporate doping in the SiC in order to create a built-in electric field and stabilize the charge traps. This approach has shown impressive results for PIN doped diodes, which are capable of reaching lifetime-limited linewidths [43]. Using the same idea of static electric fields, it is also possible to apply voltages directly to pads on top of an intrinsically doped SiC chip, which also evacuates charge traps and gives linewidths close to the lifetime limit [31].

To gain some context on the effects of doping, the optical linewidths as a function of doping configurations is given in figures 4.18 and 4.19. In all configurations listed, it is important to note that neutral divacancies only exist in intrinsically doped material. In this way, the doping layers confine where divacancies can exist in the z-direction.

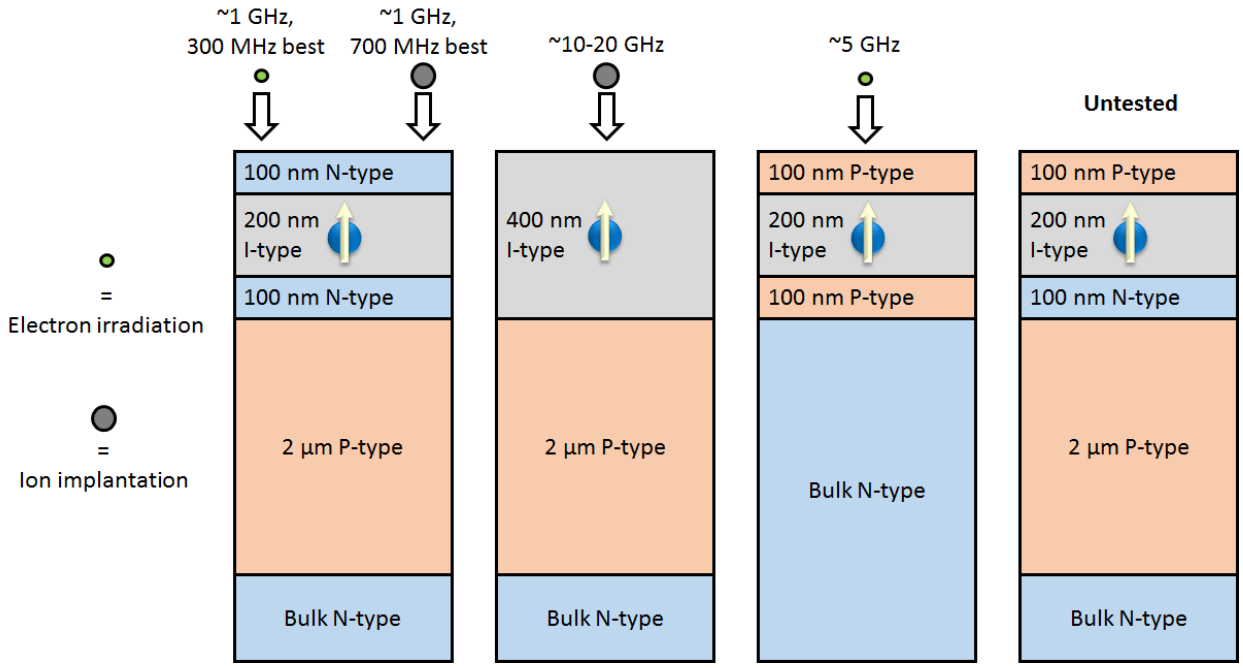

Figure 4.18 | Optical linewidths for thin doping heterostructures. SiC of different doping configurations are either electron irradiated or ^{12}C ion implanted in order to create divacancies. For all configurations the N-type doping is achieved with 1e18 cm^{-3} nitrogen dopants, the P-type doping is achieved with 1e18 cm^{-3} aluminum dopants, and the intrinsic I-type regions have <1e15 cm^{-3} residual dopants. The frequencies indicate measured optical PLE linewidths.

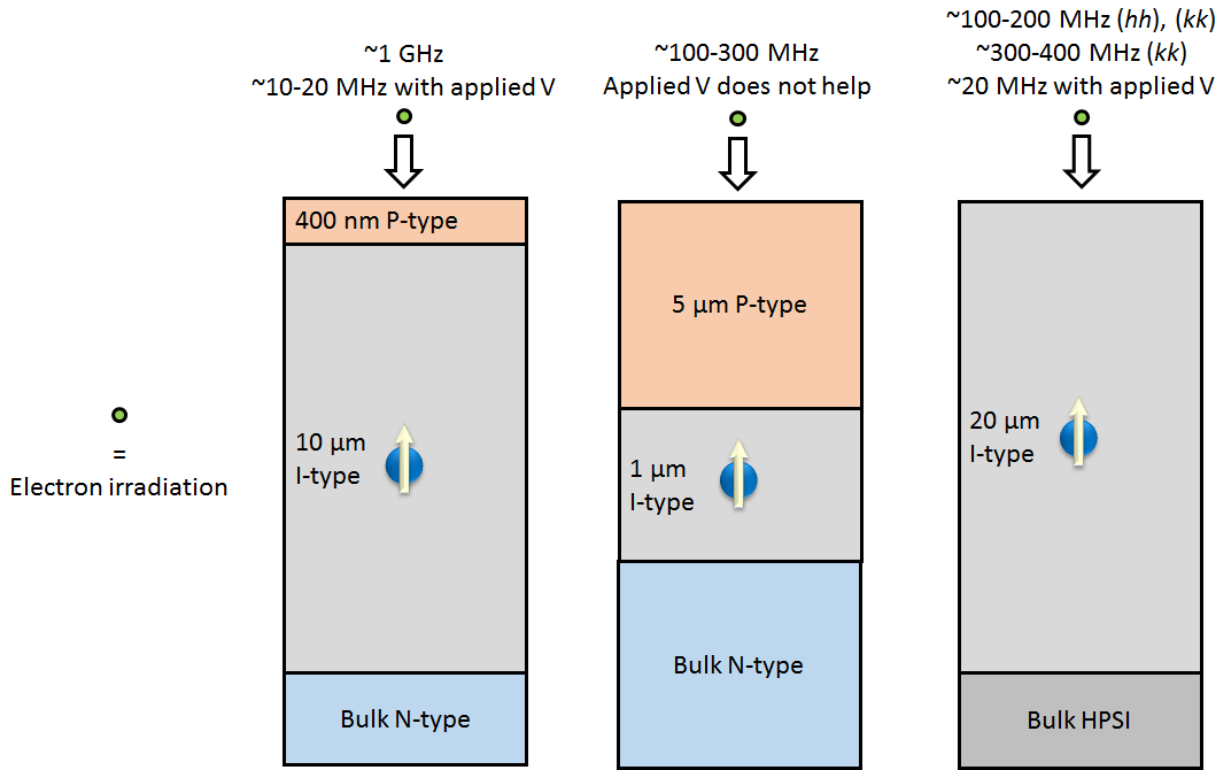

Figure 4.19 | Optical linewidths for thick doping heterostructures. SiC of different doping configurations are either electron irradiated or ^{12}C ion implanted in order to create divacancies. For all configurations the N-type doping is achieved with 1e18 cm^{-3} nitrogen dopants, the P-type doping is achieved with 1e18 cm^{-3} aluminum dopants, and the intrinsic I-type regions have <1e15 cm^{-3} residual dopants. The frequencies indicate measured optical PLE linewidths.

The overall trend is that the near surface divacancies in figure 4.18 have broader linewidths than those that are situated deeper in the lattice. Additionally, the proximity to P-doped regions may have a detrimental effect, as the PIP heterostructure has a significantly wider linewidth of ~5 GHz than the equivalent NIN heterostructure. At the same time, the absence of any doping for a thin 400 nm intrinsically doped layer has the worst linewidths of all configurations. It is difficult to say whether surface proximity or P-type proximity plays a bigger role here, but the addition of thin 100 nm layers of N-type doping appears to provide some degree of screening of field fluctuations at the defect. Unfortunately, the sub-micron PIN heterostructure has yet to be tested. Given the detrimental effect of nearby surfaces, the formation of nanostructures can pose an obstacle for maintaining thin linewidths. This issue is discussed more in chapter 7.

For thicker doping structures, divacancies that are located >1 micron away from any surface have the benefit of generally thinner linewidths. A PIN configuration in conjunction with this seclusion provides a built in electric field that further narrows linewidths, as showcased in the work in [43]. Interestingly, for the geometry of 5 μm P-type and 1 μm I-type, additional applied electric fields do not provide any further narrowing. This is in contrast to the other two heterostructures, where external applied fields can bring the optical linewidth close to the lifetime limit of ~10 MHz. Evidently, the submicron proximity to doped regions results in a broadening effect that cannot be overcome with applied fields alone.

4.5 Curve fitting with python

Fitting curves to collected data can almost universally by done using the built in scipy.optimize curve fit function. This function uses least squares regression to fit a user defined function to given data points, where the parameters of the fit function are varied to minimize the sum of the squared residuals.

The SciPy curve fit function outputs two main results labeled as "popt" and "pcov". The popt output is a 1D list containing the optimal values for the parameters in the fit function. The pcov output is a covariance matrix for the fit values in popt. The square root of each diagonal entry in pcov gives the one standard deviation error of the corresponding fit value in popt.

Additionally, the optional "sigma" parameter is typically a 1D list containing the standard deviations of error in each y data point. Then, if the optional "absolute_sigma" Boolean parameter is set to true, then these sigma values are taken at face value and will affect the covariance output. Otherwise, a false value for this parameter means that only relative values in sigma will be considered, with an overall scaling constant applied to all sigma values such that the reduced chi square value is equal to one.

It is worth briefly discussing where the error bars come from for individual data points in actual experiments. If we perform n experiments of a measured quantity x, then the average value and variance of this quantity will be given by:

$$\bar{x} = \frac{1}{n}\sum_{i=i}^{n} x_i\,, \qquad s^2 = \frac{1}{n-1}\sum_{i=i}^{n}(x_i - \bar{x})^2 \tag{4.3}$$

Where the use of $n-1$ for the sample variance s^2 instead of n is known as Bessel's correction. Thus, the error bars in our experiments are entirely determined by the number of experiments that

are averaged over. Ideally then, the number of experiments is extremely large to minimize error, but this can take prohibitively long for lengthy pulse sequences (e.g., the long waiting times in a T_1 measurement).

Here is a simple application of the SciPy fit function using a linear fit to example points. Here the data points don't have any physical meaning, and are just used for demonstration purposes.

```
from scipy.optimize import curve_fit


def fit_fxn(t, a, b):
    f = a*t+b
    return f


p0_guess = [1, 0] # initial guess of parameters
x_data = np.array([1, 2, 3, 4, 5])
y_data = np.array([0.5, 3, 6.5, 7, 9])


popt, pcov = curve_fit(fit_fxn, x_data, y_data, p0=p0_guess)
y_fit = fit_fxn(x_data, *popt)


print(popt) # best fit [a, b] values
print(np.sqrt(np.diag(pcov))) # gives 1 standard deviation errors
of [a, b] values
```

```
plt.plot(x_data, y_data, color='blue', linewidth=1.0,
label='data')
plt.plot(x_data, y_fit, color='red', linewidth=1.0, label='fit')
plt.legend()
plt.show()
```

This gives the following result:

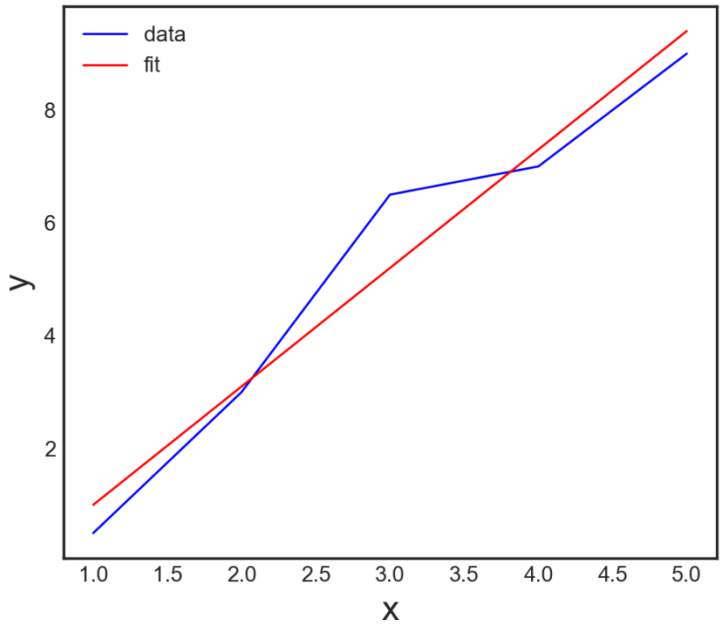

Figure 4.20 | Example result of SciPy fit function using a linear fit. A simple linear fit (red) to pseudo-linear data points (blue) are fit with using the SciPy curve_fit function using least squares regression. More complicated fits can be carried out with user-defined fit functions such as sinusoids, exponentials, or logarithms.

The choice of which fit function to use for the data depends on the type of experiment being run.

Some common fit functions are given below with some example applications.

Lorentzian function

Used for optical spectrum for narrow PLE, narrow ODMR peaks, and quality factor peaks

The Lorentzian function is a single peaked function given by:

$$f(x) = A\left(\frac{\gamma^2}{(x - x_0)^2 + \gamma^2}\right) + y_0, \qquad 2\gamma = \text{FWHM} \tag{4.4}$$

Where A is the height of the peak, γ is a parameter related to the width of the peak, and x_0, y_0 gives the center of the peak. The y offset may be due to a noise floor, for example.

Gaussian function

Used for optical spectrum for broad PLE and broad ODMR peaks

The Gaussian curve or normal curve is given by:

$$f(x) = A \cdot \exp\left(-\frac{(x - x_0)^2}{2\gamma^2}\right) + y_0, \qquad 2\sqrt{2\ln 2}\,\gamma = \text{FWHM} \tag{4.5}$$

where

$$A = \text{peak height}, \qquad x_0 = \text{peak center}, \qquad \gamma \propto \text{width} \tag{4.6}$$

Generally speaking, the Gaussian function can be used for any variable that displays a normally distributed noise. In situations where the central limit theorem applies this function can also be used as a fit.

Exponential decay

Used for excited state lifetime, T_1 decay

$$f(x) = A \cdot \exp\left(-\frac{(x - x_0)}{\tau}\right) + y_0 \tag{4.7}$$

A "stretched" exponential adds a power to the exponential argument and takes the form:

$$f = A \cdot \exp\left(-\left(\frac{(x - x_0)}{\gamma}\right)^b\right) + y_0 \tag{4.8}$$

This appears in, for example, a T_2 CPMG decay.

Sine decay

Used for T_2^* decay, decay of Rabi oscillations

$$f = -A \cdot \left(\exp\left(-\left(\frac{x}{\tau}\right)^n\right)\right) \cdot \cos(\omega x + \phi) + y_0 \tag{4.9}$$

Sine squared decay

Used for T_2 decay

$$f = -A \cdot \left(\exp\left(-\left(\frac{x}{\tau}\right)^n\right)\right) \cdot \cos^2(\omega x + \phi) + y_0 \tag{4.10}$$

Chapter 5

Cavity Quantum Electrodynamics

Quantum electrodynamics (QED) is the study of interactions between quantized electromagnetic fields and quantized matter such as single atoms. When the atom is placed inside of a resonant cavity, the study of the threefold interaction between the atom, field, and cavity is referred to as cavity quantum electrodynamics (CQED). The main takeaway is that there can be nontrivial interactions between these systems that fundamentally alter the behavior of each system individually. [47,48] In some cases, one can no longer think of the systems as being completely separate and the quantum states of the atom and cavity field fuse together to form polariton states. Such interactions are typically reserved for the "strong" coupling regime, whereas different behavior is observed with weaker coupling. Quantifying and analyzing this behavior is the main purpose of CQED.

In this chapter we will outline some of the fundamental variables and results from CQED, which we can then apply to the VV^0-cavity system in chapter 7. The discussion in this chapter will therefore be general and not focus on any particular real-life implementation. Nevertheless, the results can be very powerful in understanding how these systems behave in various coupling regimes.

5.1 Cavity QED parameters

In the broadest setting, CQED entails a single "atom" or emitter of radiation inside of a cavity with a resonant frequency. An electromagnetic field is added to the cavity and becomes confined while interacting with the atom. Here, the "atom" can be any optical emitter (such as a color center, a quantum dot, or a literal trapped atom) with a two-level system and the electromagnetic field and cavity can be at any frequency. The most common frequencies are either optical/near-infrared or microwave. This frequency can also dictate the size of the cavity involved, with higher frequencies corresponding to smaller structures. However, perhaps the simplest cavity design is the Fabry-Perot, which uses two inward facing mirrors to confine light. A general schematic of a cavity system is shown in figure 5.1, following the structure of a Fabry-Perot.

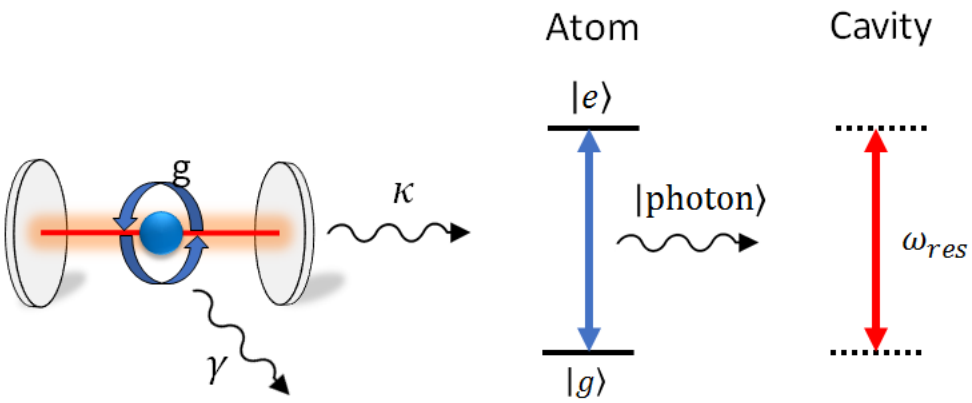

Figure 5.1 | Basic schematic for cavity QED. Here g represents the coupling between the atom and the cavity, γ is the spontaneous emission rate of the atom, and κ is the leakage rate of photons out of the cavity. The atom has a ground state $|g\rangle$ and an excited state $|e\rangle$, and the cavity has a resonant frequency of ω_{res} which may or may not be matched with the atomic transition energy.

Here the important parameters of interest $g.\gamma,\kappa$ are included in the figure. These are the main parameters used in CQED analysis, although there are several others that are arguably just as important. Well review these parameters individually in the upcoming sections.

5.1.1 Mode volume V

The mode volume of a cavity roughly represents the space that the fundamental optical mode occupies. It appears frequently as a variable in other quantities like the atom-cavity coupling constant g and the Purcell factor F. The general definition of mode volume is given by:

$$V_{mode} = \frac{\iiint \epsilon(\vec{r})\left|\vec{E}(\vec{r})\right|^2 d^3\vec{r}}{\max(\epsilon(\vec{r})E(\vec{r})^2)} \tag{5.1}$$

Where $\epsilon(\vec{r})$ is the permitivity of the material as a function of position $(\vec{r})$, $E(\vec{r})$ is electric field as a function of position $(\vec{r})$, and $\max(\epsilon(\vec{r})E(\vec{r})^2)$ is the maximum value of $\epsilon(\vec{r})E(\vec{r})^2$ in the cavity mode.

As a comparison, it is useful to recall the total energy stored in an electromagnetic field as:

$$U_{EM} = \frac{1}{2}\int_V \left(\epsilon|\mathbf{E}|^2 + \frac{1}{\mu}|\mathbf{B}|^2\right) dV \tag{5.2}$$

Taking the maximum electric field amplitude, this is equivalent to:

$$U_{EM} = \frac{1}{2}\int_V \max(\epsilon|\mathbf{E}|^2)\, dV \tag{5.3}$$

With this in mind, we can rephrase the mode volume somewhat more broadly as:

$$V_{mode} = \frac{\text{total energy}}{\text{maximum energy density}} = \frac{U_E}{\max(\rho_U)} \tag{5.4}$$

So whatever the mode volume is, we should be able to multiply it by the maximum energy density to obtain the total energy contained in the cavity mode.

For nanophotonic structures, mode volume is typically expressed as a multiplicative factor of a cubic wavelength in the cavity material:

$$V_{mode} = x_{vol} \cdot \left(\frac{\lambda_{cav}}{n}\right)^3 \tag{5.5}$$

where x_{vol} is a unitless multiplicative factor, λ_{cav} is the wavelength of the resonant cavity mode, and n is the index of refraction of the material. For typical nanophotonic crystal cavities in silicon carbide and diamond, mode volumes on the order of $V_{mode} \approx 0.5 \left(\frac{\lambda_{cav}}{n}\right)^3$ are achievable [49-60].

5.1.2 Spontaneous emission rate γ

The spontaneous emission rate γ denotes the rate of optical emission from the excited state to the ground state of a two-level system. This system can be an atom, a color center, or any other optical emitter. Typically spontaneous emission is only observed in the optical regime, as two-level systems in the microwave regime are much more stable in the excited state. The spontaneous emission rate can be written as:

$$\gamma = \frac{\mu^2 \omega^3}{6\pi\epsilon\hbar c^3} \tag{5.6}$$

Where μ is the electric dipole moment of the transition, ω is the frequency of the transition, and ϵ is the permittivity of the material the emitter is in. This γ appears in the exponential decay of the excited state population:

$$C_e(t) = e^{-\gamma t} \tag{5.7}$$

Sometimes γ is referred to as the Einstein A coefficient. Lastly, we can relate the spontaneous emission rate to the excited state lifetime by simply taking a reciprocal:

$$\tau = \frac{1}{\gamma} = \text{lifetime} \tag{5.8}$$

Experimentally, a higher emission rate (or shorter lifetime) results in a higher count rate, which generally speeds up readout, averaging of experiments, and entanglement protocols. This means that usually a higher emission rate is preferred. When taking an excitation/emission spectrum of an emitter, a higher emission rate will also correspond to a broader optical linewidth.

5.1.3 The electric dipole moment μ

The electric dipole moment μ dictates transitions between the ground and excited states of a two-level system. It is closely related to the spontaneous emission rate γ, as it is used in the formula to calculate γ. Sometimes μ is phrased as a "matrix element", or frankly, any other jambalaya of the words "transition electric dipole moment matrix element operator". To partially see why this is the case, we can examine the driven electric field Hamiltonian from the two-level system Hamiltonian from chapter one:

$$H_{field} = -\begin{pmatrix} 0 & d_{eg}E_0 \cos \omega t \\ d_{eg}E_0 \cos \omega t & 0 \end{pmatrix} = -\begin{pmatrix} 0 & 2\hbar\Omega \cos \omega t \\ 2\hbar\Omega \cos \omega t & 0 \end{pmatrix} \tag{5.9}$$

Here, the elements $d_{eg}E_0 = 2\hbar\Omega$ determine the magnitude of the off-diagonal drive and thus the rate of Rabi oscillations with Rabi frequency Ω. In this case, the dipole moment d_{eg} is exactly the same as μ.

$$\mu = d_{eg} \tag{5.10}$$

So, due to μ's placement in an off-diagonal *matrix element* and its direct tie to *transitions* between two states, these words appear frequently in alternative names for μ. Of course, for systems that are coupled with magnetic fields, it is possible to have an equivalent *magnetic* dipole matrix element. This appears when dealing with $m_s = 0 \leftrightarrow \pm 1$ transitions in the VV^0 ground state, for example. Additionally, any proper dipole moment is in fact a vector, so a slightly more precise statement for μ would be:

$$|\vec{\mu}| = \left(\vec{d} \cdot \vec{\varepsilon}_{\mathbf{k}}\right) \tag{5.11}$$

Where $\vec{\varepsilon}_{\mathbf{k}}$ is a unit vector pointing in the direction of the *k*-vector of the photon or field mode in the cavity. If one measures the Rabi frequency Ω of driven transitions and has the magnitude of electric field, E_0, the earlier relation can be used to define μ:

$$\mu = \frac{2\hbar\Omega}{E_0} \tag{5.12}$$

Perhaps more common (and accessible) definition, however, is to instead use the spontaneous emission formula

$$\gamma = \frac{\mu^2 \omega^3}{6\pi\epsilon\hbar c^3} \tag{5.13}$$

To define μ as:

$$\mu = \sqrt{\frac{6\pi\epsilon\hbar c^3}{\omega^3}\gamma} \tag{5.14}$$

Since γ can be measured directly through a lifetime measurement, μ can be inferred through the observed value of γ. Finally, dimensional analysis on this equation reveals that μ is indeed an electric dipole moment, with units of Coulomb meters.

$$[\mu] = \left[\sqrt{\frac{6\pi\epsilon\hbar c^3}{\omega^3}\gamma}\right] = \left[\sqrt{\epsilon\hbar\lambda^3\gamma}\right] = \sqrt{\frac{C}{V \cdot m} \cdot J \cdot s \cdot m^3 \cdot \frac{1}{s}} = \sqrt{\frac{C^2}{m} \cdot m^3} = C \cdot m \tag{5.15}$$

5.1.4 Quality factor Q, leakage rate κ, and finesse $\mathcal{F}$

The effectiveness of a cavity at confining light can be quantified in several ways. For the purposes of this thesis, we will mostly focus on the **quality factor** (Q) which increases as light becomes more effectively confined. In the limit of a perfect cavity where light never escapes, the quality factor is infinite. In practice this never occurs, as there will always be scattering or evanescent out-coupling losses as light cycles inside the cavity mode. For nanocavities in the optical/near-infrared regime, a quality factor of ~100-1,000 is usually considered "low", Q~1,000-10,000 is "moderate" and Q~10,000+ is "high". Of course this interpretation is highly subjective and depends on the context of the experiment. For example, even a Q of 1,000 can significantly modify an emitter if other quantities like mode volume and spatial/spectral matching are optimized. Therefore it is

important not to become overly fixated on the quality factor alone. Nevertheless, it is worth noting that the upper limits of optical/NIR Q are on the order of 10^6-10^7 for silicon-based optical nanocavities, providing a high ceiling for these devices. There are several quantitative definitions of the quality factor, which we will discuss below.

Energy loss interpretation of Q:

A common definition for Q is the ratio of the energy stored in the oscillating resonator to the energy dissipated per cycle by damping processes:

$$Q \equiv 2\pi \cdot \frac{\text{Energy stored}}{\text{Energy dissipated per field cycle}} \tag{5.16}$$

Where a field cycle refers to one cycle of the electromagnetic field in the cavity, not the cycle of a photon completing a round trip in the cavity. If the energy is represented as a function of time, such that $U = U_0 \exp\left(-\left(\frac{\omega_{res}}{Q}\right)t\right)$, then the rate of decay $\left(\frac{\omega_{res}}{Q}\right)$ defines the quality factor as the number of field oscillations to reach an energy of $e^{-2\pi} \approx 0.00187$ of the initial energy. Alternatively, the quantity $\left(\frac{Q}{\omega_{res}}\right)$ is the cavity lifetime, or the time taken for the energy to decay to 1/e of its starting value. The drawback to these definitions is that it is difficult to directly measure the energy lost in the cavity, prompting us to use another definition.

Bandwidth interpretation of Q:

When taking transmission or excitation spectra of a cavity as the excitation frequency is varied, the resulting peak (or dip) can be used to define the quality factor as follows:

$$Q = \frac{f_{res}}{\Delta f} = \frac{\omega_{res}}{\Delta \omega} \tag{5.17}$$

where f_{res}, ω_{res} is the resonant frequency of the cavity and $\Delta f, \Delta \omega$ is the full-width half-maximum (FWHM) of the spectrum peak. This relation is also approximately true for wavelength, as shown below:

$$Q = \frac{f_{res}}{\Delta f} = \frac{f_{res}}{f_1 - f_2} = \frac{\frac{c}{\lambda_{res}}}{\left(\frac{c}{\lambda_1} - \frac{c}{\lambda_2}\right)} = \frac{1}{\lambda_{res}}\left(\frac{\lambda_1 \lambda_2}{\lambda_2 - \lambda_1}\right) = \frac{1}{\lambda_{res}}\left(\frac{\lambda_1 \lambda_2}{\Delta \lambda}\right) \tag{5.18}$$

Where f_1, f_2, represent the two frequencies at the FWHM and λ_1, λ_2 the two wavelengths at the FWHM. In situations where $\lambda_{res} \gg \Delta\lambda$ (i.e. $Q \gtrsim 100$), then this simplifies to:

$$Q \approx \frac{\lambda_{res}}{\Delta \lambda} \tag{5.19}$$

This bandwidth definition of Q is what is usually used in practice to measure quality factors.

Leakage rate κ:

The decay rate mentioned earlier is more commonly represented by the letter κ, as featured in figure 5.1.

$$\kappa \equiv \frac{\omega_{res}}{Q} \tag{5.20}$$

So the decay of the cavity can be written as:

$$U = U_0 \exp(-\kappa t) \tag{5.21}$$

Finesse $\mathcal{F}$:

If we wish to phrase energy loss in terms of photon round trips instead of field cycles, then we would use the finesse instead. In this context, the finesse is defined as the number of photon round trips (around a microring cavity, for example) for the energy to decay to 1/e of its initial value. Alternatively, it is the number of trips before the probability of leakage becomes 1/e. In the case of transmission/reflection peaks that are periodically spaced in frequency, then the finesse can also be defined in terms of the free spectral range:

$$\mathcal{F} = \frac{\Delta\lambda_{FSR}}{\Delta\lambda_{fwhm}} = \frac{\Delta\omega_{FSR}}{\Delta\omega_{fwhm}} \tag{5.22}$$

Where the free spectral range $\Delta\lambda_{FSR}, \Delta\omega_{FSR}$ is the separation between consecutive peaks, and the full-width half-max $\Delta\lambda_{fwhm}, \Delta\omega_{fwhm}$ is the FWHM of an individual peak. This definition is more common for Fabry-Perot resonators and perhaps microring resonators, but photonic crystal cavities usually feature only one spectrum peak so the free spectral range does not apply.

5.1.5 Electric field in cavity mode E

The electric field E of a single photon in the mode volume V of the resonator. This parameter is important as it is involved in the calculation of the atom-cavity coupling constant g. Generally speaking, we wish to maximize the electric field of the cavity mode in order to maximize the strength of light-matter interactions.

Generally, the total energy of an electromagnetic field in a volume V is given by:

$$U_{EM} = \frac{1}{2}\epsilon \int_V \left(\left|\vec{E}\right|^2 + \frac{1}{2\mu}\left|\vec{B}\right|^2 \right) dV \tag{5.23}$$

where ϵ is the permittivity of the medium in which the field exists and μ is its magnetic permeability. In the simplistic model of a photon in a box, we can say:

$$\frac{1}{2}\epsilon E_{max}^2 V = \hbar\omega_{cav} \tag{5.24}$$

Where $\hbar\omega_{cav}$ is the energy of the single photon in the cavity. We're usually interested in $\omega_{cav} = \omega_{res}$, but this does not necessarily have to be the case. This equation can be rearranged to potentially give the electric field as:

$$E = \sqrt{\frac{2\hbar\omega_{cav}}{\epsilon V}}, \qquad \text{classical result} \tag{5.25}$$

However, this classical expression is incorrect by a factor of 2. In the proper quantization of electromagnetic field, the correct result is:

$$E = \sqrt{\frac{\hbar\omega_{cav}}{2\epsilon V}}, \qquad \text{quantized field} \tag{5.26}$$

We will use this second expression going forward.

5.1.6 Coupling parameter g

The parameter g represents the strength of the interaction between the atom and the cavity. It is referred to as the atom-cavity coupling constant or simply the coupling constant g. This constant appears in the interaction part of the Jaynes-Cummings Hamiltonian, which will be discussed in section 5.2. Ultimately, g is a key parameter to describe atom-cavity-photon dynamics, and it also represents the vacuum Rabi frequency in the strong coupling regime, which will be shown in section 5.3. The coupling constant g is given by the equation:

$$g = \frac{\mu E}{\hbar} \tag{5.27}$$

Where μ is the electric dipole moment, E is the electric field of the cavity mode, and $\hbar$ is Planck's constant. Individually, a large E means that there is a strong interaction between the optical field and the cavity mode and a large μ means the ground and excited states of the atom are strongly coupled by optical fields. It then follows that large values for both of these variables would lead to strong interactions between the atom and the cavity, which is what g represents.

Note that if we square this equation:

$$g^2 = \frac{\mu^2 E^2}{\hbar^2} \tag{5.28}$$

We can rewrite this using the earlier expressions:

$$\gamma = \frac{\mu^2 \omega^3}{6\pi\epsilon\hbar c^3}, \qquad E = \sqrt{\frac{\hbar\omega_{cav}}{2\epsilon V}} \tag{5.29}$$

Rearranging gives:

$$\mu^2 = \frac{6\pi\epsilon\hbar c^3}{\omega^3}\gamma, \qquad E^2 = \frac{\hbar\omega_{cav}}{2\epsilon V} \tag{5.30}$$

Then, if we assume the cavity and transition frequencies are the same ($\omega_{cav} = \omega$), then substituting these into the expression for g^2 gives:

$$g^2 = \frac{1}{\hbar^2}\left(\frac{6\pi\epsilon\hbar c^3}{\omega^3}\gamma\right)\left(\frac{\hbar\omega_{cav}}{2\epsilon V}\right) \tag{5.31}$$

$$g^2 = \frac{3\pi c^3\gamma}{\omega^2 V} \tag{5.32}$$

This is an alternative way of expressing g in terms of the decay rate γ, the mode volume of the cavity V, and the resonant frequency of the cavity ω. Lastly, sometimes only the substitution for E is done in equation 5.28, which gives the relation:

$$g = \sqrt{\frac{\omega_{cav}}{2\hbar\epsilon V}}\mu = \sqrt{\frac{\omega_{\mathbf{k}}}{2\hbar\epsilon V}}(\vec{\mu}\cdot\vec{\varepsilon}_{\mathbf{k}}) \tag{5.33}$$

Where **k** represents the wavevector of the photon in the cavity.

5.1.7 Purcell factor F and cooperativity C

The Purcell factor F (sometimes P in literature) represents the increase in the radiative rate of an optical emitter when it is placed in a cavity. This can be represented as a ratio of radiative rates:

$$F \equiv \frac{\gamma_{cavity}}{\gamma_{bulk}} \tag{5.34}$$

Where γ_{cavity} is the spontaneous emission rate in the cavity and γ_{bulk} is the spontaneous emission rate in the bulk material. The Purcell factor can equivalently be represented as a ratio of lifetimes:

$$F = \frac{\tau_{bulk}}{\tau_{cavity}} \tag{5.35}$$

Where $\tau_{bulk}, \tau_{cavity}$ represents the optical lifetime in the bulk or cavity. A Purcell factor for a cavity matched with an emitter will be greater than 1, which means a higher radiative rate and a reduced lifetime. However, it is possible to have a mismatched cavity that has the effect of suppressing emission and reducing the radiative rate. For the purposes of this thesis we will focus on the former case with enhanced emission. In more detail, the Purcell factor can be expressed by the following equation:

$$F = \left(\frac{\left|\vec{\mu} \cdot \vec{E}\right|}{|\vec{\mu}|\left|\vec{E}_{max}\right|}\right)^2 \left(\frac{1}{1 + 4Q^2\left(\frac{\lambda_{emitter}}{\lambda_{cavity}}\right)^2}\right) \frac{3Q}{4\pi^2 V}\left(\frac{\lambda_{cavity}}{n}\right)^3 + 1 \tag{5.36}$$

Where $\vec{\mu}$ is the electric dipole moment of the emitter, $\vec{E}$ is the electric field from the emitter, $\vec{E}_{max}$ is the maximum electric field from the cavity mode, λ_{ZPL} is the wavelength of the ZPL, λ_{cavity} is the resonant wavelength of the cavity, Q is the cavity quality factor, V is the cavity mode volume, and n is the index of refraction of the material. The first term $\left(\frac{|\vec{\mu}\cdot\vec{E}|}{|\vec{\mu}||\vec{E}_{max}|}\right)^2$ represents spatial overlap between the emitter and cavity mode, where both the position and orientation of the emitter play important roles for the overall coupling. The dot product $\vec{\mu} \cdot \vec{E}$ represents rotational alignment between the transition dipole and optical emission dipole, while the ratio $\left|\vec{E}\right|/\left|\vec{E}_{max}\right|$ represents spatial overlap between the emitter and cavity modes. The second term $\frac{1}{\left(1+4Q^2\left(\frac{\lambda_{emitter}}{\lambda_{cavity}}\right)^2\right)}$ represents spectral matching between the emitter and cavity. For higher Q cavities, this factor can result in significant losses if the spectral matching is not exact. Therefore most cavity-emitter

systems have some mechanism to tune either the two components into resonance. With perfect coupling these two terms become unity, so the Purcell factor becomes:

$$F = \frac{3}{4\pi^2}\left(\frac{\lambda}{n}\right)^3\left(\frac{Q}{V}\right) + 1, \qquad \text{perfect matching with emitter} \tag{5.37}$$

The simplified expression $F \propto \frac{Q}{V}$ is sometimes used to highlight the important figures of merit of a high quality factor with a small mode volume.

Meanwhile, the cooperativity parameter C is usually defined in terms of CQED parameters as:

$$C = \frac{g^2}{2\kappa\gamma} \tag{5.38}$$

Loosely speaking. the cooperativity is a measure of the ratio of desired coupling (g) to undesired coupling (κ, γ). A cooperativity C >> 1 generally means significant interactions between the atom and the light field in the cavity, although does not necessarily imply the strong coupling regime. To relate cooperativity to Purcell factor, we can substitute the earlier expression for g^2:

$$g^2 = \frac{3\pi c^3 \gamma}{\omega^2 V} \tag{5.39}$$

To give:

$$C = \frac{g^2}{2\kappa\gamma} = \frac{3\pi c^3\gamma}{2\kappa\gamma\omega^2 V} = \frac{3\pi c^3}{2\kappa\omega^2 V} = \frac{3\pi c^3}{2\frac{\omega}{Q}\omega^2 V} \tag{5.40}$$

$$C = \frac{3\pi c^3}{2\omega^3}\left(\frac{Q}{V}\right) = \frac{3\pi c^3}{2(2\pi)^3 f^3}\left(\frac{Q}{V}\right) = \frac{3\pi\lambda^3}{2(2\pi)^3}\left(\frac{Q}{V}\right) = \frac{1}{4}\cdot\frac{3}{4\pi^2}\lambda^3\left(\frac{Q}{V}\right) \tag{5.41}$$

When in a material instead of free space, the wavelength λ becomes (λ/n) with index of refraction n:

$$C = \frac{1}{4} \cdot \frac{3}{4\pi^2} \left(\frac{\lambda}{n}\right)^3 \left(\frac{Q}{V}\right) \tag{5.42}$$

Note that this closely resembles the perfectly matched Purcell factor F in equation 5.37. Substituting eq 5.37 equation into eq 5.42 gives:

$$C = \frac{1}{4}(F - 1) \tag{5.43}$$

Or:

$$F = 4C + 1 \tag{5.44}$$

Therefore, the Purcell factor F and the cooperativity C are equivalent within a multiplicative factor and an additive factor. The additive factor of 1 diminishes at large values of F or C. Since we substituted the Purcell factor with perfect coupling, the cooperativity inherently assumes that the emitter and cavity are perfectly matched. However, it would be possible to include the coupling factors from eq. 5.36 in the cooperativity expression to give:

$$C = \left(\frac{\left|\vec{\mu} \cdot \vec{E}\right|}{|\vec{\mu}|\left|\vec{E}_{max}\right|}\right)^2 \left(\frac{1}{1 + 4Q^2\left(\frac{\lambda_{emitter}}{\lambda_{cavity}}\right)^2}\right) \frac{g^2}{2\kappa\gamma}, \qquad \text{imperfect matching} \tag{5.45}$$

In practice this is almost never done, but it an important factor to consider when comparing Purcell factors to cooperativities.

5.2 The Jaynes Cummings Hamiltonian

The Jaynes Cumming Hamiltonian is used to model the interplay between the atom and an electromagnetic field in a cavity. In this section we will focus on obtaining a matrix form of the Hamiltonian and describing its energy eigenvalues. The Hamiltonian is typically written as the sum of three parts:

$$\widehat{H}_{JC} = \widehat{H}_{atom} + \widehat{H}_{field} + \widehat{H}_{int} \tag{5.46}$$

Where $\widehat{H}_{atom}$ is the isolated atomic Hamiltonian, $\widehat{H}_{field}$ is the electromagnetic field Hamiltonian in the cavity, and $\widehat{H}_{int}$ is the interaction Hamiltonian between the atom and the cavity field. These parts can be individually written as:

$$\widehat{H}_{atom} = \frac{\hbar\omega_a}{2}\hat{\sigma}_z, \qquad \widehat{H}_{field} = \hbar\omega_c\hat{a}^\dagger\hat{a}, \qquad \widehat{H}_{int} = \hbar g(\hat{a} + \hat{a}^\dagger)(\hat{\sigma}_+ + \hat{\sigma}_-) \tag{5.47}$$

Where:

$$\begin{gathered}
\omega_a = \text{frequency of atomic transition} \\
\omega_c = \text{frequency of resonant cavity mode} \\
\hat{\sigma}_z = |e\rangle\langle e| - |g\rangle\langle g|, \qquad \text{Pauli z spin matrix} \\
\hat{a}^\dagger = \text{photon number creation operator} \\
\hat{a} = \text{photon number annihilation operator} \\
\text{g} = \text{atom cavity coupling strength} \\
\hat{\sigma}_+ = |e\rangle\langle g|, \qquad \text{atomic raising operator} \\
\hat{\sigma}_- = |g\rangle\langle e|, \qquad \text{atomic lowering operator}
\end{gathered} \tag{5.48}$$

Immediately, it is worth distributing the interaction Hamiltonian:

$$\widehat{H}_{int} = \hbar g(\hat{a}\hat{\sigma}_+ + \hat{a}\hat{\sigma}_- + \hat{a}^\dagger\hat{\sigma}_+ + \hat{a}^\dagger\hat{\sigma}_-) \tag{5.49}$$

If we transform this Hamiltonian to the interaction picture, we obtain

$$H_{int} = \hbar g\left(\hat{a}\hat{\sigma}_+ e^{i(-\omega_c+\omega_a)t} + \hat{a}\hat{\sigma}_- e^{i(\omega_c+\omega_a)t} + \hat{a}^\dagger\hat{\sigma}_+ e^{i(\omega_c+\omega_a)t} + \hat{a}^\dagger\hat{\sigma}_- e^{-i(-\omega_c+\omega_a)t}\right) \tag{5.50}$$

Using the rotating wave approximation, we can eliminate the quickly oscillating terms to give:

$$H_{int} = \hbar g\left(\hat{a}\hat{\sigma}_{+}e^{i(-\omega_c+\omega_a)t} + \hat{a}^{\dagger}\hat{\sigma}_{-}e^{-i(-\omega_c+\omega_a)t}\right) \tag{5.51}$$

Then transforming back to the Schrodinger picture drops the complex exponentials to give:

$$H_{int} = \hbar g(\hat{a}\hat{\sigma}_{+} + \hat{a}^{\dagger}\hat{\sigma}_{-}) \tag{5.52}$$

This is the interaction Hamiltonian that is commonly used in practice, and we will also proceed with this form. This makes the Jaynes Cummings Hamiltonian:

$$\widehat{H}_{JC} = \frac{\hbar\omega_a}{2}\hat{\sigma}_z + \hbar\omega_c\hat{a}^{\dagger}\hat{a} + \hbar g(\hat{a}\hat{\sigma}_{+} + \hat{a}^{\dagger}\hat{\sigma}_{-}) \tag{5.53}$$

Shifting to the atomic portion of H_{JC}, we should recognize $\widehat{H}_{atom}$ from the two-level system outlined in chapter 1:

$$\widehat{H}_{atom}\frac{\hbar\omega_a}{2}\hat{\sigma}_z = \frac{\hbar\omega_a}{2}(|e\rangle\langle e| - |g\rangle\langle g|) \tag{5.54}$$

If we choose the basis:

$$|e\rangle = |0\rangle = \begin{pmatrix}1\\0\end{pmatrix}, \qquad |g\rangle = |1\rangle = \begin{pmatrix}0\\1\end{pmatrix} \tag{5.55}$$

Then in matrix form this becomes:

$$\widehat{H}_{atom} = \frac{\hbar\omega_a}{2}\begin{pmatrix}1 & 0\\0 & -1\end{pmatrix} \tag{5.56}$$

The eigenstates and general time evolution of $\widehat{H}_{atom}$ is the same as outlined on the two-level system section in 1.4. The field part of the Hamiltonian is more complicated. Here the eigenstates are represented by the photon number, which in the simplest case of 0/1 photons can be written as:

$$\text{photon number,} \qquad |n=0\rangle = \begin{pmatrix}1\\0\end{pmatrix}, \qquad |n=1\rangle = \begin{pmatrix}0\\1\end{pmatrix} \tag{5.57}$$

While this appears to match the form of the atomic basis states, the Hilbert space for photon number (called a Fock space) can take on *any* dimensionality greater than or equal to two. In the general n-dimensional case, the photon number creation and annihilation operators $\hat{a}^\dagger$ and $\hat{a}$ in matrix form are given by:

$$a^\dagger = \begin{pmatrix} 0 & 0 & 0 & \dots & 0 & \dots & \dots \\ \sqrt{1} & 0 & 0 & \dots & 0 & \dots & \dots \\ 0 & \sqrt{2} & 0 & \dots & 0 & \dots & \dots \\ 0 & 0 & \sqrt{3} & \dots & 0 & \dots & \dots \\ \dots & \dots & \dots & \dots & \dots & \dots & \dots \\ 0 & 0 & 0 & \dots & \sqrt{n} & \dots & \dots \\ \dots & \dots & \dots & \dots & \dots & \dots & \dots \end{pmatrix}, \qquad a = \begin{pmatrix} 0 & \sqrt{1} & 0 & 0 & \dots & 0 & \dots \\ 0 & 0 & \sqrt{2} & 0 & \dots & 0 & \dots \\ 0 & 0 & 0 & \sqrt{3} & \dots & 0 & \dots \\ \dots & \dots & \dots & \dots & \dots & \dots & \dots \\ 0 & 0 & 0 & 0 & \dots & \sqrt{n} & \dots \\ \dots & \dots & \dots & \dots & \dots & \dots & \dots \\ \dots & \dots & \dots & \dots & \dots & \dots & \dots \end{pmatrix} \tag{5.58}$$

In the 2D and 3D cases, this would become:

$$\hat{a}^\dagger = \begin{pmatrix}0 & 0\\1 & 0\end{pmatrix}, \qquad \hat{a} = \begin{pmatrix}0 & 1\\0 & 0\end{pmatrix}, \qquad \text{2D Fock space} \tag{5.59}$$

$$\hat{a}^\dagger = \begin{pmatrix}0 & 0 & 0\\1 & 0 & 0\\0 & \sqrt{2} & 0\end{pmatrix}, \qquad \hat{a} = \begin{pmatrix}0 & 1 & 0\\0 & 0 & \sqrt{2}\\0 & 0 & 0\end{pmatrix}, \qquad \text{3D Fock space} \tag{5.60}$$

This means that the general n-dimensional form of the field part of the Hamiltonian becomes:

$$\hat{H}_{field} = \hbar\omega_c \begin{pmatrix} 0 & 0 & 0 & 0 & \dots & 0 \\ 0 & 1 & 0 & 0 & \dots & 0 \\ 0 & 0 & 2 & 0 & \dots & 0 \\ 0 & 0 & 0 & 3 & \dots & 0 \\ \dots & \dots & \dots & \dots & \dots & \dots \\ 0 & 0 & 0 & 0 & \dots & n \end{pmatrix} \tag{5.61}$$

Reconciling different Hilbert spaces

The three parts of the Jaynes Cummings Hamiltonian provide us with a bit of a quandary when we try to combine them. Namely, we are adding Hamiltonians from *different Hilbert spaces*. What's more, the n-dimensional Fock space will generally not have the same dimensionality as the 2x2 atomic Hamiltonian. To work around this, we must take appropriate tensor products between these Hilbert spaces before adding the components together. Each individual operator would then take the form:

$$\hat{a} = \hat{a} \otimes I_2, \qquad \hat{a}^\dagger = \hat{a}^\dagger \otimes I_2 \tag{5.62}$$

$$\hat{\sigma}_+ = I_n \otimes \hat{\sigma}_+, \qquad \hat{\sigma}_- = I_n \otimes \hat{\sigma}_- \tag{5.63}$$

Where I_2 represents the 2-dimensional identity matrix for the atomic component and I_n represents the n-dimensional identity matrix for the field component. With the definitions for the atomic raising and lowering operators as:

$$\hat{\sigma}_- = |g\rangle\langle e| = \begin{pmatrix}0\\1\end{pmatrix}(1 \quad 0) = \begin{pmatrix}0 & 0\\1 & 0\end{pmatrix} \tag{5.64}$$

$$\hat{\sigma}_+ = |e\rangle\langle g| = \begin{pmatrix}1\\0\end{pmatrix}(0 \quad 1) = \begin{pmatrix}0 & 1\\0 & 0\end{pmatrix} \tag{5.65}$$

For demonstration, we can write out the tensor products for the individual operators for the case of a 2-dimensional Fock space:

$$\hat{\sigma}_z = I_n \otimes \hat{\sigma}_z = \begin{pmatrix}1 & 0\\0 & 1\end{pmatrix} \otimes \begin{pmatrix}1 & 0\\0 & -1\end{pmatrix} = \begin{pmatrix}1 & 0 & 0 & 0\\0 & -1 & 0 & 0\\0 & 0 & 1 & 0\\0 & 0 & 0 & -1\end{pmatrix} \tag{5.66}$$

$$\hat{a} = \hat{a} \otimes I_2 = \begin{pmatrix}0 & 1\\0 & 0\end{pmatrix} \otimes \begin{pmatrix}1 & 0\\0 & 1\end{pmatrix} = \begin{pmatrix}0 & 0 & 1 & 0\\0 & 0 & 0 & 1\\0 & 0 & 0 & 0\\0 & 0 & 0 & 0\end{pmatrix} \tag{5.67}$$

$$\hat{\sigma}_+ = I_n \otimes \hat{\sigma}_+ = \begin{pmatrix} 1 & 0 \\ 0 & 1 \end{pmatrix} \otimes \begin{pmatrix} 0 & 1 \\ 0 & 0 \end{pmatrix} = \begin{pmatrix} 0 & 1 & 0 & 0 \\ 0 & 0 & 0 & 0 \\ 0 & 0 & 0 & 1 \\ 0 & 0 & 0 & 0 \end{pmatrix} \tag{5.68}$$

$$\hat{a}^\dagger = \hat{a}^\dagger \otimes I_2 = \begin{pmatrix} 0 & 0 \\ 1 & 0 \end{pmatrix} \otimes \begin{pmatrix} 1 & 0 \\ 0 & 1 \end{pmatrix} = \begin{pmatrix} 0 & 0 & 0 & 0 \\ 0 & 0 & 0 & 0 \\ 1 & 0 & 0 & 0 \\ 0 & 1 & 0 & 0 \end{pmatrix} \tag{5.69}$$

$$\hat{\sigma}_- = I_n \otimes \hat{\sigma}_- = \begin{pmatrix} 1 & 0 \\ 0 & 1 \end{pmatrix} \otimes \begin{pmatrix} 0 & 0 \\ 1 & 0 \end{pmatrix} = \begin{pmatrix} 0 & 0 & 0 & 0 \\ 1 & 0 & 0 & 0 \\ 0 & 0 & 0 & 0 \\ 0 & 0 & 1 & 0 \end{pmatrix} \tag{5.70}$$

Which gives the following for the product of operators:

$$\hat{a}^\dagger \hat{a} = \begin{pmatrix} 0 & 0 & 0 & 0 \\ 0 & 0 & 0 & 0 \\ 1 & 0 & 0 & 0 \\ 0 & 1 & 0 & 0 \end{pmatrix} \begin{pmatrix} 0 & 0 & 1 & 0 \\ 0 & 0 & 0 & 1 \\ 0 & 0 & 0 & 0 \\ 0 & 0 & 0 & 0 \end{pmatrix} = \begin{pmatrix} 0 & 0 & 0 & 0 \\ 0 & 0 & 0 & 0 \\ 0 & 0 & 1 & 0 \\ 0 & 0 & 0 & 1 \end{pmatrix} \tag{5.71}$$

$$\hat{a}\hat{\sigma}_+ = \begin{pmatrix} 0 & 0 & 1 & 0 \\ 0 & 0 & 0 & 1 \\ 0 & 0 & 0 & 0 \\ 0 & 0 & 0 & 0 \end{pmatrix} \begin{pmatrix} 0 & 1 & 0 & 0 \\ 0 & 0 & 0 & 0 \\ 0 & 0 & 0 & 1 \\ 0 & 0 & 0 & 0 \end{pmatrix} = \begin{pmatrix} 0 & 0 & 0 & 1 \\ 0 & 0 & 0 & 0 \\ 0 & 0 & 0 & 0 \\ 0 & 0 & 0 & 0 \end{pmatrix} \tag{5.72}$$

$$\hat{a}^\dagger \hat{\sigma}_- = \begin{pmatrix} 0 & 0 & 0 & 0 \\ 0 & 0 & 0 & 0 \\ 1 & 0 & 0 & 0 \\ 0 & 1 & 0 & 0 \end{pmatrix} \begin{pmatrix} 0 & 0 & 0 & 0 \\ 1 & 0 & 0 & 0 \\ 0 & 0 & 0 & 0 \\ 0 & 0 & 1 & 0 \end{pmatrix} = \begin{pmatrix} 0 & 0 & 0 & 0 \\ 0 & 0 & 0 & 0 \\ 0 & 0 & 0 & 0 \\ 1 & 0 & 0 & 0 \end{pmatrix} \tag{5.73}$$

So in total, for the 2-dimensional Fock space:

$$\widehat{H}_{JC} = \hbar \begin{pmatrix} \frac{\omega_a}{2} & 0 & 0 & g \\ 0 & -\frac{\omega_a}{2} & 0 & 0 \\ 0 & 0 & \frac{\omega_a}{2} + \omega_c & 0 \\ g & 0 & 0 & -\frac{\omega_a}{2} + \omega_c \end{pmatrix}, \qquad \text{2D Fock space} \tag{5.74}$$

The same approach can be applied to the 3-dimensional Fock space, which gives:

$$\widehat{H}_{JC} = \hbar \begin{pmatrix} \frac{\omega_a}{2} & 0 & 0 & g & 0 & 0 \\ 0 & -\frac{\omega_a}{2} & 0 & 0 & 0 & 0 \\ 0 & 0 & \frac{\omega_a}{2} + \omega_c & 0 & 0 & \sqrt{2}g \\ g & 0 & 0 & -\frac{\omega_a}{2} + \omega_c & 0 & 0 \\ 0 & 0 & 0 & 0 & \frac{\omega_a}{2} + 2\omega_c & 0 \\ 0 & 0 & \sqrt{2}g & 0 & 0 & -\frac{\omega_a}{2} + 2\omega_c \end{pmatrix}, \qquad \text{3D Fock space} \quad (5.75)$$

Using the latter case as an example, this matrix gives the energy eigenvalues of:

$$\lambda_1 = -\frac{\hbar\omega_a}{2}, \qquad |g, 0\rangle \text{ state} \tag{5.76}$$

$$\lambda_2 = \frac{\hbar\omega_a}{2} + 2\hbar\omega_c, \qquad |e, 2\rangle \text{ state} \tag{5.77}$$

$$\lambda_{3,4} = \hbar\omega_c\left(n + \frac{1}{2}\right) \pm \hbar\sqrt{\frac{\Delta^2}{4} + g^2(n+1)}, \qquad \text{where } n = 1 \tag{5.78}$$

$$\lambda_{5,6} = \hbar\omega_c\left(n + \frac{1}{2}\right) \pm \hbar\sqrt{\frac{\Delta^2}{4} + g^2(n+1)}, \qquad \text{where } n = 0 \tag{5.79}$$

Where:

$$\Delta = \omega_a - \omega_c, \qquad \text{detuning between atom and cavity photon energies}$$

As labeled above, the λ_1 energy corresponds to the atomic ground state with no photons in the cavity, whereas the λ_2 energy corresponds to the atomic excited state with 2 photons in the cavity. In this system where the photon number is limited to $\{0,1,2\}$, these two energies serve as the extremes for the minimum and maximum energy. The intermediate energies $\lambda_{3,4}, \lambda_{5,6}$ do not

represent isolated atomic/Fock states such as $|e,1\rangle$ or $|g,2\rangle$, but rather superpositions of these states. More specifically, these so-called dressed states come in pairs that take the following form under zero detuning ($\Delta = 0$):

$$|+,n\rangle = \frac{1}{\sqrt{2}}(|e,n\rangle + |g,n+1\rangle), \qquad \text{higher energy} \tag{5.80}$$

$$|-,n\rangle = \frac{1}{\sqrt{2}}(|e,n\rangle - |g,n+1\rangle), \qquad \text{lower energy} \tag{5.81}$$

Where n is the number of photons. With this definition, we can make the relations:

$$\lambda_{3,4} = \text{energies for } |\pm, n=1\rangle \text{ states} \tag{5.82}$$

$$\lambda_{5,6} = \text{energies for } |\pm, n=0\rangle \text{ states} \tag{5.83}$$

In the most general case with n photons then, the dressed state energies take the form:

$$E_{\pm}(n) = \hbar\omega_c\left(n+\frac{1}{2}\right) \pm \hbar\sqrt{\frac{\Delta^2}{4} + g^2(n+1)}, \qquad \text{dressed state energies} \tag{5.84}$$

Focusing on only an individual pair of dressed states, we can write a 2x2 Hamiltonian that only considers the two states $|n,e\rangle$ and $|n+1,g\rangle$ for general photon number n. This can be written as:

$$H_n = \hbar\left(n+\frac{1}{2}\right)\omega_c\begin{pmatrix}1 & 0\\ 0 & 1\end{pmatrix} + \hbar\begin{pmatrix}-\frac{\Delta}{2} & g\sqrt{n+1}\\ g\sqrt{n+1} & \frac{\Delta}{2}\end{pmatrix} \tag{5.85}$$

Or combining into one matrix:

$$H_n = \hbar \begin{pmatrix} \left(n + \frac{1}{2}\right)\omega_c - \frac{\Delta}{2} & g\sqrt{n+1} \\ g\sqrt{n+1} & \left(n + \frac{1}{2}\right)\omega_c + \frac{\Delta}{2} \end{pmatrix} \tag{5.86}$$

Where the basis of this Hamiltonian is the $\{|g, n+1\rangle, |e, n\rangle\}$ states, and the energy eigenvalues exactly match the dressed state energies. This is the Hamiltonian that is more commonly used in analyses involving the Jaynes Cumming model. Plotting the energies as a function of detuning gives avoided crossings separated by $g\sqrt{(n+1)}$, as shown in the figure below:

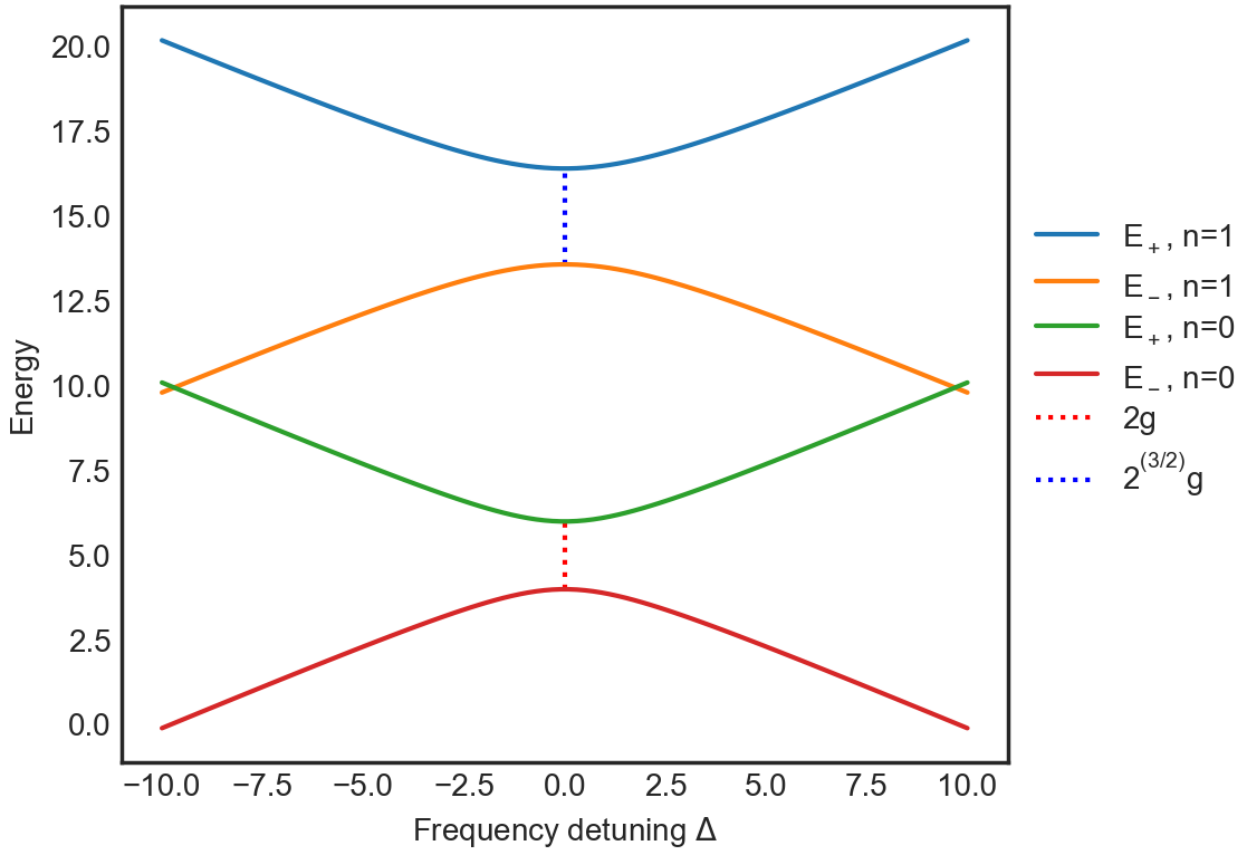

Figure 5.2 | Energy eigenvalues of the reduced Jaynes-Cummings Hamiltonian. Detuning between the cavity photon and the atomic transition is plotted on the x-axis. Here we set $\hbar = 1$, $\omega_c = 10$, and $g = 1$. Four energy eigenstates are plotted according to equation 5.84. The red and blue dotted lines indicate the separation between energies at zero detuning.

This shows that even with no photons in the cavity (n = 0) there is still a splitting of $2g$ between the energy eigenvalues of the system. This is termed the "vacuum Rabi splitting". The splitting then increases in value for higher photon number as $g\sqrt{n+1}$. The eigenstates of this reduced Hamiltonian are:

$$|n \pm\rangle = \begin{pmatrix} \frac{-\Delta \pm \sqrt{\Delta^2 + 4g^2(n+1)}}{2g\sqrt{n+1}} \\ 1 \end{pmatrix} \tag{5.87}$$

Meaning that we can write the general state evolution as:

$$\Psi(t) = c_+ \begin{pmatrix} \frac{2g\sqrt{n+1}}{\Delta + \sqrt{\Delta^2 + 4g^2(n+1)}} \\ 1 \end{pmatrix} e^{-\frac{iE_+ t}{\hbar}} + c_- \begin{pmatrix} \frac{2g\sqrt{n+1}}{\Delta - \sqrt{\Delta^2 + 4g^2(n+1)}} \\ 1 \end{pmatrix} e^{-\frac{iE_- t}{\hbar}} \tag{5.88}$$

Where $E_\pm$ are the dressed state energies. At zero detuning, this becomes:

$$\Psi(t) = c_+ \begin{pmatrix} 1 \\ 1 \end{pmatrix} e^{-\frac{iE_+ t}{\hbar}} + c_- \begin{pmatrix} -1 \\ 1 \end{pmatrix} e^{-\frac{iE_- t}{\hbar}} \tag{5.89}$$

This tells us that the $\binom{1}{1}$ and $\binom{-1}{1}$ states in the $\{|g, n+1\rangle, |e, n\rangle\}$ basis are the eigenstates of the system at zero detuning. This means that a state prepared in $|g, n+1\rangle$ will precess to the $|e, n\rangle$ state and vice versa. We will explore this behavior and the strong and weak coupling regimes in the Jaynes-Cummings model in the next section.

5.3 Strong and weak coupling regimes

Depending on the relative value of the atom-cavity coupling constant g, the behavior of the system can broadly be separated into the strong coupling and weak coupling regimes. We will discuss some of the implications of these regimes.

Strong coupling

In the strong coupling regime, the coupling constant is much greater than both the spontaneous emission rate and leakage rate of the cavity:

$$g > \gamma, \kappa, \qquad \text{strong coupling} \tag{5.90}$$

Incidentally, this also means that the Purcell factor and cooperativity are also both much greater than 1. In this regime, we can effectively ignore the effects of damping and use the results of the Jaynes-Cummings model from the previous section. The precession between the $|g, n+1\rangle$ and $|e, n\rangle$ states with zero detuning occurs regardless of the photon number n. Rewriting the general state evolution with no detuning gives:

$$\Psi(t) = c_+ \begin{pmatrix} 1 \\ 1 \end{pmatrix} e^{-i\left(\omega_c\left(n+\frac{1}{2}\right)+g\sqrt{(n+1)}\right)t} + c_- \begin{pmatrix} -1 \\ 1 \end{pmatrix} e^{-i\left(\omega_c\left(n+\frac{1}{2}\right)-g\sqrt{(n+1)}\right)t} \tag{5.91}$$

The component $e^{-i\left(\omega_c\left(n+\frac{1}{2}\right)\right)t}$ is a global phase that can be removed from the system, giving:

$$\Psi(t) = c_+ \begin{pmatrix} 1 \\ 1 \end{pmatrix} e^{-i\left(g\sqrt{(n+1)}\right)t} + c_- \begin{pmatrix} -1 \\ 1 \end{pmatrix} e^{i\left(g\sqrt{(n+1)}\right)t} \tag{5.92}$$

When n = 0, we have:

$$\Psi(t) = c_+ \begin{pmatrix} 1 \\ 1 \end{pmatrix} e^{-igt} + c_- \begin{pmatrix} -1 \\ 1 \end{pmatrix} e^{igt} \tag{5.93}$$

We can start in the $|e,0\rangle$ state by setting $c_+ = \frac{1}{2}, c_- = \frac{1}{2}$:

$$\Psi(t) = \frac{1}{2}\begin{pmatrix}1\\1\end{pmatrix}e^{-igt}\frac{1}{2}\begin{pmatrix}-1\\1\end{pmatrix}e^{igt} = \begin{pmatrix}\frac{1}{2}e^{-igt} - \frac{1}{2}e^{igt}\\ \frac{1}{2}e^{-igt} + \frac{1}{2}e^{igt}\end{pmatrix} = \begin{pmatrix}-i\sin(gt)\\ \cos(gt)\end{pmatrix} \tag{5.94}$$

Therefore, we can say that the squared amplitudes for the $|g,1\rangle$ and $|e,0\rangle$ states are:

$$\left|c_{g,1}\right|^2 = \sin^2(gt)\,, \qquad \left|c_{e,0}\right|^2 = \cos^2(gt)\,, \qquad g = \text{vacuum Rabi frequency} \tag{5.95}$$

These solutions are referred to as vacuum Rabi oscillations, where g is the vacuum Rabi frequency. Even in the presence of no photons, the state will naturally rotate between the ground and excited states. This is contrast to an atomic two-level system without a cavity, where the excited state decay is irreversible. A plot of several conditions for vacuum Rabi oscillations are shown in the figure below:

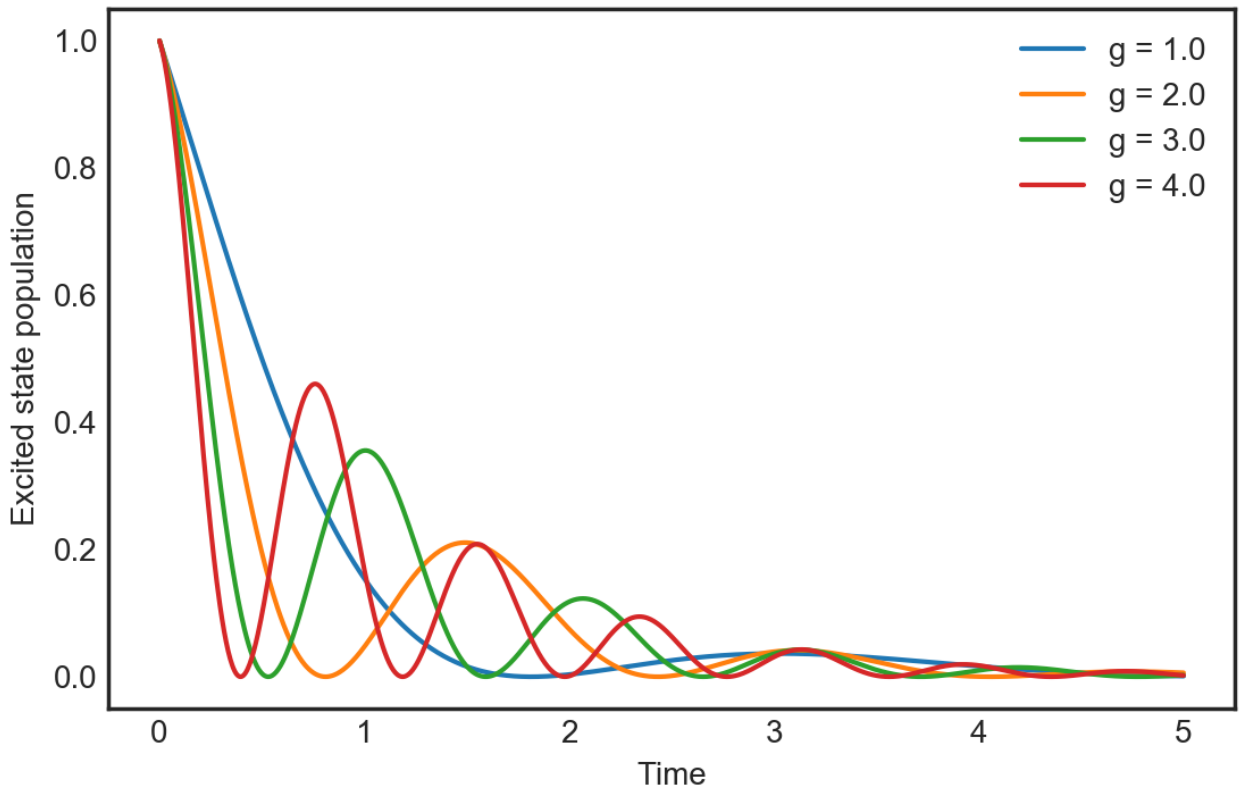

Figure 5.3 | Vacuum Rabi oscillations. In all of these theoretical plots, $\gamma = \kappa = 1$. The four curves have varying values of $g \geq 1$, resulting in observable vacuum Rabi oscillations. Higher coupling constants g result in more pronounced vacuum Rabi oscillations.

Weak coupling

An atom-cavity system in the weak coupling regime is characterized by

$$g < (\gamma, \kappa), \qquad \text{weak coupling regime} \tag{5.96}$$

It is also possible to have the ordering:

$$\kappa > g > \gamma, \qquad \text{Purcell regime} \tag{5.97}$$

Which is sometimes called the Purcell regime. In either case, the leakage out of the cavity outcompetes coupling to the atom, which means that vacuum Rabi is no longer observable. This

means that an emitted photon will escape the cavity before it has the chance to be reabsorbed. However, the spontaneous emission rate will be increased due to the increase of density of photonic states in the cavity. This speedup is given exactly by the Purcell factor as outlined earlier in this chapter:

$$F \equiv \frac{\gamma_{cavity}}{\gamma_{bulk}} = \frac{2g^2}{\kappa\gamma} + 1, \qquad \text{Purcell factor} \tag{5.98}$$

Therefore, even in the situation where $\kappa > g$, one can obtain a high Purcell factor if $g \gg \gamma$. This is why the $\kappa > g > \gamma$ condition is called the Purcell regime.

5.4 Free space spontaneous emission derivation

Our goal in this section is to derive the spontaneous emission rate γ in free space, which is widely used in other CQED calculations and predictions. For this derivation we will consider a simple two-level system with a ground $|g\rangle$ and an excited state $|e\rangle$. Here, spontaneous emission occurs when the state $|e\rangle$ decays to $|g\rangle$ and emits a photon due to the Jaynes Cummings Hamiltonian. Therefore, we will set the initial condition as the excited state:

$$\text{Initial state,} \qquad |\psi(0)\rangle = |e, 0\rangle \tag{5.99}$$

Here the "0" denotes zero photons in the cavity. In this case there is not a literal cavity since we are in free space, but we can imagine free space itself to be a cavity with infinite length. After some time, the excited state will decay and emit a photon, giving the final state of:

$$\text{Final state,} \qquad |\psi(\infty)\rangle = |g, 1_{\mathbf{k}}\rangle \tag{5.100}$$

Here the "$1_{\mathbf{k}}$" denotes one photon in the cavity with a wavevector of **k**. In between the initial and final states, we have the state:

$$\text{Time dependent state,} \qquad |\psi(t)\rangle = C_0^e(t)e^{-i\omega_0 t}|e, \{0\}\rangle + \sum_{\mathbf{k}} C_{1\mathbf{k}}^g(t)e^{-i\omega_k t}|g, 1_{\mathbf{k}}\rangle \tag{5.101}$$

Here a summation over all possible wavevectors is included in order to represent any possible photon emission. This is because prior to decay, we do not know which direction or polarization the photon will emit with, so we must use a general **k**. Each particular wavevector will have its own amplitude $C_{1\mathbf{k}}^g(t)$ associated with it. To describe the system's dynamics we will use a modified form of the Jaynes Cummings Hamiltonian:

$$\widehat{H} = \hbar\omega_0|e\rangle\langle e| + \sum_{\mathbf{k}} \hbar\omega_k a_{\mathbf{k}}^\dagger a_{\mathbf{k}} + \sum_{\mathbf{k}} \hbar g_{\mathbf{k}}\left(|e\rangle\langle g|a_{\mathbf{k}} + |g\rangle\langle e|a_{\mathbf{k}}^\dagger\right) \tag{5.102}$$

Here, the first term still represents the atomic portion, but is shifted in energy. The second term is the field portion, with a summation over all possible wavevectors. The third term is the interaction term with the coupling constant defined here as:

$$g_{\mathbf{k}} = i\sqrt{\frac{\omega_k}{2\hbar\epsilon_0 V}}(\mathbf{d}\cdot\vec{\varepsilon}_{\mathbf{k}}) \tag{5.103}$$

The time evolution of the system is given by the Schrodinger equation:

$$H|\psi(t)\rangle = i\hbar\frac{\partial|\psi(t)\rangle}{\partial t} \tag{5.104}$$

Projecting onto $\langle e, \{0\}|$ and $\langle g, 1_{\mathbf{k}}|$ gives, after a lot of algebra:

$$\frac{\partial}{\partial t} C_0^e(t) = -i \sum_{\mathbf{k}} g_{\mathbf{k}} e^{-i(\omega_k - \omega_0)t} C_{1\mathbf{k}}^g(t) \tag{5.105}$$

$$\frac{\partial}{\partial t} C_{1\mathbf{k}}^g(t) = -i g_{\mathbf{k}}^* e^{i(\omega_k - \omega_0)t} C_0^e(t) \tag{5.106}$$

We then change of variables to t' for equation (5.106):

$$\frac{\partial}{\partial t'} C_{1\mathbf{k}}^g(t') = -i g_{\mathbf{k}} e^{i(\omega_k - \omega_0)t'} C_0^e(t') \tag{5.107}$$

And integrate with respect to t':

$$\int_0^t \frac{\partial}{\partial t'} C_{1\mathbf{k}}^g(t') dt' = \int_0^t -i g_{\mathbf{k}} e^{i(\omega_k - \omega_0)t'} C_0^e(t') dt' \tag{5.108}$$

$$C_{1\mathbf{k}}^g(t) - C_{1\mathbf{k}}^g(0) = -i g_{\mathbf{k}} \int_0^t e^{i(\omega_k - \omega_0)t'} C_0^e(t') dt' \tag{5.109}$$

$$C_{1\mathbf{k}}^g(t) = C_{1\mathbf{k}}^g(0) - i g_{\mathbf{k}} \int_0^t e^{i(\omega_k - \omega_0)t'} C_0^e(t') dt' \tag{5.110}$$

At this point we can say $C_{1\mathbf{k}}^g(0) = 0$ for all $\mathbf{k}$ since we are starting in the excited state at t = 0:

$$C_{1\mathbf{k}}^g(t) = -i g_{\mathbf{k}} \int_0^t e^{i(\omega_k - \omega_0)t'} C_0^e(t') dt' \tag{5.111}$$

Substituting this into equation (5.105) then gives:

$$\frac{\partial}{\partial t} C_0^e(t) = -i \sum_{\mathbf{k}} g_{\mathbf{k}} e^{-i(\omega_k - \omega_0)t} \left(-i g_{\mathbf{k}} \int_0^t e^{i(\omega_k - \omega_0)t'} C_0^e(t') dt' \right) \tag{5.112}$$

$$\frac{\partial}{\partial t}C_0^e(t) = -\sum_{\mathbf{k}}|g_{\mathbf{k}}|^2\int_0^t dt' e^{i(\omega_k-\omega_0)(t-t')}C_0^e(t') \tag{5.113}$$

Our goal now is to deal with this summation and this integral, and try to show that our differential equation will overall become:

$$\frac{\partial}{\partial t}C_0^e(t) = -\text{constant}\cdot C_0^e(t) \tag{5.114}$$

Which is the recipe for exponential decay, which is what is observed in real systems.

We will start with the summation. Generally we can convert the summation to an integral as the discrete states **k** approach a continuum:

$$\sum_{\mathbf{k}}|g_{\mathbf{k}}|^2 = 2\int D(k)|g_{\mathbf{k}}|^2\cdot d^3k\,, \qquad D(k) = \frac{V}{(2\pi)^3} \tag{5.115}$$

Where $V \to \infty$ is the volume of free space and prefactor of 2 represents two polarizations per mode. More explicitly, the integral over k-space becomes:

$$\sum_{\mathbf{k}}|g_{\mathbf{k}}|^2 = \frac{2V}{(2\pi)^3}\int_0^{2\pi}d\phi\int_0^{\pi}\sin\theta\, d\theta\int_0^{\infty}|g_{\mathbf{k}}|^2\cdot k^2dk \tag{5.116}$$

From the definition of $g_{\mathbf{k}}$, we have:

$$|g_{\mathbf{k}}|^2 = \frac{\omega_k}{2\hbar\epsilon_0 V}(\mathbf{d}\cdot\vec{\varepsilon}_{\mathbf{k}})^2 \tag{5.117}$$

Substituting gives:

$$\sum_{\mathbf{k}} g_{\mathbf{k}}^2 = \frac{\omega_k}{2\hbar\epsilon_0 V}(\mathbf{d}\cdot\hat{\varepsilon}_{\mathbf{k}})^2\frac{2V}{(2\pi)^3}\int_0^{2\pi}d\phi\int_0^{\pi}\sin\theta\, d\theta\int_0^{\infty}k^2dk \tag{5.118}$$

$$\sum_{\mathbf{k}} |g_{\mathbf{k}}|^2 = \int_0^\infty dk\, k^2 \frac{\omega_k}{(2\pi)^3 \hbar \epsilon_0} \left(\int_0^\pi \sin\theta\, d\theta \int_0^{2\pi} d\phi (\mathbf{d} \cdot \boldsymbol{\epsilon}_{\mathbf{k}})^2 \right) \tag{5.119}$$

The integrals in parentheses can be evaluated assuming that $\mathbf{d}$ is along the z-axis:

$$\int_0^\pi \sin\theta\, d\theta \int_0^{2\pi} d\phi (\mathbf{d} \cdot \boldsymbol{\epsilon}_{\mathbf{k}})^2 = \int_0^\pi \sin\theta\, d\theta \int_0^{2\pi} d\phi (|\mathbf{d}| \cos\theta)^2 \tag{5.120}$$

$$= |\mathbf{d}|^2 \int_0^\pi \sin\theta \cos^2\theta\, d\theta \int_0^{2\pi} d\phi = |\mathbf{d}|^2 \cdot \frac{2}{3} \cdot 2\pi = \frac{4\pi}{3} |\mathbf{d}|^2 \tag{5.121}$$

Substituting this gives:

$$\sum_{\mathbf{k}} |g_{\mathbf{k}}|^2 = \frac{4\pi |\mathbf{d}|^2}{3} \int_0^\infty dk\, k^2 \frac{\omega_k}{(2\pi)^3 \hbar \epsilon_0} = \frac{|\mathbf{d}|^2}{6\pi^2 \hbar \epsilon_0} \int_0^\infty dk\, k^2 \omega_k \tag{5.122}$$

Using $\omega = ck$ then gives:

$$\sum_{\mathbf{k}} |g_{\mathbf{k}}|^2 = \frac{|\mathbf{d}|^2}{6\pi^2 \hbar \epsilon_0} \int_0^\infty \frac{d\omega}{c} \frac{\omega^2}{c^2} \omega_k \tag{5.123}$$

$$\boxed{\sum_{\mathbf{k}} |g_{\mathbf{k}}|^2 = \frac{|\mathbf{d}|^2}{6\pi^2 \hbar \epsilon_0 c^3} \int_0^\infty \omega_k^3 d\omega_k} \tag{5.124}$$

We now turn to the integral in equation (5.113):

$$\int_0^t dt' e^{i(\omega_k - \omega_0)(t-t')} C_0^e(t') \tag{5.125}$$

Under the Wigner-Weisskopf approximation, we assume that $C_0^e(t')$ will not vary much over the course of the integral, so we set $C_0^e(t') = C_0^e(t)$ and pull it out of the integral:

$$C_0^e(t)\int_0^t dt' e^{i(\omega_k-\omega_0)(t-t')} \tag{5.126}$$

This is equivalent to a "Markov approximation", where the system has no memory of the past. To evaluate the integral, we raise the upper bound to $t \to \infty$ since the tiime scale is much longer than the inverse frequencies ω_k, ω_0 of the system. This gives:

$$\int_0^\infty dt' e^{i(\omega_k-\omega_0)(t-t')} = \pi\delta(\omega_k-\omega_0) - iP\left(\frac{1}{\omega_k-\omega_0}\right) \tag{5.127}$$

Where $\delta(x)$ is the Dirac-delta function of x and $P(x)$ is the Cauchy principal part of x. The Cauchy principal part corresponds to the Lamb shift, which we are not interested in for this derivation, so it will be dropped. This gives the result:

$$\int_0^t dt' e^{i(\omega_k-\omega_0)(t-t')} C_0^e(t') = \pi\delta(\omega_k-\omega_0) C_0^e(t) \tag{5.128}$$

Combining equations (5.124) and (5.128) into equation (5.113) then gives:

$$\frac{\partial}{\partial t} C_0^e(t) = -\frac{|\mathbf{d}|^2}{6\pi^2\hbar\epsilon_0 c^3} C_0^e(t) \int_0^\infty \omega_k^3 \pi\delta(\omega_k-\omega_0) d\omega_k \tag{5.129}$$

$$\frac{\partial}{\partial t} C_0^e(t) = -\frac{|\mathbf{d}|^2}{6\pi^2\hbar\epsilon_0 c^3} C_0^e(t) \cdot \pi\omega_0^3 \tag{5.130}$$

$$\frac{\partial}{\partial t} C_0^e(t) = -\frac{|\mathbf{d}|^2\omega_0^3}{6\pi\hbar\epsilon_0 c^3} C_0^e(t) \tag{5.131}$$

As alluded to earlier, this is the differential equation for exponential decay. This means that the excited state population decays according to:

$$C_0^e(t) = e^{-\gamma t}, \qquad \gamma = \frac{|\mathbf{d}|^2 \omega_0^3}{6\pi\hbar\epsilon_0 c^3} = \frac{\mu^2 \omega_0^3}{6\pi\epsilon_0 \hbar c^3} \tag{5.132}$$

The rate γ, sometimes termed the Einstein A coefficient, is exactly the spontaneous emission rate outlined earlier in this chapter.

Chapter 6

Fabrication

6.1 General principles of lithography

The cornerstone of most fabrication procedures is the use of lithography, which selectively exposes and develops special polymers called resist in order to create a user defined pattern on a substrate. Lithography can be categorized into two main types based on the exposure source. Photolithography uses visible/UV light for exposure and is used for micron scale patterns. E-beam lithography uses energetic electrons (usually 30-100 keV) for exposure and is used for nanometer scale patterns. In either case, the effect of exposure is to chemically alter the resist in order to strengthen or weaken its adhesion to the substrate. In "positive" resists, such as PMMA, the exposed regions are chemically weakened and subsequently removed during the development step. In this case the exposure pattern exactly matches the developed resist pattern. In "negative" resists, such as HSQ, exposure causes a crosslinking or polymerization which causes only these regions to stay on the chip during development. In this case the exposure pattern is the inverse of the final resist pattern. The process of "development" involves the submergence of the substrate and resist into a chemical that removes the exposed or unexposed regions. The exact chemical used varies from resist to resist. A general procedure for lithography is given below in figure 6.1.

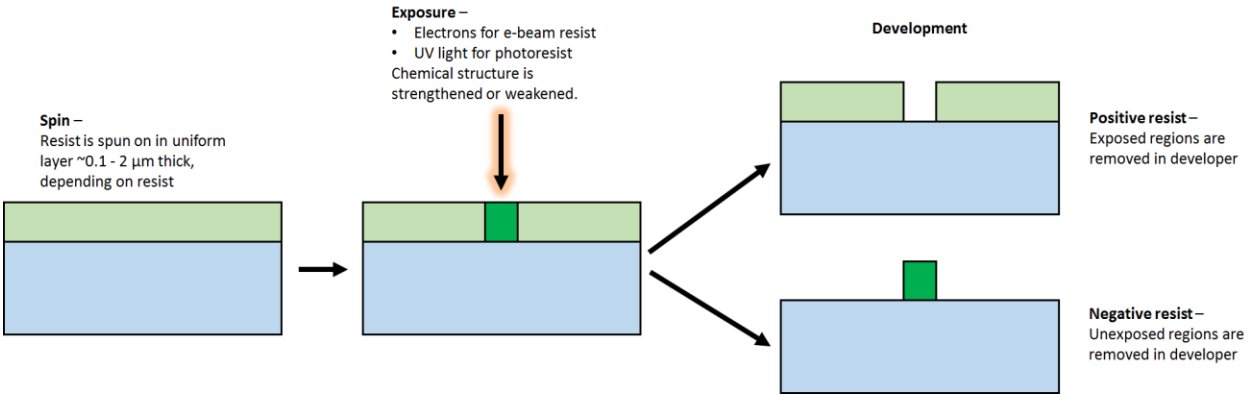

Figure 6.1 | General lithographic procedure. Photoresist or electron beam resist is spun onto a sample and baked. Subsequent exposure with either ultraviolet light or 10-100 keV electrons chemically alters the resist. A final development step either removes all exposed resist or all unexposed resist.

When performing lithography, one must be mindful to find the correct exposure dosage for the particular resist. For optical resist dosage is typically expressed in units of $\mu J/cm^2$ whereas e-beam resist typically uses $\mu C/cm^2$. If patterns are overexposed, they will become bloated and small features will merge into each other. On the other hand, underexposure will result in incomplete development of features. Likewise, the development step after exposure must be timed precisely so as not to over or underdevelop the sample and cause similar pattern distortions. It can sometimes be difficult to distinguish between exposure and development issues, and to a certain degree these errors can compound on each other or cancel each other out.

After lithography, many procedures involve the deposition and subsequent liftoff of an evaporated or sputtered material. Alternatively, the resist itself can be used as mask to protect the material below from a plasma etch ("dry" etch) or chemical etch ("wet" etch). We will discuss both of these topics.

6.2 Evaporation and liftoff

Whether photolithography or e-beam lithography is used, a common subsequent step in many procedures is to evaporate a metal or dielectric layer and then remove the resist using solvents. The process of removing the patterned resist while leaving patterned metal behind is referred to as liftoff. A basic schematic of this procedure is shown below.

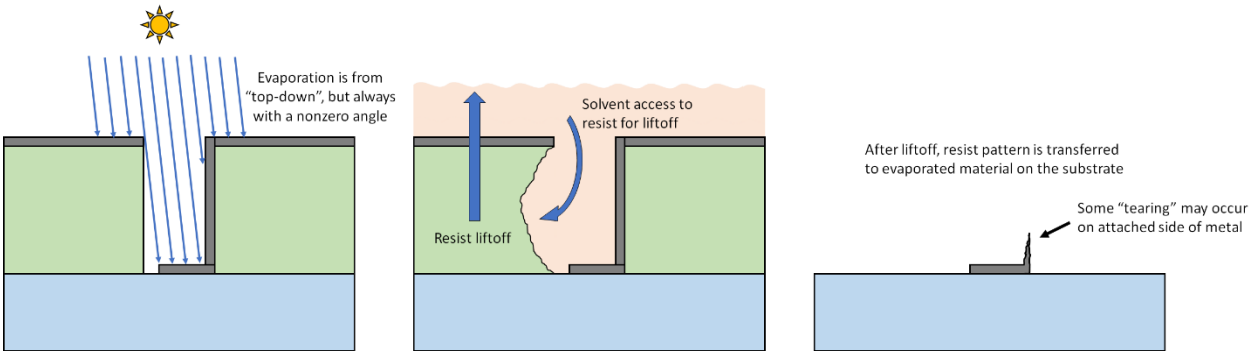

Figure 6.2 | Evaporation and liftoff. Directional evaporation of a metal or dielectric coats the top surface of the sample. Subsequent removal of the resist in a solvent solution leaves behind material that was evaporated directly onto the sample. In some instances, material that is attached to the sidewalls of the resist can result in tearing.

For evaporation onto a sample, it is vital to ensure there is suitable adhesion to the substrate surface or else the deposited material will peel off. To achieve this, a thin (~5 nm) "adhesion layer" of either Ti or Cr is deposited onto the sample before the target material is evaporated. For example, the deposition of gold electrodes on virtually all substrates involves a bilayer deposition of either Ti/Au or Cr/Au. The adhesion layer, in turn, will stick to a surface more effectively if it is oxygen plasma cleaned before deposition.

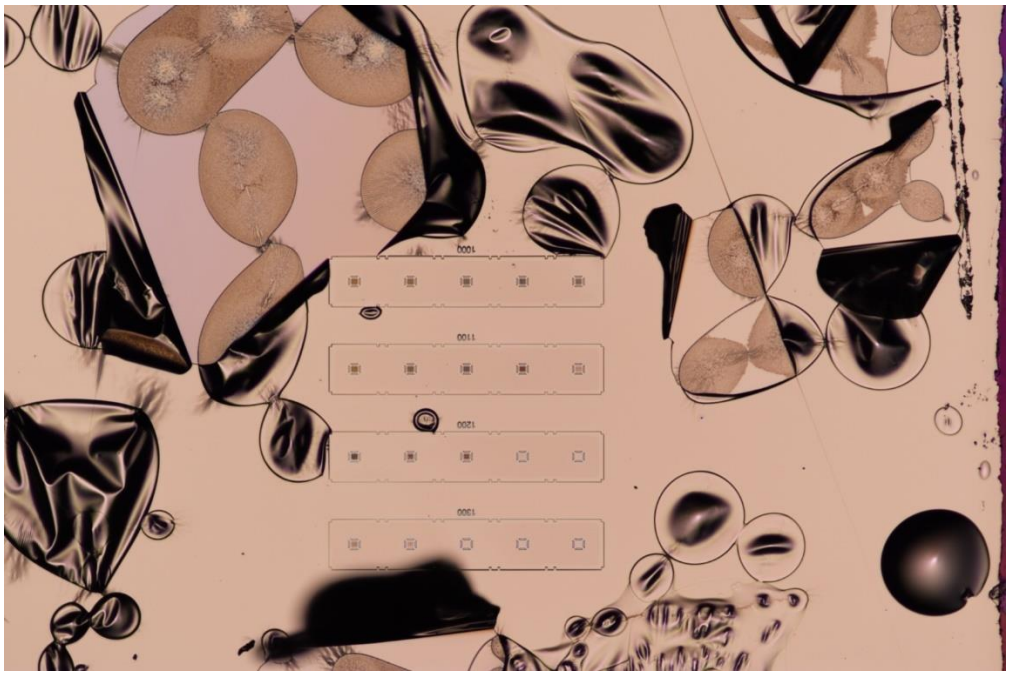

Figure 6.3 | Poor adhesion between evaporated Ni and SiC substrate. If an adhesion layer such as Ti or Cr is not used, then other evaporated metals such as Ni will not stick to the substrate. This results in the blistering and peeling shown above. Likewise, if the sample is not plasma cleaned before evaporation, then the adhesion will also be poor.

In many liftoff procedures, attachment of evaporated metal onto the sidewalls of the resist can result in unwanted "tearing" of the metal. This phenomenon is shown in the figure below, and can be avoided with either a bilayer of resist or a thin layer of resist.

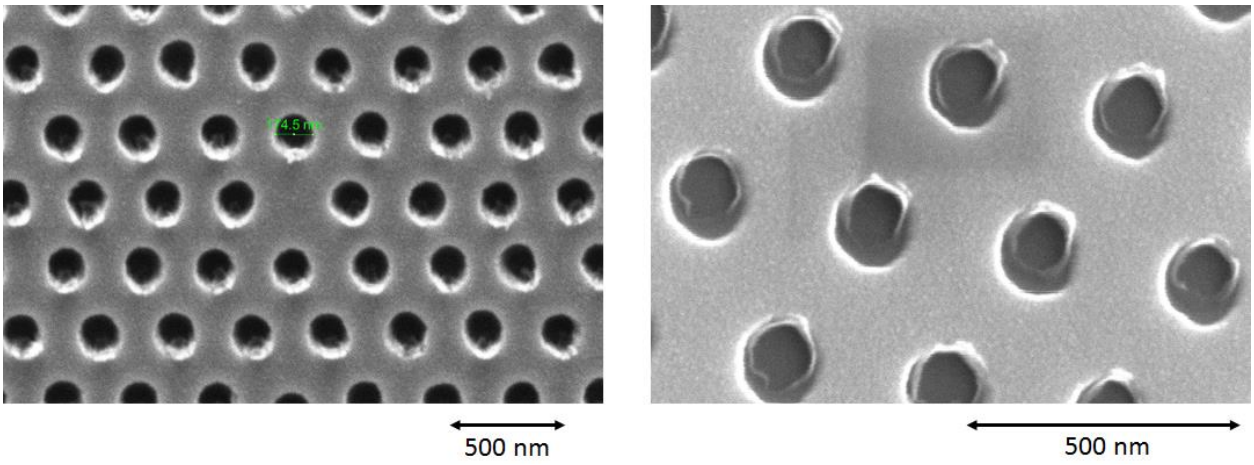

Figure 6.4 | Tearing from liftoff. Attachment of evaporated metal to the sidewalls of resist can result in unwanted tearing during liftoff, which is visible in these SEM images on the edges of the lifted off holes.

In order to achieve a successful liftoff, the resist thickness must be at least as thick as the material that is being patterned. For example, a 100 nm gold layer would require resist that is at least 100 nm thick. The thickness of resists can be measured directly with a profilometer, or estimated using the spec sheets of the resist. Finally, if the rotation option (which is used for uniform coatings) is on during evaporation, the resist will be completely coated with no solvent access and liftoff will not be possible, as outlined below:

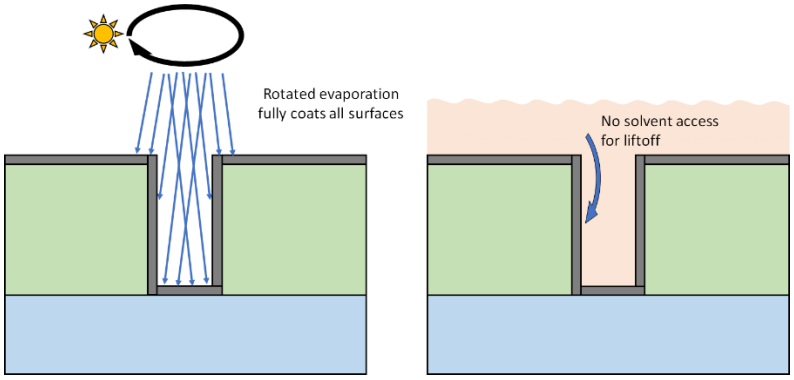

Figure 6.5 | Sample liftoff with rotated evaporation. If the rotation of the sample stage is turned on, the uniform coating of the material will make subsequent liftoff impossible, as the solvent has no direct access to the resist.

To avoid tearing during liftoff, occasionally a bilayer of resist is employed to avoid contact between the evaporated material and the sidewalls of the resist. For PMMA, different molecular weights (e.g. 495K vs. 950K) will develop at different rates, forming a window for evaporated material to deposit into. This geometry is outlined in the figure below.

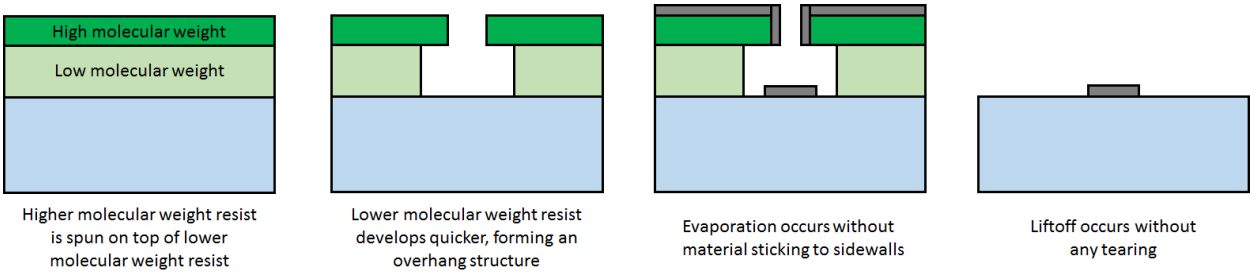

Figure 6.6 | Bilayer resist lithography. A combination of resists with different molecular weights results in a bilayer structure that avoids liftoff tearing.

A basic procedure for bilayer e-beam lithography is outlined below.

Bilayer PMMA e-beam lithography for gold electrodes

1) Solvent clean the chip with sonication
2) Drop cast PMMA 495K A6 onto chip
3) Spin at 3000 rpm, 45 s, 1000 rpm/s (~350 nm)
4) Bake at 180 ^{o}C for 5 minutes
5) Drop cast PMMA 950K A4 onto chip
6) Spin at 3000 rpm, 45 s, 1000 rpm/s (~200 nm)
7) Bake at 180 ^{o}C for 5 minutes
8) Perform Raith e-beam exposure + development
9) O2 descum the chip for 5-10 seconds to prep the surface for evaporation
10) Evaporate 10 nm Ti and 190 nm Au in the evovac evaporator with no rotation
11) Liftoff in acetone with low power sonication
12) Check sample under microscope

While the bilayer procedure works well for large features, nanoscale holes used for photonic crystals may still display unwanted artifacts from metal deposition, as shown below.

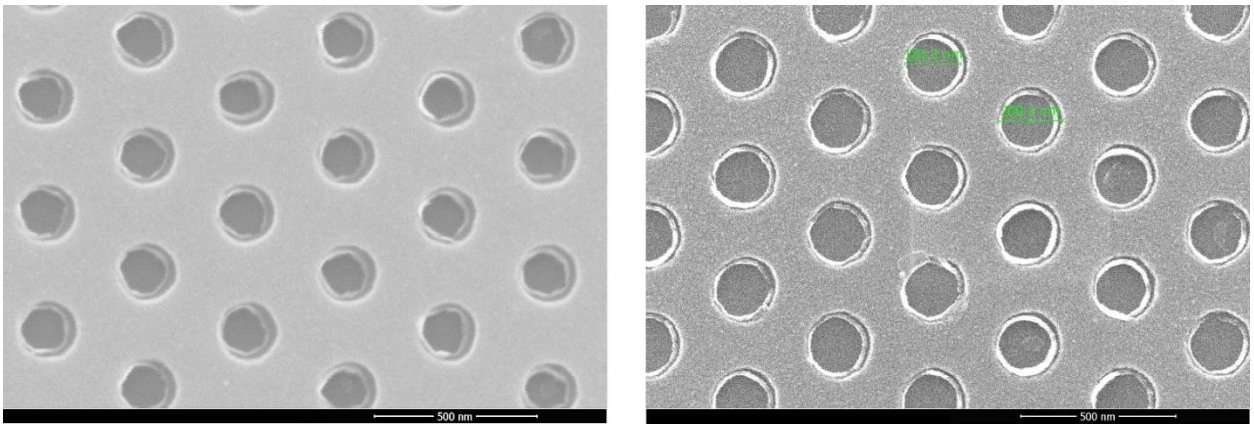

Figure 6.7 | Artifacts of evaporated metal in nanoscale features using bilayer resist lithography. For submicron features, the difference in lateral thicknesses of the two resists in a bilayer geometry can sometimes result in the deposited metal or dielectric displaying unwanted layers of coating. These features are visible as inner circles in the SEM images above.

6.3 Dry etching processes and hard masks

One of the most common ways to etch into a material is through an inductively coupled plasma (ICP) etch. In this process, a combination of chemical etching and physical bombardment of ions results in a directional etch into the target material. As a rule of thumb, the more a plasma etch relies on chemistry to react with the target, the more isotropic the etch will be. Meanwhile, the more that energetic bombardment is used, the more directional the etch will be. For silicon, there are a variety of fluorine-based gases such as SF_6, CF_4, CHF_3, XeF_2 that will readily react with silicon and etch it away from chemical reactions. For silicon carbide, one must rely on the physical impact of ions in combination with fluorine gases to achieve etching.

In order to selectively etch only targeted regions of silicon carbide, an etch mask much be used to protect regions of the sample. In principle a variety of materials can be used as a mask, such as aluminum, silicon oxide, or even resist. However, the relatively poor selectivity of these materials (~1:3 for Al, ~1:10 for SiO_2, ~1:1 for resist) can result in significantly sloped sidewalls, which has an adverse effect on photonic structures. The basic mechanism of this process, which involves degradation of the mask during the etch, is outlined in figure 6.8. Additionally, the effect of slopes sidewalls on photonic crystal designs is shown in figure 6.9.

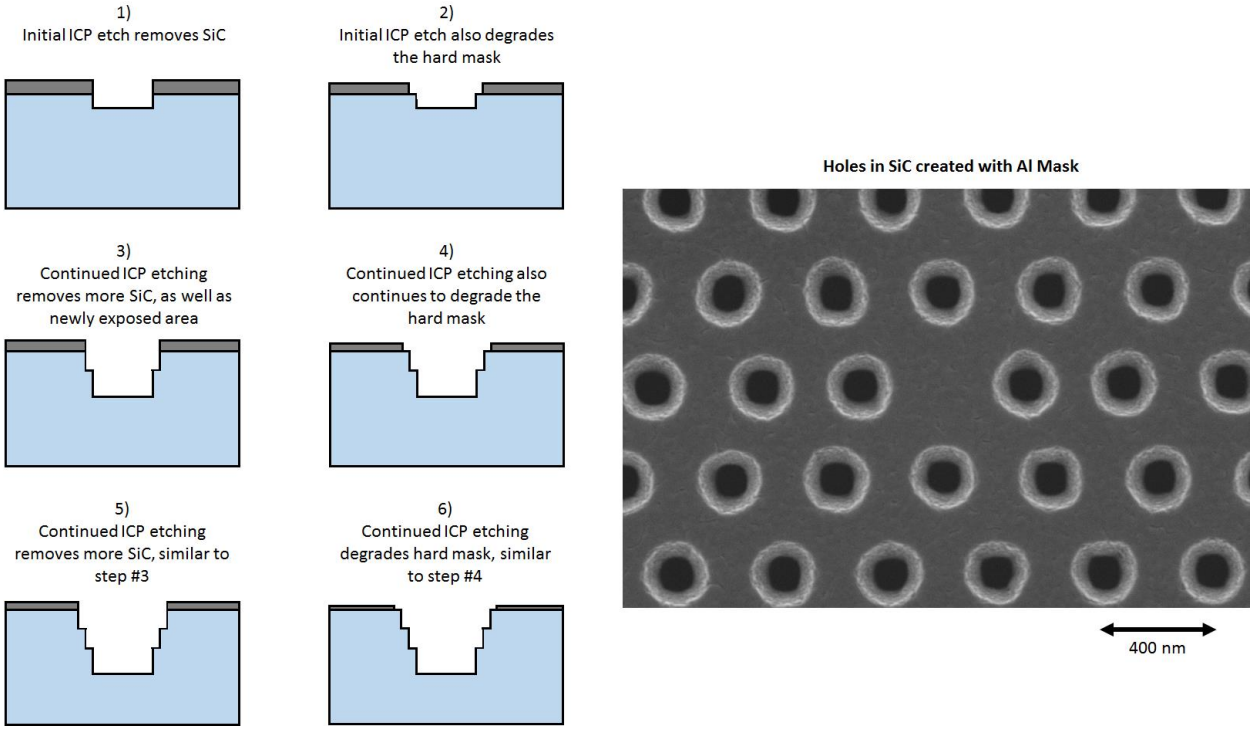

Figure 6.8 | Development of a sloped sidewall due to degradation of the hard mask. As an inductively coupled plasma removes substrate material, it also etches the hard mask, which can result in sloped sidewalls if the etch selectivity is not high.

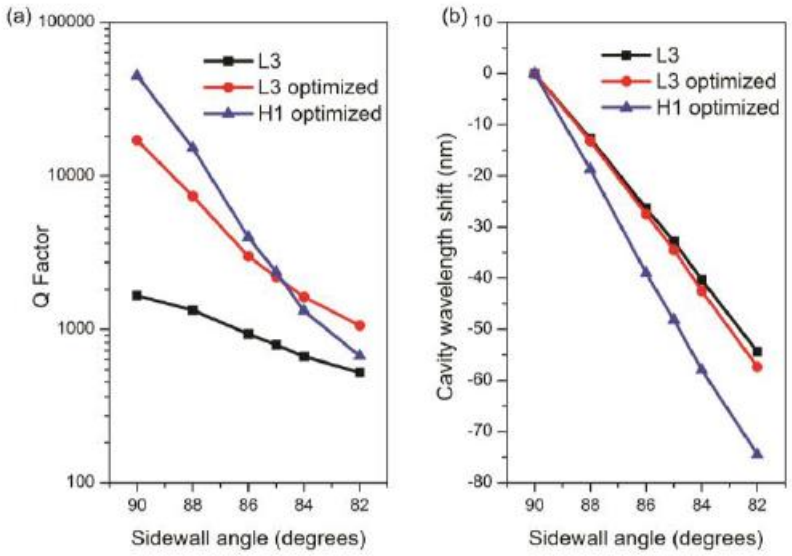

Figure 6.9 | Effect of sidewall angle on photonic crystal cavity resonances. Adapted from the supplement of [53]. Sloped sidewalls in photonic crystal cavity designs cause significant blueshifting of resonances and lowering of quality factors.

To address this issue, a hard mask with a high selectivity is desired. The most widespread hard masks for deep SiC plasma etching are nickel and copper [61]. Nickel offers a selectivity of ~1:40 with smooth sidewalls, while copper offers a higher selectivity of ~1:100 at the cost of roughened sidewalls. SEM profiles of etching using both masks are shown below.

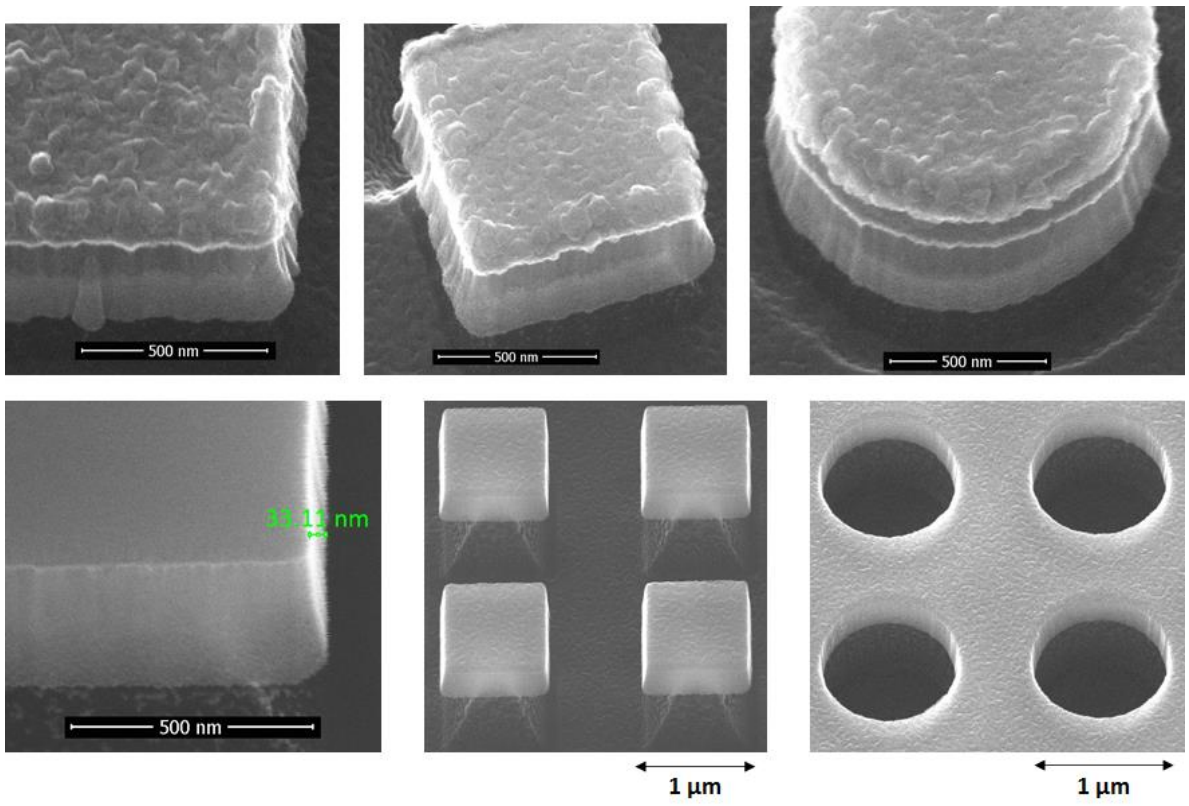

Figure 6.10 | Copper and Ni plasma etch masks for SiC. The copper etch mask (top row) has a higher selectivity of ~1:100, but results in significantly roughened SiC sidewalls. The nickel etch mask (bottom row) has a lower selectivity of ~1:40, but displays much smoother features. The sidewall angle for the Ni mask is ~85 degrees. All images are obtained with a scanning electron microscope.

In addition to the mask material, both the thickness of the resist used for liftoff and the parameters of the plasma etch can have drastic impacts on the sidewall angle and smoothness of the resulting structures. Some different parameters are shown below with a Nickel mask.

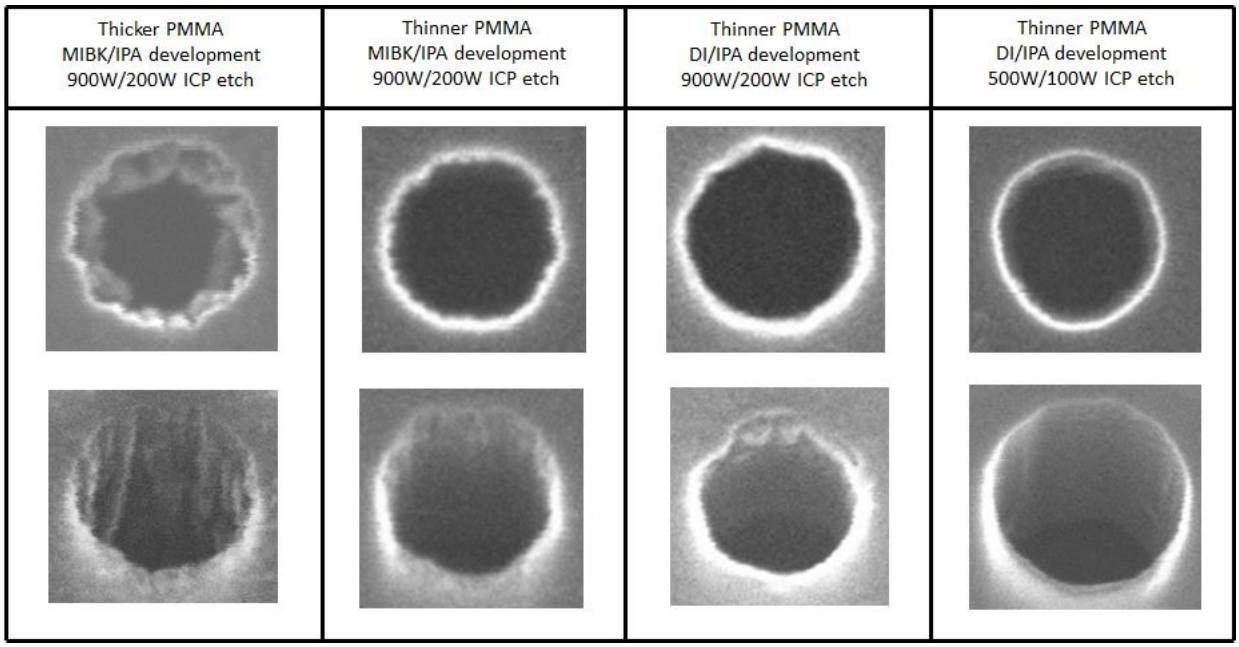

Figure 6.11 | Effect of plasma etch conditions and PMMA on feature roughness. All holes have a diameter of ~200 nm and a Nickel etch mask was used for all holes. A lower power ICP etch with thinner PMMA developed with a DI water and IPA mixture resulted in the smoothest holes. All images are obtained with a scanning electron microscope.

6.4 Photoelectrochemical etching

A prerequisite for nearly all nanophotonic structures is to isolate a submicron membrane of material either through a suspended undercut or a material heterostructure (e.g., silicon-on-insulator). For silicon carbide, thin membranes of the 3C polytype can be grown on a silicon substrate, but the same growth is not possible for 4H. Silicon-carbide-on-insulator (SiCOI) geometries are also not yet commercially available as they are for the SOI platform. Lastly, silicon carbide's near imperviousness to strong acids and bases makes it difficult to etch samples down to submicron thicknesses. Doing so usually requires a combination of mechanical polishing and time-intensive plasma etches.

As an alternative to these methods, it is possible to achieve an undercut in 4H-SiC through the use of photoelectrochemical (PEC) etching [62,63]. In this process, the doping of the silicon carbide determines whether etching will occur. In this way a selectivity can be achieved through a doping heterostructure which can be commercially obtained in SiC wafers. For our experiments, we selectively etched p-type SiC while leaving intrinsic and n-type regions unaffected. For all of our samples we used 1e18 cm^{-3} nitrogen doping for n-type, 1e18 cm^{-3} aluminum doping for p-type, and <1e15 cm^{-3} residual dopants for intrinsic I-type.

As the name implies, the PEC reaction involves a combination of photo-, electro-, and chemical processes working in tandem. Ultraviolet light is used as a source of electron-hole pairs, an applied voltage drives holes to the SiC surface, and a KOH or HF solution in combination with the surface holes oxidizes and etches the SiC. Due to the extreme danger of HF solutions, we opted to use KOH as the chemical solution. A schematic of the PEC setup can be seen in the figure below.

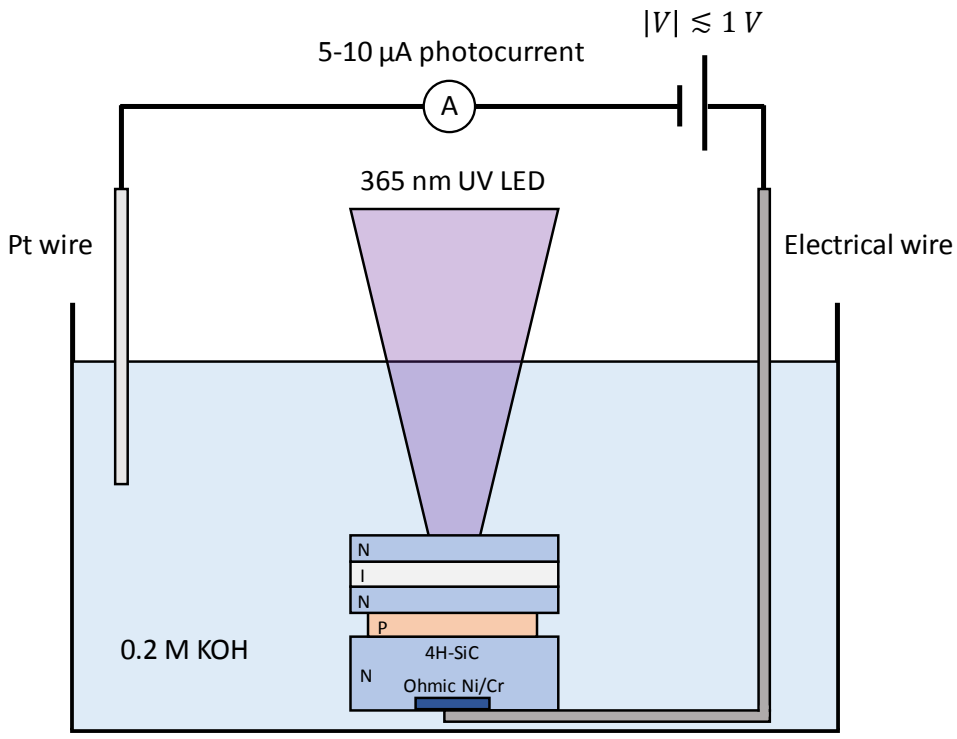

Figure 6.12 | Photoelectrochemical etching setup. A 4H-SiC sample (here with NINPN doped layers) is submerged in a 0.2 M KOH solution. electrical contacts are made with an electrical wire to Ohmic NiCr on the back of the chip and a platinum wire in solution. The voltage is varied so as to give a 5-10 μA photocurrent and is typically within a ±1 V range, although the exact voltage could be positive or negative. A 365 nm UV LED is used as a UV source.

A vital portion of the PEC electrical circuit is an Ohmic contact on the backside of the SiC chip. Otherwise, the Schottky barrier between the backside electrical contact and the chip will prevent voltage from being applied through the bulk of the SiC. To create an Ohmic contact, we sputtered ~300 nm of an 80/20 mixture of Ni/Cr on the backside surface and annealed at 950 ^{o}C for 5 minutes with Argon gas. We used a Solaris 150 RTP rapid thermal annealer for this fast anneal. For a typical PEC run, we use this backside contact as the anode, meaning it is the positive lead of the circuit. The submerged platinum wire then acts as the cathode, or negative lead. On rare occasions we had to flip this polarity to achieve etching, but this was atypical.

It is worth emphasizing that the behavior of the PEC etch varies continuously as the voltage is increased or decreased, even as it crosses from positive to negative voltage. Indeed, there is nothing "special" about zero voltage. The true electrical balance of the system is determined by the potential energy differences at the doped SiC interfaces, between the SiC surface and the KOH solution, and between the electrical wire and the backside contact. As result, one should not attach too much significance to the numerical value of the applied voltage. What is more important is the resultant photocurrent of the reaction. Here we define the photocurrent as the change in current that occurs when the UV light is turned on. Note that the ionic solution forms a complete circuit, so some magnitude of current will always be flowing with applied voltage. However, if this current does not change with the addition of UV light, then no etching is happening!

To achieve selective etching, we found that a photocurrent of 5-10 μA was ideal balance between selectivity and etch rate. Under these conditions PEC etch rates are typically on the order

of 100 nm/hour, so a total etch time of 5-6 hours is typical for a sample, usually across multiple runs. Depending on the sample, this photocurrent would sometimes result in wildly different applied voltages. For the most part, however, the voltage was usually within a ±1 V range. Generally, photocurrent can be raised or lowered by varying the applied voltage. More positive voltage will result in higher photocurrent magnitudes. If the photocurrent is too high, however, you will lose etch selectivity and etch both p- and n-type SiC. More negative voltage will result in lower photocurrent magnitudes. This is raises etch selectivity, but lowers the etch rate or stops etching altogether. It is worth noting that the appropriate voltage to obtain the desired photocurrent can change over the course of a run, so it should be checked approximately every 10 minutes. For the ultraviolet source, we use a Thorlabs 1150 mW 365 nm LED focused through a lens and operating at approximately two thirds power for most runs. The KOH solution is a 0.2 M concentration and is flowed with a peristaltic pump to aid the reaction process. SEM images of the PEC etching after several consecutive runs are shown in the figure below.

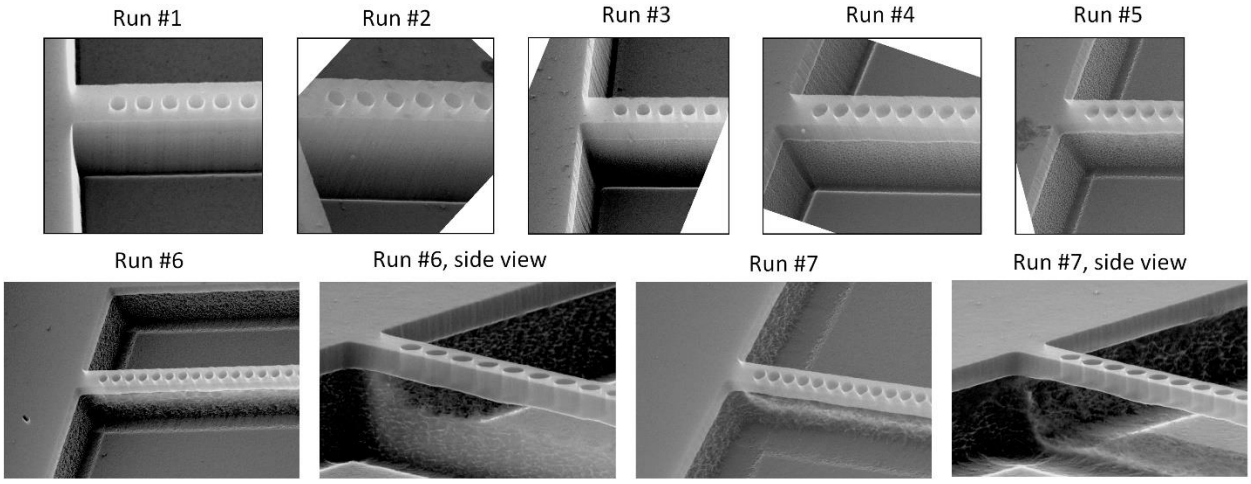

Figure 6.13 | Photoelectrochemical etch of p-doped silicon carbide across several runs. In the first four runs, a gradual degradation of the p-type SiC is observed. In runs 5-7, the p-type SiC steadily etches while the intrinsically doped (or n-type) SiC remains intact. All images are obtained with a scanning electron microscope. The hole lattice spacing is approximately 350 nm.

Chemical reaction:

The chemical reaction of PEC etching involves the surface oxidation of SiC followed by dissolution into the KOH. The total chemical reaction is outlined below.

$$SiC + 8OH^- + (n)e^+ \rightarrow SiO_2 + CO_2 + 4H_2O + (8-n)e^- \quad (6.1)$$

$$SiO_2 + 2KOH \rightarrow K_2SiO_3 + H_2O \quad (6.2)$$

$$\boxed{\mathrm{SiC + 8OH^- + (}n\mathrm{)e^+}} \rightarrow \mathrm{SiO_2 + CO_2 + 4H_2O + (8-}n\mathrm{)e^-}$$

$$\mathrm{SiO_2 + 2KOH} \rightarrow \mathrm{K_2SiO_3 + H_2O}$$

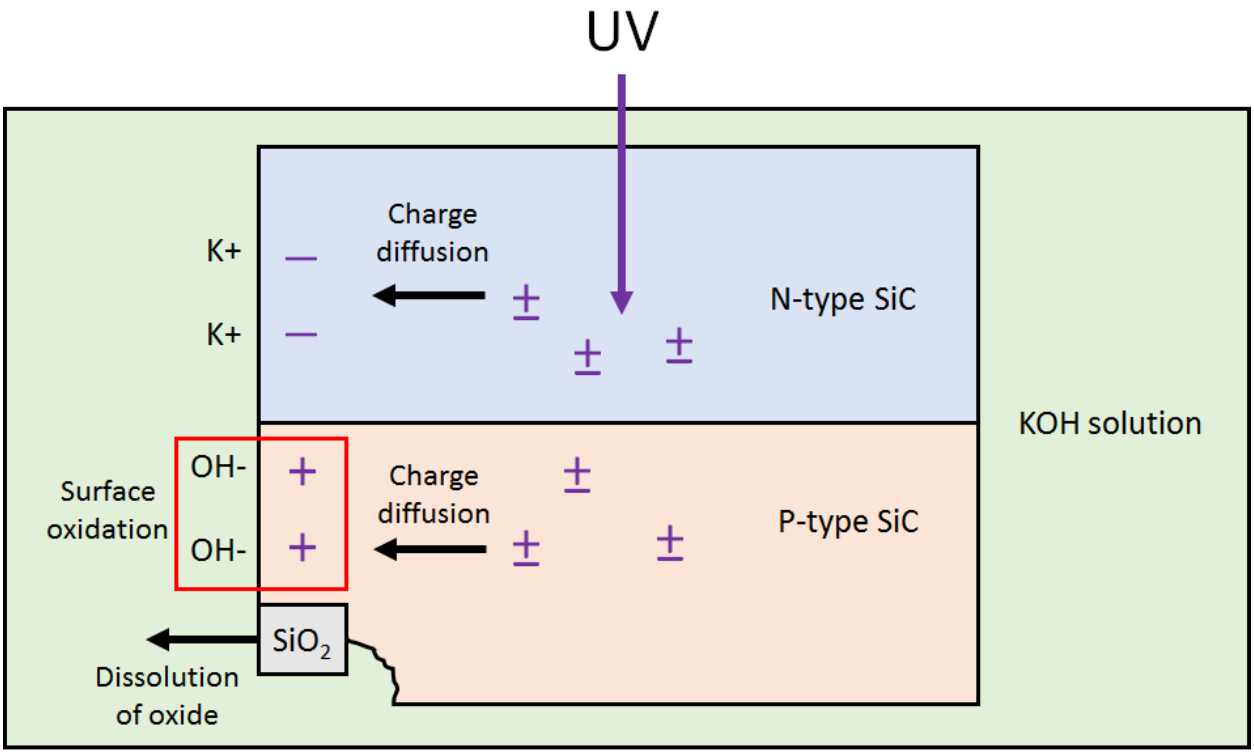

Figure 6.14 | Photoelectrochemical etch chemical reaction. UV irradiation causes electron-hole pairs to form (purple ±). As the holes are gated toward the p-type SiC surface, they combine with hydroxide ions in the KOH to form silicon oxide. This is the key part of the PEC reaction, and is boxed in the above equations and in the figure. The formed oxide is subsequently etched away with the KOH. The applied voltage is set to induce hole diffusion to the p-type SiC surface while keeping holes away from the n-type SiC surface.

Oxide growth

A full PEC run is typically 2-3 hours. It is not recommended to run longer than that, as there is a risk of undercut features breaking off from oxide growth. This means that a full undercut usually takes multiple PEC runs.

Drying undercut structures

Silicon carbide is structurally strong enough for IPA drying without using critical point drying that is common for silicon nanostructures. Air drying directly from water may cause collapse, however due to the higher surface tension of water.

Anisotropy of PEC etch

The PEC etch is anisotropic and predominantly to etch horizontally rather than vertically. This means that a photonic structure for a 2-micron p-type SiC layer requires etch holes that go through the 2 microns of p-type then PEC etch horizontally to achieve the undercut. If these holes are not close to the photonics, a full undercut becomes difficult.

6.5 Nanobeam photonic crystal fabrication procedure

The total procedure for the nanobeam photonic crystal fabrication in 4H-SiC is outlined below. Figure 6.15 gives a general schematic of the steps involved, while the steps discussed below elaborate on the procedure. This procedure is divided into 14 parts:

1) Pattern file creation and conversion
2) Cleaning the chip and depositing a conduction layer
3) Spinning PMMA and baking

4) Raith pre-measurement and sample loading
5) Raith writing and unloading
6) Development
7) Ni hard mask deposition
8) Liftoff
9) Liftoff characterization
10) ICP etching
11) Acid cleaning
12) Etch characterization
13) PEC etch
14) Final acid clean

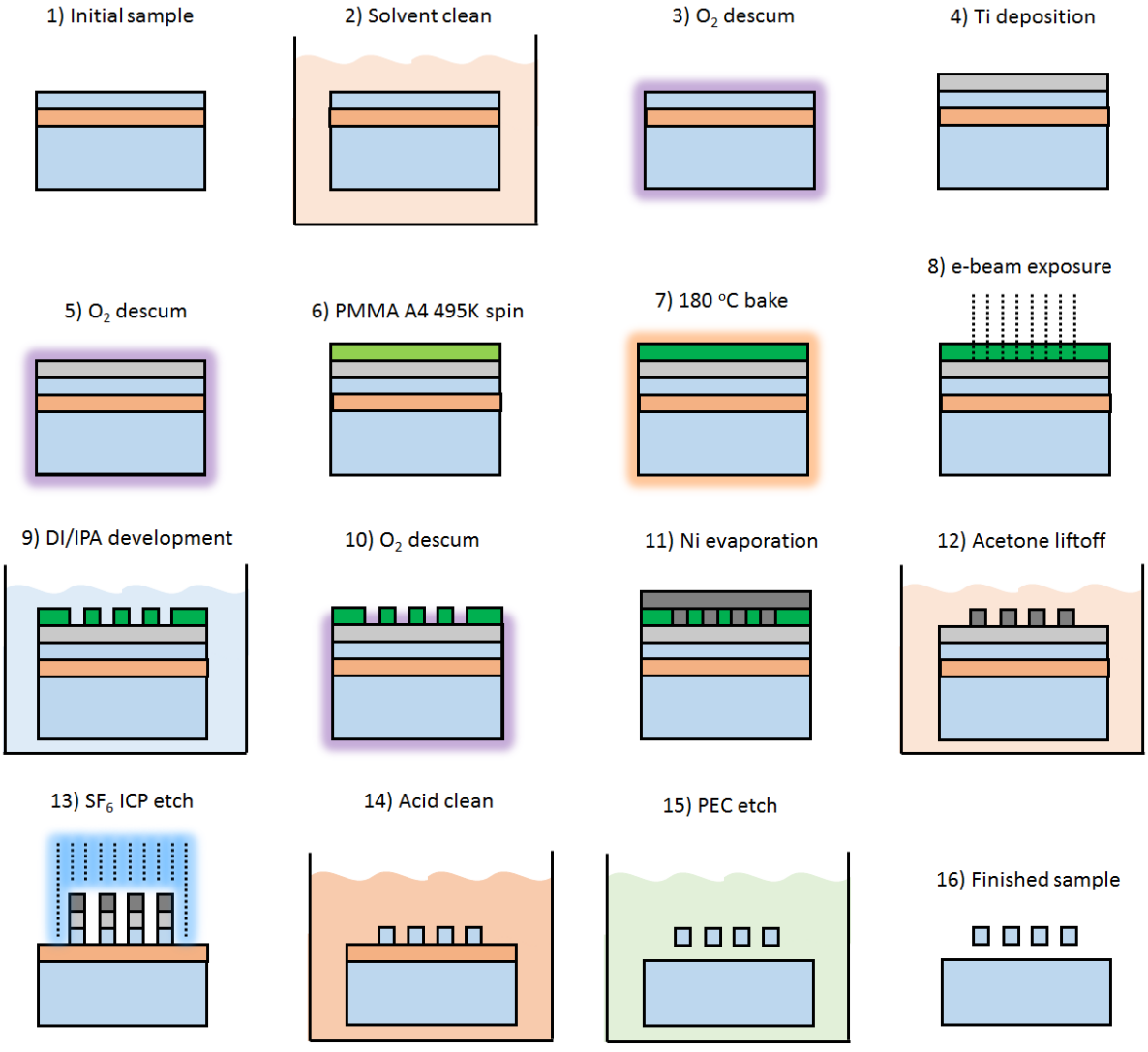

Figure 6.15 | Fabrication procedure for nanobeam photonic crystals in silicon carbide. In the initial SiC sample, the blue regions represent n-type or intrinsically doped SiC, while the red region represents p-type SiC to be etched via PEC. All pictures represent a side view of the sample.

1) Pattern file creation and conversion

Note that before entering the clean room, the pattern file for writing should be prepared and uploaded onto Box or email, where it can be accessed from the clean room computers. It is worth stressing that external USB flash drives are not used in the clean room, so file transfers must be done online. The full file conversion can also be done at any point outside of the fabrication procedure, and it may be a good idea to work through these conversions before processing the sample to save time. The general file conversion proceeds as follows:

$$\mathrm{PY} \rightarrow \mathrm{GDS} \rightarrow \mathrm{GPF} \rightarrow \mathrm{CJOB} \rightarrow \mathrm{JOB} \tag{6.3}$$

We use the python GDS CAD package to make pattern files. The python file outputs a GDS pattern file. This GDS file can be uploaded onto Box, then downloaded onto the clean room computer with Beamer software (just outside the Raith control room, opposite of the wet benches). Using beamer, the GDS file can be converted to a GPF file with appropriate electron beam conditions and resolution. This file can then be uploaded onto Box and downloaded from the Raith control computer, where it can be used as part of a CJOB file. The CJOB includes other components of the writing job such as placement and repetition of patterns, beam currents, optional labels, and optional alignment procedures. Once the CJOB file is complete, it is exported to a JOB file, which is what is literally run when an e-beam run is performed.

2) Cleaning the chip and depositing a conduction layer

Solvent clean the sample with 1-2 minutes of sonication in acetone and IPA. Inspect the sample under the microscope to ensure the surface is as clean as possible. Perform an O_2 plasma clean as both a cleaning step and a surface preparation for metal evaporation. Coat the topside of the sample with a conduction layer such as 5 nm of titanium. After the metal has been deposited, this is a "stable point" in the procedure. The sample can be left at this step for days or weeks and then resumed at a later time.

3) Spinning PMMA and baking

Preheat the hot plate for 180 ^{o}C. Note that this preheat may take several minutes, so it should be completed before doing any spins. Meanwhile, perform another O_2 plasma clean on the sample with the Ti conduction layer. This will prevent resist from balling up on the surface when it is drop cast. Once the hot plate is ready, spin a monolayer of PMMA A4 495K at 3000 rpm for 45 s with a 1000 rpm/s ramp. This should result in ~180-190 nm of resist. Slight edge beading will occur on the perimeter of the chip, but most of the interior of the chip will be usable for e-beam lithography. After the spin, bake the resist at 180 ^{o}C for 5 minutes.

4) Raith pre-measurement and sample loading

Vent the Raith sample loading chamber, which takes 5-7 minutes. Do not vent the main chamber of the instrument! Once the loading chamber is vented, remove the appropriate cassette and secure the sample onto the cassette. Load the cassette onto the microscope stage and write down the coordinates of the sample relative to the Faraday cup. Make sure the chip is at the right

height and level (no z-tilt). Laser height on microscope must read $0 < h < 50\ \mu m$. Place the cassette back into the loading chamber and pump it down.

5) Raith writing and unloading

Run the job writing file, with the pattern and beam conditions specified by the cjob file and gpf pattern file. An e-beam dose of ~400 μC/cm^2 is typical for PMMA A4 495K, although a dose array could be used for calibration. Once writing is finished, vent the Raith loading chamber and unload the sample.

6) Development

Development should occur immediately after writing. Prepare two dishes for development. One dish of 1:3 DI:IPA (e.g., 10 mL DI and 30 mL of IPA for 40 mL total) and another dish of pure IPA. Develop in the DI:IPA mixture for 2 minutes with occasional swirling. Place the chip in the IPA dish for 1 minute, with occasional swirling. N_2 dry the chip and inspect it under the microscope to make sure all the features are properly. Since PMMA is an e-beam resist, there is no risk of accidental exposure from room lights or microscope light. If the patterns are satisfactory, this is a "stable point" in the procedure. The next steps can be continued on the next day or multiple days later.

7) Ni hard mask deposition

Perform a 5-10 second oxygen plasma descum to prepare the chip's surface for Ni evaporation. A longer time will result in the PMMA starting to degrade. Evaporate 25 nm of Ni in the Nexdep evaporator with the tilted stage and no rotation. The tilted stage is so that the source evaporates at

a normal incidence to the sample. Nickel should be evaporated on manual mode, as the automatic PID is sometimes unable to handle the drastic increase in rate once the Ni reaches a high temperature.

8) Liftoff

Liftoff of PMMA is performed in acetone. Start by leaving the sample in acetone for 5-10 minutes, then sonicate at low power for 30 seconds. The liftoff might be incomplete, meaning further sonication for longer times at higher powers may be necessary. Even under full power sonication for several minutes, the Ni mask should be intact.

9) Liftoff characterization

SEM image the device to see what the Ni mask looks like. This is a vital step as it sets the tone for the rest of the fabrication run. If the mask looks bad (e.g., with liftoff tearing), the resulting etch will not be smooth. The procedure is also restartable at this point as the SiC has not been etched.

10) ICP etching

ICP fluorine etch for 2-3 minutes. We used a mixture of SF_6 and Ar gases at 40 and 10 sccm, respectively, with a bias power of 90 W and an ICP run power of 500 W at a process pressure of 6 mTorr. The SiC etch rate is roughly 350-400 nm/min under these conditions. The Ni mask selectivity is 1 : ~40-50. So, 25 nm Ni should give 1000-1250 nm of SiC etch.

11) Acid cleaning

Acid clean the residual Ni away with a piranha solution of 1:3 H_2O_2:H_2SO_4 followed by a 1:1 mixture of HF:HNO_3. Sometimes, multiple acid cleans and a O_2 descum is necessary to get rid of all the Ni residue.

12) Etch characterization

SEM the sample to examine the etched holes. If they look acceptable, proceed to PEC etching.

13) PEC etch

Perform the photoelectrochemical etch as outlined earlier in this chapter. Multiple PEC runs are usually needed to achieve a full undercut, with intermittent SEM to monitor the progress of the etch.

14) Final acid clean

Once PEC is complete, a final acid clean of HF/nitric and piranha should remove all residue from the completed devices. SEM images of completed devices are shown below.

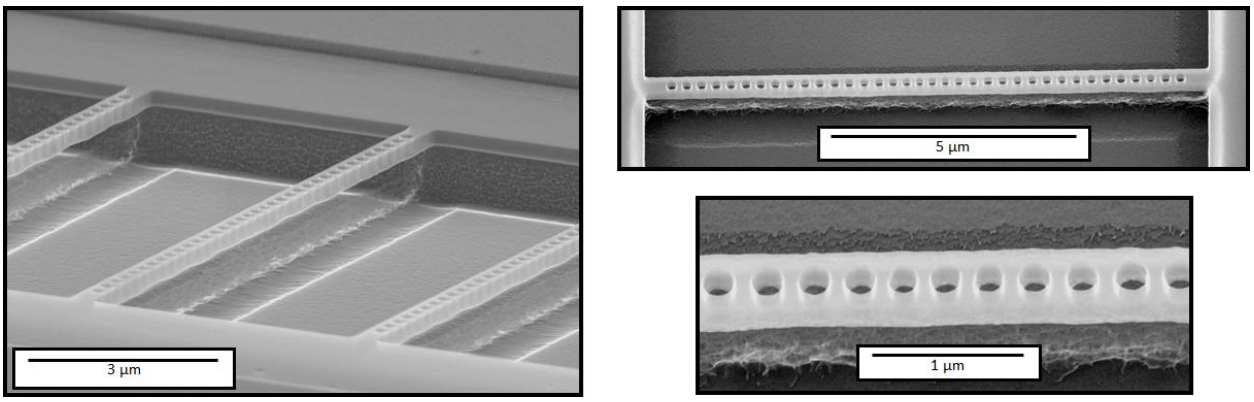

Figure 6.16 | Scanning electron microscope images of silicon carbide photonic crystals. Completed devices show relatively smooth etched holes with a sidewall angle of ~85 degrees. The etching of the p-type layer under the nanobeam provides a full undercut for photonic confinement in the z-direction.

6.6 E-beam lithography alignment on the Raith

Alignment is used in e-beam lithography when it is necessary to position separate patterns precisely relative to each other. This is most commonly achieved through the use of global alignment markers that serve as a reference for all pattern positioning. In order for the Raith software to recognize the presence of alignment markers, there needs to be a high material contrast under SEM imaging. This is achieved through a difference in atomic number between the marker material and the underlying sample. This also means that higher atomic weight metals such as gold (Z = 79) work best. If gold is not possible, the next best options are silver (Z = 47) and niobium (Z = 41), although thicker layers will need to be deposited to compensate for the lower atomic number. In order to utilize alignment markers on the Raith, the following procedure can be used:

Alignment procedure:

1) After mounting the chip in the microscope setup, make the alignment markers square such that there's less than a 1/300 deviation for x/y. E.g. if two alignment markers are separated in y by 300 microns, then the x offset has to be less than 1 micron. This corresponds to the rotation angle being less than the 0.2-degree threshold for the instrument.
2) Write down the center coordinates of each alignment marker
3) In cjob, put markers under the "exposure" tab. Click the checkbox: "Fixed Global Markers"
4) Then select the appropriate marker such as p20 (positive 20x20 micron square) or use the custom "joy" marker.

5) Enter the markers coordinates in a clockwise fashion. E.g., entering the coordinates for the upper left marker, then the upper right marker, and so on.
6) The program will rarely find the markers with -f coordinates, meaning you'll have to use SEM to find the marker absolute coordinates.
7) Switch to the beam current to be used for writing.
8) Use the terminal commands given below to go to each -f coordinate. Turn on the SEM, center on the marker, use "mvm" to find the marker, and then print out and write down the absolute coordinate for each marker. Toggle "SEM on" and "SEM off" to see the sample (and hopefully markers), but be careful because this exposes the sample. Here the viewing window of exposure is up to ±250 microns. Any other metal in this viewing window will interfere with the pattern marker recognition algorithm.
9) The program needs these absolute coordinates of the markers to run correctly.
10) As an example, the inputted coordinates could be something like:
"69909,124633 70809,124633 70809,123733 69909,123733"
11) If there is a rotation error, try removing the 4th marker from cjob and running with three markers instead.

Common terminal commands

You can run the following commands from the terminal of the Raith computer in Applications → System tools → Terminal

```
>mcur
```

move to faraday cup

```
>pg move pos --rel 55043,30667
```

Relative movement (relative to faraday cup)

```
>pg move pos 69864,112869
```

Absolute movement

```
>mvm /rel 0,0 p20
```

Look for a “p20” marker relative to the current location by the given coordinates.

In this case, 0,0 means search at the current location.

```
>mpg tab
```

Print out the current absolute coordinates

```
-f 55043,30667
```

This is a relative coordinate, relative to the faraday cup

```
69864,112869
```

This is an absolute coordinate

6.7 Miscellaneous procedures

In addition to the other procedures outlined in this chapter, other miscellaneous processes have been compiled below. For designing various processes, the reference [64] is incredibly helpful to determine which materials get etched by which chemicals. This information is vital for both etch masks and acid cleans of the sample.

PMMA A4 bonding recipe

This is used to bond small samples to carrier wafers, either for spin purposed or for use in instruments that only accept full wafers

1) Drop cast the PMMA A4 on the carrier wafer and perform the following spin:
    a. 5 seconds at 500 rpm (300 rpm/s ramp)
    b. 10 seconds at 2000 rpm (800 rpm/s ramp)
2) Place the small sample on the carrier wafer
3) Bake the wafer at 95 ^{o}C for 2 minutes (dehydration bake to prevent bubbling of resist)
4) Bake the wafer at 185 ^{o}C for 10 minutes to solidify the PMMA bond

HSQ (negative e-beam resist)

Spin:

4000 rpm for 30 seconds, 800 rpm/s ramp

Bake at 95 C for 2 minutes

Expose:

~775 $\mu C/cm^2$.

Develop:

Use TMAH in the acid hood for 70 s, then 70 s in DI water.

After development bake for 10 minutes at 300^{o}C to make the HSQ more uniform

AZ 1512 photolithography procedure

1) Solvent clean the same with acetone/IPA/DI/N2 dry
2) O_2 plasma clean
3) 1 minute hot plate bake at 150-200 ^{o}C as a dehydration bake
4) For < 1 cm chips, bond the chip to a carrier Si wafer with resist.
5) Use AZ 1518 resist, which is a positive resist. Spin at 3000 rpm, 60s, 2000 rpm/s.
6) Bake at 95 ^{o}C for 60 sec
7) Expose using 405 nm, dose array with 50-150 mJ/cm^2 in steps of 10 (most likely dose is 80-110)
8) Bake at 115 ^{o}C for 60 sec
9) Wait 3 minutes for rehydration
10) Develop in AZ300 MIF for 60 sec. Then rinse in DI water and N_2 dry
11) O_2 plasma clean
12) Use profilometry to measure resist thickness
13) Lift off by sonicating in acetone for 5 min (or longer if necessary) and then IPA for 1-3 min

HNA acid undercut (silicon wet etch)

An acid mixture termed “HNA” can be used to wet etch silicon. This consists of 5.5 parts acetic acid, 3.5 parts nitric acid, and 2 parts tracemetal grade HF (not buffered HF). The plastic pipettes provided by the clean room can be used to denote 1 “unit” of liquid. The etch rate is typically ~3-5 microns/minute. The main mechanism of this reaction is oxidation of the silicon by the nitric acid followed by subsequent etching of the silicon oxide with hydrofluoric acid. The role of acetic acid is to slow the reaction process. If a pure mixture of 1:1 nitric acid and HF is used, the exothermic reaction will occur so rapidly that the solution will fume and violently boil. If the sample is silicon carbide, however, this HF/nitric acid will not etch the material and serves as an excellent acid clean to remove most residue.

SF_6 plasma etch of silicon:

Time	60 seconds
Pressure	15 mTorr
HF power	20 W
ICP Power	80 W
O_2	5 sccm
SF_6	50 sccm
Temperature	20 ^oC
Helium backside pressure	10 Torr

This recipe has a fairly uniform etch, with an etch rate of 2-3 nm/s. One minute was not enough to get through 200 nm of silicon. I used a relatively low power to try to get a uniform etch, which seemed to work well. For the etch mask I used 20 nm of chromium. The recipe itself is one of the standard recipes for etching silicon. The other attempted recipes with polymers (CF4, CHF3) are intended for much deeper vertical etches of hundreds of microns, but they didn't work well with the 200 nm etch. The walls also appear to be relatively smooth, as can be seen in SEM imaging.

6.8 Microwave stripline B-field calculation

Here we calculate the magnetic field amplitude from a microwave stripline. The Biot-Savart law states:

$$d\vec{B} = \frac{\mu_0 I}{4\pi r^2} d\vec{L} \times \hat{r} \tag{6.4}$$

Where

$d\vec{L}$ is the infinitesimal length of conductor carrying electric current I. It points along the wire.

$\hat{r}$ is a unit vector pointing from the current to the point of interest.

I is the current running through the wire

r is the distance between the wire and the point of interest.

We normally have:

$$B_{wire} = \frac{\mu_0 I}{2\pi r} \tag{6.5}$$

So for a sheet of current, we have contributions of many small magnetic fields dB from infinitesimal line currents dI along the sheet:

$$dB = \frac{\mu_0}{2\pi r} dI \tag{6.6}$$

Assuming the current is uniformly distributed along a sheet of width w, an infinitesimal current dI should be determined by how wide your "mini-sheet" is (dr) compared to the total width w:

$$dI = \frac{dr}{w} \cdot I \tag{6.7}$$

So:

$$B = \int_{r=a}^{r=a+w} dB = \int_{r=a}^{r=a+w} \frac{\mu_0}{2\pi r} \cdot \frac{dr}{w} \cdot I \tag{6.8}$$

Where "r" is the distance from the point of interest to somewhere on the stripline. The way this is set up, the closer edge will be at r = a and the farther edge will be at r = a + w:

$$B = \frac{\mu_0 I}{2\pi w} \int_a^{a+w} \frac{dr}{r} \tag{6.9}$$

$$B = \frac{\mu_0 I}{2\pi w} {}_a^{a+w}|\ln(r) \tag{6.10}$$

$$B = \frac{\mu_0 I}{2\pi w} (\ln(a+w) - \ln(a)) \tag{6.11}$$

$$B = \frac{\mu_0 I}{2\pi w} \left(\ln\left(\frac{a+w}{a} \right) \right) \tag{6.12}$$

For a distance a away from the edge of a MW stripline that is w wide. This equation can be used when determining the distances and thicknesses needed for microwave striplines as a part of pattern files. As a general rule of thumb, the stripline should be within 100 microns of the divacancy of interest.

Chapter 7

Purcell enhancement of a divacancy

7.1 Motivation and overview

It is an overarching goal for many optically active qubit systems to extend the range of qubit-qubit interactions and scale to networks of many interconnected nodes. This holds true for quantum dots, color centers in semiconductors, rare-earth ions, and atomic vapor systems. In what is sometimes terms a "quantum network", photons act as the travelling carriers of quantum information, whereas electron and nuclear spins typically act as "stationary" qubits with long coherence times and the capability for local gate operations and entanglement. In the extreme limit, the communication distance between qubits could potentially extend beyond the range of single photons through fiber (~100 km). A device capable of such a long-distance interaction is generally called a "quantum repeater". Some proof of principle demonstrations of long-distance entanglement have been demonstrated with remote entanglement in the NV^- center in diamond [40,65,66]. For macroscopic length scales >1 m, there are three main ways to facilitate coherent interactions between remote stationary qubits through interconnected photons.

1) Direct absorption or interaction with a photon emitted from another qubit.
2) Two qubits simultaneously absorbing/interacting with each photon in an entangled photon pair generated from an EPR-like source.
3) Two qubits simultaneously emitting identical photons that impinge upon a central beamsplitter and detector.

These are outlined in figure 7.1 below:

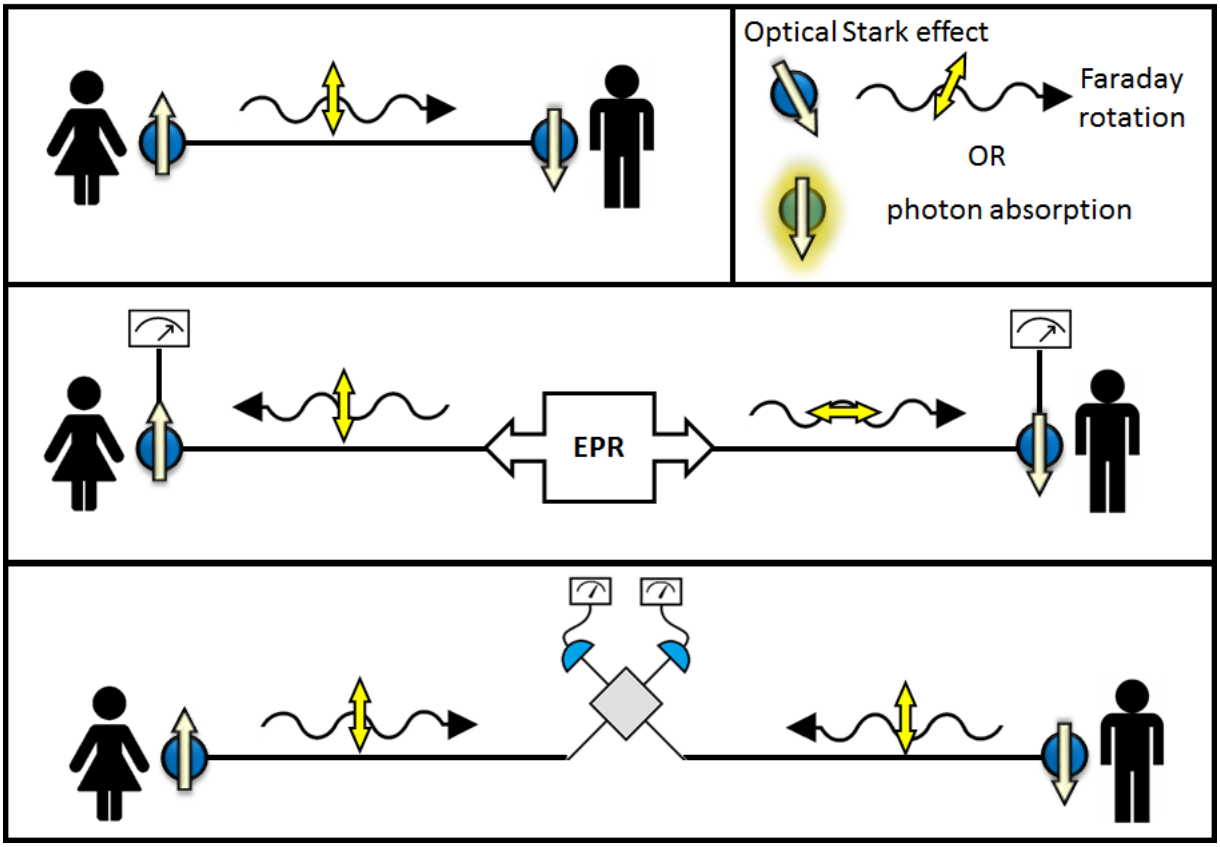

Figure 7.1 | Methods of photon-mediated distant spin-spin interactions. Top: A single photon emitted from the first spin coherently interacts with a second spin, either through the optical Stark effect/Faraday rotation or direct absorption. Middle: An EPR source of entangled photons is sent to equidistant spins, whose subsequent absorption and emission can herald entangled states. Bottom: Simultaneous emission from both spins impinges on a central beamsplitter, whose measurement can herald an entangled state [40].

Given the low absorption cross section of the VV^0 in SiC and weak interactions with single photons, the emission based strategy in #3 is perhaps the most promising idea. Critically, the zero-phonon line (ZPL) is the only source of indistinguishable photons for this approach that does not also leak quantum information to the environment through phonon emission. This means that a fundamental limit the effectiveness of this scheme is the probabilistic nature of the ZPL photon emission needed for remote interference. For the VV^0, only ~5% of emission is naturally in the ZPL. This means that in a spin-spin entanglement attempt, for example, there will only be a $(0.05)^2 = 2.5 \cdot 10^{-3}$ chance of success. This rate drops exponentially as the number of nodes increases.

As a potential remedy to this issue, the quantum community has turned to incorporating photonic nanocavities to modify the optical emission properties of the atom or defect in question [49-56, 67]. For the VV^0, a properly designed nanocavity can dramatically increase the percentage of light emitted into the ZPL, also known as the Debye-Waller factor. The increase of light into the ZPL is related to the Purcell factor, which was discussed in chapter 5. The direct relation, which will be derived in the next section, is given by:

$$\beta = \frac{F\alpha}{1 - \alpha + F\alpha} = \alpha\left(\frac{F}{1 - \alpha(F + 1)}\right) \tag{7.1}$$

Where β is the Debye-Waller factor in the cavity, α is the unmodified Debye-Waller factor, and F is the Purcell factor. As discussed in chapter 5, the Purcell factor is maximized with a high quality factor in a small mode volume, which motivates the use of nanoscale photonic cavities. In previous work with diamond and silicon carbide, photonic cavities have been fabricated with Q's on the order of ~10^3-10^4 with small mode volumes of $\sim(\lambda\backslash n)^3$, where λ is the cavity wavelength and n is the index of refraction of the material [49-56]. In silicon carbide, however, previous work

had not explored the coupling of photonic cavities with single divacancies, leaving the full potential of this system unfulfilled. It is therefore a major goal of this thesis work to explore single-VV^0 cavity interactions, as will be discussed in this chapter.

The experimental results presented in this chapter are adapted from the work [68]. The main result is the achievement of Purcell enhancement for a single VV^0 embedded in a photonic nanocavity. We also demonstrate control and coherence of the VV^0 ground state spin inside the cavity. The photonic cavity was fabricated in silicon carbide with a one-dimensional nanobeam photonic crystal design, with measured quality factors of ~5,000. The Purcell factor was measured to be F ~ 50 through multiple experiments, which included spectral enhancement and decreased excited state lifetime. The Debye-Waller factor is observed to improve from ~5% to ~70-75%, which greatly aids in potential spin-spin entanglement protocols that rely on this percentage.

7.2 Calculating Purcell enhancement for a VV^0-cavity system

Before we delve into sample and data specifics, we must establish some theoretical foundations on how to measure a Purcell factor for a cavity-VV^0 system generally. We will start with the basic definition of the Purcell factor presented in chapter 5:

$$F \equiv \frac{\gamma_{cavity}}{\gamma_{bulk}} = \frac{\tau_{bulk}}{\tau_{cavity}} \tag{7.2}$$

In the case of the VV^0, the "cavity" emission is not the entire VV^0 spectrum, but rather only its zero-phonon line. Therefore we write the Purcell factor as:

$$F = \frac{\Gamma_{ZPL,on}}{\Gamma_{ZPL,off}} = \frac{\tau_{ZPL,off}}{\tau_{ZPL,on}} \tag{7.3}$$

Where $\{\Gamma_{ZPL,on}, \Gamma_{ZPL,off}\}$ are the ZPL emission rates on/off cavity resonance, and $\{\tau_{ZPL,on}, \tau_{ZPL,off}\}$ are the ZPL lifetimes on/off cavity resonance. It is worth noting that we can immediately interpret the rates as intensities in a spectrum and write the relation:

$$F = \frac{I_{ZPL,on}}{I_{ZPL,off}} \tag{7.4}$$

Where $\{I_{ZPL,on}, I_{ZPL,off}\}$ in the intensity of light (number of counts) emitted into the ZPL when the cavity is on/off resonance. When we measure the lifetime of a divacancy, we are convolving all possible decays to the ground state. This can be represented by the equation:

$$\frac{1}{\tau_{off}} = \frac{1}{\tau_{ZPL}} + \frac{1}{\tau_{PSB}} + \frac{1}{\tau_{dark}} \tag{7.5}$$

Where τ_{off} is the measured lifetime from an excited state decay (as outlined in chapter 3) off cavity resonance. Here τ_{ZPL} is the ZPL lifetime, τ_{PSB} is the phonon sideband lifetime, τ_{dark} is the dark state lifetime from all nonradiative decays (such as ISC and ionizing/recharging). When on cavity resonance, the only quantity that should change is the τ_{ZPL}, as given by equation (7.3). This gives the on-resonance measured lifetime as:

$$\frac{1}{\tau_{on}} = \frac{F}{\tau_{ZPL}} + \frac{1}{\tau_{PSB}} + \frac{1}{\tau_{dark}} \tag{7.6}$$

Where τ_{on} is the measured lifetime from an excited state decay on cavity resonance. For upcoming derivations we will also need the lifetime definition of the Debye-Waller factor:

$$\alpha = \frac{\tau_{PSB}}{\tau_{ZPL} + \tau_{PSB}}, \qquad \text{Debye Waller factor} \tag{7.7}$$

These starting equations can then be used to derive all relevant measures of the Purcell factor in terms of experimentally measurable quantities. We will outline three measures here:

1) Purcell factor in terms of lifetimes
2) Purcell factor in terms of Debye-Waller factor
3) Purcell factor in terms of count rates

Purcell factor in terms of lifetimes

We start by rearranging equation (7.6) to isolate F:

$$F = \tau_{ZPL}\left(\frac{1}{\tau_{on}} - \frac{1}{\tau_{PSB}} - \frac{1}{\tau_{dark}}\right) \tag{7.8}$$

Experimentally, it is difficult to directly measure τ_{PSB} or τ_{ZPL}, but τ_{on}, τ_{off} can be obtained from lifetime measurements and τ_{dark} can be inferred from an autocorrelation measurement. Keeping this in mind, we can rearrange equations (7.5) and (7.7) to give:

$$\tau_{ZPL} = \frac{\tau_{off}\tau_{dark}\tau_{PSB}}{(\tau_{dark} - \tau_{off})\tau_{PSB} - \tau_{off}\tau_{dark}} \tag{7.9}$$

$$\tau_{PSB} = \frac{\tau_{ZPL}\alpha}{1 - \alpha} \tag{7.10}$$

Substituting (7.9) into (7.10) gives:

$$\tau_{ZPL} = \frac{\tau_{dark}\tau_{off}}{\alpha\left(\tau_{dark} - \tau_{off}\right)} \tag{7.11}$$

$$\tau_{PSB} = \frac{\tau_{dark}\tau_{off}}{(1-\alpha)\left(\tau_{dark} - \tau_{off}\right)} \tag{7.12}$$

Finally, substituting τ_{PSB} into equation (7.8) gives the Purcell factor as:

$$F = \frac{\tau_{dark}\left(\tau_{off} - \tau_{on}\right)}{\alpha\tau_{on}\left(\tau_{dark} - \tau_{off}\right)} + 1 \tag{7.13}$$

Under no enhancement, $\tau_{off} = \tau_{on}$ and this quantity approaches $F = 1$.

Purcell factor in terms of Debye-Waller factor

The Debye-Waller factor in equation (7.7) can be rewritten assuming cavity resonance by setting $\tau_{ZPL} \rightarrow \frac{\tau_{ZPL}}{F}$. This gives the equation:

$$\beta = \frac{\tau_{PSB}}{\frac{\tau_{ZPL}}{F} + \tau_{PSB}} \tag{7.14}$$

Where β is the Debye-Waller factor of the VV^0 on cavity resonance. Substituting in the expressions for τ_{ZPL}, τ_{PSB} in equations (7.11) and (7.12) then gives:

$$\beta = \frac{\frac{\tau_{dark}\tau_{off}}{(1-\alpha)\left(\tau_{dark} - \tau_{off}\right)}}{\frac{\tau_{dark}\tau_{off}}{F\alpha\left(\tau_{dark} - \tau_{off}\right)} + \frac{\tau_{dark}\tau_{off}}{(1-\alpha)\left(\tau_{dark} - \tau_{off}\right)}} = \frac{\frac{\tau_{dark}\tau_{off}}{(1-\alpha)}}{\frac{\tau_{dark}\tau_{off}}{F\alpha} + \frac{\tau_{dark}\tau_{off}}{(1-\alpha)}} = \frac{\frac{1}{(1-\alpha)}}{\frac{1}{F\alpha} + \frac{1}{(1-\alpha)}} \tag{7.15}$$

$$\beta = \frac{\frac{1}{(1-\alpha)}}{\frac{(1-\alpha) + F\alpha}{F\alpha(1-\alpha)}} = \frac{F\alpha}{1 - \alpha + F\alpha} \tag{7.16}$$

$$\beta = \alpha\left(\frac{F}{1+\alpha(F-1)}\right) \tag{7.17}$$

This equation is an important result in its own right, as it demonstrates how a Purcell enhancement can increase the percentage of light emitted into the zero-phonon line. A plot of β vs. F for some example values of α are shown in the plot below:

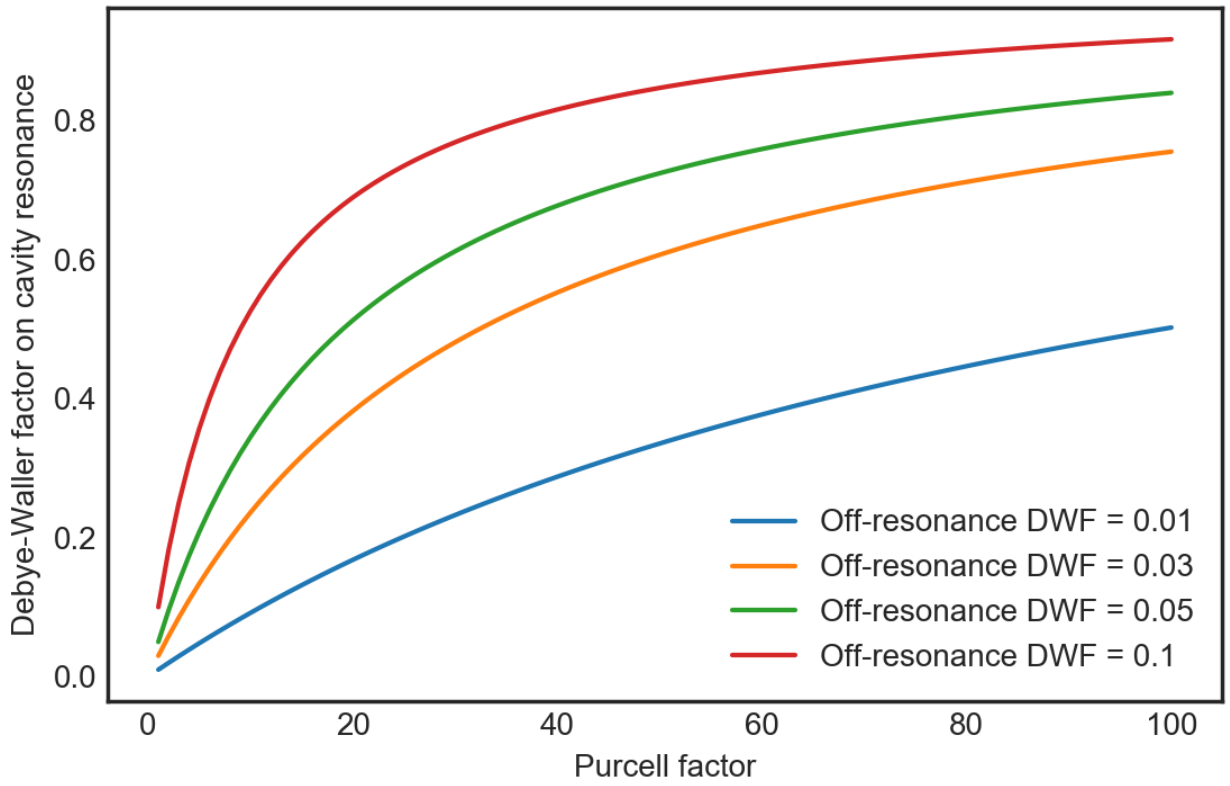

Figure 7.2 | Increased Debye-Waller factor from Purcell enhancement. Plotted here is the Debye-Waller factor vs. Purcell factor F for example values of the initial Debye-Waller factor without any enhancement (F = 1). Higher enhanced Debye-Waller factors (β) require correspondingly higher Purcell factors (F) and unenhanced Debye-Waller factors (α).

Isolating F from equation (7.17) then gives:

$$F = \frac{\beta(\alpha-1)}{\alpha(\beta-1)} \tag{7.18}$$

In this way, the Purcell factor can be expressed in terms of the Debye-Waller factors on and off cavity-resonance.

Purcell factor in terms of count rates

Taking the literal definition of the Debye-Waller factor, we can express α, β in terms of intensities:

$$\alpha = \frac{I_{ZPL,off}}{I_{off}}, \qquad \beta = \frac{I_{ZPL,on}}{I_{on}} \tag{7.19}$$

If we assume the increase of total counts on cavity resonance is solely due to increased counts into the ZPL, this gives another equation:

$$I_{on} - I_{off} = I_{ZPL,on} - I_{ZPL,off} \tag{7.20}$$

When measuring total count rates, this means we have:

$$\{\alpha,\ I_{off},\ I_{on}\}, \qquad \text{known} \tag{7.21}$$

$$\{\beta,\ I_{ZPL,off},\ I_{ZPL,on}\}, \qquad \text{unknown} \tag{7.22}$$

Luckily this is a situation with three equations and three variables, so each quantity is algebraically solvable. The equations in (7.19) can be combined to give:

$$I_{ZPL,on} - I_{ZPL,off} = \beta I_{on} - \alpha I_{off} \tag{7.23}$$

Substituting this into equation (7.20) gives:

$$I_{on} - I_{off} = \beta I_{on} - \alpha I_{off} \tag{7.24}$$

Rearranging then gives β:

$$\beta = \frac{I_{on} - I_{off} + \alpha \cdot I_{off}}{I_{on}} \tag{7.25}$$

This equation can be used to estimate an improved Debye-Waller factor from total count rates. Meanwhile, $I_{ZPL,off}$ and $I_{ZPL,on}$ can be isolated using equations (7.19) and (7.20) to give:

$$I_{ZPL,off} = \alpha \cdot I_{off} \tag{7.26}$$

$$I_{ZPL,on} = I_{on} - I_{off} + \alpha \cdot I_{off} \tag{7.27}$$

Which, taking a ratio, then immediately gives F as:

$$F = \frac{I_{on} - I_{off} + \alpha I_{off}}{\alpha I_{off}} \tag{7.28}$$

Thus, if we assume all count increases on cavity resonance are due Purcell enhancements, we can use the total count rates to obtain the Purcell factor.

7.3 Photonic crystal design

Given that the centerpiece of this chapter's work is photonic enhancement, it is worth discussing the concept of photonic cavities and some of the designs that were explored. In the broadest sense, a photonic cavity is any structure that spatially confines light. Since there is no way to make photons or light rays "hold still", confinement is achieved through the repeated reflection off of cavity boundaries. The simplest photonic cavity is the Fabry-Perot cavity, which involves two

parallel mirrors facing towards each other. While physical mirrors can of course be made from reflective surfaces, there are other methods for reflecting light. For example, any interface with differing indices of refraction on both sides will have a component of reflection (see Fresnel reflections in chapter 3). For a suitably sharp angle of incidence, light will be completely reflected through total internal reflection. This confinement of light is the key operating principle behind fiber optics and microring and microdisk resonators.

In addition to the total internal reflection mechanism, three-dimensional confinement can also be achieved through the use of Bragg mirrors for reflection. A Bragg mirror consists of a periodic array of dielectric materials with varying refractive indices that combine to give an overall reflection. The simplest example is the one-dimensional Bragg stack, which uses alternating layers of material to achieve reflection. On the nanoscale, Bragg mirrors can be formed out of a one-dimensional or two-dimensional patterning of finite sized holes in a dielectric material instead of the pseudo-infinite planes in a Bragg stack. These then form the basis of one- or two-dimensional photonic crystal designs.

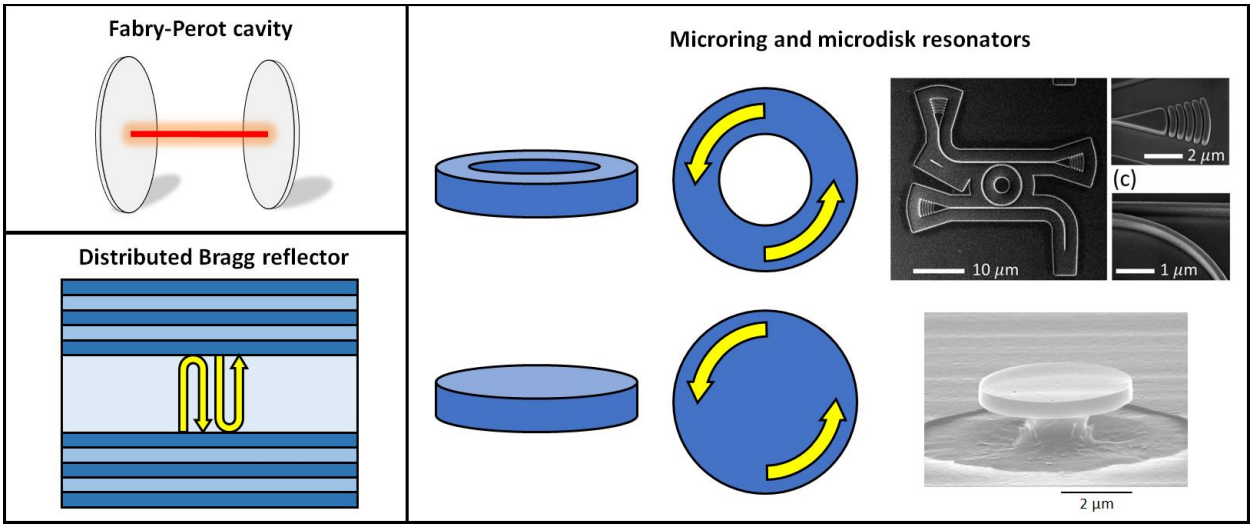

Figure 7.3 | Common photonic cavity designs. Fabry-Perot and distributed Bragg reflector cavities rely on continual back and forth reflection of light for confinement. In microring and microdisk resonators, the light is confined to the edges of the structure in a whispering gallery mode. The structure must be thin enough (usually sub-micron) for total internal reflection to confine the light in the z-direction. Microring resonator SEM adapted from [69]. Microdisk resonator is made in 4H-SiC with a PEC undercut.

In the most general sense, a photonic crystal is any periodic patterning of dielectric material. For optical cavities, photonic crystals are designed on the length scale of the wavelength of visible or infrared light. Creating a defect in the periodic dielectric structure can then from an optical cavity that traps photons, in a similar way to how a defect in an atomic crystal can form a trap for electrons (e.g., the divacancy). Creating an idealized photonic crystal cavity is an entire field of study that we will avoid getting into too much detail about in this thesis. However, some common photonic crystal cavity designs are shown in the figure below, with quality factors of up to 11 million [70-72].

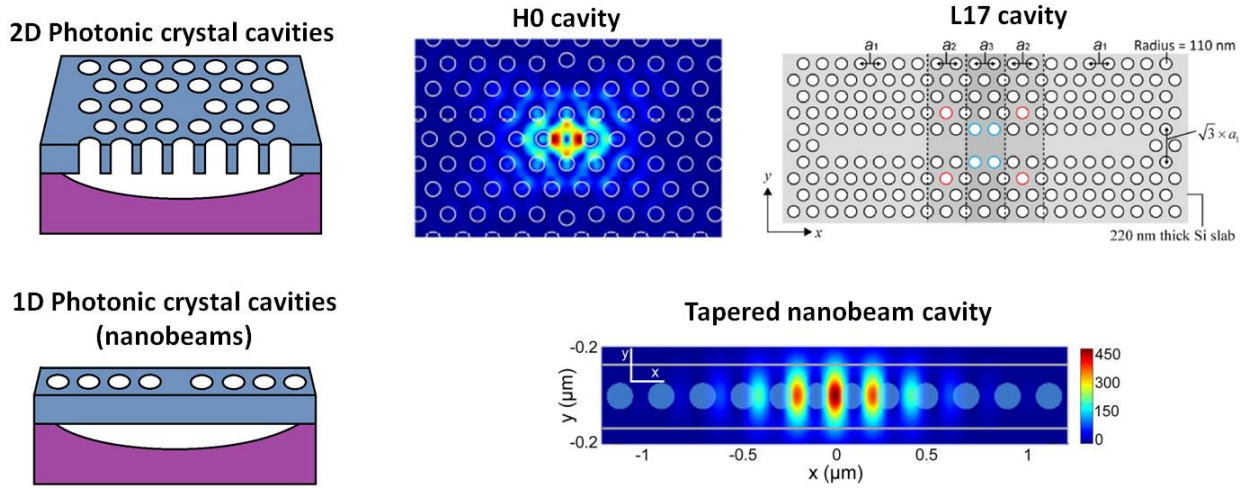

Figure 7.4 | Common photonic crystal cavity designs. Both 2D and 1D photonic crystal designs rely on Bragg mirrors (holes) to confine light laterally and total internal reflection (TIR) for confinement in the z-direction. The 1D nanobeam design uses TIR for two axes, so the beam must have a suitably thin height and width (usually submicron). H0 cavity adapted from [70]. L17 cavity adapted from [72]. Tapered nanobeam cavity adapted from [55].

For this work, we selected a nanobeam photonic crystal design due to its small mode volume and smaller footprint compared to the two-dimensional photonic crystal designs [55,56,73]. This is important for iterating over design parameters and for proximity to microwave lines for spin control. The design consists of a linear tapering of both the lattice spacing and the minor axis radii of the central 8 holes (4 on each side of the center) to 84% of an original value. Here the minor axis is along the long axis of the beam. The design of the pattern in shown below:

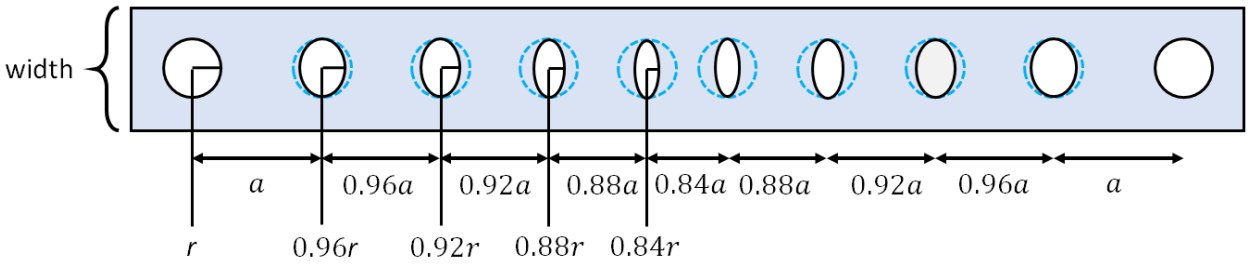

Figure 7.5 | Nanobeam photonic crystal cavity design. The lattice spacing and hole width are linearly tapered over 4 holes to 84% of their bulk values. The cavity mode is located between the two centermost elliptical holes.

We used *Lumerical FDTD Solutions* to model various nanobeam designs in silicon carbide. We obtained high simulated quality factors of ~300,000 at ~1130 nm with the following design parameters:

Hole radius = 83 nm

Lattice spacing (hole-to-hole) = 337 nm

Beam thickness = 322 nm

Beam width = 415 nm

The ratio of these dimensions (approximately 1:4:4:5 for radius, lattice spacing, thickness, and width) can be maintained while scaling the entire structure up or down while maintaining a high simulated quality factor above 100,000. Larger scale structures will have longer resonant wavelengths and vice versa. The Lumerical model of the resonant mode of the above cavity design is shown in the figure below:

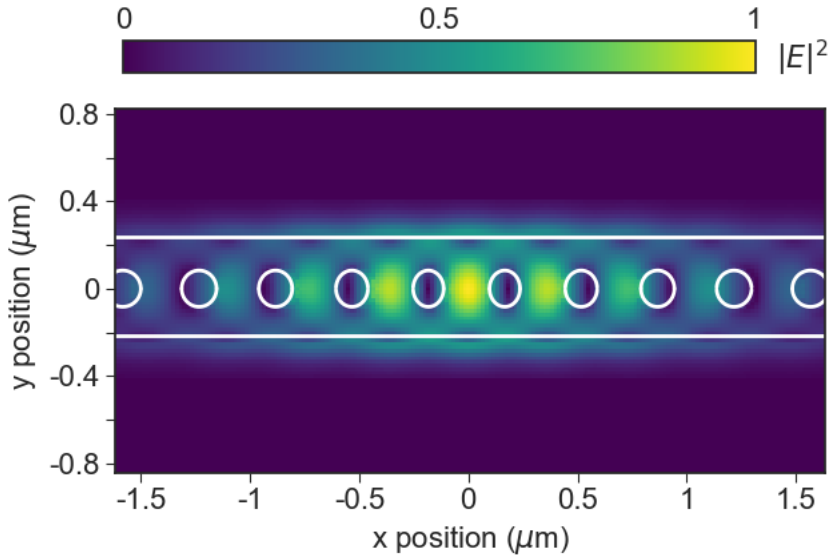

Figure 7.6 | Lumerical simulation of nanobeam photonic crystal mode. The cavity mode is concentrated between the centermost two holes, with a simulated quality factor of ~300,000 at $\lambda = 1130\ nm$ and a mode volume on the order of $(\lambda/n_{SiC})^3$, where $n_{SiC} \approx 2.6$.

With this cavity design selected, we fabricated this structure in suspended silicon carbide and measured the resulting quality factors, as discussed in the next section.

7.4 Photonic crystal fabrication and characterization

The photonic cavities were fabrication in the Pritzker Nanofabrication Facility (PNF) using a combination of e-beam lithography, inductively coupled plasma etching, and photoelectrochemical etching. The full procedure is described in more detail in chapter 6, but an abbreviated procedure is given below:

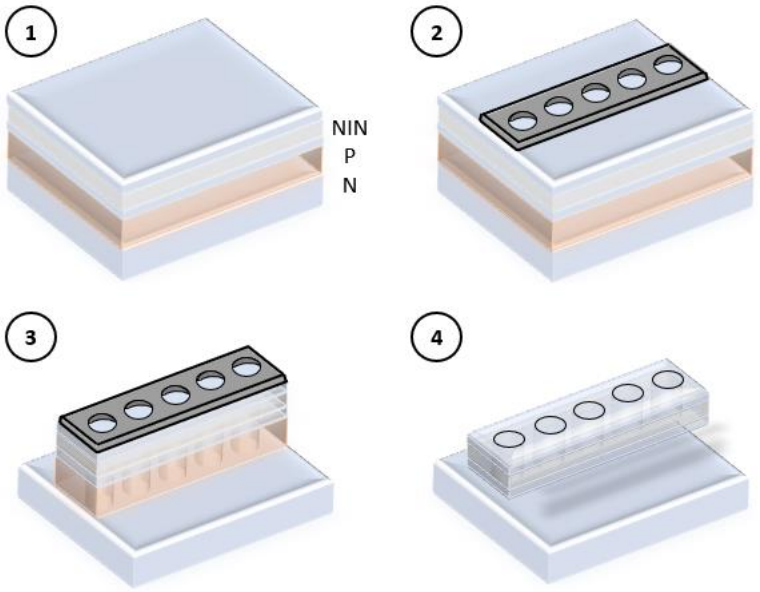

Figure 7.7 | Fabrication procedure for SiC nanobeam photonic crystals. (1) A NINPN doped SiC chip is used as the starting material, where N denotes n-type, I denotes intrinsically doped with residual dopants, and P denotes p-type. (2) Electron beam lithography defines a 25 nm thick nickel mask. (3) A SF_6-based ICP etch transfers the mask pattern to the SiC substrate. (4) A PEC selectively etches p-type SiC and creates an undercut structure.

After a large amount of troubleshooting, this procedure eventually succeeded on selectively doped silicon carbide chips with a 400 nm thick NIN photonic layer. Scanning electron microscope (SEM) images of some completed devices are shown below:

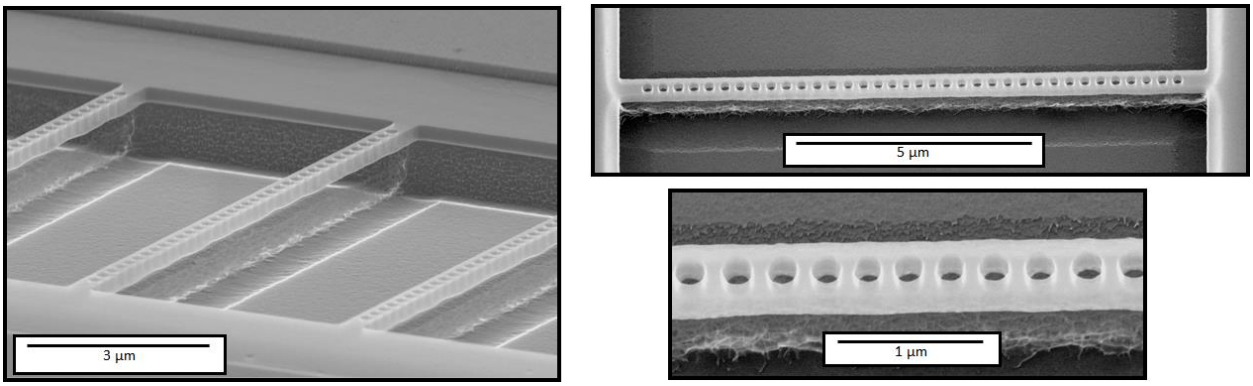

Figure 7.8 | Scanning electron microscope images of nanobeam photonic crystals. The photonic crystals display a full undercut with relatively straight and smooth sidewalls, which are critical for achieving a high quality factor.

Although the samples were uniformly populated with divacancies, only a small fraction of the nanobeams contained a divacancy in the mode volume at the exact center of the beam. For those that did have an embedded divacancy, we took a room temperature excitation spectrum to characterize the cavity quality. An example of such a scan is shown below.

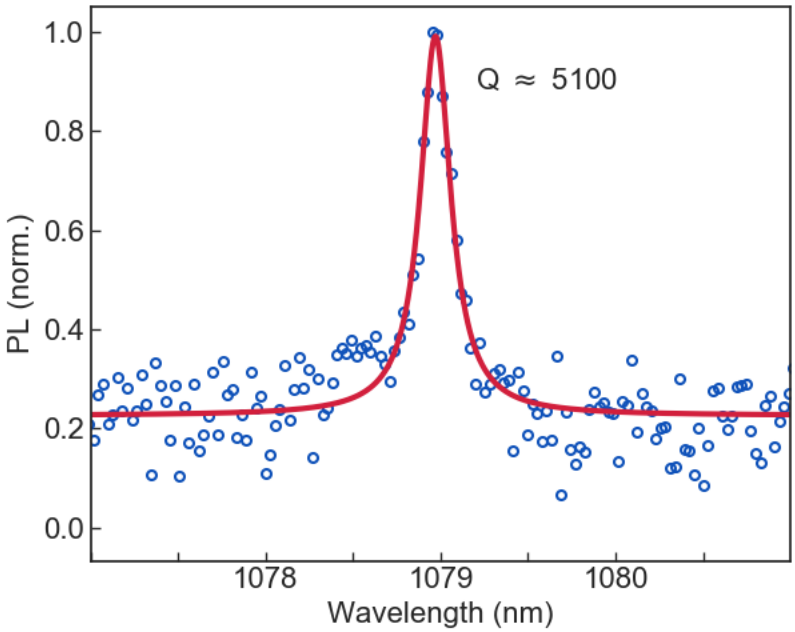

Figure 7.9 | Quality factor measurement on nanobeam photonic crystal. Based on a Lorentzian fit of the full-width half-maximum, this cavity has a quality factor of roughly 5,100.

For the particular nanobeam that will be used for cavity-VV^0 interactions in this chapter, scanning electron microscope (SEM) images give the following approximate dimensions:

Beam width = 450 nm

Beam thickness = 400 nm

Hole radius = 125 nm

Lattice spacing (hole-to-hole) = 342 nm

Sidewall angle = 86 degrees

Simulating these dimensions in *Lumerical* gives two resonances at 1077 nm and 1103 nm with quality factors of 18,000 and 22,000, respectively at 1103 nm. This approximately matches with the measured quality factor of ~5,000 at 1078 nm, with the loss in in quality coming from fabrication imperfections such as surface roughness and sidewall slope.

7.5 Sample preparation

The work carried out in this thesis was for 4H silicon carbide custom ordered from Norstel with doping configurations described below. An initial 4-inch wafer was diced into small ~5x5 mm pieces, providing approximately 300 samples to work with. Many of these samples were used for fabrication tests, fine tuning photonic crystal designs, and photoelectrochemical etch tests. A smaller subset was used for divacancy creation, also discussed below.

Divacancy creation

Divacancies were created in the silicon carbide with a combination of electron irradiation and high temperature annealing. We sent samples to the National Institutes for Quantum and Radiological Science and Technology in Takasaki, Japan for irradiation with relativistic 2 MeV electrons that damage the SiC lattice and create individual silicon and carbon vacancies. We then perform a high temperature anneal at 850 °C for 30 minutes with argon gas at atmospheric pressure. This causes the vacancies in the SiC lattice to diffuse and form more stable divacancies when they coincide. For the samples in this thesis, we used an electron irradiation dose of 10^{15} electrons per square centimeter in order to create a high enough divacancy density to populate most nanobeams with a defect. We also performed the irradiation and annealing before fabrication to verify its success. A schematic of the process is shown below.

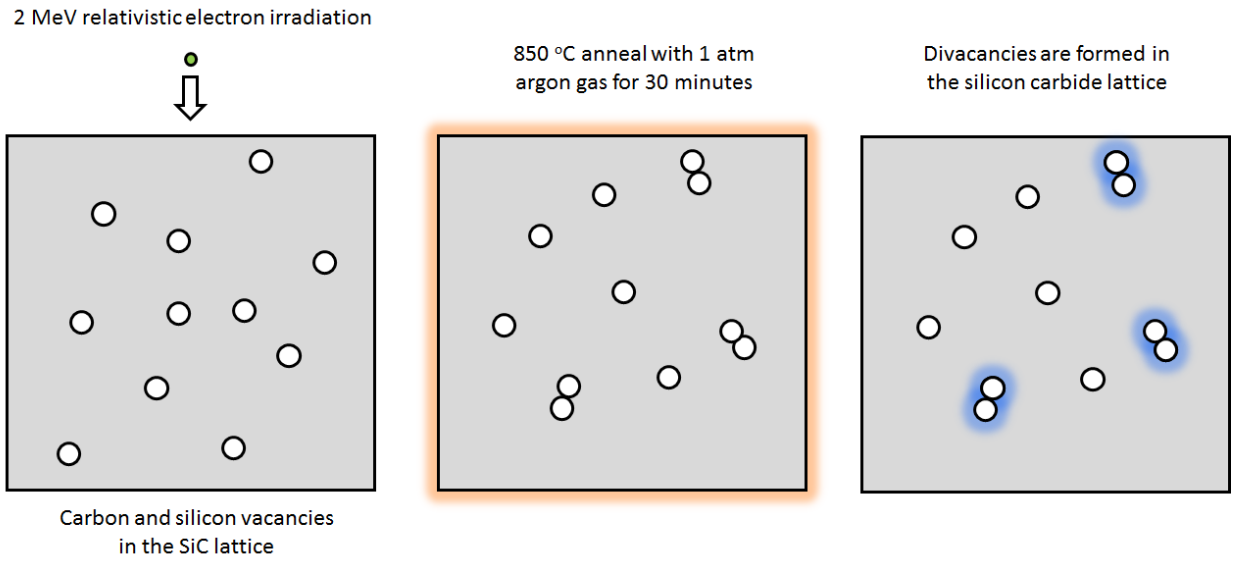

Figure 7.10 | Divacancy creation procedure for SiC. The sample is irradiated with relativistic 2 MeV energy electrons to create uniform damage in the lattice, which creates individual atomic vacancies. Under a high temperature (850 °C) anneal, these vacancies diffuse in the lattice until they pair together and form a thermodynamically stable divacancy.

Silicon carbide doping

In order to create suspended silicon carbide structures for photonics, we used a custom doping heterostructure in wafers ordered from Norstel. For our samples, the bulk substrate for growth was N-type 4H silicon carbide with 12-30 mΩ·cm resistivity and a 4 degree off-axis growth. We used a NINPN doping configuration with the following parameters, from the top down:

1) 100 nm N-type (10^{18} cm^{-3} Nitrogen)
2) 200 nm of I-type (<10^{15} cm^{-3} residual dopants)
3) 100 nm N-type (10^{18} cm^{-3} Nitrogen)
4) 3 µm of P-type (10^{18} Aluminum)
5) 500 µm of standard N-type buffer (10^{18} cm^{-3} Nitrogen)

This is shown schematically below:

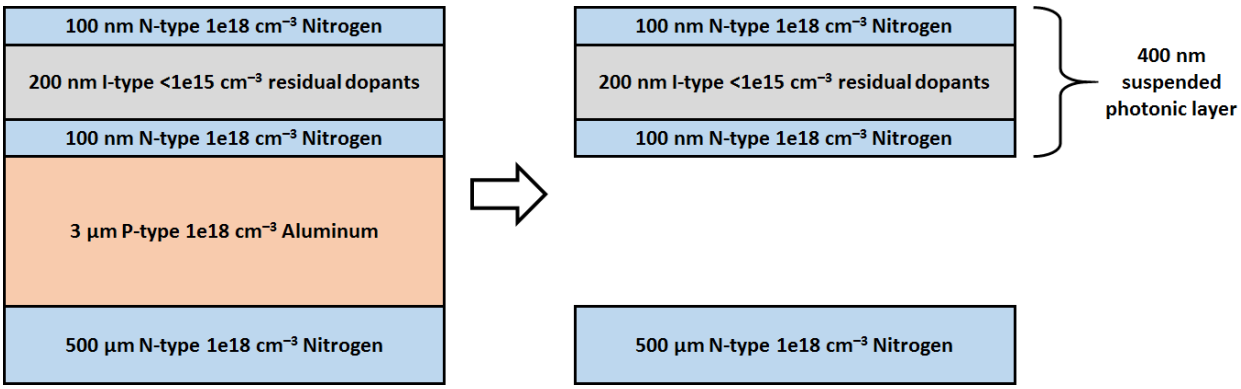

Figure 7.11 | Doping configuration of 4H-SiC wafer. The 3-micron P-type layer is etched away during photoelectrochemical etching, leaving a 400 nm thick suspended NIN layer to form photonic structures.

7.6 Single VV^0 characterization

Before exploring any cavity-defect interactions, it is important to verify the presence of a single VV^0 and characterize its baseline behavior in the nanobeam cavity. Since the divacancy is in a dramatically different environment than in "normal" circumstances in the bulk of electrically neutral SiC, we may expect some of the usual benchmarks to be different. Indeed, we observe significantly modified values for nearly all measurements. In this section we will discuss the following topics:

- Nanobeam selection and PL counts
- Photoluminescence excitation (PLE)
- Optically detected magnetic resonance (ODMR)
- $g^{(2)}$ autocorrelation

Note that all measurements from here on out are performed at cryogenic temperatures of 5 K.

Nanobeam selection and PL counts

We iterated over many nanobeams and focused only on those with a bright spot at its center that matched with one of the divacancy wavelengths. Of these nanobeams, we further narrowed to only those that also had a nearby cavity resonance at this wavelength. Out of the hundreds of cavities in the sample, only one matched both conditions. Below is a spatial photoluminescence scan with off-resonant excitation collected on this particular cavity.

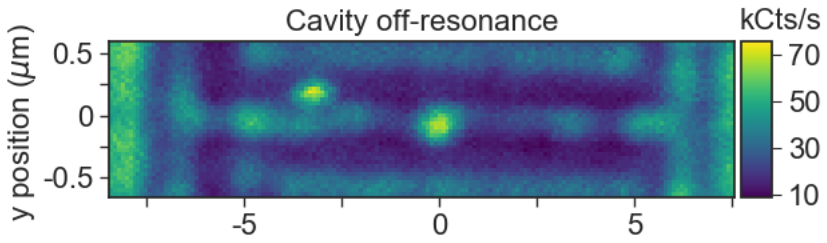

Figure 7.12 | Spatial photoluminescence scan of the nanobeam photonic crystal of interest. Collected at 5K. 905 nm light was used for excitation and all light above 1000 nm was collected. The bright spot in the center corresponds to a VV^0 in the center of the photonic cavity, which is off resonance with the defect in this scan. A fast steering mirror was used to raster the laser spot over the sample.

PLE

Photoluminescence excitation (PLE) measurements of this cavity VV^0 reveal two broad peaks at frequencies of 277.984 THz and 278.027 THz, or approximately 1079 nm. The scan is shown below:

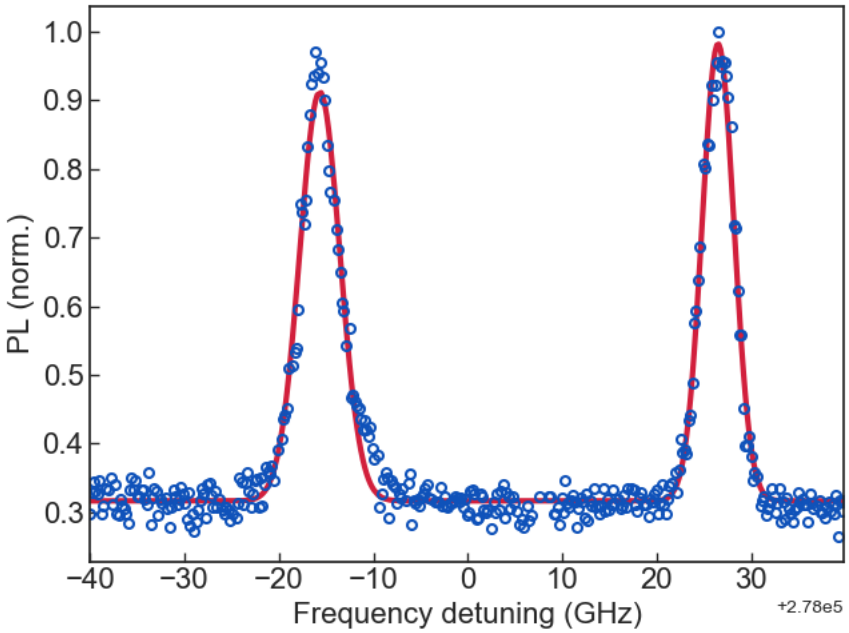

Figure 7.13 | Photoluminescence excitation (PLE) of cavity VV^0. Detuning is from 278.000 THz. The left peak is at 277.984 THz and the right peak is at 278.027 THz. The full-width half-maximum of the left and right peaks, obtained with Gaussian fits, are 5.02 ± 0.08 and 3.98 ± 0.06 GHz, respectively. The errors represent 95% confidence intervals.

The moderate splitting between these peaks of ~40-50 GHz indicates that there is either a built-in strain or electric field within the plane of the sample (that is, in the x or y direction). There is nothing in the doping configuration to break symmetry in the x or y direction, so we suspect this is due to strain. Other silicon carbide samples typically display a strain splitting of ~5-20 GHz, so the strain is slightly higher here. This may be due to the nanobeam structure, or due to the high doping levels. We will discuss strain more in an upcoming section.

The other figure of merit from the PLE scan is the linewidth of each peak. Here we have linewidths of 4-5 GHz for both peaks, which is above the typical 0.3-1 GHz value for divacancies in unpatterned SiC samples and well above the lifetime limit of ~10 MHz. The 4-5 GHz linewidth also means that the individual spin sublevels are not well-resolved, which makes resonantly addressing selective transitions difficult. The usual culprit for broadened optical linewidths is spectral diffusion in the sample, which was discussed in chapter 4. We believe this is also the case here with extra broadening from the nearby surfaces of the nanobeam. This will be discussed in more detail in the next section.

Optically detected magnetic resonance (ODMR)

Optically detected magnetic resonance reveals the microwave frequencies of transitions between the ground state levels. For this defect, we perform ODMR with a nearby wire bond and observe a Zeeman splitting with the application of a *c*-axis magnetic field, which indicates that it is a *c*-axis oriented defect. This is somewhat at odds with the 1079 nm emission of the zero-phonon line, which matches more closely with a (*kh*) basal VV^0. To investigate more closely, we take several scans at different magnetic fields and observe a frequency shift given by ~2.76 MHz/G,

which closely matches the 2.8 MHz/G value seen for *c*-axis defects [4]. Furthermore the zero-field ODMR scan shows only one peak, which is only possible if there is no E term in the Hamiltonian, as is the case for *c*-axis divacancies. The central ODMR frequency is at 1.328 GHz, which most closely matches to the (*hh*) transition at 1.336 GHz. Lastly, we also performed ODMR with off-resonant excitation, which produces a negative contrast on both peaks. As we saw in chapter 4, this only occurs for the (*hh*) divacancy. Based on all of this evidence we assign the defect to be a (hh) divacancy despite it's shifted optical emission, which we will address in an upcoming section on strain. The ODMR scans discussed here are shown below.

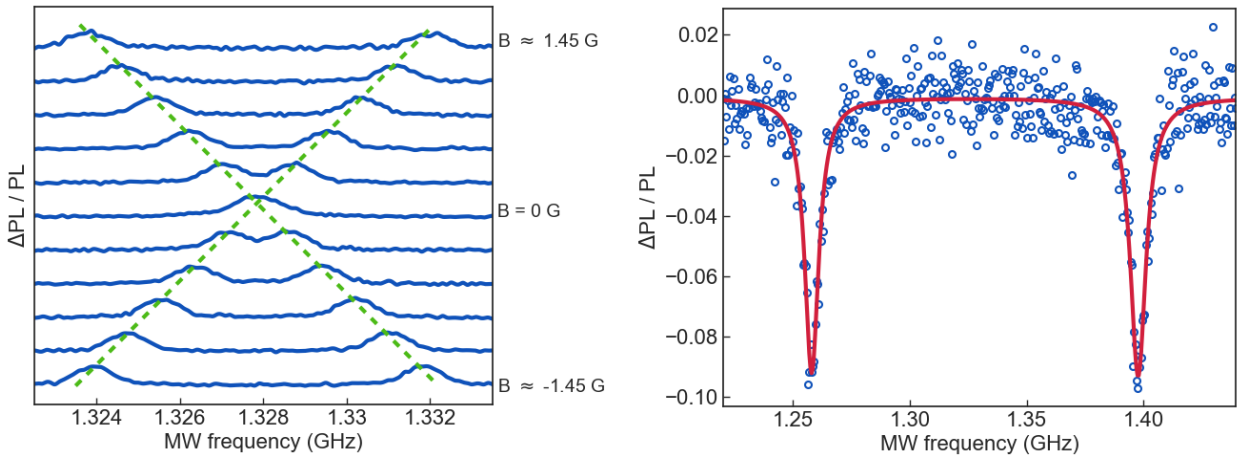

Figure 7.14 | Optically detected magnetic resonance (ODMR) of the cavity VV^0. The left shows several resonant ODMR scans at varying *c*-axis magnetic fields, showing a clear Zeeman splitting. The center frequency at zero-field is 1.328 GHz. The right figure shows off-resonant ODMR with a *c*-axis magnetic field. It has a negative contrast consistent with the (*hh*) VV^0 and is also centered at 1.328 GHz.

$g^{(2)}$ autocorrelation

As discussed in chapter 3, a $g^{(2)}$ autocorrelation measurement can be used to verify the presence of a single emitter. We perform a $g^{(2)}$ measurement with both resonant and off-resonant optical excitation. Even without background subtraction, both $g^{(2)}$ dips drop below the threshold of 0.5,

confirming the presence of a single emitter. Notably, the resonant $g^{(2)}$ curve displays significantly more bunching than the off-resonant curve. Following the discussion in chapter 3, this is most likely due to a higher rate to a nonradiative state, which in this case would be the ionized divacancy state (likely VV^-). It is known that resonant optical excitation more quickly causes ionization, which is consistent with this idea. The ISC is also present for all divacancies, although its rate should not depend on the type of laser excitation. Explicitly using the rate equation model from chapter 3 for the resonant g2 gives an effective dark state lifetime of ~60 ns. Both $g^{(2)}$ curves are shown below:

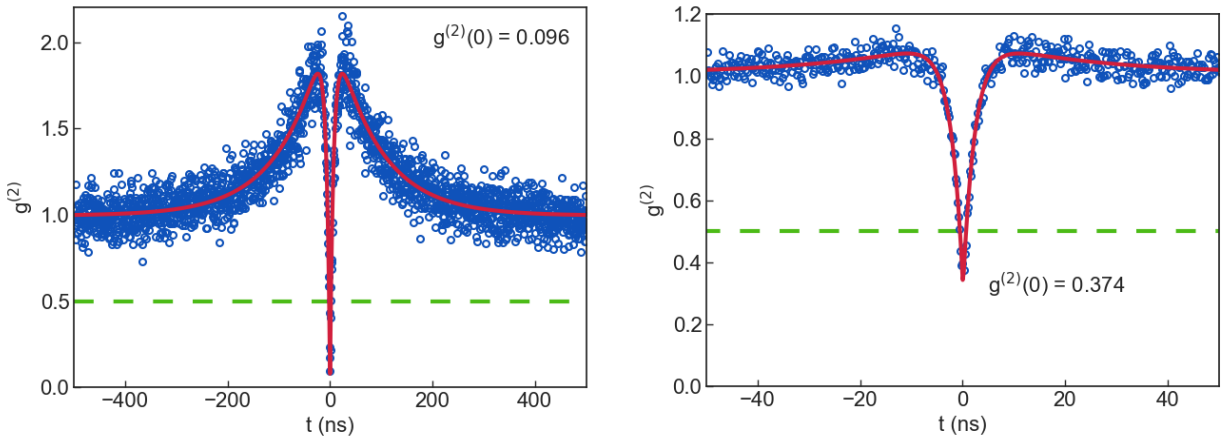

Figure 7.15 | $g^{(2)}$ autocorrelation measurements of the cavity VV^0. The left curve was collected with resonant optical excitation and the right curve was collected with off-resonant 905 nm optical excitation. Both curves confirm the presence of a single emitter with a $t = 0$ dip below 0.5. There is significantly more bunching in the resonant scan, indicating ionization with a dark state lifetime of $\tau_{dark} \approx 60\ ns$. In the off-resonant scan there are more background counts, resulting in a higher minimum value of 0.374.

7.7 Effect of nanostructures on optical linewidths

As we saw in the previous section the PLE linewidths of 4-5 GHz in the cavity VV^0 are broader than usual for divacancies in control samples. It is known that spectral diffusion causes broadened linewidths, but the charge fluctuations could come from any number of sources including nearby dopants, defects impurities, or surface charge traps. To investigate this issue, also collected PLE on "bulk" defect from the same NINPN sample without any photonic nanostructures. The linewidth from a single peak is shown below:

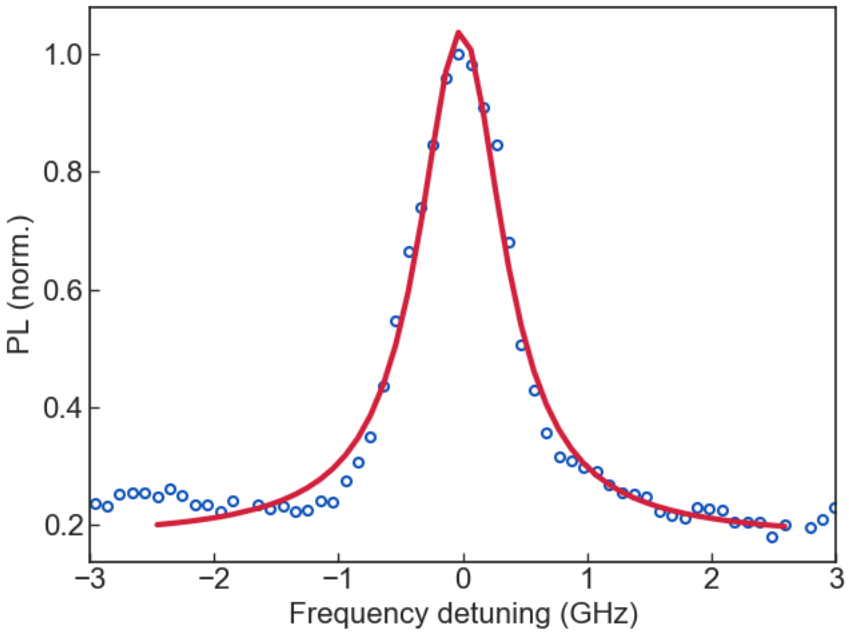

Figure 7.16 | PLE of a bulk NIN VV^0. Detuning is 278.0015 THZ. The full-width half-maximum is 825 ± 66 MHz with a 95% confidence interval, obtained with a Lorentzian fit.

Given this narrower linewidth of ~1 GHz for a defect in the same material in the same sample, it seems that the broadened ~4-5 GHz linewidths are due to nearby fabricated surfaces. The fluorine-based SF_6 plasma etch used to create holes and nanobeams could possibly create dangling surface bonds that could serve as electric field noise sources. To corroborate this comparison

between bulk and nanostructure divacancies, we collected optical linewidths and center frequencies of several more defects. The results are outlined below:

Optical linewidths:

$$\text{Bulk } (n = 16), \quad \mu = 1.37\ GHz, \quad \sigma_{sample} = 0.86\ GHz, \quad \text{range} = 0.5 \rightarrow 3.5\ GHz \tag{7.29}$$

$$\text{Nanobeam } (n = 10), \quad \mu = 5.20\ GHz, \quad \sigma_{sample} = 2.50\ GHz, \quad \text{range} = 2 \rightarrow 10\ GHz \tag{7.30}$$

Center frequencies:

$$\text{Bulk } (n = 16), \quad \mu = 277.957\ THz, \quad \sigma_{sample} = 39.52\ GHz, \quad \text{range} = 106\ GHz \tag{7.31}$$

$$\text{Beam } (n = 10), \quad \mu = 278.016\ THz, \quad \sigma_{sample} = 34.03\ GHz, \quad \text{range} = 126\ GHz \tag{7.32}$$

Evidently the broader linewidths of the nanobeam divacancies is a fairly consistent result, although some of the best nanobeam defects were in fact narrower than some of the worst bulk defects. Nevertheless, it appears that some aspect of the fabrication process causes unwanted additional spectral diffusion. The exact mechanism for this is not currently known and could be the subject of a future study.

7.8 Effect of strain

As highlighted in the single VV^0 characterization section, the zero field ODMR frequency and ZPL emission of the cavity defect do not match the expected values from a more typical (*hh*) divacancy. We attribute these differences to a large strain present throughout the sample caused by the high doping levels used during growth [74-77], which we will discuss in this section.

To get an idea of what is considered "normal" for a divacancy, we can use the following table that has been compiled from past work in our group [78]:

Name	ZPL (nm)	ODMR 1 (GHz)	ODMR 2 (GHz)	D (GHz)	D_{ES} (GHz)	E (MHz)
PL1 (*hh*)	1132	1.336	-	1.336	0.84	0
PL2 (*kk*)	1131	1.305	-	1.305	0.78	0
PL3 (*hk*)	1108	1.140	1.304	1.222	-	82.0
PL4 (*kh*)	1078	1.316	1.353	1.334	-	18.7
PL5	1042	1.356	1.389	1.373	-	16.5
PL6	1038	1.365	-	1.365	0.94	0
PL7		1.333	-	-	-	-

Table 7.1 | Optical emission and ground state parameters for different 4H-SiC divacancies. The (*hh*) and (*kk*) divacancies are *c*-axis, while (*hk*) and (*kh*) are basal. The PL5/6/7 defects have an unconfirmed structure suspected to be stacking faults. Values are adapted from [78].

Assuming the cavity defect is a (*hh*) VV^0, we thus see a –8 MHz shift in the central ODMR frequency and a –50 nm shift in the ZPL emission. A high strain can result in both of these shifts. In the ground state, strain will modify the zero-field splitting (ZFS) tensor $\overleftrightarrow{D}$, which in turn determines the D and E parameters according to:

$$D = \frac{3}{2} D_{zz}, \qquad E = \frac{1}{2}\left(D_{xx} - D_{yy}\right) \tag{7.33}$$

Where $\{D_{xx}, D_{yy}, D_{zz}\}$ are the diagonal entries of $\overleftrightarrow{D}$. To quantify the change in of $\overleftrightarrow{D}$, we must invoke the spin-strain coupling tensor $\overleftrightarrow{G}$. Together, these tensors follow the relation[14]:

$$\begin{pmatrix} \Delta D_{xx} \\ \Delta D_{yy} \\ \Delta D_{zz} \\ \Delta D_{yz} \\ \Delta D_{xz} \\ \Delta D_{xy} \end{pmatrix} = \overleftrightarrow{\boldsymbol{G}} \begin{pmatrix} \varepsilon_{xx} \\ \varepsilon_{yy} \\ \varepsilon_{zz} \\ 2\varepsilon_{yz} \\ 2\varepsilon_{xz} \\ 2\varepsilon_{xy} \end{pmatrix} \tag{7.34}$$

Where ΔD_{ij} is the change in the element D_{ij} from the strain terms ε_{ij}. More explicitly, we have:

$$\begin{pmatrix} \Delta D_{xx} \\ \Delta D_{yy} \\ \Delta D_{zz} \\ \Delta D_{yz} \\ \Delta D_{xz} \\ \Delta D_{xy} \end{pmatrix} = \begin{pmatrix} G_{11} & G_{12} & G_{13} & G_{14} & 0 & 0 \\ G_{12} & G_{11} & G_{13} & -G_{14} & 0 & 0 \\ -G_{11}-G_{12} & -G_{11}-G_{12} & -2G_{13} & 0 & 0 & 0 \\ G_{41} & -G_{41} & 0 & G_{44} & 0 & 0 \\ 0 & 0 & 0 & 0 & G_{44} & G_{41} \\ 0 & 0 & 0 & 0 & G_{14} & \frac{G_{11}-G_{12}}{2} \end{pmatrix} \begin{pmatrix} \varepsilon_{xx} \\ \varepsilon_{yy} \\ \varepsilon_{zz} \\ 2\varepsilon_{yz} \\ 2\varepsilon_{xz} \\ 2\varepsilon_{xy} \end{pmatrix} \quad (7.35)$$

The $\overleftrightarrow{G}$ terms have not been measured for the divacancy, but have been predicted using DFT calculations [27] as follows for the (*hh*) and (*kk*) divacancies:

$$\{G_{11}, G_{12}, G_{13}, G_{14}, G_{41}, G_{44}\}_{hh} = \{-3.99, -0.42, 1.74, 0.34, 0.30, 0.46\}_{hh}\ GHz \quad (7.36)$$

$$\{G_{11}, G_{12}, G_{13}, G_{14}, G_{41}, G_{44}\}_{kk} = \{-3.35, -0.93, 1.26, 1.93, -0.10, 0.47\}_{kk}\ GHz \quad (7.37)$$

Using the (*hh*) parameters we can map a strain profile to the change in the ZFS tensor entries, or vice versa. The –8 MHz shift in D corresponds to $\Delta D_{zz} = -5.33$ MHz, and E is observed to be zero. We also impose that $\overleftrightarrow{D}$ traceless and assume that there is no shear in the sample ($\Delta D_{yz} = \Delta D_{xz} = \Delta D_{xy} = 0$). This gives the unique strain values of:

$$\varepsilon_{xx} = \varepsilon_{yy} = -4.61 \cdot 10^{-4}, \qquad \varepsilon_{zz} = 3.64 \cdot 10^{-4} \quad (7.38)$$

This is consistent with the strain magnitudes found in SiC nanoparticles [79], meaning that strain is a plausible source for the shift in the ODMR central frequency. A similar analysis can be done for the NV^- center in diamond [80]. For the ZPL shift, the excited state analysis in chapter 2 reveals that z-strain can uniformly shift the optical emission of the VV^0, dependent on the excited state spin-strain coupling parameter, which unfortunately has not been measured. However, work done by Falk *et al*. reported a ~2,900 THz/strain splitting for the SiC *c*-axis VV^0 $|E_x\rangle$ and $|E_y\rangle$

states [25]. If the strain shifting also shows a high sensitivity, then it is possible to have significant changes in the ZPL emission.

For comparison, we also collected ODMR from a defect in the bulk of the NIN epilayer without any fabricated nanostructures (see below). We observed a similarly shifted central frequency of ~1.328 GHz, indicating that the attributed strain is present throughout the sample and not due to fabrication. It is known that the use of high doping during growth can generate a significant amount of strain [74-77], which we suspect is likely happening with the high concentrations used in the NINPN epilayers.

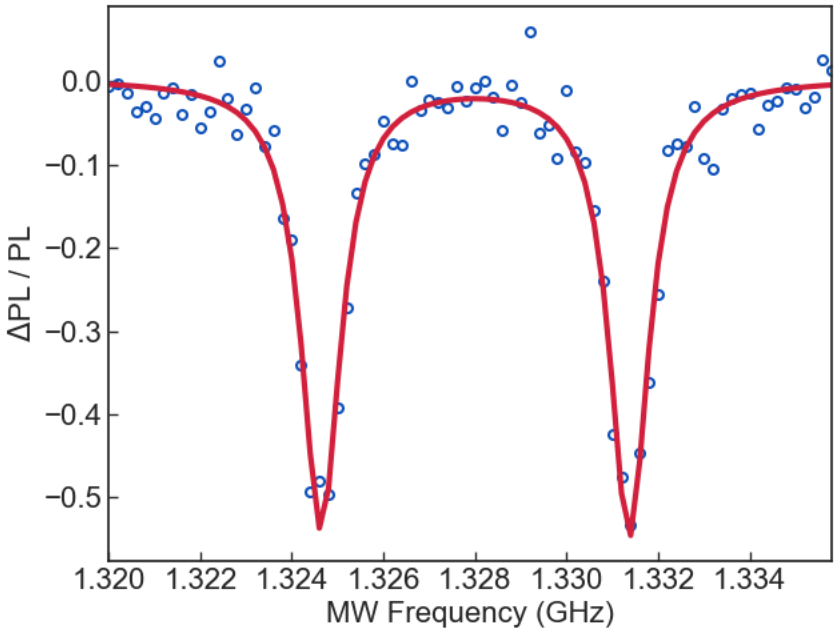

Figure 7.17 | Optically detected magnetic resonance of a bulk NIN VV^0. Collected with resonant optical excitation and a low magnetic field of ~1.2 G parallel to the *c*-axis. The central frequency is ~1.328 GHz.

7.9 Measurements of Purcell enhancement

With the cavity divacancy fully characterized, it is time to move on to measurements of cavity-emitter interactions. As a prerequisite for these experiments, the cavity resonance must be precisely tuned to match the frequency of the VV^0 ZPL emission in order to facilitate defect-cavity coupling. This is achieved through deliberate heating of different stages of the Montana cryostat. This has the effect of releasing the gases adsorbed onto to surfaces during cryo pumping, which then redeposit on the sample and the nanobeam. This condensation of gases slightly increases the overall index of refraction of the beam, causing a redshift of the cavity wavelength. Conversely, the sample itself can be heated to ~30-40 K while keeping all other stages cooled, which causes gases to evaporate from the nanobeam and onto surrounding surfaces. This causes a blueshift of the cavity resonance. We can reach a tuning range of ~5 nm with this method, which is close enough for this sample to achieve resonance matching.

With cavity-VV^0 resonance, we will use the equations outlined earlier in this chapter to measure the Purcell factor. This will be based on the following measurements:

1) Optical spectrum
2) Excited state lifetime measurements
3) Overall count rate

We will also comment on the Purcell enhancement's effect on the Debye-Waller factor.

Optical spectrum

For these measurements, we optically excite the defect with off-resonant 905 nm laser light and direct all emission through a 1000 nm longpass filter and into a spectrometer with a InGaAs camera cooled to ~100 K. This gives the total emission spectrum across all relevant wavelengths. Spectra are obtained with the cavity both off and on resonance with the VV^0. Because the PLE spectrum of the VV^0 features two main peaks ~40-50 GHz apart, there are two candidate emission wavelengths to match the cavity to. The resulting spectra from matching to both of these peaks is shown below.

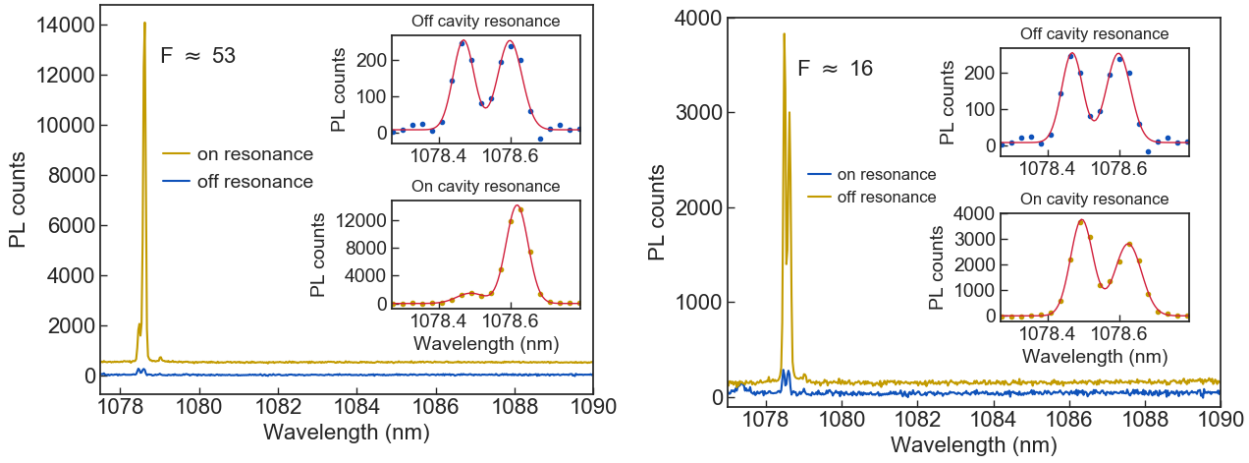

Figure 7.18 | VV^0 emission spectrum on and off cavity resonance. On the left is the VV^0 emission spectrum with cavity matching to the higher energy $|E_x\rangle$ branch. On the right is the VV^0 emission spectrum with cavity matching to the lower energy $|E_y\rangle$ branch. A ratio of emission intensities gives Purcell factors of ~53 for the $|E_x\rangle$ transition and ~16 for the $|E_y\rangle$ transition. Insets provide non-overlapped spectrum off and on cavity resonance. The on-resonance traces for the combined plots are offset vertically for clarity. Off-resonant 905 nm laser light was used for excitation in all measurements.

There is a clear enhancement of the ZPL counts when the cavity is matched to either the $|E_x\rangle$ or $|E_y\rangle$ transition. To extract a Purcell factor we can use equation (2) from earlier in this chapter:

$$F = \frac{I_{ZPL,on}}{I_{ZPL,off}} \tag{7.39}$$

To obtain the intensity of light emitted into the ZPL, we integrate the Gaussian fits to the spectral peaks to obtain the total number of counts. This gives a Purcell factor of ~53 for the higher energy $|E_x\rangle$ transition and ~16 for the lower energy $|E_y\rangle$ transition. The discrepancy of these factors is due to the orthogonal dipole orientations of the $|E_x\rangle, |E_y\rangle$ transitions. Evidently, the $\frac{|\vec{\mu}\cdot\vec{E}|}{|\vec{\mu}||\vec{E}_{max}|}$ factor that appears in the explicit expression for the Purcell factor (see chapter 5) is better aligned to the cavity mode for the $|E_x\rangle$ dipole moment.

Since we have taken a direct spectrum, we may also be tempted to use equation (14) to calculate a Purcell factor using the change in Debye-Waller factor. Unfortunately, however, a spatially varying background signal from n-type dopants makes estimating the Debye-Waller factor quite difficult using the spectrometer. However, we will be able to estimate a Debye-Waller using total counts, as will be shown later in this section.

Lifetime measurements

The next method to verify a Purcell enhancement is to directly measure excited state lifetimes on and off cavity resonances. In this measurement, the VV^0 is excited with a short pulse of resonant excitation light gated with an EOM, then photoluminescence is collected as it decays to the ground state. Averaging over many experiments gives an exponential fit, from which the lifetime is obtained. The dynamics of this measurement were discussed more in chapter 3, but for here we'll focus on the results. The lifetime plots are given below:

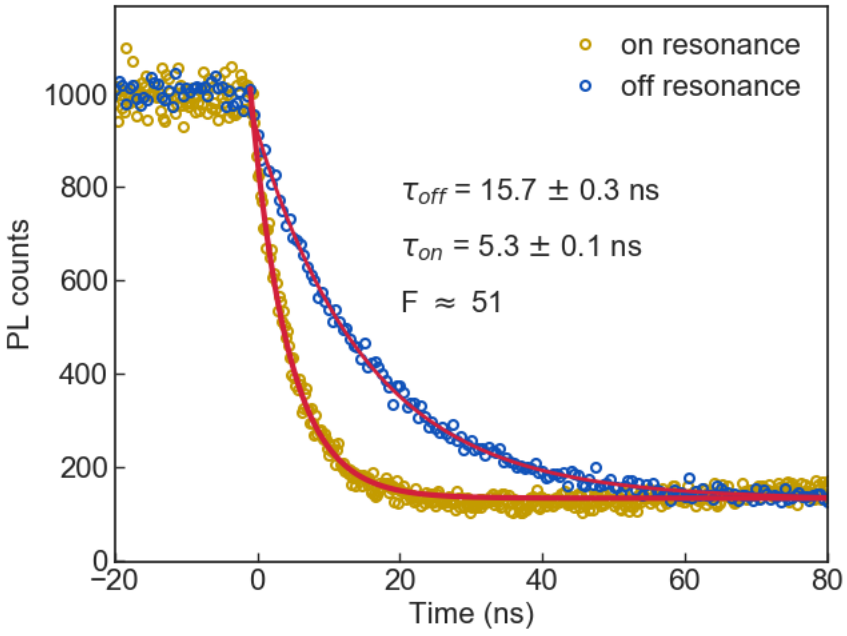

Figure 7.19 | Excited state lifetime measurements on and off cavity resonance. Here the VV^0 is resonantly excited a photoluminescence is collected as a function of time. Exponential fits of $\exp(-t/\tau)$ give lifetime values of $\tau_{off} = 15.7 \pm 0.3\, ns$ and $\tau_{on} = 5.3 \pm 0.1\, ns$ for off and on cavity resonance, respectively. Error bars are given with 95% confidence intervals. These lifetimes give a Purcell factor of ~51. All measurements were taken at 5 K.

As can be seen, there is a clear increase in the spontaneous emission rate on cavity resonance, as predicted by the Purcell/weak coupling regime in cavity QED (see chapter 5). To extract a Purcell factor, we use equation (7.13) from this chapter

$$F = \frac{\tau_{dark}\left(\tau_{off} - \tau_{on}\right)}{\alpha\tau_{on}\left(\tau_{dark} - \tau_{off}\right)} + 1 \tag{7.40}$$

Using a τ_{dark} value of 60 ns extracted from the $g^{(2)}$ fit and an off-resonance Debye-Waller factor of $\alpha = 0.053$ for the (*hh*) VV^0 [3], this gives a Purcell factor of F ~ 51. This factor matches closely with the F ~ 53 obtained from optical spectra.

It is worth commenting further on the exact value of τ_{dark} and its effect on the Purcell factor. The $g^{(2)}$ model uses five free parameters in fitting the experimental data, which means that the

uncertainty in fitting any particular parameter is quite high, even if the overall fit matches well. Further independent measurements would be needed to lower the uncertainty on τ_{dark}. To get a sense of how different τ_{dark} values would affect the Purcell factor, we have plotted the dependence below using the values of $\tau_{off} = 15.7\ ns$, $\tau_{on} = 5.3\ ns$, and $\alpha = 0.053$.

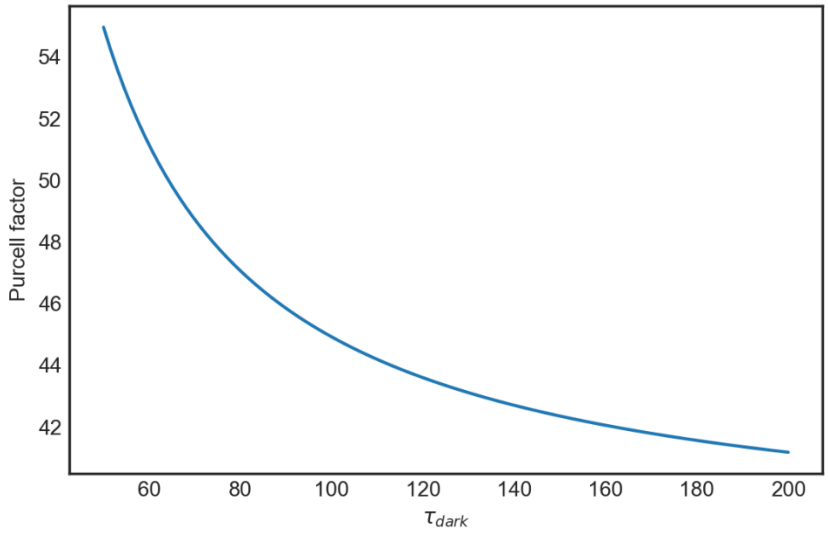

Figure 7.20 | Effect of τ_{dark} on Purcell factor. Using $\tau_{off} = 15.7\ ns$, $\tau_{on} = 5.3\ ns$, and $\alpha = 0.053$. Over a wide range of τ_{dark} values, the Purcell factor is generally in the range of 42-55. Shorter τ_{dark} values result in a higher Purcell factor, with a divergence as τ_{dark} approaches τ_{off}.

Overall count rate

If we assume that all increases in photoluminescence on cavity resonance are from a Purcell enhancement, then we can use equation (7.28) from this chapter to obtain the Purcell factor:

$$F = \frac{I_{on} - I_{off} + \alpha I_{off}}{\alpha I_{off}} \tag{7.41}$$

These intensities can be obtained by examining the spatial luminescence scans on and off cavity resonance, which are shown below:

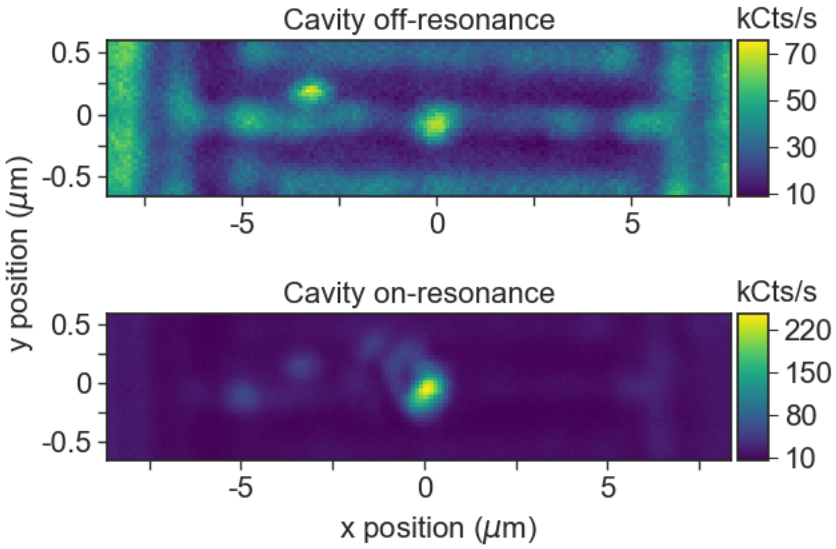

Figure 7.21 | Spatial photoluminescence scan off and on cavity resonance. 905 nm laser rastering was performed with a fast-steering mirror. The top scan shows the nanobeam of interest off cavity resonance, with the normal VV^0 emission in the center of the beam. The bottom shows the same device with the cavity tuned into resonance with the VV^0. The count rates are half their actual values, due to a fiber splitting into two detection ports that was present during this measurement.

These measurements were collected while the collection fiber was split into two ports for $g^{(2)}$ measurements so the observed counts must be doubled. Subsequently subtracting the constant background for each measurement gives peak count values of 120 and 460 kCts/s for the VV^0 off and on cavity resonance, respectively. These can be used directly for the values of I_{on} and I_{off}. Using the same unenhanced Debye-Waller factor of $\alpha = 0.053$ then gives F ~ 54, which matches closely to the previously measured values of F ~ 51 and F ~ 53.

We can also use these same values to determine the increase in the Debye-Waller factor, using equation (7.25) from this chapter:

$$\beta = \frac{I_{on} - I_{off} + \alpha \cdot I_{off}}{I_{on}} \tag{7.42}$$

Plugging in gives $\beta \approx 75\%$, which is a substantial improvement over the unenhanced value of $\alpha = 5.3\%$. Given the agreement between the independent measures of the Purcell factor, we can be reasonably confident that the factor is at least 50. If we plug this value into equation (7.17), we can obtain another measure of β:

$$\beta = \alpha\left(\frac{F}{1 + \alpha(F-1)}\right) \tag{7.43}$$

Using F = 50 here gives $\beta \approx 74\%$. Therefore, we can also be reasonably confident that the Debye-Waller factor has increased to ~70-75% due to the cavity Purcell enhancement.

7.10 Coherent spin control

In addition to Purcell enhancement of the excited state optical transitions, we demonstrate control and coherence of the ground state. As outlined in chapter 2, this is achieved with external alternating magnetic fields, which we employ through the use of a nearby wire bond. Depending on the measurement, we also apply a *c*-axis magnetic with an external neodymium magnet in order to Zeeman split the $|\pm 1\rangle$ states of the (*hh*) VV^0. These measurements, which are all collected at 5 K, are categorized as follows:

- Rabi oscillations
- Ramsey measurement (T_2^*)
- Hahn echo measurement (T_2)

- Dynamical decoupling
- T_1 measurement

Rabi oscillations

Rabi oscillations were performed by performing an off-resonant optical initialization, a variable MW rotation, and then a resonant optical excitation to readout the defect. For this measurement, the microwave pulse was kept at a constant duration of 400 ns with a linearly increasing power. This is similar to the "power pi calibration" outlined in chapter 4. The microwave frequency was matched to the $|0\rangle \leftrightarrow |+1\rangle$ transition under Zeeman splitting. The result is shown below:

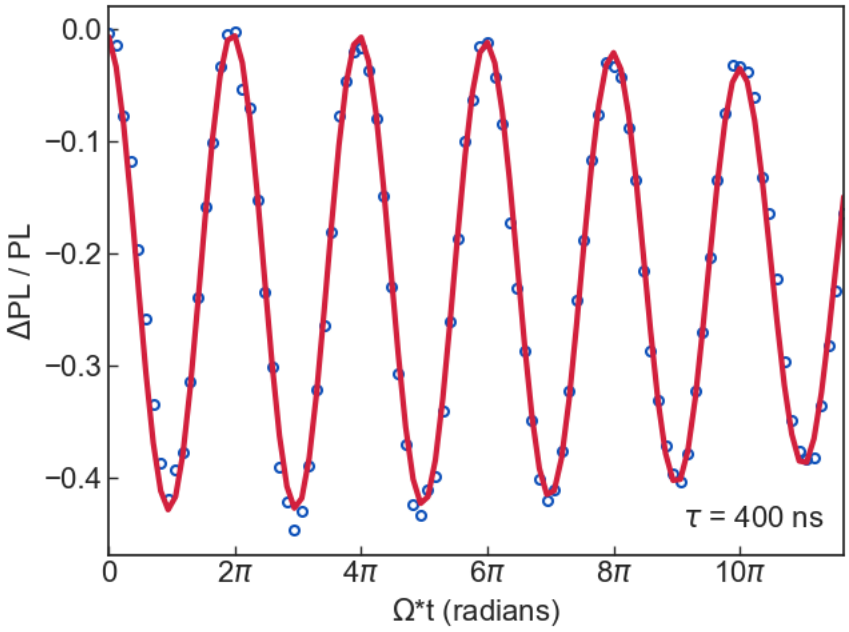

Figure 7.22 | Rabi oscillations of the cavity VV^0. A 400 ns microwave pulse of varying power (x-axis) is used to drive transitions between the $|0\rangle$ and $|+1\rangle$ states of the cavity VV^0, achieving a contrast of ~40%. 905 nm light was used for initialization and resonant light was used for readout.

The Rabi contrast of 40% is between the typical off-resonant readout levels of ~10-15% [2] and resonant readout levels of 94-99% [39,43]. Due to the broadened PLE optical transitions, some of

the spin excitation selectivity is lost with resonant excitation. However, a significant amount of contrast remains, indicating that the different regions of the PLE peak correspond to different spin character.

Ramsey measurement (T_2^*)

To measure spin dephasing time T_2^*, Ramsey interferometry is performed using the $|0\rangle \leftrightarrow |+1\rangle$ transition addressed with Rabi oscillations. The pulse sequence follows the canonical Ramsey sequence outlined in chapter 3. We perform these measurements under a *c*-axis magnetic field of ~6 G and ~218 G. A detuning of 3 MHz is introduced into the microwave drive frequency in order to induce oscillations and obtain a better fit. A Ramsey that is collected exactly on resonance can display an artificially shortened T_2^*. The results of these measurements are shown below:

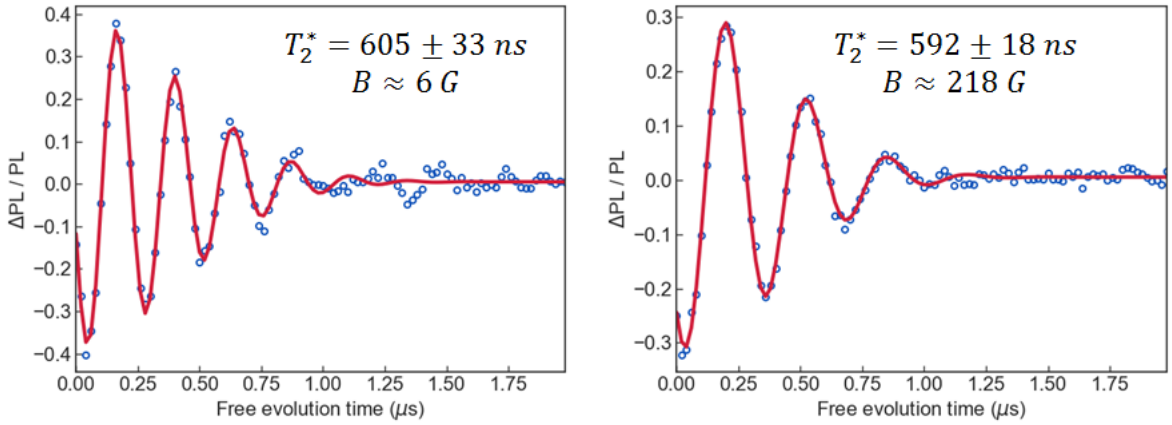

Figure 7.23 | Ramsey interferometry for cavity VV^0. Scans are collected at a low magnetic field of 6 G (left) and a high magnetic field of 218 G with a 3 MHz drive detuning in both cases. Fits to the function $\exp(-(t/T_2^*)^n)$ give $T_2^* = 605 \pm 33\ ns$ and $T_2^* = 592 \pm 18\ ns$ with $n \approx 2$ in both cases. Errors denote a 95% confidence interval.

Compared to typical bulk VV^0 values of $T_2^* \approx 1\ \mu s$, the dephasing times of $T_2^* = 605\ ns$, $592\ ns$ are reasonable. The loss of coherence is likely due to dipolar coupling to unpaired electrons

in the highly doped nearby n-type regions with nitrogen donors. Dangling bonds from nearby fabricated surfaces could also contribute to spin dephasing.

As a comparison, we also performed Ramsey interferometry on a defect in the unfabricated NIN material of the same sample, with the result shown below:

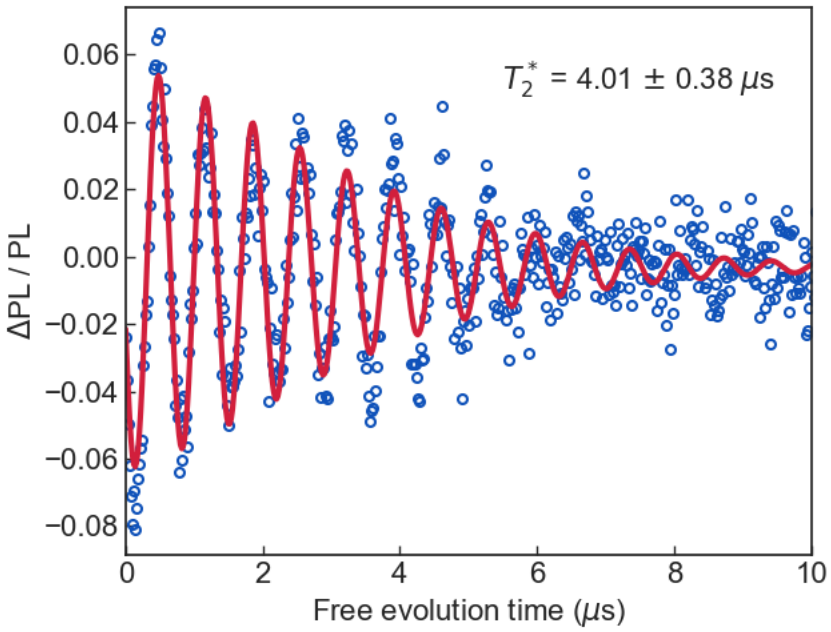

Figure 7.24 | Ramsey interferometry for bulk NIN VV^0. Collected with 218 G magnetic field and 3 MHz detuning. An exponential sinusoidal fit gives $T_2^* = 4.01 \pm 0.38\,\mu s$ with a 95% confidence interval.

Curiously, the NIN T_2^* appears to be slightly longer than the typical values measured for divacancies. The reasons for this are not well understood, but the surrounding n-type layers could provide a degree of shielding from the environment. We see this effect for optical linewidths, where there is a dramatic improvement from ~10+ GHz to ~1 GHz going from a 400 nm I-type layer to a 100-200-100 nm heterostructure of NIN.

Hahn echo measurement (T_2)

To measure the spin decoherence time T_2, we use the Hahn echo sequence outlined in chapter 4. We use the same $|0\rangle \leftrightarrow |+1\rangle$ transition utilized in previous measurements. We also perform this measurement under relatively high and low *c*-axis magnetic fields. The results of these measurements are shown below:

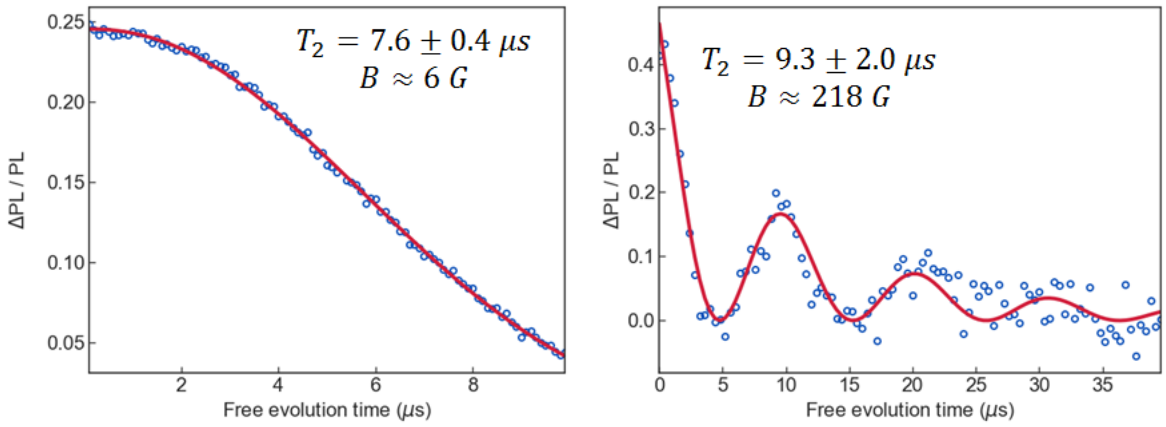

Figure 7.25 | Hahn echo measurement of cavity VV^0. Scans are collected at a low magnetic field of 6 G (left) and a high magnetic field of 218 G. Fits to the function $\exp(-(t/T_2)^n)$ give $T_2 = 7.6 \pm 0.4\ \mu s$ and $T_2 = 9.3 \pm 2.0\ \mu s$ with $n \approx 1$ in both cases. Errors denote a 95% confidence interval.

In contrast with the T_2^* measurements, the T_2 measurements here of $T_2 \approx 7,9\ \mu s$ are dramatically shorter than typical values of $T_2 \approx 1\ ms$ [2]. This is due to dipolar interactions with nearby n-type dopants and nearby surface defects. In a bulk VV^0, there is a significant improvement to T_2 from applying a strong external magnetic field. In this case, however, we only see a marginal improvement. This indicates that the nuclear spin bath does not play a dominant role in decoherence for this sample, as the strong magnetic field is meant to polarize the nuclear spins. For comparison we also collected a decoherence time for a divacancy in the bulk NIN, as shown below:

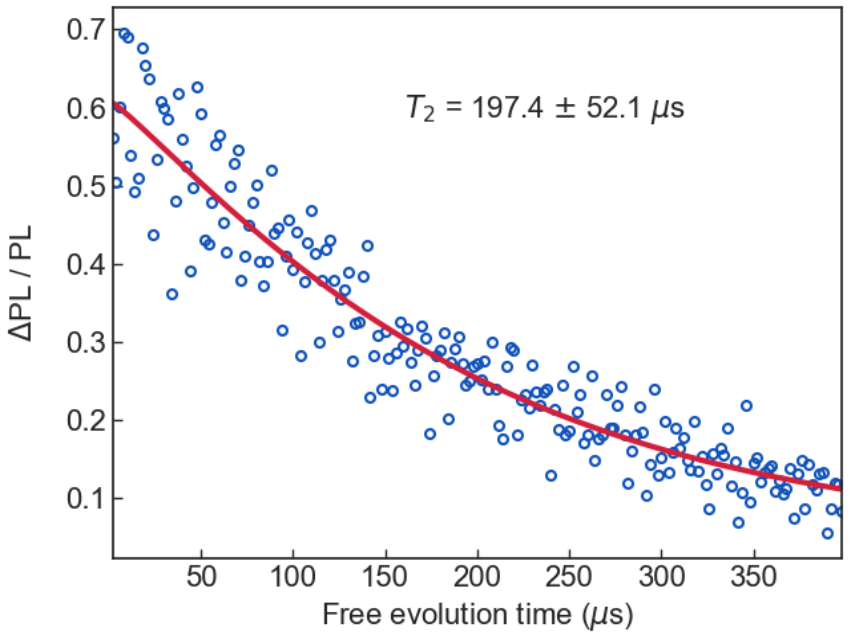

Figure 7.26 | Hahn echo measurement for bulk NIN VV^0. Collected with 218 G magnetic field. An exponential fit gives $T_2 = 197.4 \pm 52.1\ \mu s$ with a 95% confidence interval.

In this case we obtain a much more reasonable value of $T_2 \approx 200\ \mu s$. This ~5x discrepancy to bulk values is likely due to the doped layers and nearby top surface. The dramatic ~20x improvement from the nanobeam VV^0 T_2 indicates that the fabricated structures have a significant detrimental effect on coherence. Near-surface proximity alone is not enough to explain the difference, as both defects are ~200 nm away from the top surface. The sidewall surfaces introduced by SF_6 plasma etching could introduce Fluorine based surface terminations, which may couple strongly to the divacancy. This effect has not been explored in the literature, but could be the subject of a future study.

For the purposes of remote spin-spin entanglement protocols, the T_2 needs to be long enough for the spin to remain coherent during the long-distance photon interference. In this case a $T_2 \approx 10\ \mu s$ would only correspond to ~ 2 km of travel through fiber. Therefore we are interested in extending this coherence time, which can be achieved through dynamical decoupling.

Dynamical decoupling

While a single Hahn echo pulse has the effect of increasing coherence, this idea can be extended to include multiple "echo" pulses. This is the idea of the Carr-Purcell-Meiboom-Gill (CPMG) sequence [30]. Theoretically this should provide an improvement in T_2 up to the T_1 limit. We performed this sequence with 1, 2 and 4 pulses with the results shown below:

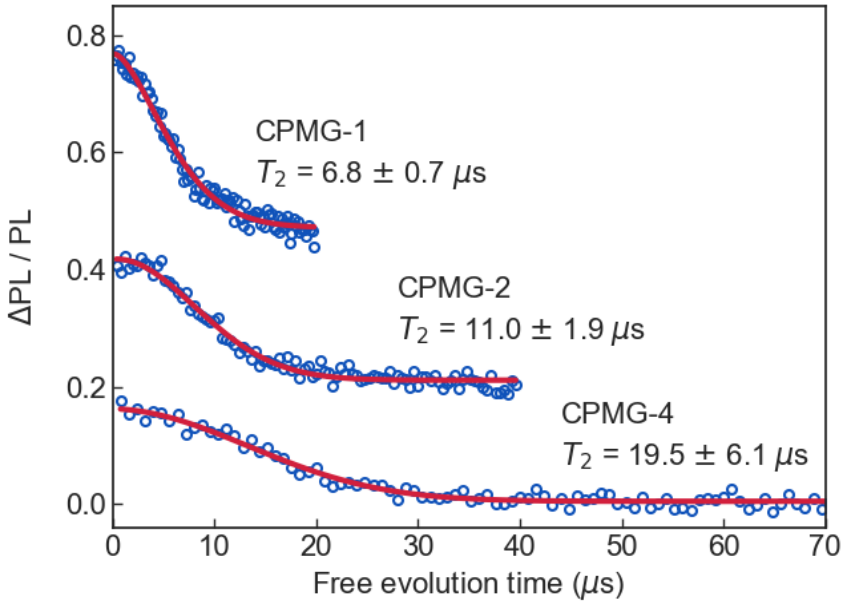

Figure 7.27 | T_2 extension through dynamical decoupling for cavity VV⁰. Carr-Purcell-Meiboom-Gill (CPMG) sequences with 1, 2 and 4 pulses are tested under a ~6 G external *c*-axis magnetic field. Plots are vertically offset for clarity. Fits to $\exp(-(t/T_2)^n)$ give $T_2 = 6.8 \pm 0.7\ \mu s$, $n = 1.6 \pm 0.2$ for CPMG-1, $T_2 = 11.0 \pm 1.9\ \mu s$, $n = 2.0 \pm 0.4$ for CPMG-2, and $T_2 = 19.5 \pm 6.1\ \mu s$, $n = 2.1 \pm 0.6$ for CPMG-4. Error bars indicate 68% confidence intervals.

The steadily increasing coherence times indicates the viability of this technique, at the cost of receiving less averaged signal as more pulses are included.

T_1 measurement

Lastly, a spin-relaxation T_1 measurement provides an upper bound on the coherence times capable for the divacancy. This measurement follows the description in chapter 3, where the spin is simply initialized and then measured after a waiting period. The results of this measurement are shown below:

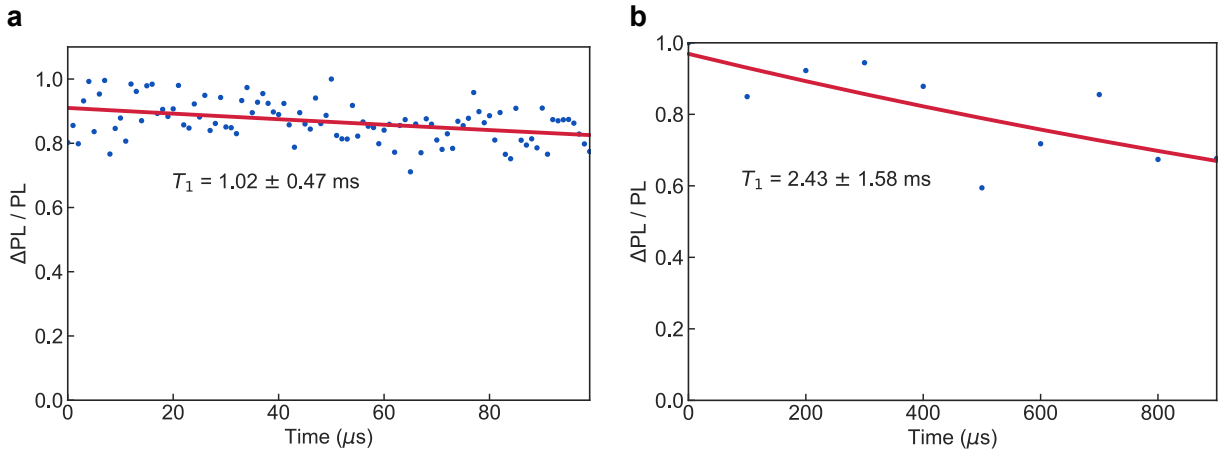

Figure 7.28 | Spin relaxation times of cavity VV^0. Measurements are collected at a ~6 G *c*-axis magnetic field and T = 5 K. **(a)** 100 μs time window with an exponential decay fit giving $T_1 = 1.02 \pm 0.47$ ms. **(b)** 1 ms time window with an exponential decay fit giving $T_1 = 2.43 \pm 1.58$ ms. Errors indicate 95% confidence intervals.

Here the spin relaxation times of ~1 ms are reasonably long, although other measurements of divacancies indicate that they could be much longer at cryogenic temperatures. This could be an indication that rather than phonon processes limiting the T_1, nearby fluctuations near the Larmor frequency could be causing spin flips. Nevertheless, the ~1 ms value, if mapped to a T_2 time extended with dynamical decoupling, would correspond to over 200 km of optical transmission through fiber before decoherence. Given that the fiber attenuation limit is ~100 km, this would be a long enough coherence time to carry out the limits of long-distance spin-spin entanglement.

7.11 Discussion and next steps

The Purcell enhancement of the divacancy's zero-phonon emission has important implications for entanglement protocols and spin readout. Most directly, the increase in the Debye-Waller factor from ~5% to ~70-75% means that significantly more photons will be emitted into the ZPL. These photons are directly used in spin-photon entanglement, and also employed in remote spin-spin entanglement that relies on the interference of indistinguishable photons. For the entanglement between two spins, the probability of success increases from 0.05^2 = 0.0025 to 0.75^2 = 0.5625, which is approximately a 200-fold increase. This speedup becomes more dramatic when the entanglement is scaled up to more than two nodes. For three nodes, for example, entanglement rates increase by approximately 50,000 since four ZPL photons are now necessary. This scaling continues as $2^{(n-1)}$ ZPL photons are necessary for an n-node network.

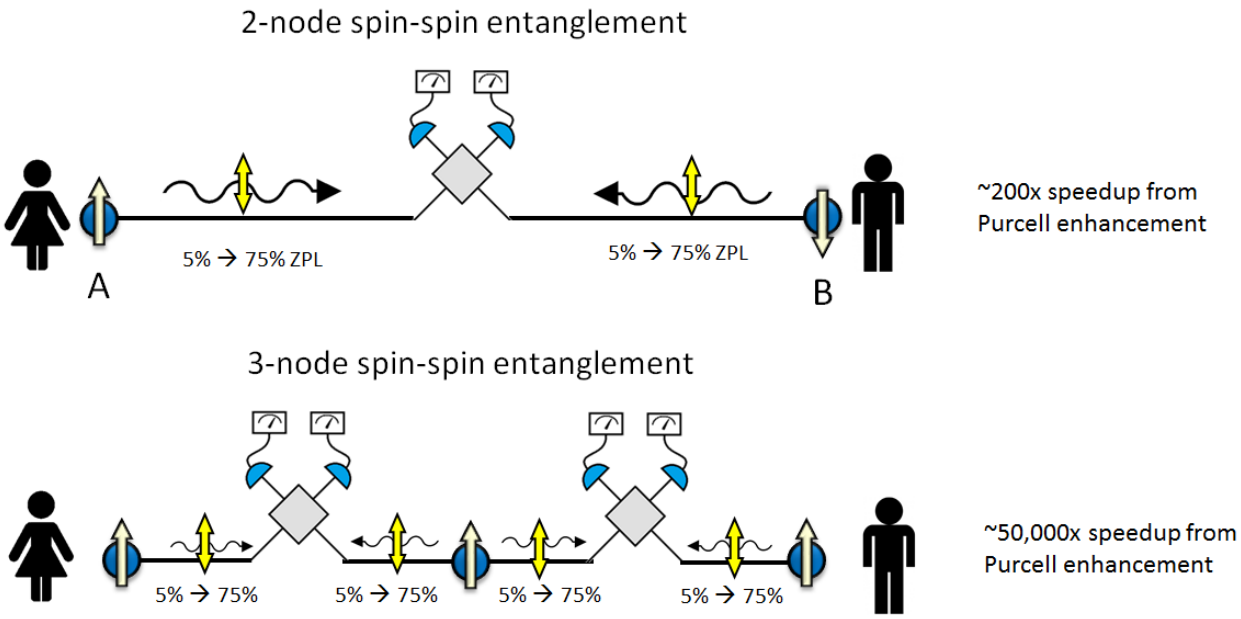

Figure 7.29 | Speedup for spin-spin entanglement. The Purcell enhancement presented in this thesis results in a projected 200x speedup for two node spin-spin entanglement. This speedup increases exponentially as more nodes are added, reaching ~50,000x for a 3-node network.

In addition to increasing zero-phonon emission, Purcell enhancement also results in a relative suppression of other decay pathways from the excited state. This is important for single-shot readout experiments that rely on the cyclicity of a radiative spin transition between the ground and excited states [81,82]. With the threefold reduction in overall lifetime, we would expect a threefold increase in the number of photons emitted in a cycling transition before a spin flip occurs through the ISC. The various decay pathways are outlined in figure 7/30.

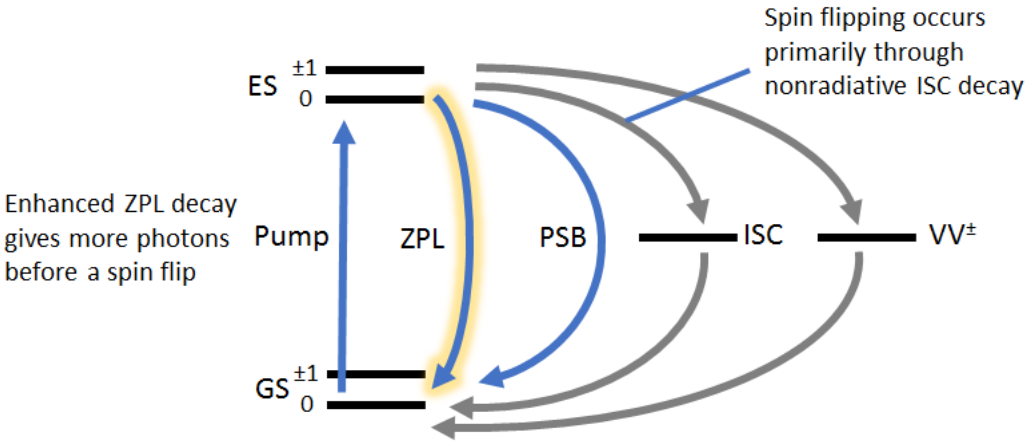

Figure 7.30 | Decay pathways for the cavity-VV^0 system. The radiative decays (blue arrows) can be categorized as zero-phonon line (ZPL) emission or phonon sideband (PSB) emission. The highlighted ZPL decay is enhanced through the cavity. Nonradiative decays (gray arrows) through the ISC or an ionized VV^-/VV^+ charge state compete with the radiative decays and lengthen the overall optical lifetime. The ISC pathway is the primary source of spin flipping, which becomes mitigated when the ZPL transition is Purcell enhanced.

Single-shot readout is a key component of spin-spin entanglement experiments, as it is used to verify the correlation between entangled spin states [81,82]. In addition to allowing for more

photons to be emitted to raise single-shot readout fidelity, the presence of a cavity can also raise the overall collection efficiency into the top-down objective used for bulk divacancies. In our experiments, the increase of off-cavity-resonance PL (~120 kCts/s) compared to bulk VV^0 emission of ~40-50 kCts/s indicates at least a factor of two improvement in collection efficiency. Combined with the lifetime reduction, the increased photon counts may bring single-shot readout into the realm of possibility for divacancies interfaced with nanophotonics. The incorporation of directed optical components such as grating couplers and tapered fibers would serve to further increase the collection efficiency, which is on the order of 1% for most experiments.

As part of the Barret-Kok spin-spin entanglement protocol, it is necessary to address each spin with a resonant excitation pulse that is spin selective, as outlined in figure 7.31 [40]. In the cavity-enhanced divacancy featured here, the PLE excitations are merged together for each excited state branch as can be seen in figure 7.13. Thus, to carry out the entanglement procedure it is necessary to either narrow these lines or achieve spin selectivity through another method. As outlined in chapter 2, each excited state transition is coupled through a specific photon polarization. In this way, if the $|m_s = +1\rangle$ and $|m_s = -1\rangle$ states are selected as the qubit basis, then the photon polarizations that excite the VV^0 will be completely orthogonal. This means that spin selectivity can be achieved despite the spectral overlap of transitions. As given in the entanglement procedure, the spin would be prepared in a superposition of $|\pm 1\rangle$ and given an excitation pulse that is either left or right circularly polarized.

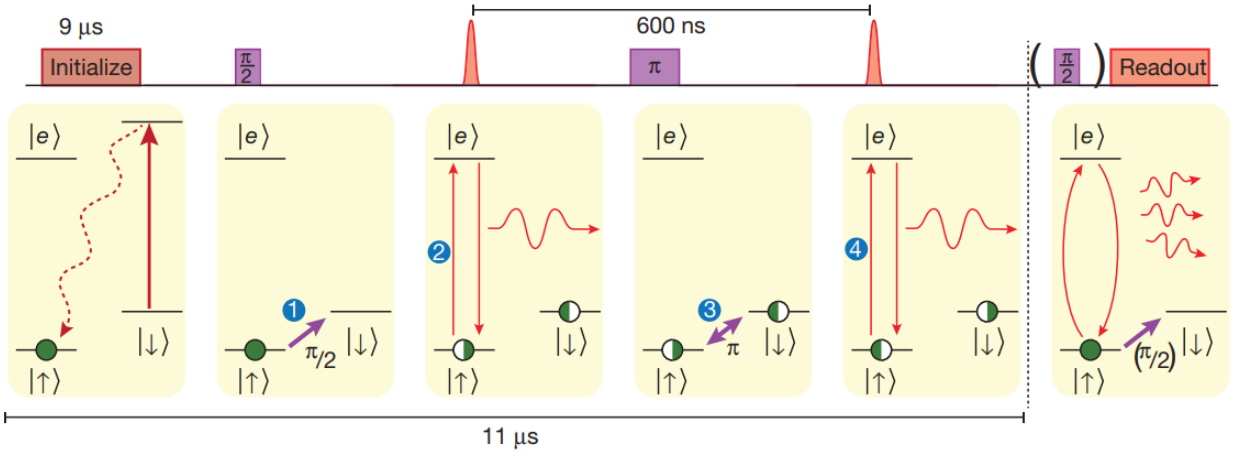

Figure 7.31 | Remote spin-spin entanglement procedure. Adapted from [40]. In steps 2 and 4, an optical excitation for the $|\uparrow\rangle$ to $|e\rangle$ transition is used to excite a superposition state, which implies the spectral distinguishability for the spin sublevel optical transitions.

Alternatively, it may be possible to actively narrow the optical linewidth of the VV^0 through the application of a static electric field, as demonstrated in work in reference [31,43]. In this approach, the electric field polarizes fluctuating charges that are responsible for spectral diffusion. Electric field could be applied through nearby gated electrodes, as shown in figure 7.32, or present naturally in a PIN doped heterostructure. The cavity presented here contained an NIN structure for the nanobeam, so the topmost N-doped layer would be swapped with a P-doped layer.

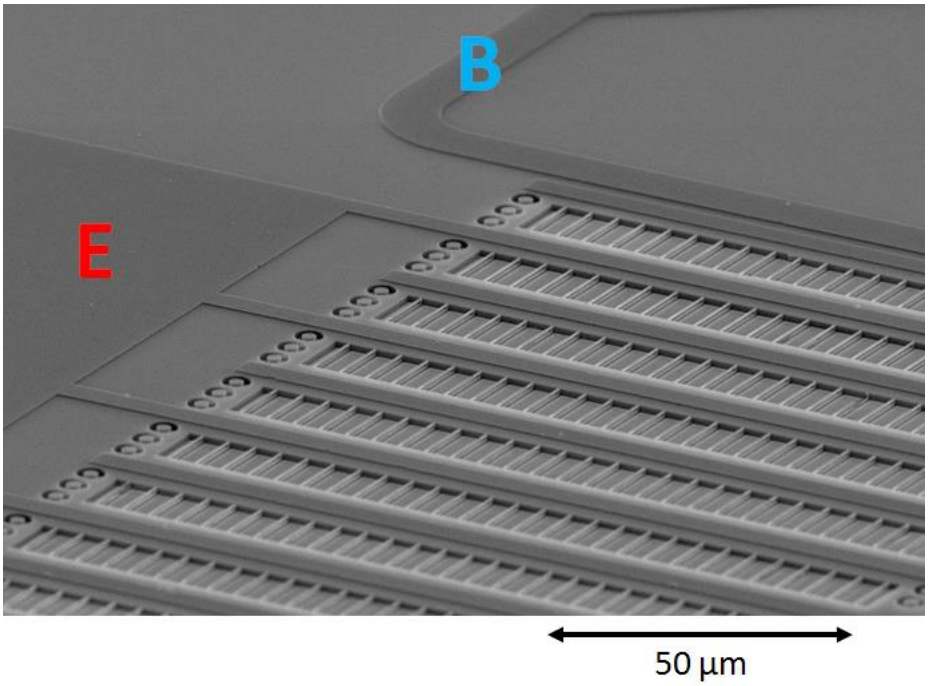

Figure 7.32 | Photonic device geometry for microwave and electric field control. Nanobeam photonic crystals are tiled in an array with intermittent electric field pads (E) for both Stark tuning and potential linewidth narrowing. A microwave stripline (B) provides alternating magnetic fields to drive spin transitions.

Another approach for narrowing linewidths would be to simply make a larger cavity, such that the nearby etched surfaces of the photonic crystal are further away. The linewidths of divacancies in the intrinsic layer of the sample 100-300 nm from the top surface display PLE linewidths of 1 GHz or less, which is narrow enough to distinguish spin sublevels. This means that a cavity design with at least 100-300 nm spacing between the divacancy at the etched holes should be sufficient to main suitably narrow linewidths.

Beyond the scope of entanglement and single-shot readout, the cavity interactions of this system provide an ideal platform for facilitating single-spin/single-photon interactions. Each pass of a photon that is near resonance with the divacancy transition results in a slight rotation of the spin state (the optical Stark effect) and a corresponding rotation of the photon polarization (Faraday rotation). Because the coupling strength between a bare divacancy and a photon is relatively weak,

this rotation is only on the order of microradians and is only measurable through extensive averaging, as has been demonstrated in reference [83] for the NV^- center in diamond. In a photonic cavity, a single photon will undergo multiple passes of the embedded spin defect and accumulate this rotation before leaking to the environment. In order to achieve a substantial rotation from a single photon, the quality factor of the cavity would have to be in the strong coupling regime such that $g > \kappa$. In this regime, it would be possible to establish significant single spin-photon interactions [84] and long distance quantum logic gates between spatially separated spins mediated by single photons [85].

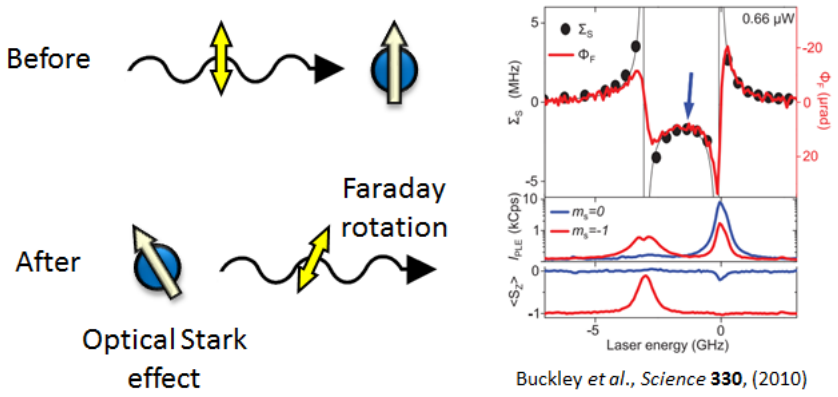

Figure 7.33 | Optical Stark effect and Faraday rotation. As a photon near resonance passes by an electron spin, the spin-photon interaction results in an equivalent rotation of the spin state and the polarization state. As many of these passes are accumulated in a photonic cavity, the effect becomes more pronounced. On the right is a demonstration of the optical Stark effect (top, black) and Faraday rotation (top, red) for an NV center in diamond after averaging many experiments. The right figure is adapted from [83].

To gauge how far the presented VV^0-cavity system is from strong coupling, we must obtain values for the key CQED parameters g, κ, γ. The leakage rate κ and spontaneous emission rate γ can be quickly obtained from the cavity quality factor and the optical lifetime:

$$\kappa = \frac{\omega_{cav}}{Q} = 3.5 \cdot 10^{11}\ Hz \tag{7.44}$$

$$\gamma = \frac{1}{15.7\ ns} = 6.37 \cdot 10^{7}\ Hz \tag{7.45}$$

An expression for g can be obtained based on its relation to the cooperativity and Purcell factor:

$$C = \frac{g^2}{2\kappa\gamma} \tag{7.46}$$

$$\frac{F-1}{4} = \frac{g^2}{2\kappa\gamma} \tag{7.47}$$

$$g = \sqrt{\frac{(F-1)\kappa\gamma}{2}} \tag{7.48}$$

If we use the $F \approx 50$ for the cavity presented in this work, then:

$$g \approx 2.4 \cdot 10^{10} \tag{7.49}$$

This is roughly a factor of 15 smaller than the cavity leakage rate, implying that a quality factor of 15*5,000 = 75,000 would be necessary to achieve strong coupling for this system. Alternatively, the Purcell factor can be substantially increased with improved spatial matching between the divacancy and the cavity mode. If we take the expression for the maximum Purcell factor with perfect atom/emitter matching:

$$F_{max} = \frac{3}{4\pi^2}\left(\frac{\lambda}{n}\right)^3\left(\frac{Q}{V}\right) + 1, \qquad \text{perfect matching with emitter} \tag{7.50}$$

And substitute Q = 5,000 and $V \approx 0.5\left(\frac{\lambda}{n}\right)^3$ for the nanobeam design, then:

$$F_{max} = \frac{3}{2\pi^2}(5000) + 1 = 761 \tag{7.51}$$

Which, coincidentally, is also a factor of ~15 greater than the observed Purcell factor of ~50. This implies that even with the current quality factor of 5,000, strong coupling could potentially be achieved if the emitter was perfectly spatially and spectrally matched to the cavity mode. Since this is extremely difficult to achieve in practice, a combination of higher Q and better coupling will be necessary to push this system into the strong coupling regime.

In conclusion, we have presented the fabrication and operation of an atom-cavity platform for the divacancy in silicon carbide that results in substantial enhancement of zero-phonon emission. Through multiple independent measurements, we have observed a Purcell factor of ~50, which results in an increase in the Debye-Waller factor from ~5% to ~70-75%. Additionally, we have demonstrated coherent spin control of the VV^0 ground state and coherence times that can be extended through the use of dynamical decoupling. Looking ahead, this system provides exciting opportunities to facilitate long-distance entanglement protocols and single spin/photon interactions. Scaling up to multi-node quantum networks, the photonically enhanced VV^0 system provides an attractive platform that is compatible with long-distance optical transmission through telecom fibers.

References

[1] William F. Koehl, Bob B. Buckley, F. Joseph Heremans, Greg Calusine, and David D. Awschalom. Room temperature coherent control of defect spin qubits in silicon carbide. *Nature*, 479:84-87, nov 2011.

[2] David J. Christle, Abram L. Falk, Paolo Andrich, Paul V. Klimov, Jawad Ul Hassan, Nguyen T. Son, Erik Janzén, Takeshi Ohshima, and David D. Awschalom. Isolated electron spins in silicon carbide with millisecond coherence times. *Nature Materials*, 14:160-163, feb 2015.

[3] David J. Christle, Paul V. Klimov, Charles F. de las Casas, Krisztián Szász, Viktor Ivády, Valdas Jokubavicius, Jawad Ul Hassan, Mikael Syväjärvi, William F. Koehl, Takeshi Ohshima, Nguyen T. Son, Erik Janzén, Ádám Gali, and David D. Awschalom. Isolated Spin Qubits in SiC with a High-Fidelity Infrared Spin-to-Photon Interface. *Physical Review X*, 7:021046, jun 2017.

[4] Abram L. Falk, Bob B. Buckley, Greg Calusine, William F. Koehl, Viatcheslav V. Dobrovitski, Alberto Politi, Christian A. Zorman, Philip X.-L. Feng, and David D. Awschalom. Polytype control of spin qubits in silicon carbide. *Nature Communications*, 4:1819, may 2013.

[5] Nguyen T. Son, Christopher P. Anderson, Alexandre Bourassa, Kevin C. Miao, Charles Babin, Matthias Widmann, Matthias Niethammer, Jawad Ul Hassan, Naoya Morioka, Ivan G. Ivanov, Florian Kaiser, Joerg Wrachtrup, and David D. Awschalom. Developing silicon carbide for quantum spintronics. *Applied Physics Letters*, 116:190501, may 2020.

[6] N. T. Son, P. Carlsson, J. ul Hassan, E. Janzén, T. Umeda, J. Isoya, A. Gali, M. Bockstedte, N. Morishita, T. Ohshima, and H. Itoh. Divacancy in 4H-SiC. *Physical Review Letters*, 96:055501, feb 2006.

[7] Stefania Castelletto, Lorenzo Rosa, and Brett C. Johnson. Silicon Carbide for Novel Quantum Technology Devices. Advanced Silicon Carbide Devices and Processing, *Intech Open*, 222−248, sep 2015.

[8] Xiaorui Guo, Qian Xun, Zuxin Li, and Shuxin Du. Silicon carbide converters and MEMS devices for high-temperature power electronics: A critical review. *Micromachines*, 10(6):406, jun 2019.

[9] Christian A. Zorman and Rocco J. Parro. Micro- and nanomechanical structures for silicon carbide MEMS and NEMS. *Physica Status Solidi (B)*, 245(7):1404-1424, jun 2008.

[10] Matthias Widmann, Sang-Yun Lee, Torsten Rendler, Nguyen Tien Son, Helmut Fedder, Seoyoung Paik, Li-Ping Yang, Nan Zhao, Sen Yang, Ian Booker, Andrej Denisenko, Mohammad Jamali, S. Ali Momenzadeh, Ilja Gerhardt, Takeshi Ohshima, Adam Gali, Erik Janzén, and Jörg Wrachtrup. Coherent control of single spins in silicon carbide at room temperature. *Nature Materials*, 14:164168, dec 2014.

[11] Roland Nagy, Matthias Niethammer, Matthias Widmann, Yu-Chen Chen, Péter Udvarhelyi, Cristian Bonato, Jawad Ul Hassan, Robin Karhu, Ivan G. Ivanov, Nguyen Tien Son, Jeronimo R. Maze, Takeshi Ohshima, Öney O. Soykal, Ádám Gali, Sang-Yun Lee, Florian Kaiser, and Jörg Wrachtrup. High-fidelity spin and optical control of single silicon vacancy centres in silicon carbide. *Nature Communications*, 10:1954 apr 2019.

[12] Hunter B. Banks, Öney O. Soykal, Rachael L. Myers-Ward, D. Kurt Gaskill, T.L. Reinecke, and Samuel G. Carter. Resonant optical spin initialization and readout of single silicon vacancies in 4H-SiC. *Physical Review Applied*, 11:024013, feb 2019.

[13] N. Mizuochi, S. Yamasaki, H. Takizawa, N. Morishita, T. Ohshima, H. Itoh, and J. Isoya. Continuous-wave and pulsed EPR study of the negatively charged silicon vacancy with S=3/2 and C3v symmetry in n-type 4H-SiC. *Physical Review B*, 66:235202, dec 2002.

[14] Roland Nagy, Matthias Widmann, Matthias Niethammer, Durga B. R. Dasari, Ilja Gerhardt, Öney O. Soykal, Marina Radulaski, Takeshi Ohshima, Jelena Vučković, Nguyen Tien Son, Ivan G. Ivanov, Sophia E. Economou, Cristian Bonato, Sang-Yun Lee, and Jörg Wrachtrup. Quantum properties of dichroic silicon vacancies in silicon carbide. *Physical Review Applied*, 9:034022, mar 2018.

[15] S. A. Zargaleh, S. Hameau, B. Eble, F. Margaillan, H. J. von Bardeleben, J. L. Cantin, and Weibo Gao. Nitrogen vacancy center in cubic silicon carbide: A promising qubit in the 1.5 m spectral range for photonic quantum networks. *Physical Review B*, 98:165203, oct 2018.

[16] H. J. von Bardeleben, J. L. Cantin, A. Csóré, A. Gali, E. Rauls, and U. Gerstmann. NV centers in 3C, 4H, and 6H silicon carbide: A variable platform for solid-state qubits and nanosensors. *Physical Review B*, 94:121202, sep 2016.

[17] A. Csóré, H. J. von Bardeleben, J. L. Cantin, and A. Gali. Characterization and formation of NV centers in 3C, 4H and 6H SiC: An ab initio study. *Physical Review B*, 96:085204, aug 2017.

[18] Jun-Feng Wang, Fei-Fei Yan, Qiang Li, Zheng-Hao Liu, He Liu, Guo-Ping Guo, Li-Ping Guo, Xiong Zhou, Jin-Ming Cui, Jian Wang, Zong-Quan Zhou, Xiao-Ye Xu, Jin-Shi Xu, Chuan-Feng Li, and Guang-Can Guo. Coherent control of nitrogen-vacancy center spins in silicon carbide at room temperature. *Physical Review Letters*, 124:223601, jun 2020.

[19] Gary Wolfowicz, Christopher P. Anderson, Berk Diler, Oleg G. Poluektov, F. Joseph Heremans, and David D. Awschalom. Vanadium spin qubits as telecom quantum emitters in silicon carbide. *Science Advances*, 6(18):eaaz1192, may 2020.

[20] Berk Diler, Samuel J. Whiteley, Christopher P. Anderson, Gary Wolfowicz, Marie E. Wesson, Edward S. Bielejec, F. Joseph Heremans, and David D. Awschalom. Coherent control and high-fidelity readout of chromium ions in commercial silicon carbide. *npj Quantum Information*, 6(11), jan 2020.

[21] Marcus W.Doherty, Neil B.Manson, Paul Delaney, Fedor Jelezko, Jörg Wrachtrup, and Lloyd C.L.Hollenberg. The nitrogen-vacancy colour centre in diamond. *Physics Reports*, 528 (1):1-45, jul 2013.

[22] V.V. Dobrovitski, G.D. Fuchs, A.L. Falk, C. Santori, and D.D. Awschalom. Quantum Control over Single Spins in Diamond. *Annual Review of Condensed Matter Physics*, 4:23-50, apr 2013.

[23] F. Joseph Heremans, Christopher G. Yale, and David D. Awschalom. Control of Spin Defects in Wide-Bandgap Semiconductors for Quantum Technologies. *Proceedings of the IEEE*, 104(10):2009-2023, may 2016.

[24] Paul V. Klimov, Abram L. Falk, David J. Christle, Viatcheslav V. Dobrovitski, and David D. Awschalom. Quantum entanglement at ambient conditions in a macroscopic solid-state spin ensemble. *Science Advances*, 1(10):e1501015, nov 2015.

[25] Abram L. Falk, Paul V. Klimov, Bob B. Buckley, Viktor Ivády, Igor A. Abrikosov, Greg Calusine, William F. Koehl, Ádám Gali, and David D. Awschalom. Electrically and Mechanically Tunable Electron Spins in Silicon Carbide Color Centers. *Physical Review Letters*, 112:187601, may 2014.

[26] Charles F. de las Casas, David J. Christle, Jawad Ul Hassan, Takeshi Ohshima, Nguyen T. Son, and David D. Awschalom. Stark tuning and electrical charge state control of single divacancies in silicon carbide. *Applied Physics Letters*, 111:262403, dec 2017.

[27] Samuel J. Whiteley, Gary Wolfowicz, Christopher P. Anderson, Alexandre Bourassa, He Ma, Meng Ye, Gerwin Koolstra, Kevin J. Satzinger, Martin V. Holt, F. Joseph Heremans, Andrew N. Cleland, David I. Schuster, Giulia Galli, and David D. Awschalom. Spin-phonon interactions in silicon carbide addressed by Gaussian acoustics. *Nature Physics*, 15:490-495, feb 2019.

[28] Péter Udvarhelyi and Adam Gali. Ab Initio Spin-Strain Coupling Parameters of Divacancy Qubits in Silicon Carbide. Physics Review Applied, 10:054010, nov 2018.

[29] Hosung Seo, Abram L. Falk, Paul V. Klimov, Kevin C. Miao, Giulia Galli, and David D. Awschalom. Quantum decoherence dynamics of divacancy spins in silicon carbide. *Nature Communications*, 7:12935, sep 2016.

[30] S. Meiboom and D. Gill. Modified spin-echo method for measuring nuclear relaxation times. *Review of Scientific Instruments*, 29:688-691, 1958.

[31] Kevin C. Miao, Alexandre Bourassa, Christopher P. Anderson, Samuel J. Whiteley, Alexander L. Crook, Sam L. Bayliss, Gary Wolfowicz, Gergő Thiering, Péter Udvarhelyi, Viktor Ivády, Hiroshi Abe, Takeshi Ohshima, Ádám Gali, and David D. Awschalom. Electrically driven optical interferometry with spins in silicon carbide. *Science Advances*, 5(11):eaay0527, nov 2019.

[32] Christopher G. Yale, Bob B. Buckley, David J. Christle, Guido Burkard, F. Joseph Heremans, Lee C. Bassett, and David D. Awschalom. All-optical control of a solid-state spin using coherent dark states. *Proceedings of the National Academy of Sciences*, 110(19):7595-7600, mar 2013.

[33] J. R. Maze, A. Gali, E. Togan, Y. Chu, A. Trifonov, E. Kaxiras, and M. D. Lukin. Properties of nitrogen-vacancy centers in diamond: the group theoretic approach. *New Journal of Physics*, 13:025025, feb 2011.

[34] Yiwen Chu and Mikhail D. Lukin. Quantum optics with nitrogen-vacancy centres in diamond. DOI:10.1093/oso/9780198768609.003.0005, 2017.

[35] E. Togan, Y. Chu, A. S. Trifonov, L. Jiang, J. Maze, L. Childress, M. V. G. Dutt, A. S. Sørensen, P. R. Hemmer, A. S. Zibrov, and M. D. Lukin. Quantum entanglement between an optical photon and a solid-state spin qubit. *Nature*, 466:730–734, aug 2010.

[36] M. L. Goldman, M. W. Doherty, A. Sipahigil, N. Y. Yao, S. D. Bennett, N. B. Manson, A. Kubanek, and M. D. Lukin. State-selective intersystem crossing in nitrogen-vacancy centers. *Physical Review B*, 91:165201, apr 2015.

[37] M. L. Goldman, A. Sipahigil, M. W. Doherty, N. Y. Yao, S. D. Bennett, M. Markham, D. J. Twitchen, N. B. Manson, A. Kubanek, and M. D. Lukin. Phonon-Induced Population Dynamics and Intersystem Crossing in Nitrogen-Vacancy Centers. *Physical Review Letters*, 114:145502, apr 2015.

[38] Kevin C. Miao, Joseph P. Blanton, Christopher P. Anderson, Alexandre Bourassa, Alexander L. Crook, Gary Wolfowicz, Hiroshi Abe, Takeshi Ohshima, and David D. Awschalom. Universal coherence protection in a solid-state spin qubit. *Science*, 369(6510):1493-1497, sep 2020.

[39] Alexandre Bourassa, Christopher P. Anderson, Kevin C. Miao, Mykyta Onizhuk, He Ma, Alexander L. Crook, Hiroshi Abe, Jawad Ul-Hassan, Takeshi Ohshima, Nguyen T. Son, Giulia Galli, and David D. Awschalom. Entanglement and control of single nuclear spins in isotopically engineered silicon carbide. *Nature Materials*, 19:1319-1325, sep 2020.

[40] H. Bernien, B. Hensen, W. Pfaff, G. Koolstra, M. S. Blok, L. Robledo, T. H. Taminiau, M. Markham, D. J. Twitchen, L. Childress, and R. Hanson. Heralded entanglement between solid-state qubits separated by three metres. *Nature* 497:86-90, apr 2013.

[41] Gary Wolfowicz, Christopher P. Anderson, Andrew L. Yeats, Samuel J. Whiteley, Jens Niklas, Oleg G. Poluektov, F. Joseph Heremans, and David D. Awschalom. Optical charge state control of spin defects in 4H-SiC. *Nature Communications*, 8:1876, nov 2017.

[42] Nguyen T. Son and Ivan G. Ivanov. Charge state control of the silicon vacancy and divacancy in silicon carbide. *Journal of Applied Physics*, 129:215702, may 2021.

[43] Christopher P. Anderson, Alexandre Bourassa, Kevin C. Miao, Gary Wolfowicz, Peter J. Mintun, Alexander L. Crook, Hiroshi Abe, Jawad Ul Hassan, Nguyen T. Son, Takeshi Ohshima, and David D. Awschalom. Electrical and optical control of single spins integrated in scalable semiconductor devices. *Science*, 366(6470):1225-1230, dec 2019.

[44] D. A. Golter and C. W. Lai. Optical switching of defect charge states in 4H-SiC. *Scientific Reports* 7:13406, oct 2017.

[45] Ariana Beste, DeCarlos E. Taylor, D. Andrew Golter, and Chih W. Lai. Charge state switching of the divacancy defect in 4H-SiC. *Physical Review B*, 98:214107, dec 2018.

[46] L. Gordon, A. Janotti, and C. G. Van de Walle. Defects as qubits in 3C- and 4H-SiC. *Physical Review B*, 92(4):045208, jul 2015.

[47] Andreas Reiserer and Gerhard Rempe. Cavity-based quantum networks with single atoms and optical photons. *Reviews of Modern Physics*, 87(1379):1379-1418, dec 2015.

[48] Matthew Pelton. Modified spontaneous emission in nanophotonic structures. *Nature Photonics*, 9:427-435, jun 2015.

[49] Luozhou Li, Tim Schröder, Edward H. Chen, Michael Walsh, Igal Bayn, Jordan Goldstein, Ophir Gaathon, Matthew E. Trusheim, Ming Lu, Jacob Mower, Mircea Cotlet, Matthew L. Markham, Daniel J. Twitchen, and Dirk Englund. Coherent spin control of a nanocavity-enhanced qubit in diamond. *Nature Communications*, 6:6173, jan 2015.

[50] B. J. M. Hausmann, B. J. Shields, Q. Quan, Y. Chu, N. P. de Leon, R. Evans, M. J. Burek, A. S. Zibrov, M. Markham, D. J. Twitchen, H. Park, M. D. Lukin, and M. Loncăr. Coupling of NV centers to photonic crystal nanobeams in diamond. *Nano Letters*, 13(12):5791-5796, oct 2013.

[51] Jonathan C. Lee, David O. Bracher, Shanying Cui, Kenichi Ohno, Claire A. McLellan, Xingyu Zhang, Paolo Andrich, Benjamin Alemán, Kasey J. Russell, Andrew P. Magyar, Igor Aharonovich, Ania Bleszynski Jayich, David Awschalom, and Evelyn L. Hu. Deterministic coupling of delta-doped nitrogen vacancy centers to a nanobeam photonic crystal cavity. *Applied Physics Letters*, 105:261101, dec 2014.

[52] Andrei Faraon, Charles Santori, Zhihong Huang, Victor M. Acosta, and Raymond G. Beausoleil. Coupling of nitrogen-vacancy centers to photonic crystal cavities in monocrystalline diamond. *Physical Review Letters*, 109:033604, jul 2012.

[53] Greg Calusine, Alberto Politi, and David D. Awschalom. Silicon carbide photonic crystal cavities with integrated color centers. *Applied Physics Letters*, 105:011123, jul 2014.

[54] Greg Calusine, Alberto Politi, and David D. Awschalom. Cavity-Enhanced Measurements of Defect Spins in Silicon Carbide. *Physical Review Applied*, 6:014019, jul 2016.

[55] David O. Bracher and Evelyn L. Hu. Fabrication of High-Q Nanobeam Photonic Crystals in Epitaxially Grown 4H-SiC. *Nano Letters*, 15(9):6202-6207, aug 2015.

[56] David O. Bracher, Xingyu Zhang, and Evelyn L. Hu. Selective Purcell enhancement of two closely linked zero-phonon transitions of a silicon carbide color center. *Proceedings of the National Academy of Sciences*, 114(16):4060-4065, mar 2017.

[57] Marina Radulaski, Thomas M. Babinec, Sonia Buckley, Armand Rundquist, J Provine, Kassem Alassaad, Gabriel Ferro, and Jelena Vučković. Photonic crystal cavities in cubic (3C) polytype silicon carbide films. *Optics Express*, 21(26):32623-32629, 2013.

[58] Shota Yamada, Bong-Shik Song, Seungwoo Jeon, Jeremy Upham, Yoshinori Tanaka, Takashi Asano, and Susumu Noda. Second-harmonic generation in a silicon-carbide-based photonic crystal nanocavity. *Optics Letters*, 39(7):1768-1771, 2014.

[59] Jonathan Y. Lee, Xiyuan Lu, and Qiang Lin. High-Q silicon carbide photonic-crystal cavities. *Applied Physics Letters*, 106:041106, jan 2015.

[60] Bong-Shik Song, Takashi Asano, Seungwoo Jeon, Heungjoon Kim, Changxuan Chen, Dongyeon Daniel Kang, and Susumu Noda. Ultrahigh-Q photonic crystal nanocavities based on 4H silicon carbide. *Optica*, 6(8):991-995, 2019.

[61] Mehmet Ozgur, Michael Pedersen, and Michael Huff. Comparison of the Etch Mask Selectivity of Nickel and Copper for a Deep, Anisotropic Plasma Etching Process of Silicon Carbide (SiC). *ECS Journal of Solid State Science and Technology*, 7:55-59, jan 2018.

[62] Feng Zhao, Mohammad M.Islam, Chih-Fang Huang. Photoelectrochemical etching to fabricate single-crystal SiC MEMS for harsh environments. *Materials Letters*, 65(3):409-412, feb 2011.

[63] Shojan P. Pavunny, Rachael L. Myers-Ward, Kevin M. Daniels, Wendy Shia, Karthik Sridhara, Matthew T. DeJarld, Anthony K. Boyd, Francis J. Kub, Paul A. Kohl, Samuel G. Carter, and D. Kurt Gaskill. On the doping concentration dependence and dopant selectivity of

photogenerated carrier assisted etching of 4H-SiC epilayers. *Electrochimica Acta*, 323(10):134778, nov 2019.

[64] K.R. Williams K. Gupta, and M. Wasilik. Etch Rates for Micromachining Processing-Part II. *Journal of Microelectromechanical Systems*, 12(6):761-778, dec 2003.

[65] W. Pfaff, B. J. Hensen, H. Bernien, S. B. van Dam, M. S. Blok, T. H. Taminiau, M. J. Tiggelman, R. N. Schouten, M. Markham, D. J. Twitchen, and R. Hanson. Unconditional quantum teleportation between distant solid-state quantum bits. *Science*, 345(6196):532-535, aug 2014.

[66] B. Hensen, H. Bernien, A. E. Dréau, A. Reiserer, N. Kalb, M. S. Blok, J. Ruitenberg, R. F. L. Vermeulen, R. N. Schouten, C. Abellán, W. Amaya, V. Pruneri, M. W. Mitchell, M. Markham, D. J. Twitchen, D. Elkouss, S. Wehner, T. H. Taminiau, and R. Hanson. Loophole-free Bell inequality violation using electron spins separated by 1.3 kilometres. *Nature* 526:682–686, oct 2015.

[67] Amy Butcher, Xinghan Guo, Robert Shreiner, Nazar Delegan, Kai Hao, Peter J. Duda III, David D. Awschalom, F. Joseph Heremans, and Alexander A. High. High-Q Nanophotonic Resonators on Diamond Membranes using Templated Atomic Layer Deposition of TiO_2. *Nano Letters*, 20(6):4603-4609, may 2020.

[68] Alexander L. Crook, Christopher P. Anderson, Kevin C. Miao, Alexandre Bourassa, Hope Lee, Sam L. Bayliss, David O. Bracher, Xingyu Zhang, Hiroshi Abe, Takeshi Ohshima, Evelyn L. Hu, and David D. Awschalom. Purcell enhancement of a single silicon carbide color center with coherent spin control. *Nano Letters*, 20(5):3427-3434, mar 2020.

[69] Chuting Wang, Evan Miyazono, Ioana Craiciu, and Andrei Faraon. Hybrid silicon on silicon carbide integrated photonics platform. *Applied Physics Letters*, 115:141105, oct 2019.

[70] Ulagalandha Perumal Dharanipathy, Momchil Minkov, Mario Tonin, Vincenzo Savona, and Romuald Houdré. High-Q silicon photonic crystal cavity for enhanced optical nonlinearities. *Applied Physics Letters*, 105:101101, sep 2014.

[71] Hiroshi Sekoguchi, Yasushi Takahashi, Takashi Asano, and Susumu Noda. Photonic crystal nanocavity with a Q-factor of ~9 million. *Optics Express*, 22(1):916-924, 2014.

[72] Takashi Asano, Yoshiaki Ochi, Yasushi Takahashi, Katsuhiro Kishimoto, and Susumu Noda. Photonic crystal nanocavity with a Q factor exceeding eleven million. *Optics Express*, 25(3) 1769-1777, 2017.

[73] Parag B. Deotare, Murray W. McCutcheon, Ian W. Frank, Mughees Khan, and Marko Lončar. High quality factor photonic crystal nanobeam cavities. *Applied Physics Letters*, 94:121106, mar 2009.

[74] H. Jacobson, J. Birch, C. Hallin, A. Henry, R. Yakimova, T. Tuomi, and E. Janzén. Doping-induced strain in N-doped 4H-SiC crystals. *Applied Physics Letters*, 82:3689–3691, may 2003.

[75] H. J. Chung, J. Q. Liu, and M. Skowronski. Stacking fault formation in highly doped 4H-SiC epilayers during annealing. *Applied Physics Letters*, 81:3759, nov 2002.

[76] Robert S. Okojie and Thomas Holzheu. X-ray diffraction measurement of doping induced lattice mismatch in n-type 4H-SiC epilayers grown on p-type substrates. *Applied Physics Letters*, 83:1971, sep 2003.

[77] S. W. Huh, H. J. Chung, M. Benamara, M. Skowronski, J. J. Sumakeris, and M. J. Paisley. Doping-induced strain and relaxation of Al-doped 4H-SiC homoepitaxial layers. *Journal of Applied Physics*, 96:4637, oct 2004.

[78] Paul V. Klimov. Quantum information processing with electronic and nuclear spins in semiconductors. PhD thesis, University of Chicago, 2016.

[79] S. O. Hruszkewycz, S. Maddali, C. P. Anderson, W. Cha, K. C. Miao, M. J. Highland, A. Ulvestad, D. D. Awschalom, and F. J. Heremans. Strain annealing of SiC nanoparticles revealed through Bragg coherent diffraction imaging for quantum technologies. *Physical Review Materials*, 2:086001, aug 2018.

[80] Kenneth W. Lee, Donghun Lee, Preeti Ovartchaiyapong, Joaquin Minguzzi, Jero R. Maze, and Ania C. Bleszynski Jayich. Strain Coupling of a Mechanical Resonator to a Single Quantum Emitter in Diamond. *Physical Review Applied*, 6:034005, sep 2016.

[81] Lucio Robledo, Lilian Childress, Hannes Bernien, Bas Hensen, Paul F. A. Alkemade, and Ronald Hanson. High-fidelity projective read-out of a solid-state spin quantum register. *Nature*, 477:574-578, sep 2011.

[82] Mouktik Raha, Songtao Chen, Christopher M. Phenicie, Salim Ourari, Alan M. Dibos, and Jeff D. Thompson. Optical quantum nondemolition measurement of a solid-state spin without a cycling transition. *Nature Communications*, 11:1605, mar 2020.

[83] B. B. Buckley, G. D. Fuchs, L. C. Bassett, and D. D. Awschalom. Spin-Light Coherence for Single-Spin Measurement and Control in Diamond. *Science*, 330(6008):1212-1215, nov 2010.

[84] T. G. Tiecke, J. D. Thompson, N. P. de Leon, L. R. Liu, V. Vuletić, and M. D. Lukin. Nanophotonic quantum phase switch with a single atom. *Nature*, 508:241-244, apr 2014.

[85] Severin Daiss, Stefan Langenfeld, Stephan Welte, Emanuele Distante, Philip Thomas, Lukas Hartung, Olivier Morin, and Gerhard Rempe. A quantum-logic gate between distant quantum-network modules. *Science*, 371(6529):614-617, feb 2021.